Investigation of Nanostructured Materials for CO_2 Conversion and Urea Electrooxidation

A Thesis Submitted for the Degree of

Doctor of Philosophy

By

Nijita Mathew

JNCASR

Chemistry and Physics of Materials Unit

Jawaharlal Nehru Centre for Advanced Scientific Research

(An Institution deemed to be University)

Bangalore-560064 (India)

January 2025

Dedicated to my adorable parents,

Jitin and Amal

DECLARATION

I hereby declare that the thesis entitled "***Investigation of nanostructured materials for CO_2 Conversion and Urea Electrooxidation***" is an authentic record of research work carried out by me at the Chemistry and Physics of Materials Unit, Jawaharlal Nehru Centre for Advanced Scientific Research, Bangalore, India, under the supervision of **Prof. M. Eswaramoorthy** and that it has not been submitted elsewhere for the award of any degree or diploma.

In keeping with the general practice in reporting scientific observations, due acknowledgements have been made whenever the work described is based on the findings of other investigators. Any omission that might have occurred due to oversight or error in judgement is regretted.

Nijita Mathew

Jawaharlal Nehru Centre for Advanced Scientific Research

Prof. M. Eswaramoorthy

Chemistry and Physics of
Materials Unit
Jawaharlal Nehru Centre for
Advanced Scientific Research
(JNCASR)
Bangalore-560064, India

Phone: +91 80 2208 2870
Email: eswar@jncasr.ac.in

Date: 3rd February 2025

CERTIFICATE

I hereby certify that the matter embodied in this thesis entitled "***Investigation of nanostructured materials for CO_2 Conversion and Urea Electrooxidation***" has been carried out by **Ms. Nijita Mathew** at the Chemistry and Physics of Materials Unit, Jawaharlal Nehru Centre for Advanced Scientific Research, Bangalore, India, under my supervision and it has not been submitted elsewhere for the award of any degree or diploma.

Bangalore, India

Prof. M. Eswaramoorthy

(Research Supervisor)

ACKNOWLEDGEMENTS

*I would like to take this opportunity to express my heartfelt gratitude to everyone who has provided their invaluable support during my Ph.D. First and foremost, I would like to express my heartfelt gratitude to my thesis supervisor, **Prof. M. Eswaramoorthy**, for his invaluable support and guidance throughout my research journey. I am deeply thankful to him for introducing me to the fascinating field of nanostructured materials and catalysis. His expertise and critical insights have been instrumental in helping me develop a profound understanding of this domain. I sincerely appreciate the freedom he granted me to explore and design my own research projects, which greatly enriched my learning experience. I have come to value the importance of patience, perseverance, dedication, and discipline in achieving research goals and in life. His impeccable ethics and unwavering commitment have been truly inspiring. It has been an honour to work under his guidance and to learn from his wealth of knowledge and experience.*

*I sincerely thank **Prof. C.N.R. Rao, FRS,** for being a constant source of inspiration. I am deeply grateful to him for fostering such a dynamic and innovation-driven research environment at JNCASR.*

I thank the past and present chairpersons of CPMU for allowing me to use the various facilities at the centre

I would like to thank my GSAC committee members Prof. Tapas K. Maji, Prof. Subi J. George and Prof. A. Sundaresan for their invaluable inputs and guidance.

I would like to thank the faculty members at JNCASR Prof. Balasubramanian, Prof. Eswaramoorthy, Prof. Swapan Pati, Dr. Sarit Agasti, Prof. Chandrabhas, Prof. Ranjan Datta, Prof. Shobhana Narasimhan, Prof. Rajesh Ganapathy, Prof. Kanishka Biswas, Prof. Sebastian Peter, Prof. Premkumar Senguttuvan, Prof. Umesh Waghmare, Prof. Sundaresan, and Prof. Ravishankar from IISC for their informative course works.

I would like to thank Prof. Subi George and Dr. Shikha Dhiman for their guidance and support during my MS summer project in the Supramolecular Chemistry lab.

I express my gratitude to my collaborators for the insightful discussion and fruitful collaborations: Dr. Radha Rathod, Prof. Pralay K . Santra, Dr. Soumitra, Prof. T.K. Maji, Sougata Saha, Prof. Swapan K. Pati for the fruitful collaborations.

I am grateful to Prof. Kanishka Biswas and India@DESY, DST for selecting our proposal and providing the necessary funding to conduct XAS experiments at PETRA III, DESY, Germany. I would also like to sincerely thank Prof. Wolfgang A. Caliebe for his invaluable support in conducting the experiments and for patiently teaching us every aspect of the analysis.

A heartfelt thanks to my ever enthusiastic past and present labmates, the Nanocats, for their support and guidance throughout this journey. They fostered a collaborative and enriching environment where we could freely exchange ideas and learn from one another, making this experience truly unforgettable: Dr. Sisir Maity, Dr. Dheeraj Kumar Singh, Dr. Sonu K.P., Dr. Shivanna, Dr. Mehraj, Dr. Subrahmanya, Dr. Sushumna, Dr. Monoj, Dr. Sudhakar, Dr. Suchismita Biswas, Dr. Soumita Chakraborty, Dr. Momin Ahamed, Dr. Surishi Vashishth, Dr. Divya Bhutani, Dr. Swaraj Sarvottam, Abhishek, Ujjwal, Daizy, Avinash, Yadhu, Sneha, Elizabeth, Dr. Vismita, Pankaj, Atif, Deepak, Himani, Bibekannanda. Special thanks to Arunava Saha for being an exceptional colleague and a dear friend, his memory lives on in our heart.

I would like to thank the summer students Kapil, Sirichandana, Keerthana and Nisha for their help in carrying out the experiments.

I would like to thank Dr. Monis, Dr. Arjun, Dr. Ashutosh, Dr. Bitan, Dr. Saptarishi, Dr. Anupam and Nilutpal for all the support and the fruitful scientific discussions.

I would like to thank the JNC technical staff for their help with various characterization techniques: Mrs. Usha (TEM), Mr. Kanan (FESEM), Mr. Vasu (CPMU instrumentation lab), Mr. Alla Srinavas Rao (CPMU), Mr. Anil (PXRD and Raman Spectroscopy), Ms. Meenakshi (FESEM), Mr. Arun (TEM), Ms, Selvi (FESEM), Mr. Mahesh (ICMS instruments), Mr. Shiva (NCU instruments), Mrs. Durgasri (NMR), Mr. Deepak (NMR), Mr. Sachin (XPS), Mrs. Remya (XPS), Mr. Rahul (TEM), Mr. Srihari (FESEM), Ms. Manju (FESEM). I would also like to thank Mr. Rajkumar (workshop) and Mr. Nandkishore (glassblower) for their help in creating different setups for the experiments.

I would like to thank Mr. Raja (TES) and Mr. Guruprasad (Agilent) for providing research assistance. I would also like to thank Rajesh and CeNS Bangalore for the HAADF-STEM- Elemental Mapping measurement.

I sincerely acknowledge the staff in Academic, Admin, Complab, Library, Hostel, Mess, Dining hall, Accounts, Dhanvantari, Administrative office, Mr. Nandish (ICMS gas bank), Mr. Balaraj (CPMU gas bank), Mr. Arun (Safety officer), Mrs. Usha (CPMU office) and Mrs. Ramya(ICMS office) for their support whenever needed.

I sincerely acknowledge JNCASR for the financial assistance and ICMS, SaMat, JNCASR for the advanced research facilities.

I am deeply grateful to my friends in JNCASR. The countless moments of laughter, conversations, and shared experiences have been truly priceless, and I will cherish them forever: Arjun, Momin, Monis, Mehraj, Subrahmanyam, Abhishek, Rohit, Shashank, Ashutosh, Manaswee, Bitan, Anu, Janaky, Niloy, Sreyan, Vinita, Surabhi, Divya C, Devesh, Aditi, Ankit, Bhupesh, Reetendra, Sushmita, Ruchika, Brijesh, Tarandeep, Prajwal, Meenakshi Tayade and Nikita. I would also like to thank my friends back at home who have been my childhood companions and hold a special place in my heart: Maitri, Aastha, Harshal, Rosmy, Ruchi, Christina and Deepali.

I would like to thank a special bunch of people. Their companionship has brought immense joy, helping me navigate both the highs and lows of this journey. I will always treasure the memories that we have created together: Suchi di, Soumita di, Surishi, Himani, Daizy and Anjana.

I would like to express my deepest gratitude to my family especially my parents, parents in law, Anjana and Jitin for their unconditional love, unwavering support, and endless encouragement throughout this journey. Their belief in me has been my greatest source of strength and motivation.

Last but not the least, I am forever grateful to my life partner and best friend Amal for standing by me through every challenge, celebrating my successes, and providing me with the comfort and guidance I needed.

Nijita Mathew

PREFACE

This thesis is divided into two parts. **Part 1** deals with the development of a catalyst for CO_2 conversion to formic acid by thermocatalytic and electrocatalytic methods. **Part 2** deals with the development of an electrocatalyst for urea electrooxidation by modifying nickel hydroxide catalysts.

PART 1

Chapter 1.1. discusses the significance of developing Carbon Capture and Utilization technology as a strategy to mitigate anthropogenic CO_2. The primary challenge in CO_2 conversion lies in activating the molecule due to its inherent chemical stability. This chapter emphasizes the crucial role of catalytic methods in overcoming this stability and facilitating the activation of CO_2. The chapter is further divided into two parts. The first part focuses on the thermocatalytic conversion of CO_2 to methanol and formic acid, providing an overview of various catalysts and discussing strategies for their modification to enhance efficiency. The second part addresses the electrocatalytic conversion of CO_2, elaborating on the reaction mechanisms and the spectrum of products generated. It categorizes metal catalysts based on their product selectivity and examines key factors influencing catalytic performance, such as the role of electrolytes and electrolyzers.

Chapter 1.2. deals with the development of NiPd/C_3N_4 as an efficient catalyst for the thermocatalytic conversion of CO_2 to formic acid under high pressure and temperature conditions. The catalyst was synthesized at room temperature by $NaBH_4$ assisted reduction. It was evaluated using various characterization techniques such as PXRD, FESEM, TEM, and XPS to identify the nature of the active site. The role of the different components of the catalyst was established. It was identified that Ni exists as $Ni(OH)_2$ and aids in the activation of CO_2, Pd aids in the activation of H_2, while C_3N_4 aids in the adsorption of the CO_2 closer to the metal active site. These components work in tandem, resulting in high catalytic activity. With this catalyst, a maximum TON of 2432 was obtained for a reaction duration of 24 h. CO_2 TPD and *operando* DRIFTS were used to gain mechanistic insights into the catalytic process. Further, the post reaction characterization of the catalyst has been used to identify the reason behind the loss in activity in subsequent cycles.

Chapter 1.3. deals with the development of a trimetallic CuSnBi nanostructured catalyst for the electrochemical reduction of CO_2. Herein, the synergistic interaction between the three metal species results in improved catalytic activity. The introduction of Bi results in an increase in the formation of the catalytically active CuOx-SnOx interface. The formation of this interface has led to low overpotentials and a high formate faradaic efficiency of 80% at 1.45 V (vs. RHE) in comparison to CuSn nanostructures and SnO_2. The catalyst also exhibits stability of upto 6 h at 1.05V (vs RHE). Post reaction characterization shows that the reduction of the oxides to the metallic state is minimized, resulting in the retention of the active interface. Furthermore, *operando* ATR-FTIR spectroscopy has been used to determine the intermediates formed during the reaction.

PART 2

Chapter 2.1. discusses the importance of using H_2 as a fuel and thereby a shift to hydrogen economy as an alternative to the conventional way of producing energy. The chapter discusses the significance of electrochemical water splitting as an energy efficient method to produce hydrogen in comparison to steam reforming. It identifies oxygen evolution reaction (OER) as a significant bottleneck of water electrolysis. The chapter highlights the importance of hybrid water electrolysis, mainly focusing on urea assisted water electrolysis (UOR), as an effective strategy to reduce the overall potential for H_2 production. It discusses the challenges associated with UOR, followed by a detailed discussion of the analytical tools used to identify the mechanistic pathway. Finally, the different electrocatalysts explored and the strategies utilized to develop them have also been reviewed.

Chapter 2.2. deals with the Pd/Ni(OH)$_2$ as an efficient catalyst for urea electrooxidation. The introduction of Pd led to enhanced kinetics, resulting in a higher current density and a decrease in the overpotential in comparison to Ni(OH)$_2$. The catalyst also exhibits a stability of upto 300 h. Additionally, a significant improvement in intrinsic activity was observed in comparison to Ni(OH)$_2$. TPD studies with CO$_2$ show that the presence of Pd helps weaken the CO$_2$ binding with Ni(OH)$_2$, thereby preventing active site poisoning. Mechanistic pathway for urea electrooxidation was investigated using potentiostatic impedance spectroscopy, *operando* ATR-FTIR, and Raman spectroscopy.

Chapter 2.3 deals with elucidating the mechanistic pathway for urea electrooxidation on Ni$_3$N. In this work, A-Ni$_3$N was synthesized by nitridation of electrodeposited Ni(OH)$_2$ on Ni foam, followed by activation using chronopotentiometry. A-Ni$_3$N demonstrated remarkable stability for up to 300 hours at 100 mA cm^{-2} and a maximum current density of 800 mA cm^{-2} at 1.5 V$_{RHE}$. *Operando* Raman spectroscopy and PEIS studies were conducted to understand the electrooxidation pathway, showing that urea electrooxidation follows a direct pathway on A-Ni$_3$N.

TABLE OF CONTENTS

PART -1

Chapter 1.1. Introduction to CO_2 conversion

Summary

Chapter 1.2. Investigation of CO_2 hydrogenation over $NiPd/C_3N_4$ catalyst

Summary

Chapter 1.3. Synergistic effects of Bismuth on CO_2 electroreduction to formate in CuSn catalyst

Summary

PART-2

Chapter 2.1. Introduction to electrochemical Urea oxidation

Summary

Chapter 2.2. Improvement in the overall performance for electrochemical urea oxidation by introduction of Pd in $Ni(OH)_2$

Summary

Chapter 2.3. Investigation of the urea electrooxidation pathway on Ni_3N

Summary

PART 1

Chapter 1.1. Introduction to CO_2 conversion

Chapter 1.2. Investigation of CO_2 hydrogenation over NiPd/C_3N_4 catalyst

Chapter 1.3. Synergistic Effects of Bismuth on CO_2 electroreduction to formate in Cu-Sn catalyst

Chapter- 1.1

An introduction to carbon dioxide conversion

Summary:

The conversion of CO_2 into value-added chemicals offers a sustainable approach to tackling the challenges of global warming, making the development of these carbon dioxide removal technologies crucial. Thermocatalytic and electrocatalytic methods are key techniques for studying this conversion process. A comprehensive understanding of the fundamentals of these catalytic processes is essential to design an efficient catalyst. This chapter provides a detailed discussion of these two approaches, reviewing catalytic pathways and various catalysts explored in the field.

1.1.1. Carbon Capture Utilization and Storage (CCUS)

The onset of the industrial revolution sparked a notable surge in the utilization of fossil fuels to produce energy, consequently amplifying CO_2 emissions, as shown in *Figure 1.1.1*[1]. The 2023 IPCC report highlights this trend, emphasizing a consistent increase in greenhouse gas emissions[2]. In line with the 2015 Paris Agreement, there is a strong global commitment to limiting the increase in global surface temperatures to well below 2 °C above pre-industrial levels, with a preferred target of 1.5 °C. Adhering to this threshold is necessary to address the adverse impacts of climate change.

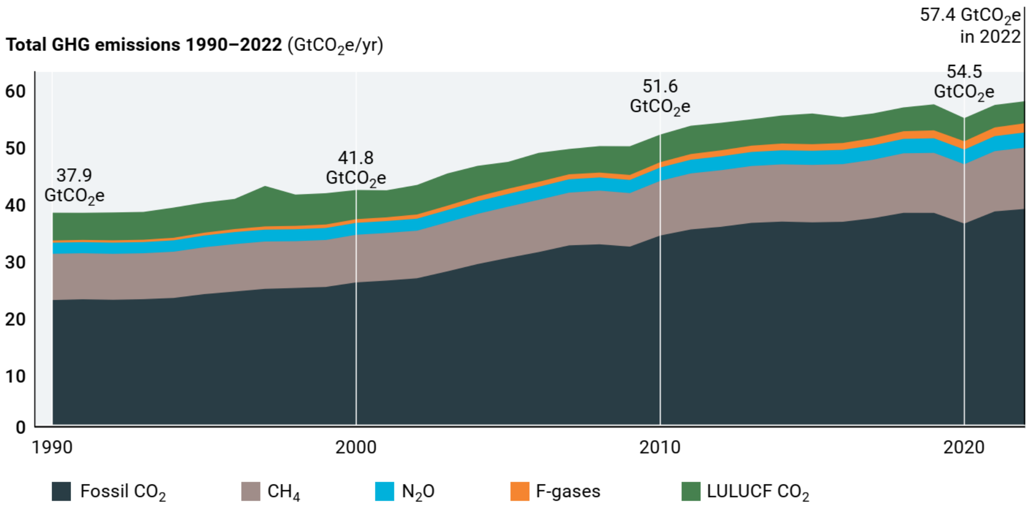

Figure 1.1.1: Total Net anthropogenic GHG emissions (adapted from *Emissions Gap Report 2023: Broken Record – Temperatures hit new highs, yet world fails to cut emissions (again).* United Nations Environment Programme (2023))

Achieving the ambitious target of net-zero emissions by 2030 requires decisive and immediate action. As a result, there has been a significant increase in attention toward carbon dioxide removal technologies in recent years. Progress in this direction has seen exploration into two primary forms of Carbon Dioxide Removal (CDR) technologies: Carbon Capture and Storage (CCS) and Carbon Capture and Utilization (CCU)[3,4]. Among these, CCU has emerged as a focal point, garnering heightened interest due to its potential to facilitate a circular economy, as shown in *Figure 1.1.2*. This approach focuses on utilizing emitted CO_2 as a feedstock for producing essential chemicals.

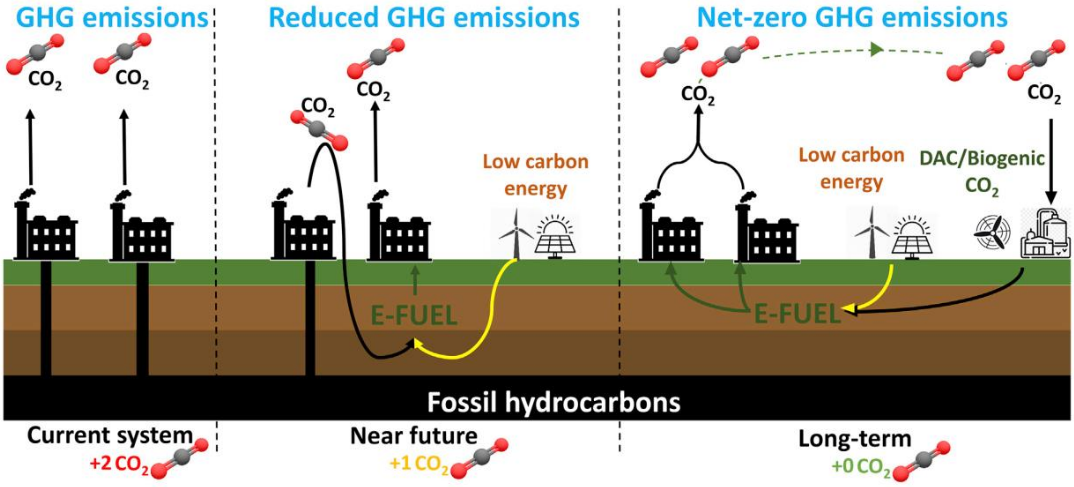

Figure 1.1.2: Carbon Capture and Utilization technology facilitates the circular economy, leading to net zero GHG emissions. Reproduced with permission from reference (4)

Carbon Capture and Utilization (CCU) becomes even more compelling when paired with renewable energy sources like solar and wind. This integration not only reduces CO_2 emissions but also promotes the efficient use of sustainable resources, contributing to broader environmental and innovation goals.

1.1.2. Stability of CO_2 molecule

Although CO_2 can be used as an essential feedstock, its usage is limited owing to its high thermodynamic stability. CO_2 is a linear molecule with strong C=O bonds of length 1.16 Å [5,6]. The reduction of CO_2 takes place by the formation of the C-C and C-H bonds by the cleavage of the C-O bonds.

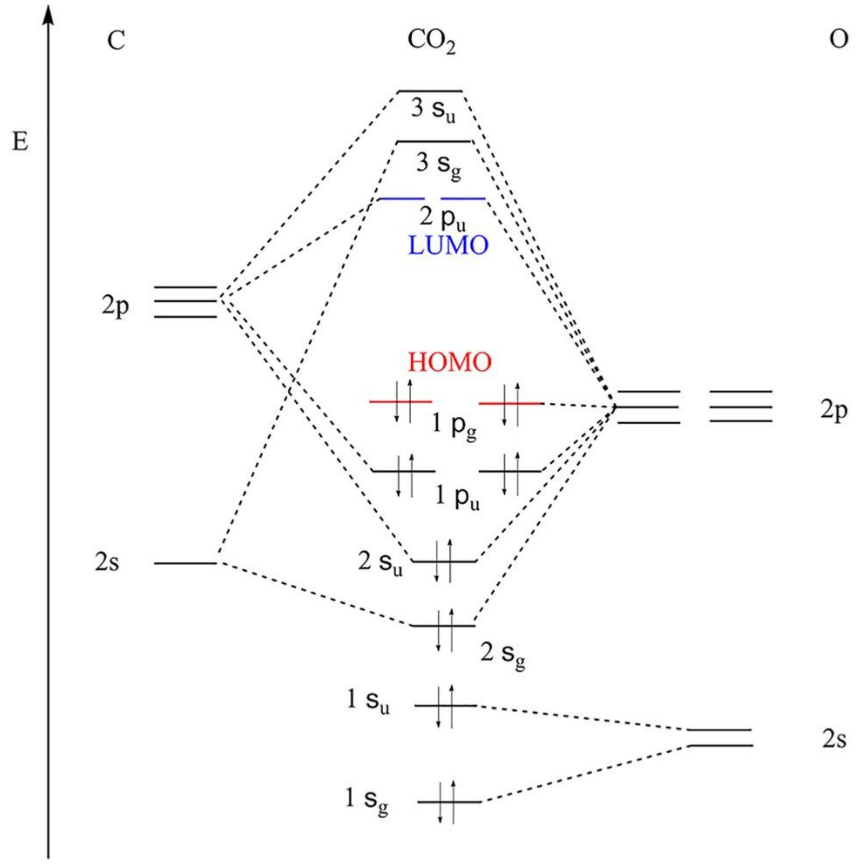

Figure 1.1.3: Molecular Orbital diagram of CO_2. Reproduced with permission from reference (6)

The molecular orbitals of CO_2 are formed by the interaction of the 2s and 2p atomic orbitals of carbon and oxygen, as shown in *Figure 1.1.3*. The doubly occupied non-bonding $1\pi_g$ orbital forms the highest occupied molecular orbital (HOMO), with its electrons primarily contributed by the oxygen atoms. The lowest unoccupied molecular orbital (LUMO) is the antibonding $2\pi_u$ orbital, predominantly contributed by the carbon atom. The oxygen atoms act as Lewis bases, while the carbon atom behaves as a Lewis acid. The stability of the CO_2 molecule is attributed to its large HOMO-LUMO gap, which results in a high Gibbs free energy barrier for activation and conversion. Consequently, the activation of CO_2 is the rate-determining step in its reduction, making the process endergonic. However, the electronegativity difference between carbon and oxygen imparts polarity to the C–O bonds. This polarity makes the carbon atom susceptible to nucleophilic attack, critical for the activation and subsequent reduction of CO_2.

1.1.3. Thermocatalytic conversion of CO_2

Thermocatalytic conversion of CO_2 is performed under high pressure and temperature conditions. It is predominantly converted to methanol and formic acid. These two products find application in various industrial sectors and are essential precursors for synthesizing other value-added chemicals.

1.1.3.1. CO_2 hydrogenation to Methanol

The conversion of CO_2 to methanol has garnered significant attention for two primary reasons: firstly, methanol serves as an efficient fuel, and secondly, it can be used as an important platform chemical for synthesizing value-added products such as hydrocarbons, olefins, etc. Industrially, methanol is predominantly produced from syngas. This process has been commercialized since 1966 and uses $Cu/ZnO/Al_2O_3$ catalyst, operating at temperatures of 200-300 ^{o}C and pressures between 50 and 100 bar[7]. A major discovery by Joo et al. revealed that blending CO_2 with syngas enhances the methanol yield[8]. Consequently, CO_2 blended syngas has been widely adopted for the synthesis of methanol. However, direct conversion of CO_2 to methanol will prove to be less energy intensive and thus is an attractive alternative. The reactions involved in the conversion of CO_2 to methanol are as follows:

CO_2 hydrogenation: $CO_2 + H_2 \rightarrow CH_3OH + H_2O$ $\Delta H^{o}_{298K} = -49.5\ kJ\ mol^{-1}$

Reverse water-gas shift: $CO_2 + H_2 \rightarrow CO + H_2O$ $\Delta H^{o}_{298K} = 41.0\ kJ\ mol^{-1}$

CO hydrogenation: $CO + 2H_2 \rightarrow CH_3OH$ $\Delta H^{o}_{298K} = -90.5\ kJ\ mol^{-1}$

The hydrogenation of CO_2 and CO is an exothermic process, while the reverse water-gas shift reaction (RWGS) is endothermic. Thermodynamically, the hydrogenation of CO_2 to methanol is favorable under low reaction temperatures and high pressure conditions. At higher temperatures, the reverse water gas shift dominates and, along with methanol, CO, hydrocarbons, and other oxygenates, are also obtained[9–12].

There are two possible pathways for this hydrogenation reaction: the formate and carboxyl pathways. HCOO* is the major intermediate in the formate pathway, which gets hydrogenated to form methanol. In the carboxyl pathway, $COOH^*$ becomes the dominant intermediate, which is hydrogenated to methanol. The preferred pathway depends on the chosen catalyst and reaction conditions.

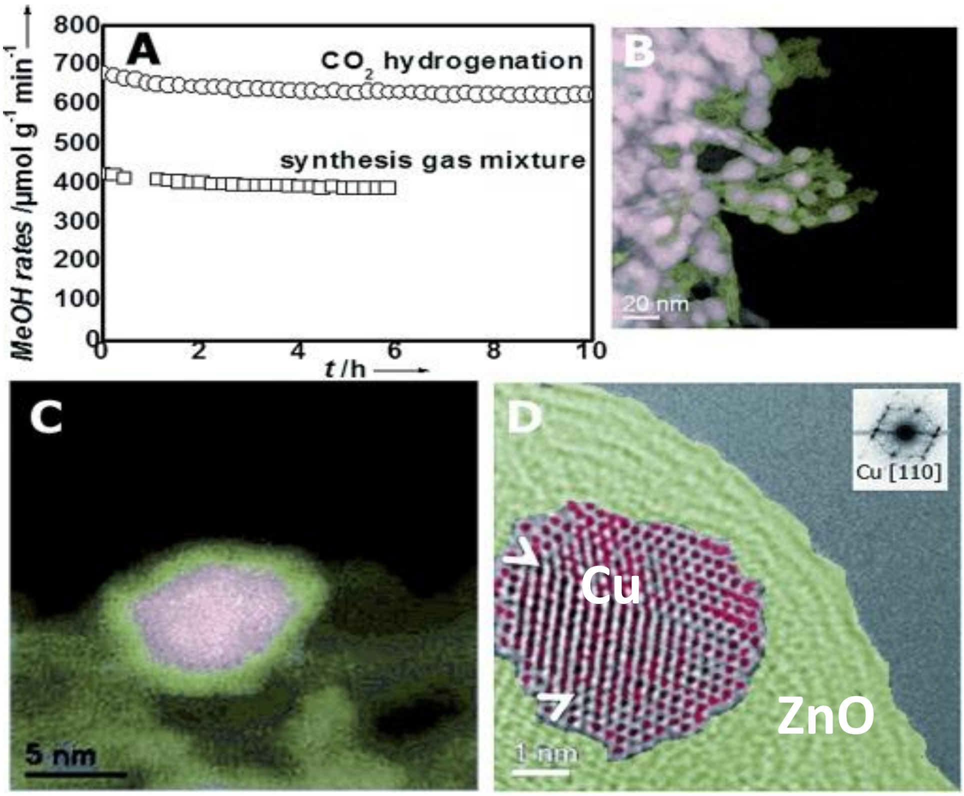

Figure1.1.4: (a) Plot of methanol formation rate vs time for a syngas mixture and CO_2 hydrogenation, **(b)** and **(c)** HAADF STEM image of $Cu/ZnO/Al_2O_3$ and **(d)** HRTEM image of $Cu/ZnO/Al_2O_3$. Reproduced with permission from reference (15)

Copper based catalysts have been extensively studied for this reaction. Herein, the Cu-ZnO interface *(Figure 1.1.4)* has been identified as crucial for methanol synthesis[13–15]. The primary role of ZnO is to stabilize Cu^+ species and the key intermediates during methanol synthesis. For instance, in $Cu/ZnO/Al_2O_3$ catalyst, it is observed that due to the dynamic, strong metal support interaction (SMSI), ZnO_x is present at the defect rich Cu edge sites. The presence of Zn strengthens the binding of the oxygen bound intermediates, resulting in enhanced catalytic activity[16].

The introduction of promoters can further enhance the catalytic activity. Alkali and alkaline earth metals, such as Ba and K, have been utilized as promoters for Cu/Al_2O_3 catalysts. Their addition influences the catalytic pathway, guiding it toward either methanol synthesis or the reverse water-gas shift (RWGS) reaction[17]. Metal oxides such as Al_2O_3, CeO_2, ZrO_2, and TiO_2 can be used both as promoters and as supports. For instance, the introduction of bimetallic oxides such as Ti-Zr, Ce-Zr, and Ce-Ti improves the Cu surface area and the surface basicity, which helps to improve the adsorption capacity of CO_2 and H_2.[18–20]

In addition to Cu-based catalysts, In_2O_3-based catalysts are also employed. These catalysts have garnered attention due to their superior water tolerance and high methanol selectivity. In_2O_3 supported on ZrO_2 has proven to be an effective catalyst with stability upto 1000 h in comparison to the commercial Cu-based system, which deactivates in 100 h. The major role of ZrO_2 in this catalyst is to maintain the oxygen vacancies and prevent the sintering of the In_2O_3 particles[21]. The introduction of promoters such as Cu, Pt, Ga, and Pd can further improve the activity of In_2O_3 based catalysts. The primary role of these metals is to aid in the dissociative adsorption of H_2. [22–26]

Gallium based catalysts such as Ni-Ga alloy[27,28] and Pd-Ga alloy[29] have also been studied for this reaction. For instance, $Ni_{75}Ga_{25}$ alloy nanoparticles supported on SiO_2 have shown a methanol selectivity of 54% compared to the alloys with lower GaO_x content. This enhancement in the activity was attributed to the Ga induced isolation of the Ni sites. This modifies the electronic structure such that Ni has a partial positive charge while Ga has a partial negative charge. Moreover, the isolation of the Ni sites prevents the methanation, while the Ga/GaO_x aids in the selective formation of methanol[27].

1.1.3.2.CO_2 hydrogenation to formic acid

Owing to the high hydrogen volumetric capacity of 53 g /L, formic acid is a potential liquid hydrogen storage material. It is highly stable, non-toxic, and portable unlike gaseous hydrogen[30]. Apart from this, formic acid finds its application in various sectors such as pharmaceuticals, leather, rubber,etc[31] *(Figure1.1.5).*

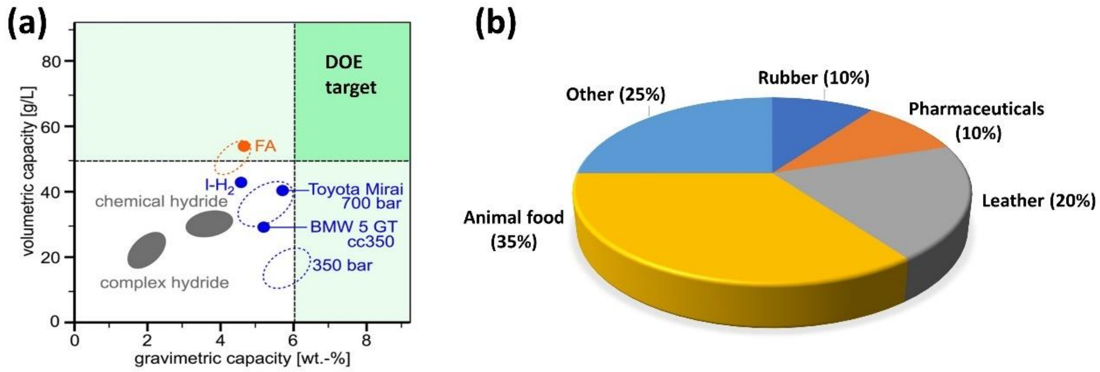

Figure 1.1.5: (a) Plot of volumetric capacity vs. gravimetric capacity for H_2 comparing formic acid with other H_2 storage options (reproduced with permission from reference 30) and **(b)** Uses of formic acid in different sectors (reproduced with permission from reference 31)

Conversion of CO_2 to formic acid is thermodynamically unfavorable in the gaseous phase primarily due to the positive Gibbs free energy.

$$CO_2\ (g) + H_2\ (g) \leftrightarrow HCOOH\ (l)) \qquad 32.9\ kJ\ mol^{-1}$$

However, the dissolution of CO_2 in the aqueous medium results in a decrease in entropy, thereby lowering the Gibbs free energy to -4 kJ mol^{-1}, making the process spontaneous.[32,33]

$$CO_2\ (aq) + H_2\ (g) \leftrightarrow HCOOH\ (l)) \qquad -4\ kJ\ mol^{-1}$$

The equilibrium can be further shifted in the forward direction through esterification by reacting formic acid with methanol[34] or by its reaction with amines[35] or inorganic bases, such as bicarbonates or carbonates[36].

The use of a heterogeneous catalyst for formate synthesis was first reported in 1914, with Pd black serving as the catalyst where $KHCO_3$ was used as the carbon source.[33] This was followed by the report by Farlow et al., where the hydrogenation was performed using Raney Nickel as the catalyst in the presence of amine as the base in ethanol[37]. The primary challenge with these bulk catalysts was their low activity and rapid deactivation. Nanostructuring these metal catalysts addresses this issue by modifying their electronic structure and increasing the exposure of active sites, thereby enhancing their catalytic activity.

Pd based catalysts

Palladium based catalysts are extensively studied for this reaction. The ability of Pd to adsorb and dissociate H_2, forming reactive surface hydrides, makes it an excellent choice for this reaction[38–40]. Several monometallic Pd based catalysts have been explored. In these catalysts, the size of the Pd nanoparticles and the choice of the support played a crucial role in directing the catalytic activity. Supports containing nitrogen functional groups are of enormous interest owing to their abundant basic functional groups, such as amines, Schiff base, pyridinic-N, pyrrolic-N, and graphitic-N etc. These functional groups govern the catalytic performance of these metal nanoparticles by facilitating CO_2 adsorption and activation. They also act as anchoring sites for Pd nanoparticles, ensuring their uniform dispersion and modulating their electronic properties[41,42]. Likewise, the size of the metal nanoparticles controls the formation of the catalytically active interfaces. For instance, in Pd/C_3N_4, the decrease in particle size from 7.2 to 3.4 nm showed an enhancement in the TOF. This is attributed to the increased interaction of the Pd nanoparticles with the nitrogen functional groups of C_3N_4, thereby increasing the number of interfacial sites. At these active sites, the hydrides formed on the Pd surface interacted with the CO_2 bound to the basic sites of the support to yield formic acid[43].

Metal oxides such as CeO_2, ZrO_2, ZnO, and TiO_2 have also been employed as supports[44–46]. The basicity of these supports facilitates the activation of CO_2 and H_2. For instance, in Pd/CeO_2, the high basicity of CeO_2 facilitates the activation of CO_2 on its surface, making the activation of H_2 the rate-determining step. Conversely, in the Pd/ZnO catalyst, the low basicity of ZnO shifts the rate-determining step to the activation of CO_2[47]. Similarly, the moderate basicity of TiO_2 offers optimal adsorption strength for CO_2, thereby promoting its activation and subsequent reaction with hydrides on the Pd surface, exhibiting a TOF of 1369 for formate[45]. Likewise, Pd supported on tetragonal ZrO_2 showed a high production rate of 2817 in comparison to the monoclinic phase primarily due to the higher concentration of the basic sites on the tetragonal phase that are responsible for CO_2 activation[48].

Palladium based bimetallic catalysts have been widely investigated for CO_2 conversion to formic acid. Compared to monometallic catalysts, incorporating a second metal alters the electronic properties, thereby influencing the adsorption behaviour of reactive intermediates. Yamashita and co-workers have reported several PdAg based catalysts, which have been found to show exceptional activity toward this reaction [36,49–52]. For instance, in Pd@Ag/TiO_2, most of the Pd formed the core of the nanoparticle, with very few Pd sites exposed on the surface surrounded by Ag atoms. The addition of Ag to Pd enhanced the intrinsic activity of the catalyst by enabling electron transfer from Ag to Pd. This increased the electronegativity of the Pd atoms, thereby improving the adsorption of reaction intermediates. The catalyst showed a high TON of 14839, which was calculated with respect to the surface exposed Pd sites[52]. In another report, PdAg encapsulated in polyethyleneimine(PEI)-functionalized hollow mesoporous organosilica spheres (HMOS) exhibited a TON of 2754 *(Figure 1.1.6)*. Herein, PEI was found to play a key role in the adsorption and activation of CO_2 through the formation of a carbamate intermediate, which concentrates activated CO_2 near the metal active sites where it reacts with the surface hydrides to form formate[49].

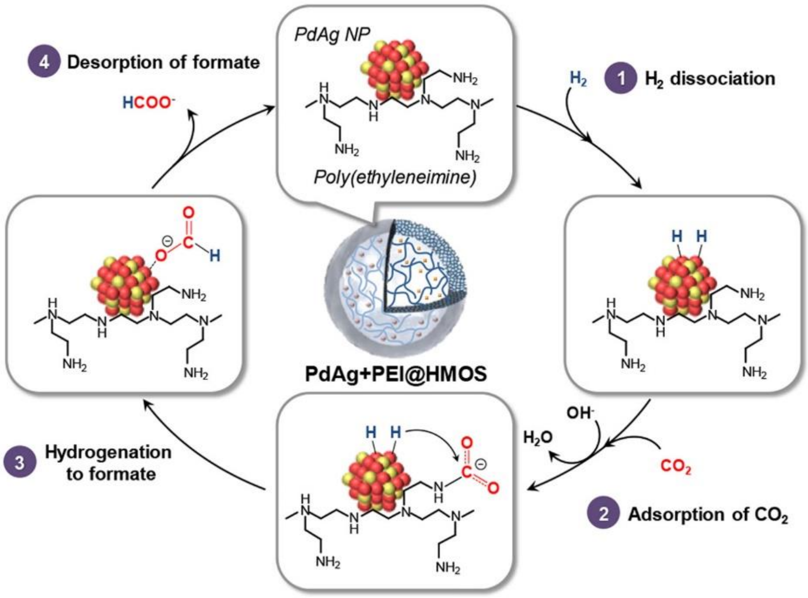

Figure 1.1.6: Mechanism of CO_2 hydrogenation on PdAg+PEI@HMOS. Reproduced with permission from reference (49)

Non-noble metals such as Co, Mn, Cu, V, and Ni have been used to replace Ag for preparing cost-effective catalyst[35,53–56]. Sun et al. reported PdCo confined within mesoporous silica nanospheres as an effective catalyst for the hydrogenation reaction[53]. In this catalyst, the electron transfer from CoO to Pd enhances the hydrogenation of bicarbonate, achieving a high turnover frequency (TOF) of 1824 h^{-1}. Likewise, in the case of PdMn alloy encapsulated in silicalite, it was observed that Mn species play two major role. First it facilitates the formation of the bicarbonates which is the key intermediate, and secondly, it induces the charge transfer from Mn to Pd, forming an electron enriched Pd surface, which promotes the hydrogenation to formate[35].

Ru based Catalysts

Like Pd, the H_2 dissociation ability of Ru has attracted significant attention for hydrogenation reactions. It has been observed that Ru in the form of Ru hydroxide or as single atoms exhibits higher activity compared to RuO_2[57–59]. The choice of the catalyst support plays a crucial role in generating the active sites. For instance, the hydroxyl group content on γ-Al_2O_3 is higher than that on MgO. Hydroxyl groups on metal oxides serve two key functions: (i) they promote the formation of highly dispersed amorphous Ru species and Ru single atoms, and (ii) they increase the electron density of Ru through hydroxyl ligands. The pH of the catalyst preparation solution influences active site formation on these supports. At low pH, the interaction between Ru and hydroxyl groups on γ-Al_2O_3 is not favored. The resultant catalyst shows decreased CO_2 hydrogenation activity. Similarly, at pH>13, Ru hydroxides convert to RuO_2, leading to reduced activity. However, at an optimal pH of 12.8, the catalyst achieves a maximum TON of 139, attributed to the formation of active sites. Additionally, the Ru loading also impacted the catalytic activity. The Ru/γ-Al_2O_3 exhibited excellent performance at a loading of ~2 wt%. However, increasing the metal loading to 6 wt% causes the amorphous Ru hydroxide to aggregate into RuO_2 crystallites, thereby reducing the activity[57].

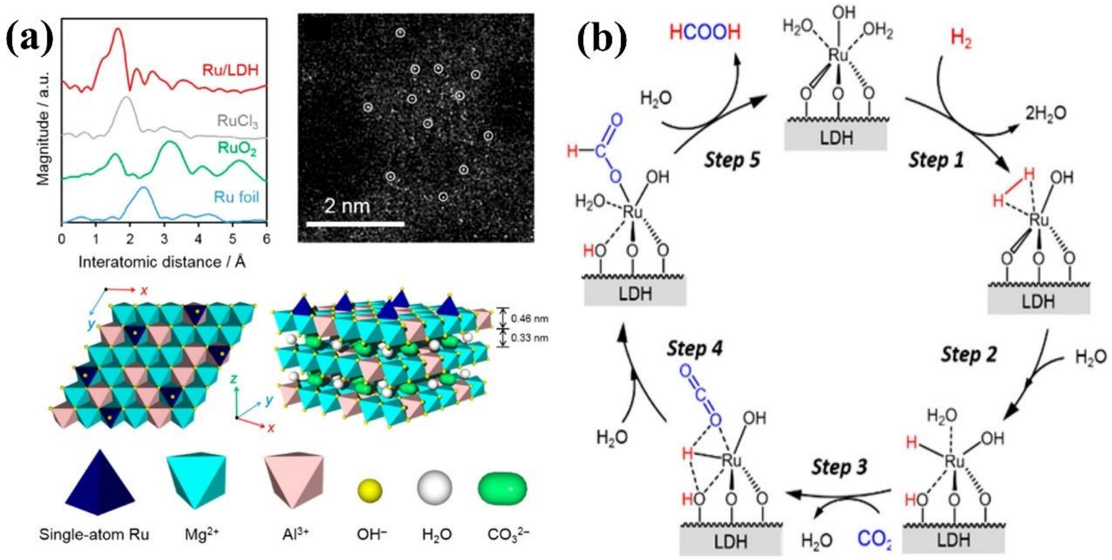

Figure 1.1.7: (a) Ru single atom supported on LDH and **(b)** Reaction mechanism for CO_2 hydrogenation to formate on Ru/Mg-Al LDH. Reproduced with permission from reference (59)

Layered double hydroxides are a class of layered material with a general formula $[M_{1-x}^{2+}M_x^{3+}(OH)_2]^{x+}(A^{n-})_{x/n}\cdot yH_2O$. Here, M^{2+} and M^{3+} stand for divalent and trivalent cations, respectively; A^{n-} represents the anion. They are made up of positively charged brucite like layers wherein the metal cations are octahedrally coordinated with hydroxide ions. Some of the M^{2+} is substituted with M^{3+}, creating positively charged layers, which are balanced by the intercalated anions and water molecules present in the interlayer region[60,61]. The presence of the hydroxyl ion makes it a suitable support for anchoring Ru. For instance, in the case of Ru supported on Mg-Al LDH *(Figure 1.1.7)*, it is observed that the isolated single atomic Ru species were formed by coordination with the hydroxyl group on the LDH surface. The hydroxyl ions make the Ru site electron rich, thereby enhancing its catalytic activity. Additionally, the hydroxyl sites show high CO_2 adsorption, thereby concentrating the CO_2 near the active site[59].

Au based Catalysts

The first report on the use of Au in hydrogenation reactions was published by Bond et al. in 1973, wherein the small sized Au nanoparticles were found to be catalytically active for olefin hydrogenation[62]. Since then, Au based catalysts have been extensively explored for the hydrogenation reactions. These reactions are structure sensitive, with the highly dispersed Au species serving as the real active site. However, the stabilization of ultra small Au nanoparticles remains a significant challenge. Au/TiO_2 catalyst (AUROlite) was the first Au based catalyst used for the continuous hydrogenation of CO_2 to formate in the presence of NEt_3. The catalyst showed exceptional activity upto 37 days and a total TON of 18040[63].

To understand the role of the support, Filonenko et al. screened a wide variety of supports, such as Al_2O_3, TiO_2, ZnO, CeO_2, MgAl-HT, MgCr-HT, and $CuCr_2O_4$. Among these supports, Au supported on Al_2O_3 displayed exceptional activity wherein Al_2O_3 assisted in the heterolytic dissociation of H_2 on the metallic Au site as well as in adsorbing CO_2 in the form of bicarbonates[64].

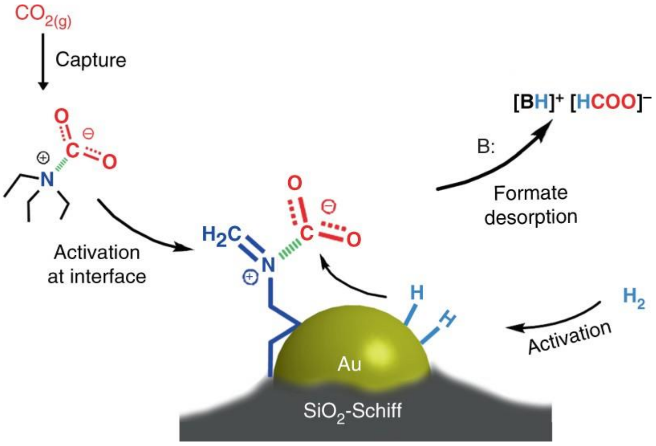

Figure 1.1.8: CO_2 hydrogenation at Au-Schiff base interface. Reproduced with permission from reference (34)

Functionalizing supports with N-containing moieties appears to be an effective approach to improving the catalytic performance of Au catalysts. Liu et al. demonstrated that the Schiff base modified SiO_2 serves as an excellent support for dispersing ultra small Au nanoparticles, which were highly active for the direct reduction of CO_2 to formate[34]. The Schiff base moiety has a dual function. First, the Schiff base acts as a Lewis base and adsorbs CO_2 on the surface in the form of a zwitter-ion adduct *(Figure 1.1.8)*. Second, the electron donation from the nitrogen groups renders Au negatively charged, favoring the formation of reactive hydride species. Moreover, the activity of the Au nanoparticles was found to be size dependent, wherein the increasing size of the Au nanoparticle lowers the catalytic activity while a decrease in the particle size results in electron rich Au species, making it a highly reactive site.

Noble metal free catalyst

The high cost and the low abundance of noble metals limited their use for large scale applications of CO_2 hydrogenation to formate. Hence, there is a need to develop noble metal free catalysts[65–67]. Recently, Z. Wang et al. reported edge rich MoS_2 (ER-MoS_2) as a potential catalyst for this reaction[66]. The activity was compared with bulk MoS_2, nanoporous MoS_2 (NP-MoS_2) and large sheet MoS_2 ((LS-MoS_2). The catalysts showed the following activity trend: (ER-MoS_2) >(NP-MoS_2)> (LS-MoS_2)> (bulk-MoS_2). The sulfur vacancies in edge rich MoS_2 act as the active site. Water dissociatively adsorbs as OH* and H* on these sulfur vacancies and serves as the hydrogenating agents, resulting in a TOF of 780.7 h^{-1}.

1.1.4. Electrocatalytic CO_2 reduction

An energy efficient alternative to the thermocatalytic conversion of CO_2 is the electrochemical conversion of CO_2. Herein, electric potential is applied to convert CO_2 into value added products. The falling cost of renewable energy has further drawn attention to this process as the electric energy required can be drawn from these sources. The major advantage of this process is that these can be carried out under ambient conditions and in aqueous medium. Furthermore, CO_2 can be converted into a plethora of products such as CO, HCOOH, CH_3OH, C_2H_4, CH_4, etc. The selectivity for a particular product can be tuned by choosing the appropriate catalyst and by varying the applied potential.

1.1.4.1.Mechanistic Pathway

Electrochemical conversion of CO_2 is a multistep proton-electron transfer process. The first step in this conversion is the activation of the CO_2 molecule. Herein, CO_2 is bound to the catalytically active site either through C or O linkage. In the CO_2 molecule, C is in its highest oxidation state, i.e. +4. Thus, an electron transfer takes place to the CO_2 molecule, making it into $CO_2^{\bullet-}$ anion radical. The thermodynamic potential required for this process is -1.9 V_{SHE}. The competing reaction to CO_2 electroreduction is the electrochemical water splitting to produce H_2, which has the thermodynamic potential of 0 V_{SHE}. Hence, the choice of the catalyst and the applied potential plays a crucial role in driving the CO_2 conversion. The formation of the $CO_2^{\bullet-}$ is followed by protonation, resulting in the formation of intermediates such as *COOH, *OCHO, and *CO. The formation of the *OCHO intermediate results in formate as the final product, while the formation of *COOH results in CO as the major product. During the reaction, the *CO formed can also undergo dimerization or protonation. The direct protonation of *CO can result in CH_3OH, CH_4, and HCHO, while the dimerization of the *CO results in the formation of C_{2+} products such as ethanol, propanol, C_2H_4, C_2H_6 etc. The thermodynamic potential required for each product is provided in *Table 1.1.1*, and the reaction mechanism is shown in *Figure 1.1.9*[68–70].

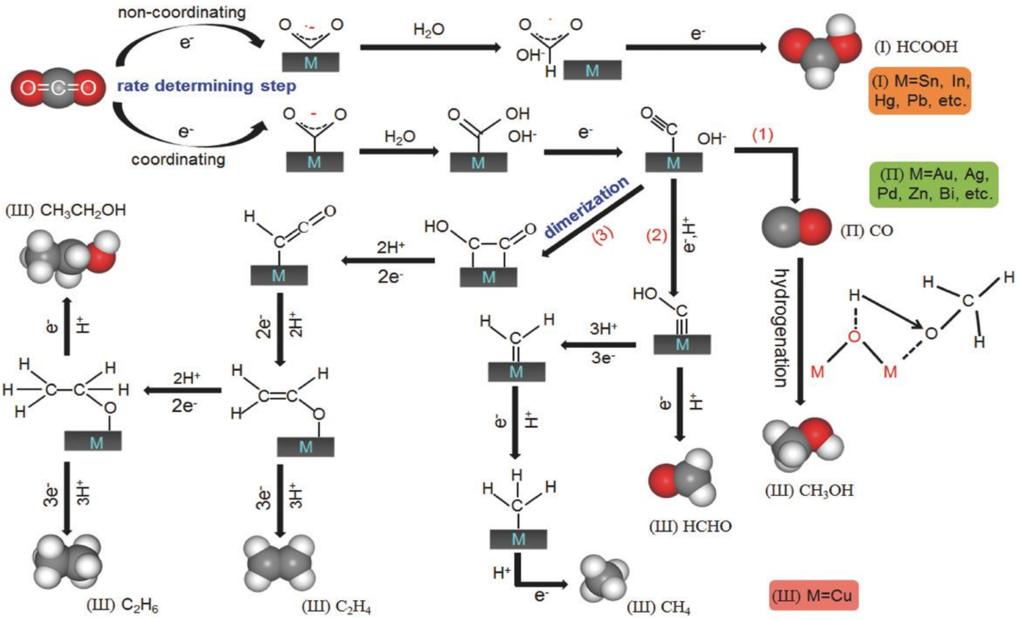

Figure 1.1.9: Mechanistic pathway for the electroreduction of CO_2 to different products in aqueous solution. Reproduced with permission from reference (68)

Table 1.1.1: Electrochemical potential of possible CO_2 reduction reactions in aqueous solutions. Rreproduced with permission from reference (68)

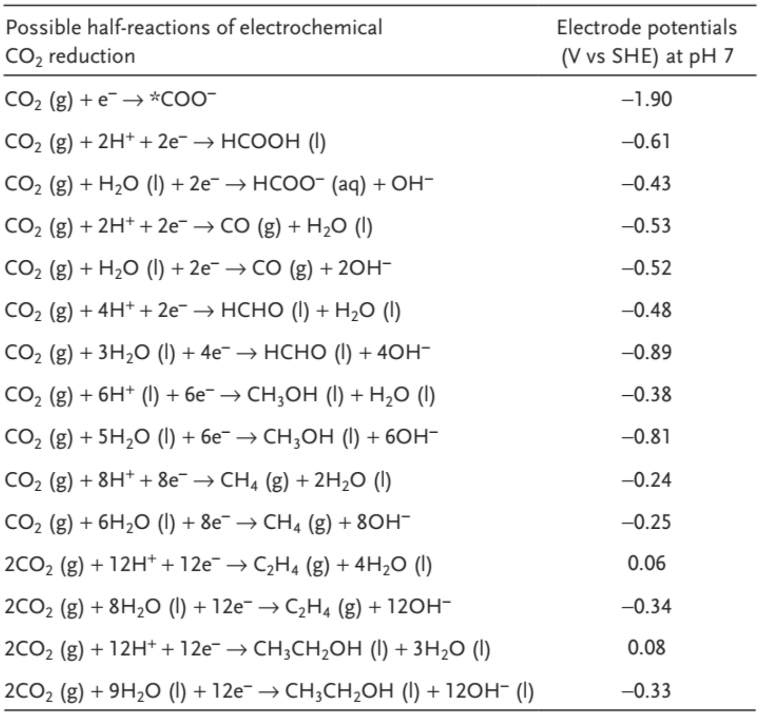

Possible half-reactions of electrochemical CO_2 reduction	Electrode potentials (V vs SHE) at pH 7
CO_2 (g) + e^- → $*COO^-$	−1.90
CO_2 (g) + $2H^+$ + $2e^-$ → HCOOH (l)	−0.61
CO_2 (g) + H_2O (l) + $2e^-$ → $HCOO^-$ (aq) + OH^-	−0.43
CO_2 (g) + $2H^+$ + $2e^-$ → CO (g) + H_2O (l)	−0.53
CO_2 (g) + H_2O (l) + $2e^-$ → CO (g) + $2OH^-$	−0.52
CO_2 (g) + $4H^+$ + $2e^-$ → HCHO (l) + H_2O (l)	−0.48
CO_2 (g) + $3H_2O$ (l) + $4e^-$ → HCHO (l) + $4OH^-$	−0.89
CO_2 (g) + $6H^+$ (l) + $6e^-$ → CH_3OH (l) + H_2O (l)	−0.38
CO_2 (g) + $5H_2O$ (l) + $6e^-$ → CH_3OH (l) + $6OH^-$	−0.81
CO_2 (g) + $8H^+$ + $8e^-$ → CH_4 (g) + $2H_2O$ (l)	−0.24
CO_2 (g) + $6H_2O$ (l) + $8e^-$ → CH_4 (g) + $8OH^-$	−0.25
$2CO_2$ (g) + $12H^+$ + $12e^-$ → C_2H_4 (g) + $4H_2O$ (l)	0.06
$2CO_2$ (g) + $8H_2O$ (l) + $12e^-$ → C_2H_4 (g) + $12OH^-$	−0.34
$2CO_2$ (g) + $12H^+$ + $12e^-$ → CH_3CH_2OH (l) + $3H_2O$ (l)	0.08
$2CO_2$ (g) + $9H_2O$ (l) + $12e^-$ → CH_3CH_2OH (l) + $12OH^-$ (l)	−0.33

1.1.4.2.Classification of electrocatalyst

One of the pioneering studies on CO_2 electroreduction was conducted by Hori et al., where CO_2 electrolysis was carried out at a constant current density of 5 mA cm^{-2} on various metal electrodes, and both gaseous and liquid products were quantified. This work classified the metal electrode into CO selective (Ag, Au, Zn, Pd), formate selective (Pb, Hg, In, Sn, Cd, Tl), and C_{2+} products selective (Cu) metals[71]. This categorization was further supported by theoretical investigations conducted by Bagger et al. *(Figure 1.1.10)*, where the selectivity of the products was based on the optimal binding energies of the *H, *COOH, *OCHO, and *CO intermediates[72].

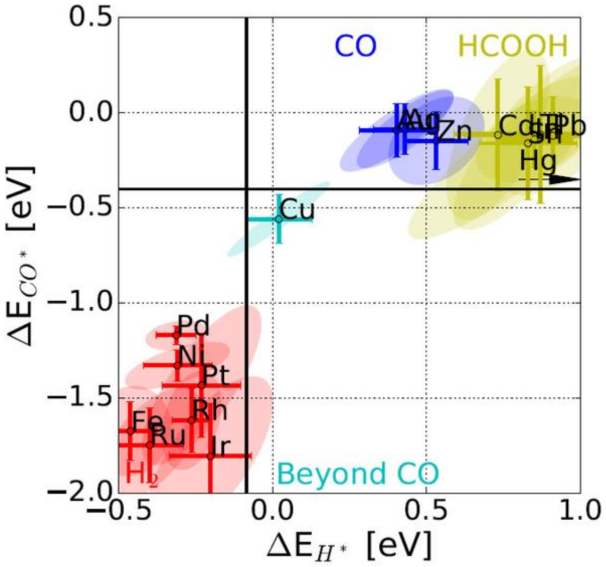

Figure 1.1.10: Categorization of metals into CO selective, formate selective, and C_{2+} product selective groups. Reproduced with permission from reference (72)

Metals selective for CO

Electrochemical reduction of CO_2 to CO is a 2 e^- transfer process. Metals such as Au, Ag, Pd, and Zn have been popularly studied for this conversion[73,74]. Recently, Fe, Co, and Ni single atom catalysts supported on nitrogen-doped carbon are also being explored[75].

$$CO_2 + 2H^+ + 2e^- \rightarrow CO + H_2O \quad E^o = -0.52\ V$$

Theoretical studies have been used to determine the volcano plot for CO formation using the binding energy of *COOH as the descriptor *(Figure 1.1.11)*. It has been observed that Au lies at the top of the volcano plot, providing optimum binding of *COOH intermediate[76].

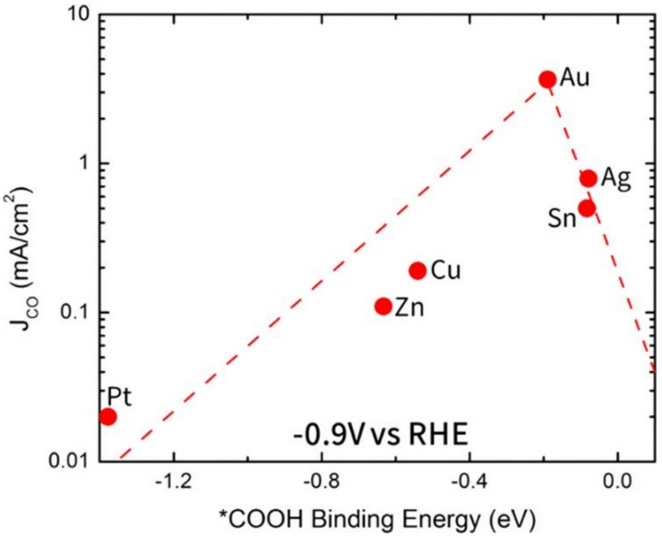

Figure 1.1.11: Volcano plot for CO using *COOH binding energy as a descriptor. Reproduced with permission from reference (76)

Several nanostructured Au based catalysts have been explored, such as Au nanoparticles[77–79], nanowires[80–82], nanoclusters, nanofilms[83–85] and nanoporous structures[86,87]. For Au nanoparticles, the size significantly influenced the faradaic efficiency for CO production. W. Zhu et al. investigated the CO_2 electroreduction activity on monodisperse Au nanoparticles of varying sizes and found that nanoparticles of size 8 nm exhibited high faradaic efficiency for CO. This enhanced selectivity was attributed to the optimal number of exposed edge sites, which effectively stabilized the *COOH intermediate, in contrast to corner sites that favored the hydrogen evolution reaction [79]. Likewise, Ag based catalyst[88,89] such as Ag nanoparticles[90,91], Ag nanowires[92,93], silver sulfide[94,95], oxide derived Ag[96,97], etc., have also been extensively studied. For instance, K. Ye et al. reported the transformation of the Ag_2S hollow cube into a coral like structure, which resulted in the formation of the active heterogeneous Ag_2S/Ag interface. This reconstructed interface demonstrated remarkable performance, achieving 99% faradaic efficiency for CO in a flow cell across a broad potential range from -0.34 V to -0.7 V_{RHE}.[94] Furthermore, combining Au and Ag with other elements, such as Cu, Zn, Pd, etc., has helped in tuning the d-band center, which has led to an improvement in catalytic activity[98–102].

Recently, single atom catalysts based on Pd, Ni, Fe, and Co have been studied[103–109]. In these systems, generally, the metal atoms are supported on N containing supports to form M-N bonds, which are responsible for the enhanced catalytic activity. For instance, Pd supported on N doped carbon results in the formation of the active site consisting of Pd-

N_4. It provides optimum adsorption to the *HOCO intermediate compared to *H, favoring the formation of CO and suppressing the HER. Additionally, the desorption of *CO is facilitated on PdN_4 in comparison to the Pd site, thereby improving the Faradaic efficiency[110]. Likewise, in the case of Ni single atom anchored on microporous hollow carbon nanospheres (Ni-N-HCN), the hydrophobic nature of the carbon prevents the competing hydrogen evolution side reaction. The microporous structure, however, increases the CO_2 adsorption capacity of the catalyst, and the Ni-N sites provide optimum adsorption for the *COOH intermediate. This, in turn, results in 95% Faradaic efficiency for CO at a wide potential range[111]. Non- noble metal Zn based catalysts are also extensively studied[112]. For instance, in a recent report, Q.W. Liu et al. investigated Zn cyanamide catalyst for CO_2 reduction to CO. Herein, the delocalized Zn d- electrons and the resonant structure of the cyanamide ligand prevent Zn from getting reduced under the cathodic condition, i.e., the Zn is retained as $Zn^{\delta+}$ sites. These sites are responsible for stabilizing the *COOH intermediate and thereby result in a 93.9 % Faradaic efficiency for CO at $-1.28V_{RHE}$[113].

Metals selective for HCOOH

Technoeconomic analysis of various products obtained by CO_2 electroreduction shows that formate is the most economically feasible product. This is attributed to the fact that the production of formate has the highest value per kWh of electrical energy input, i.e., 0.43 $/kWh, as shown in *Figure 1.1.12*.[114]

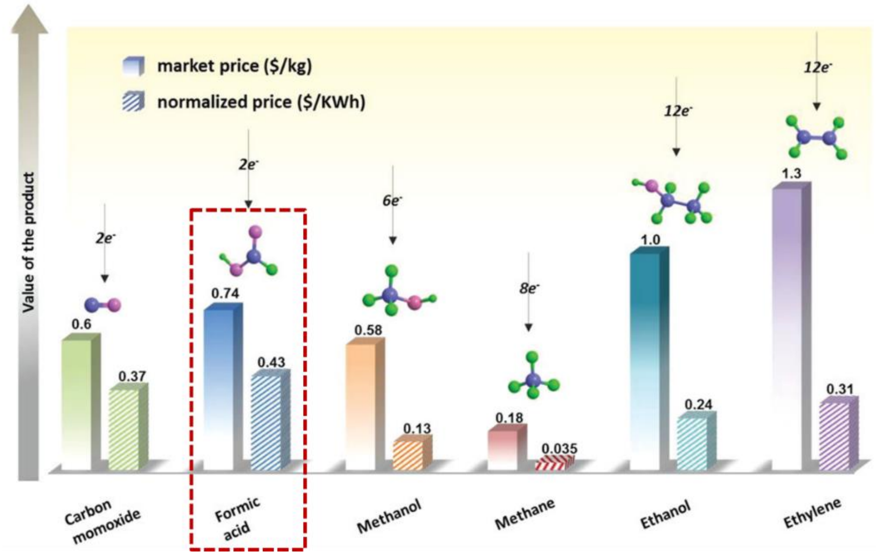

Figure 1.1.12: Comparison of various CO_2ER products in terms of their market price and the normalized price with respect to the input electrical energy. Reproduced with permission from reference (114)

CO_2 electroreduction to formate is a 2 e^- transfer process. The selectivity towards the formate depends on the optimum binding energy of the *OCHO intermediate. Elements such as In, Bi, and Sn are extensively studied for this conversion reaction.

$$CO_2 + 2H^+ + 2e^- \rightarrow HCOOH \quad E^o = -0.61\ V$$

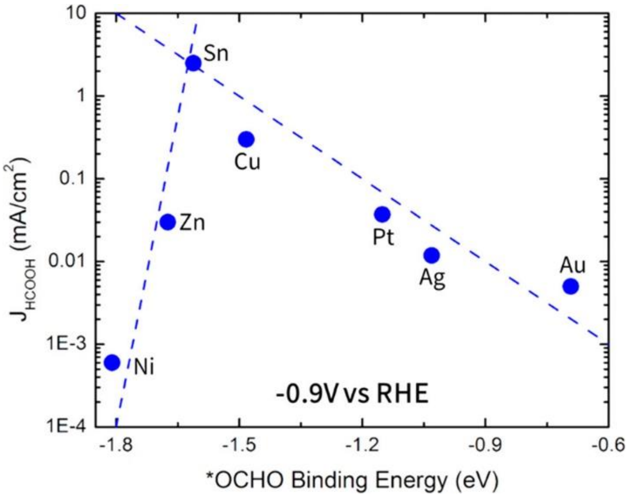

Figure 1.1.13: Volcano plot for formic acid using *OCHO binding energy as the descriptor. Reproduced with permission from reference (76)

Out of these, Sn based catalysts have received significant attention due to its position at the top of the volcano plot *(Figure 1.1.13)*. Comparison of CO_2 electroreduction to formate on metallic Sn and SnO_x has shown that the SnO_x where the Sn exists in the +2/+4 oxidation states are the active sites to achieve higher Faradaic efficiencies[115]. Introduction of halogens such as Cl, F, Br, and I prevent the reduction of SnO_x by inducing electron transfer from Sn to the more electronegative halogen atoms, which promotes the CO_2ER to formate and suppresses the competing CO formation and HER[116]. Likewise, the incorporation of Cu[117,118], Pd[119], CeO_2[120], etc., has also helped in improving the Faradaic efficiency of formate. For instance, the formation of the active site consisting of $PdSnO_2$ in PdSn alloy catalyst provided optimum binding energy to the *OCHO intermediate, resulting in a 100% Faradaic efficiency for formate at very low potentials[119].

Owing to their low toxicity, low cost, and high selectivity for formate, Bi based catalysts have gained increased attention[121,122]. However, the major challenge with this system is the low conductivity of metallic Bi which is responsible for the high overpotentials and low current densities to achieve higher Faradaic efficiencies. Compared to metallic Bi, Bi_2O_3 is the effective electrocatalyst for CO_2ER[123]. Nanostructures of Bi have been developed to achieve high Faradaic efficiency for formate. For instance, the porous nanosheets of Bi, with a stronger Bi-O bond and a vacancy rich surface, provide optimum adsorption for the *OCHO intermediate, resulting in ~95% Faradaic efficiency for formate. Bi can be alloyed with other elements such as Cu[124,125], In, and Sn[126,127] to attain enhanced electrochemical activity. For instance, the Sn-Bi/SnO_2 catalyst showed highly stable CO_2ER for 2400 h (100 days), maintaining a Faradaic efficiency of 95% at 100 mA cm^{-2}. DFT calculation was used to build a volcano relationship highlighting the Bi to Sn ratio, identifying Bi_4Sn_{64} as the most active combination, leading to the optimum binding energy of the *OCHO intermediate[127]. In the case of lattice Cu foam @Bi nanowires electrode, the Bi_2O_3 layer on the catalyst undergoes reduction to form twisted Bi nanowires with lattice dislocations, which are responsible for the optimum binding of the *OCHO intermediate. The as formed catalyst showed 95 % Faradaic efficiency for formate at -0.69 V at a formate partial current density of -15 mA cm^{-2}[124].

Indium based catalysts are another group of compounds that show enhanced activity towards formate[123]. Operando FTIR studies have shown that In_2O_3 is the main active component in these catalysts. In_2O_3 reacts to form $In(OH)_3$. It reacts with the dissolved CO_2 to form In-CO_3 on the surface, which is reduced to formate[128]. The addition of sulfur to the Indium surface has proven to boost the CO_2ER activity. The adsorbed S^{2-} species interact with the hydrated metal cations, contributing to the dissociation of H_2O to form H*. This interacts with the CO_2 molecule and forms the $*HCOO^-$ intermediate, thereby improving the Faradaic efficiency of formate[129].

Metal Selective for hydrocarbon and alcohols

The electrochemical conversion of CO_2 to hydrocarbons and alcohols is performed using Cu based catalyst *(Figure 1.1.14)*. Electroreduction to these products involves multi electron-proton coupled transfer steps via multiple pathways, which makes the process non-selective[130–133]. However, the ability of Cu-based catalysts to optimally bind the CO intermediate makes them a key focus for these products[134].

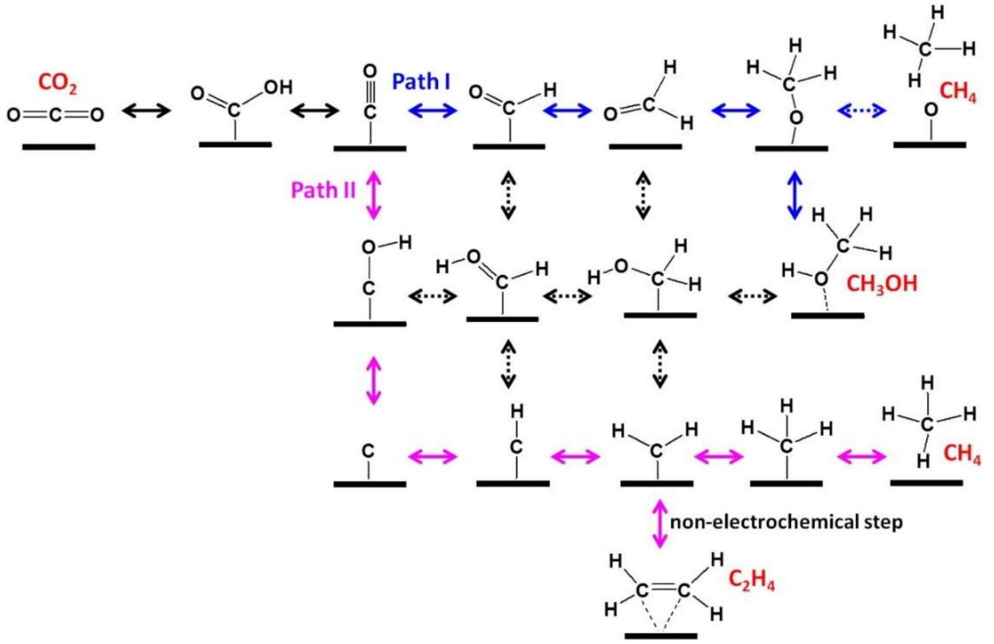

Figure 1.1.14: Proposed reaction pathways for producing CH_4, CH_3OH, and C_2H_4 on Cu(111). Reproduced with permission from reference (134)

The formation of CH_4 takes place by the hydrogenation of the *CO intermediate. In a recent work, J. Cai et al. investigated Cu (111) foil electrocatalyst with dense twin boundaries for CH_4 production. A Faradaic efficiency of 86 % for methane was obtained at a potential of -1.2 V_{RHE}. DFT calculations showed that the presence of twin boundaries lowers the energy barrier for the C1 product while increasing the barrier for C-C coupling, resulting in a high selectivity for CH_4[135]. The C_{2+} hydrocarbons are formed by C-C coupling followed by electron- proton transfer. Copper oxides[136,137] and oxide derived Cu[138–140] have been studied for their ability to produce C_{2+} products. For example, oxygen rich ultrathin CuO nanoplate arrays form a stable Cu/Cu_2O interface during the reaction. This helped in achieving 84.5% Faradaic efficiency for ethylene in the flow cell at a current density of 200 mA cm^{-2}. The formation of the Cu/Cu_2O interface lowers the energy barrier for C-C coupling and accelerates the desorption of C_2H_4, resulting in its high selectivity[137]. In a recent work by C. Long et al., oxide derived Cu was investigated for the electroreduction of CO_2 to n-propanol. In this work, it was observed that the oxide derived Cu formed from CuO had a higher density of Cu sites on the surface. Operando Raman spectroscopy showed that these sites are responsible for the generation of *CO and *(H)OCCOH species, resulting in a Faradaic efficiency of 17.9 % for n-propanol. The catalyst also exhibited a stable performance for 150 h[141].

The electrochemical activity can be enhanced further by alloying Cu with other elements such as Ag, Zn, Pd etc[142–146]. For instance, in the case of Cu-Ag tandem catalyst, CO produced on the surface of Ag undergoes C-C bonding with the CO produced on Cu to generate the C_{2+} product ethylene, acetate, and ethanol[146]. Likewise, CuPd bimetallic catalyst with the composition $Cu_{98}Pd_2$ exhibited exceptional activity towards C_{2+} product formation. Herein, the synergistic effect of Cu and Pd promotes the charge transfer kinetics and increases the local CO concentration, thereby favoring C-C coupling to form ethanol, propanol, acetate, and ethylene[145].

1.1.4.3.Electrolyte

Effect of pH

CO_2 electroreduction is generally carried out in the aqueous electrolyte. The dissolution of CO_2 in the aqueous electrolyte modifies the pH of the solution. Herein, CO_2 interacts with water to form bicarbonates/carbonates. The CO_2/bicarbonate system not only acts as the reactant but also as a buffer, which helps maintain the local pH. Upon electroreduction of CO_2, the pH of the solution near the electrode becomes more alkaline in comparison to the bulk, creating a pH gradient. To compensate for the change in the local pH, the dissolution of CO_2 into the aqueous medium decreases, thereby acting as a buffer. In an alkaline medium, the OH^- attacks the CO_2 and forms the bicarbonate, which is always in equilibrium with the carbonate[130].

In the aqueous medium:

$$CO_2\ (g) \leftrightarrow CO_2\ (aq) \qquad K_s = 30\ \text{mM/bar}$$

$$CO_2\ (aq) + H_2O \leftrightarrow HCO_3^- + H^+ \quad pK_a = 6.4$$

$$HCO_3^- \leftrightarrow CO_3^{2-} + H^+ \quad pK_a = 10.3$$

In the alkaline medium, i.e., pH> 7:

$$CO_2\ (aq) + OH^- \leftrightarrow HCO_3^-$$

$$HCO_3^- + OH^- \leftrightarrow CO_3^{2-}$$

During the electroreduction, the local pH at the electrode interface changes due to the formation of OH^- by both CO_2 reduction and the competing hydrogen evolution reaction (HER). The change in the local pH affects the product distribution and the kinetics of the hydrogen evolution reaction[147–149]. The effect of pH on product distribution was first reported by Hori et al., where the electroreduction of CO was investigated on the Cu surface. It was observed that the formation of CH_4 was pH dependent while the formation of ethylene was pH independent[150]. Similar observations were made by Varela et al. [151]. Herein, the CO_2 electroreduction was studied on a smooth Cu surface. For this study, the concentration of the $KHCO_3$ electrolyte was varied, i.e., 0.05 M, 0.1 M, and 0.2 M. It was observed that bicarbonate solution of 0.2 M concentration with a higher buffering capacity in comparison to 0.05 M and does not cause much change to the local pH. The local pH was found to vary as follows: 0.2 M < 0.1 M< 0.05 M. This results in an increase in the Faradaic efficiency of CH_4 in 0.2 M electrolyte attributed to the higher proton concentration near the interface. However, the concentration of ethylene was unaffected by the pH of the solution. These observations were in line with the theoretical studies on Cu surface reported by F.C Vallejo et al., which showed that the reaction proceeds by two different pathways: The CO dimerization mechanism is pH independent and results in ethylene as the final product while the CO protonation mechanism is pH dependent and results in CH_4 as the product[152].

Effect of cation and anion

The type of cation and anion present in the electrolyte alters the local pH and affects the product selectivity and kinetics of both HER and CO_2ER[148,153]. One of the early reports on the effect of alkali metal cations was reported by Murata and Hori. In this work, CO_2 and CO electroreduction were studied on the Cu electrode in the bicarbonate solution. It was observed that in Li^+ electrolyte, H_2 evolution was the predominant reaction. However, in Na^+, K^+, and Cs^+ solution, CO_2 reduction prevails. This was attributed to the specific adsorption of the cation on the electrode, which is dependent on its hydration. Li^+, being strongly hydrated, is not adsorbed, while Cs^+ is the least hydrated and is therefore adsorbed. This alters the local pH at the electrode surface in the order $Cs^+ > K^+ > Na^+ < Li^+$ and favors the H_2 evolution reaction in Li^+ solution[154].

In another report by M.R. Singh et al., the effect of the cation was studied during CO_2ER on Ag and Cu electrodes. It was observed that the hydrated metal cations in the bulk of the electrolyte are stable to hydrolysis. However, near the electrode surface, it undergoes hydrolysis due to the coulombic interaction with the increasing negative charge on the electrode surface. The hydrated cations act as pH buffers. The buffering capacity of the cation is found to decrease with the increase in its size: $Cs^+ > Rb^+ > K^+ > Na^+ > Li^+$. This affects the CO_2 concentration near the electrode *(Figure 1.1.15)*. In the presence of Cs^+ cations, the concentration of CO_2 is comparatively higher. In the case of the Cu electrode, a decrease in the polarization losses with an increase in the cation size results in an increase in the total current density. Furthermore, a decrease in the Faradaic efficiencies for H_2 and CH_4 and an increase in the Faradaic efficiencies of CO, C_2H_4, and EtOH were observed[155].

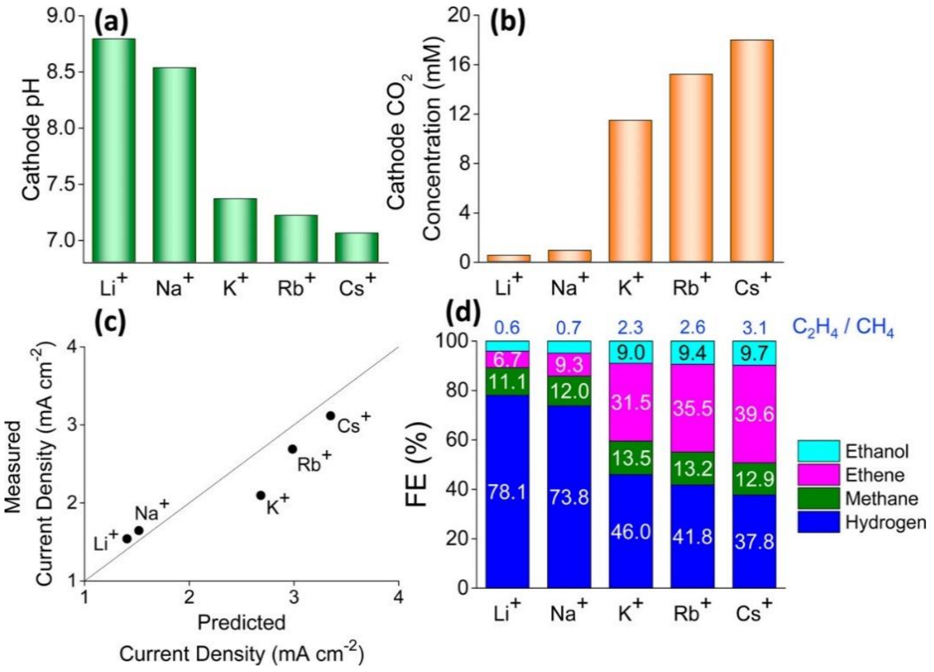

Figure 1.1.15: Effect of electrolyte cation on the **(a)** local pH, **(b)** CO_2 concentration at the cathode, **(c)** total current density, and **(d)** Faradaic efficiency of CO and H_2 for Cu electrode. Reproduced with permission from reference (155)

Hori et al. also studied the effect of anion on the CO_2 electroreduction activity on the Cu electrode. It was observed that the formation of C_2H_4 and alcohols is favored on KCl, K_2SO_4, $KClO_4$, and in dilute HCO_3^- solution, while methane is produced in phosphate and concentrated HCO_3^- solution[156]. In the case of buffering electrolytes like concentrated bicarbonate and phosphate, sufficient HCO_3^- and $H_2PO_4^-$ are available to neutralize the OH^- generated during the electrolysis, thereby maintaining the near neutral pH. This favors HER over CO_2ER, resulting in lower Faradaic yields of the CO_2ER products. However, in the case of the non-buffering electrolytes like KCl, K_2SO_4, $KClO_4$, and in dilute HCO_3^-, there is an increase in the local pH, which favors the CO_2ER over HER, leading to C_{2+} products over C_1 products[157].

In a recent report, Lukatsakaya et al. investigated the effect of anions on the CO_2ER activity on Au catalysts. It was observed that compared to bicarbonate, inorganic anions such as perchlorate, sulfate, and chloride suppress HER and increases the CO_2ER overpotentials resulting in low CO Faradaic efficiencies. However, the carboxylate anion with propionate molecular structure suppresses HER and promotes CO_2 reduction kinetics resulting in 99% Faradaic efficiency for CO[158].

1.1.4.4. Electrolyser

There are three types of electrolyzers that are extensively used for studying CO_2 electroreduction, namely: H-cell, flow cell, and Membrane electrode assembly (MEA)[70,159]. The H-cell electrolyzer is used to study the electrochemical reduction of CO_2 at the lab scale *(Figure 1.1.16)*. It consists of a cathodic and an anodic chamber. The two chambers are separated by an ion-exchange membrane. The electroreduction of CO_2 takes place in the cathodic chamber, while OER takes place at the anode in the anodic chamber. The separation of the two chambers minimizes the mixing of the reaction products. The major limitation of this electrolyzer is the polarisation losses attributed to the limited solubility of CO_2 in the electrolyte and the distance between the working and the counter electrode. This results in mass transport limitation, leading to low Faradaic efficiencies, low current densities, and high overpotentials.

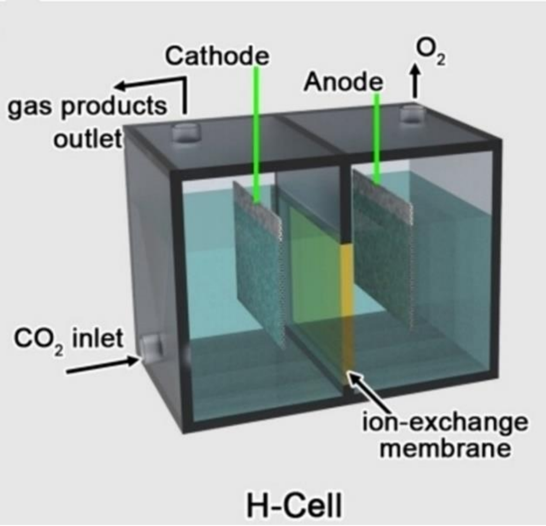

Figure 1.1.16: Schematic of CO_2 electrolysers: H-cell. Reproduced with permission from reference (70)

The limitations of an H-Cell can be overcome by using a flow cell or an MEA. In a flow cell, a gas diffusion electrode coated with the catalyst is used as the working electrode *(Figure 1.1.17 a)*. Ni foam, Pt foil, or IrO_2/ RuO_2 coated titania are generally used as the anode. Like the H-cell, the anode and the cathode are separated using an ion exchange membrane. In these cells, the distance between the membrane and the electrodes are reduced by varying the thickness of the chambers. This brings the anode and the cathode closer, which helps overcome the ohmic losses. The electrolyte is continuously circulated in both chambers, and an additional gas chamber is used to regulate CO_2 flow.

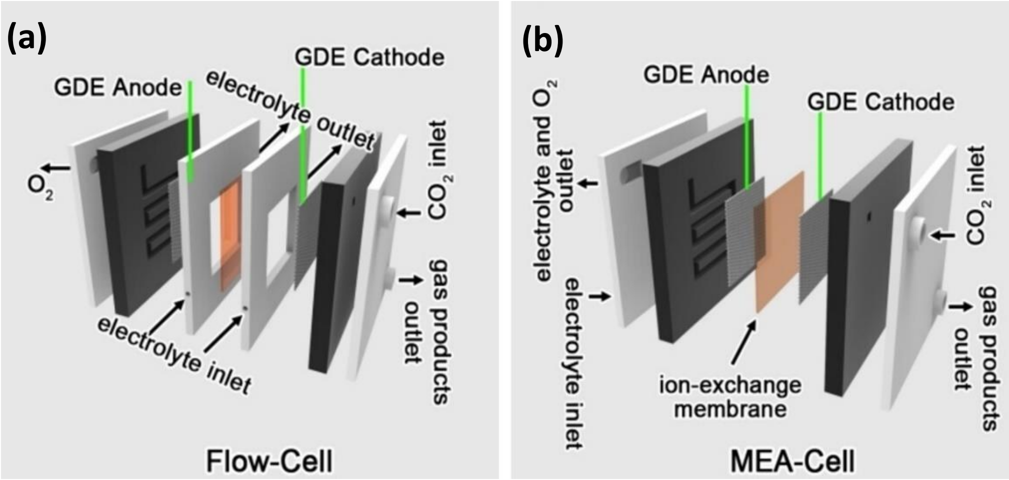

Figure 1.1.17: Schematic of CO_2 electrolyzers **(a)** Flow Cell and **(b)** MEA cell. Reproduced with permission from reference (70)

The gas diffusion electrode consists of two layers *(Figure 1.1.18)*. A macroporous gas diffusion layer (GDL) in contact with the gas chamber, and a hydrophobic microporous layer in contact with the circulating electrolyte in the cathodic chamber. The catalyst is generally coated on the surface of the microporous layer. The macroporous layer ensures the diffusion of CO_2 to the catalyst surface as well as the diffusion of the gaseous product away from the catalyst surface. This direct contact of the CO_2 with the catalyst helps in overcoming the mass transfer limitation, thereby enhancing the Faradaic efficiency[160–162]. In this configuration, the catalyst can also achieve higher current densities ($\geq$ $\mathbf{100\ mA}$ cm^{-2}) and long term stability ($\geq$ $\mathbf{24}$ h).

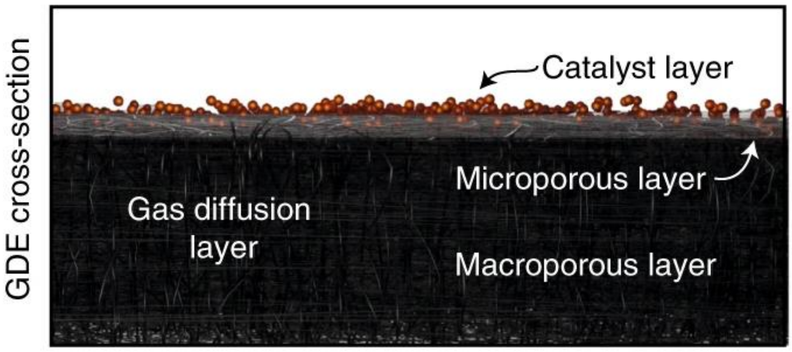

Figure 1.1.18: Schematic of gas diffusion electrode. Reproduced with permission from reference (162)

Ohmic losses can be further minimized by employing a membrane electrode assembly (MEA) electrolyzer, where the cathode, membrane, and anode are tightly sandwiched together *(Figure 1.1.17 b)*. This configuration significantly reduces ohmic resistance, enabling the achievement of higher current densities. The major limitation in the flow cell and MEA is the flooding of the GDE, wherein the catholyte penetrates the microporous layer. Consequently, the CO_2ER decreases, and the competing HER takes over. The flooding gets accelerated when the electrode is operated at higher current densities. Another challenge faced is the carbonate precipitation. Under continuous operation, it is observed that the increase in the local pH causes the carbonates to precipitate and block the microporous layer, resulting in the degradation of the catalytic activity.

1.1.5. Conclusion

In this chapter, the advancements in both thermocatalytic and electrocatalytic conversion of CO_2 are explored, highlighting their potential for sustainable chemical production. The significance of CO_2 conversion and the inherent stability of the CO_2 molecule, which poses a challenge for its activation, has been discussed. The first part of this chapter is focused on the thermocatalytic conversion of CO_2 into methanol and formic acid. A detailed overview of the catalysts developed for these processes has been provided. The second part delved into the electrochemical conversion of CO_2. Herein, various electrochemical pathways leading to different products have been highlighted. This is followed by a discussion on the various catalysts employed for tuning the selectivity. Additionally, the influence of electrolytes and reactor configurations on electrocatalytic activity was discussed, emphasizing their critical roles in optimizing performance.

1.1.6. References

(1) *Emissions Gap Report 2023: Broken Record – Temperatures Hit New Highs, yet World Fails to Cut Emissions (Again)*; United Nations Environment Programme, 2023. https://doi.org/10.59117/20.500.11822/43922.

(2) Calvin, K.; Dasgupta, D.; Krinner, G.; Mukherji, A.; Thorne, P. W.; Trisos, C.; Romero, J.; Aldunce, P.; Barret, K.; Blanco, G.; Cheung, W. W. L.; Connors, S. L.; Denton, F.; Diongue-Niang, A.; Dodman, D.; Garschagen, M.; Geden, O.; Hayward, B.; Jones, C.; Jotzo, F.; Krug, T.; Lasco, R.; Lee, Y.-Y.; Masson-Delmotte, V.; Meinshausen, M.; Mintenbeck, K.; Mokssit, A.; Otto, F. E. L.; Pathak, M.; Pirani, A.; Poloczanska, E.; Pörtner, H.-O.; Revi, A.; Roberts, D. C.; Roy, J.; Ruane, A. C.; Skea, J.; Shukla, P. R.; Slade, R.; Slangen, A.; Sokona, Y.; Sörensson, A. A.; Tignor, M.; van Vuuren, D.; Wei, Y.-M.; Winkler, H.; Zhai, P.; Zommers, Z.; Hourcade, J.-C.; Johnson, F. X.; Pachauri, S.; Simpson, N. P.; Singh, C.; Thomas, A.; Totin, E.; Alegría, A.; Armour, K.; Bednar-Friedl, B.; Blok, K.; Cissé, G.; Dentener, F.; Eriksen, S.; Fischer, E.; Garner, G.; Guivarch, C.; Haasnoot, M.; Hansen, G.; Hauser, M.; Hawkins, E.; Hermans, T.; Kopp, R.; Leprince-Ringuet, N.; Lewis, J.; Ley, D.; Ludden, C.; Niamir, L.; Nicholls, Z.; Some, S.; Szopa, S.; Trewin, B.; van der Wijst, K.-I.; Winter, G.; Witting, M.; Birt, A.; Ha, M. *IPCC, 2023: Climate Change 2023: Synthesis Report, Summary for Policymakers. Contribution of Working Groups I, II and III to the Sixth Assessment Report of the Intergovernmental Panel on Climate Change [Core Writing Team, H. Lee and J. Romero (Eds.)]. IPCC, Geneva, Switzerland.*; Arias, P., Bustamante, M., Elgizouli, I., Flato, G., Howden, M., Méndez-Vallejo, C., Pereira, J. J., Pichs-Madruga, R., Rose, S. K., Saheb, Y., Sánchez Rodríguez, R., Ürge-Vorsatz, D., Xiao, C., Yassaa, N., Romero, J., Kim, J., Haites, E. F., Jung, Y., Stavins, R., Birt, A., Ha, M., Orendain, D. J. A., Ignon, L., Park, S., Park, Y., Eds.; 2023. https://doi.org/10.59327/IPCC/AR6-9789291691647.001.

(3) Energy Agency, I. *Technology Perspectives Energy Special Report on Carbon Capture Utilisation and Storage CCUS in Clean Energy Transitions*. www.iea.org/t&c/.

(4) Mertens, J.; Breyer, C.; Arning, K.; Bardow, A.; Belmans, R.; Dibenedetto, A.; Erkman, S.; Gripekoven, J.; Léonard, G.; Nizou, S.; Pant, D.; Reis-Machado, A. S.; Styring, P.; Vente, J.; Webber, M.; Sapart, C. J. Carbon Capture and Utilization: More than Hiding CO2 for Some Time. *Joule*. Cell Press March 15, 2023, pp 442–449. https://doi.org/10.1016/j.joule.2023.01.005.

(5) Freund, H.-J.; Roberts~surface, M. W. *Surface Chemistry of Carbon Dioxide*; **1996**; Vol. 25, 225-273

(6) Zhang, H.; Liang, Q.; Xie, K. How to Rationally Design Homogeneous Catalysts for Efficient CO2 Electroreduction? *iScience* **2024**, *27* (2), 108973. https://doi.org/10.1016/j.isci.2024.108973.

(7) Bowker, M. Methanol Synthesis from CO2 Hydrogenation. *ChemCatChem* **2019**, *11* (17), 4238–4246. https://doi.org/10.1002/cctc.201900401.

(8) Joo, O.-S.; Jung, K.-D.; Moon, I.; Rozovskii, A. Ya.; Lin, G. I.; Han, S.-H.; Uhm, S.-J. Carbon Dioxide Hydrogenation To Form Methanol via a Reverse-Water-Gas-Shift Reaction (the CAMERE Process). *Ind Eng Chem Res* **1999**, *38* (5), 1808–1812. https://doi.org/10.1021/ie9806848.

(9) Gao, B.; Wen, Z.; Wang, Y.; Chen, D.; Yang, B.; Ishihara, T.; Guo, L. Recent Advances in Alloy Catalysts for CO2 Hydrogenation to Methanol. *ChemCatChem* **2024**, *16* (19), e202400814. https://doi.org/10.1002/cctc.202400814.

(10) Liang, H.; Zhang, G.; Li, Z.; Zhang, Y.; Fu, P. Catalytic Hydrogenation of CO2 to Methanol over Cu-Based Catalysts: Active Sites Profiling and Regulation Strategy as Well as Reaction Pathway Exploration. *Fuel Processing Technology* **2023**, *252*, 107995. https://doi.org/10.1016/j.fuproc.2023.107995.

(11) Jiang, X.; Nie, X.; Guo, X.; Song, C.; Chen, J. G. Recent Advances in Carbon Dioxide Hydrogenation to Methanol via Heterogeneous Catalysis. *Chem Rev* **2020**, *120* (15), 7984–8034. https://doi.org/10.1021/acs.chemrev.9b00723.

(12) Roy, S.; Cherevotan, A.; Peter, S. C. Thermochemical CO2 Hydrogenation to Single Carbon Products: Scientific and Technological Challenges. *ACS Energy Lett* **2018**, *3* (8), 1938–1966. https://doi.org/10.1021/acsenergylett.8b00740.

(13) Kuld, S.; Thorhauge, M.; Falsig, H.; Elkjær, C. F.; Helveg, S.; Chorkendorff, I.; Sehested, J. Quantifying the Promotion of Cu Catalysts by ZnO for Methanol Synthesis. *Science,* **2016**, *352* (6288), 969–974. https://doi.org/10.1126/science.aaf0718.

(14) Kuld, S.; Conradsen, C.; Moses, P. G.; Chorkendorff, I.; Sehested, J. Quantification of Zinc Atoms in a Surface Alloy on Copper in an Industrial-Type Methanol Synthesis Catalyst. *Angewandte Chemie International Edition* **2014**, *53* (23), 5941–5945. https://doi.org/10.1002/anie.201311073.

(15) Lunkenbein, T.; Schumann, J.; Behrens, M.; Schlögl, R.; Willinger, M. G. Formation of a ZnO Overlayer in Industrial Cu/ZnO/Al2O3 Catalysts Induced by Strong Metal–Support Interactions. *Angewandte Chemie International Edition* **2015**, *54* (15), 4544–4548. https://doi.org/10.1002/anie.201411581.

(16) Behrens, M.; Studt, F.; Kasatkin, I.; Kühl, S.; Hävecker, M.; Abild-Pedersen, F.; Zander, S.; Girgsdies, F.; Kurr, P.; Kniep, B.-L.; Tovar, M.; Fischer, R. W.; Nørskov, J. K.; Schlögl, R. The Active Site of Methanol Synthesis over Cu/ZnO/Al2O3 Industrial Catalysts. *Science,* **2012**, *336* (6083), 893–897. https://doi.org/10.1126/science.1219831.

(17) Bansode, A.; Tidona, B.; von Rohr, P. R.; Urakawa, A. Impact of K and Ba Promoters on CO2 Hydrogenation over Cu/Al2O3 Catalysts at High Pressure. *Catal Sci Technol* **2013**, *3* (3), 767–778. https://doi.org/10.1039/C2CY20604H.

(18) Xiao, J.; Mao, D.; Guo, X.; Yu, J. Effect of TiO2, ZrO2, and TiO2–ZrO2 on the Performance of CuO–ZnO Catalyst for CO2 Hydrogenation to Methanol. *Appl Surf Sci* **2015**, *338*, 146–153. https://doi.org/10.1016/j.apsusc.2015.02.122.

(19) Guo, H.; Li, Q.; Zhang, H.; Peng, F.; Xiong, L.; Yao, S.; Huang, C.; Chen, X. CO2 Hydrogenation over Acid-Activated Attapulgite/Ce0.75Zr0.25O2 Nanocomposite Supported Cu-ZnO Based Catalysts. *Molecular Catalysis* **2019**, *476*, 110499. https://doi.org/10.1016/j.mcat.2019.110499.

(20) Chang, K.; Wang, T.; Chen, J. G. Methanol Synthesis from CO2 Hydrogenation over CuZnCeTi Mixed Oxide Catalysts. *Ind Eng Chem Res* **2019**, *58* (19), 7922–7928. https://doi.org/10.1021/acs.iecr.9b00554.

(21) Martin, O.; Martín, A. J.; Mondelli, C.; Mitchell, S.; Segawa, T. F.; Hauert, R.; Drouilly, C.; Curulla-Ferré, D.; Pérez-Ramírez, J. Indium Oxide as a Superior Catalyst for Methanol Synthesis by CO2 Hydrogenation. *Angewandte Chemie International Edition* **2016**, *55* (21), 6261–6265. https://doi.org/10.1002/anie.201600943.

(22) Akkharaphatthawon, N.; Chanlek, N.; Cheng, C. K.; Chareonpanich, M.; Limtrakul, J.; Witoon, T. Tuning Adsorption Properties of GaxIn2−xO3 Catalysts for Enhancement of Methanol Synthesis Activity from CO2 Hydrogenation at High Reaction Temperature. *Appl Surf Sci* **2019**, *489*, 278–286. https://doi.org/10.1016/j.apsusc.2019.05.363.

(23) Shi, Z.; Tan, Q.; Tian, C.; Pan, Y.; Sun, X.; Zhang, J.; Wu, D. CO2 Hydrogenation to Methanol over Cu-In Intermetallic Catalysts: Effect of Reduction Temperature. *J Catal* **2019**, *379*, 78–89. https://doi.org/10.1016/j.jcat.2019.09.024.

(24) Men, Y.-L.; Liu, Y.; Wang, Q.; Luo, Z.-H.; Shao, S.; Li, Y.-B.; Pan, Y.-X. Highly Dispersed Pt-Based Catalysts for Selective CO2 Hydrogenation to Methanol at Atmospheric Pressure. *Chem Eng Sci* **2019**, *200*, 167–175. https://doi.org/10.1016/j.ces.2019.02.004.

(25) Frei, M. S.; Mondelli, C.; García-Muelas, R.; Kley, K. S.; Puértolas, B.; López, N.; Safonova, O. V; Stewart, J. A.; Curulla Ferré, D.; Pérez-Ramírez, J. Atomic-Scale Engineering of Indium Oxide Promotion by Palladium for Methanol Production via CO2 Hydrogenation. *Nat Commun* **2019**, *10* (1), 3377. https://doi.org/10.1038/s41467-019-11349-9.

(26) Snider, J. L.; Streibel, V.; Hubert, M. A.; Choksi, T. S.; Valle, E.; Upham, D. C.; Schumann, J.; Duyar, M. S.; Gallo, A.; Abild-Pedersen, F.; Jaramillo, T. F. Revealing the Synergy between Oxide and Alloy Phases on the Performance of Bimetallic In–Pd Catalysts for CO2 Hydrogenation to Methanol. *ACS Catal* **2019**, *9* (4), 3399–3412. https://doi.org/10.1021/acscatal.8b04848.

(27) Zimmerli, N. K.; Rochlitz, L.; Checchia, S.; Müller, C. R.; Copéret, C.; Abdala, P. M. Structure and Role of a Ga-Promoter in Ni-Based Catalysts for the Selective

Hydrogenation of CO2 to Methanol. *JACS Au* **2024**, *4* (1), 237–252. https://doi.org/10.1021/jacsau.3c00677.

(28) Studt, F.; Sharafutdinov, I.; Abild-Pedersen, F.; Elkjær, C. F.; Hummelshøj, J. S.; Dahl, S.; Chorkendorff, I.; Nørskov, J. K. Discovery of a Ni-Ga Catalyst for Carbon Dioxide Reduction to Methanol. *Nat Chem* **2014**, *6* (4), 320–324. https://doi.org/10.1038/nchem.1873.

(29) Docherty, S. R.; Phongprueksathat, N.; Lam, E.; Noh, G.; Safonova, O. V; Urakawa, A.; Copéret, C. Silica-Supported PdGa Nanoparticles: Metal Synergy for Highly Active and Selective CO2-to-CH3OH Hydrogenation. *JACS Au* **2021**, *1* (4), 450–458. https://doi.org/10.1021/jacsau.1c00021.

(30) Eppinger, J.; Huang, K.-W. Formic Acid as a Hydrogen Energy Carrier. *ACS Energy Lett* **2017**, *2* (1), 188–195. https://doi.org/10.1021/acsenergylett.6b00574.

(31) Du, D.; Lan, R.; Humphreys, J.; Tao, S. Progress in Inorganic Cathode Catalysts for Electrochemical Conversion of Carbon Dioxide into Formate or Formic Acid. *J Appl Electrochem* **2017**, *47* (6), 661–678. https://doi.org/10.1007/s10800-017-1078-x.

(32) Álvarez, A.; Bansode, A.; Urakawa, A.; Bavykina, A. V; Wezendonk, T. A.; Makkee, M.; Gascon, J.; Kapteijn, F. Challenges in the Greener Production of Formates/Formic Acid, Methanol, and DME by Heterogeneously Catalyzed CO2 Hydrogenation Processes. *Chem Rev* **2017**, *117* (14), 9804–9838. https://doi.org/10.1021/acs.chemrev.6b00816.

(33) Sun, R.; Liao, Y.; Bai, S.-T.; Zheng, M.; Zhou, C.; Zhang, T.; Sels, B. F. Heterogeneous Catalysts for CO2 Hydrogenation to Formic Acid/Formate: From Nanoscale to Single Atom. *Energy Environ Sci* **2021**, *14* (3), 1247–1285. https://doi.org/10.1039/D0EE03575K.

(34) Liu, Q.; Yang, X.; Li, L.; Miao, S.; Li, Y.; Li, Y.; Wang, X.; Huang, Y.; Zhang, T. Direct Catalytic Hydrogenation of CO2 to Formate over a Schiff-Base-Mediated Gold Nanocatalyst. *Nat Commun* **2017**, *8* (1), 1407. https://doi.org/10.1038/s41467-017-01673-3.

(35) Sun, Q.; Chen, B. W. J.; Wang, N.; He, Q.; Chang, A.; Yang, C.-M.; Asakura, H.; Tanaka, T.; Hülsey, M. J.; Wang, C.-H.; Yu, J.; Yan, N. Zeolite-Encaged Pd–Mn Nanocatalysts for CO2 Hydrogenation and Formic Acid Dehydrogenation. *Angewandte Chemie International Edition* **2020**, *59* (45), 20183–20191. https://doi.org/10.1002/anie.202008962.

(36) Mori, K.; Konishi, A.; Yamashita, H. Interfacial Engineering of PdAg/TiO2 with a Metal–Organic Framework to Promote the Hydrogenation of CO2 to Formic Acid. *The Journal of Physical Chemistry C* **2020**, *124* (21), 11499–11505. https://doi.org/10.1021/acs.jpcc.0c02457.

(37) Farlow, M. W.; Adkins, H. The Hydrogenation of Carbon Dioxide and a Correction of the Reported Synthesis of Urethans. *J Am Chem Soc* **1935**, *57* (11), 2222–2223. https://doi.org/10.1021/ja01314a054.

(38) Zhang, L.; Zhou, M.; Wang, A.; Zhang, T. Selective Hydrogenation over Supported Metal Catalysts: From Nanoparticles to Single Atoms. *Chem Rev* **2020**, *120* (2), 683–733. https://doi.org/10.1021/acs.chemrev.9b00230.

(39) Zhao, X.; Chang, Y.; Chen, W.-J.; Wu, Q.; Pan, X.; Chen, K.; Weng, B. Recent Progress in Pd-Based Nanocatalysts for Selective Hydrogenation. *ACS Omega* **2022**, *7* (1), 17–31. https://doi.org/10.1021/acsomega.1c06244.

(40) Aireddy, D. R.; Ding, K. Heterolytic Dissociation of H2 in Heterogeneous Catalysis. *ACS Catal* **2022**, *12* (8), 4707–4723. https://doi.org/10.1021/acscatal.2c00584.

(41) Wang, F.; Xu, J.; Shao, X.; Su, X.; Huang, Y.; Zhang, T. Palladium on Nitrogen-Doped Mesoporous Carbon: A Bifunctional Catalyst for Formate-Based, Carbon-Neutral Hydrogen Storage. *ChemSusChem* **2016**, *9* (3), 246–251. https://doi.org/10.1002/cssc.201501376.

(42) Kim, E. H.; Choi, Y. H.; Lee, M. H.; Kim, J.; Kim, H. Bin; Kim, K. Y.; Ra, E. C.; Lee, J. H.; Lee, J. S. Base-Free CO2 Hydrogenation to Formic Acid over Pd Supported on Defective Carbon Nitride Modified by Microwave and Acid Treatments. *J Catal* **2021**, *396*, 395–401. https://doi.org/10.1016/j.jcat.2021.03.016.

(43) Park, H.; Lee, J. H.; Kim, E. H.; Kim, K. Y.; Choi, Y. H.; Youn, D. H.; Lee, J. S. A Highly Active and Stable Palladium Catalyst on a G-C3N4 Support for Direct Formic Acid Synthesis under Neutral Conditions. *Chemical Communications* **2016**, *52* (99), 14302–14305. https://doi.org/10.1039/C6CC07401D.

(44) Fan, L.; Zhang, J.; Ma, K.; Zhang, Y.; Hu, Y. M.; Kong, L.; Jia, A. ping; Zhang, Z.; Huang, W.; Lu, J. Q. Ceria Morphology-Dependent Pd-CeO2 Interaction and Catalysis in CO2 Hydrogenation into Formate. *J Catal* **2021**, *397*, 116–127. https://doi.org/10.1016/j.jcat.2021.03.025.

(45) Zhang, J.; Liao, W.; Zheng, H.; Zhang, Y.; Xia, L.; Teng, B.-T.; Lu, J.-Q.; Huang, W.; Zhang, Z. Morphology-Engineered Highly Active and Stable Pd/TiO2 Catalysts for CO2 Hydrogenation into Formate. *J Catal* **2022**, *405*, 152–163. https://doi.org/10.1016/j.jcat.2021.11.035.

(46) Zhang, J.; Fan, L.; Zhao, F.; Fu, Y.; Lu, J.-Q.; Zhang, Z.; Teng, B.; Huang, W. Zinc Oxide Morphology-Dependent Pd/ZnO Catalysis in Base-Free CO2 Hydrogenation into Formic Acid. *ChemCatChem* **2020**, *12* (21), 5540–5547. https://doi.org/10.1002/cctc.202000934.

(47) Zhang, Z.; Zhang, L.; Yao, S.; Song, X.; Huang, W.; Hülsey, M. J.; Yan, N. Support-Dependent Rate-Determining Step of CO2 Hydrogenation to Formic

Acid on Metal Oxide Supported Pd Catalysts. *J Catal* **2019**, *376*, 57–67. https://doi.org/10.1016/j.jcat.2019.06.048.

(48) Zhang, Z.; Zhang, L.; Hülsey, M. J.; Yan, N. Zirconia Phase Effect in Pd/ZrO2 Catalyzed CO2 Hydrogenation into Formate. *Molecular Catalysis* **2019**, *475*, 110461. https://doi.org/10.1016/j.mcat.2019.110461.

(49) Kuwahara, Y.; Fujie, Y.; Mihogi, T.; Yamashita, H. Hollow Mesoporous Organosilica Spheres Encapsulating PdAg Nanoparticles and Poly(Ethyleneimine) as Reusable Catalysts for CO2 Hydrogenation to Formate. *ACS Catal* **2020**, *10* (11), 6356–6366. https://doi.org/10.1021/acscatal.0c01505.

(50) Mori, K.; Masuda, S.; Tanaka, H.; Yoshizawa, K.; Che, M.; Yamashita, H. Phenylamine-Functionalized Mesoporous Silica Supported PdAg Nanoparticles: A Dual Heterogeneous Catalyst for Formic Acid/CO2-Mediated Chemical Hydrogen Delivery/Storage. *Chemical Communications* **2017**, *53* (34), 4677–4680. https://doi.org/10.1039/C7CC00864C.

(51) Masuda, S.; Mori, K.; Futamura, Y.; Yamashita, H. PdAg Nanoparticles Supported on Functionalized Mesoporous Carbon: Promotional Effect of Surface Amine Groups in Reversible Hydrogen Delivery/Storage Mediated by Formic Acid/CO2. *ACS Catal* **2018**, *8* (3), 2277–2285. https://doi.org/10.1021/acscatal.7b04099.

(52) Mori, K.; Sano, T.; Kobayashi, H.; Yamashita, H. Surface Engineering of a Supported PdAg Catalyst for Hydrogenation of CO2 to Formic Acid: Elucidating the Active Pd Atoms in Alloy Nanoparticles. *J Am Chem Soc* **2018**, *140* (28), 8902–8909. https://doi.org/10.1021/jacs.8b04852.

(53) Sun, Q.; Fu, X.; Si, R.; Wang, C.-H.; Yan, N. Mesoporous Silica-Encaged Ultrafine Bimetallic Nanocatalysts for CO2 Hydrogenation to Formates. *ChemCatChem* **2019**, *11* (20), 5093–5097. https://doi.org/10.1002/cctc.201901167.

(54) Wang, Y.; Dong, M.; Li, S.; Chen, B.; Liu, H.; Han, B. The Superiority of Pd2+ in CO2 Hydrogenation to Formic Acid. *Chem Sci* **2024**, *15* (15), 5525–5530. https://doi.org/10.1039/D3SC06925G.

(55) Yang, G.; Kuwahara, Y.; Mori, K.; Louis, C.; Yamashita, H. Pd–Cu Alloy Nanoparticles Confined within Mesoporous Hollow Carbon Spheres for the Hydrogenation of CO2 to Formate. *The Journal of Physical Chemistry C* **2021**, *125* (7), 3961–3971. https://doi.org/10.1021/acs.jpcc.0c10962.

(56) Nguyen, L. T. M.; Park, H.; Banu, M.; Kim, J. Y.; Youn, D. H.; Magesh, G.; Kim, W. Y.; Lee, J. S. Catalytic CO2 Hydrogenation to Formic Acid over Carbon Nanotube-Graphene Supported PdNi Alloy Catalysts. *RSC Adv* **2015**, *5* (128), 105560–105566. https://doi.org/10.1039/C5RA21017H.

(57) Hao, C.; Wang, S.; Li, M.; Kang, L.; Ma, X. Hydrogenation of CO2 to Formic Acid on Supported Ruthenium Catalysts. *Catal Today* **2011**, *160* (1), 184–190. https://doi.org/10.1016/j.cattod.2010.05.034.

(58) Jaleel, A.; Haider, A.; Nguyen, C. Van; Lee, K. R.; Choung, S.; Han, J. W.; Baek, S.-H.; Shin, C.-H.; Jung, K.-D. Structural Effect of Nitrogen/Carbon on the Stability of Anchored Ru Catalysts for CO2 Hydrogenation to Formate. *Chemical Engineering Journal* **2022**, *433*, 133571. https://doi.org/10.1016/j.cej.2021.133571.

(59) Mori, K.; Taga, T.; Yamashita, H. Isolated Single-Atomic Ru Catalyst Bound on a Layered Double Hydroxide for Hydrogenation of CO2 to Formic Acid. *ACS Catal* **2017**, *7* (5), 3147–3151. https://doi.org/10.1021/acscatal.7b00312.

(60) Wang, Q.; O'Hare, D. Recent Advances in the Synthesis and Application of Layered Double Hydroxide (LDH) Nanosheets. *Chem Rev* **2012**, *112* (7), 4124–4155. https://doi.org/10.1021/cr200434v.

(61) Altalhi, A. A.; Mohamed, E. A.; Negm, N. A. Recent Advances in Layered Double Hydroxide (LDH)-Based Materials: Fabrication, Modification Strategies, Characterization, Promising Environmental Catalytic Applications, and Prospective Aspects. *Energy Advances* **2024**, *3* (9), 2136–2151. https://doi.org/10.1039/D4YA00272E.

(62) Bond, G. C.; Sermon, P. A.; Webb, G.; Buchanan, D. A.; Wells, P. B. Hydrogenation over Supported Gold Catalysts. *J Chem Soc Chem Commun* **1973**, No. 13, 444b–4445. https://doi.org/10.1039/C3973000444B.

(63) Preti, D.; Resta, C.; Squarcialupi, S.; Fachinetti, G. Carbon Dioxide Hydrogenation to Formic Acid by Using a Heterogeneous Gold Catalyst. *Angewandte Chemie International Edition* **2011**, *50* (52), 12551–12554. https://doi.org/10.1002/anie.201105481.

(64) Filonenko, G. A.; Vrijburg, W. L.; Hensen, E. J. M.; Pidko, E. A. On the Activity of Supported Au Catalysts in the Liquid Phase Hydrogenation of CO2 to Formates. *J Catal* **2016**, *343*, 97–105. https://doi.org/10.1016/j.jcat.2015.10.002.

(65) Wang, H.-H.; Zhang, S.-N.; Zhao, T.-J.; Liu, Y.-X.; Liu, X.; Su, J.; Li, X.-H.; Chen, J.-S. Mild and Selective Hydrogenation of CO2 into Formic Acid over Electron-Rich MoC Nanocatalysts. *Sci Bull (Beijing)* **2020**, *65* (8), 651–657. https://doi.org/10.1016/j.scib.2020.02.004.

(66) Wang, Z.; Kang, Y.; Hu, J.; Ji, Q.; Lu, Z.; Xu, G.; Qi, Y.; Zhang, M.; Zhang, W.; Huang, R.; Yu, L.; Tian, Z.; Deng, D. Boosting CO2 Hydrogenation to Formate over Edge-Sulfur Vacancies of Molybdenum Disulfide. *Angewandte Chemie International Edition* **2023**, *62* (45), e202307086. https://doi.org/10.1002/anie.202307086.

(67) Fu, X.-P.; Peres, L.; Esvan, J.; Amiens, C.; Philippot, K.; Yan, N. An Air-Stable, Reusable Ni@Ni(OH)2 Nanocatalyst for CO2/Bicarbonate Hydrogenation to Formate. *Nanoscale* **2021**, *13* (19), 8931–8939. https://doi.org/10.1039/D1NR01054A.

(68) Zhang, W.; Hu, Y.; Ma, L.; Zhu, G.; Wang, Y.; Xue, X.; Chen, R.; Yang, S.; Jin, Z. Progress and Perspective of Electrocatalytic CO2 Reduction for Renewable Carbonaceous Fuels and Chemicals. *Advanced Science* **2018**, *5* (1), 1700275. https://doi.org/10.1002/advs.201700275.

(69) Lin, J.; Zhang, Y.; Xu, P.; Chen, L. CO2 Electrolysis: Advances and Challenges in Electrocatalyst Engineering and Reactor Design. *Materials Reports: Energy* **2023**, *3* (2), 100194. https://doi.org/10.1016/j.matre.2023.100194.

(70) She, X.; Wang, Y.; Xu, H.; Chi Edman Tsang, S.; Ping Lau, S. Challenges and Opportunities in Electrocatalytic CO2 Reduction to Chemicals and Fuels. *Angewandte Chemie International Edition* **2022**, *61* (49), e202211396. https://doi.org/10.1002/anie.202211396.

(71) Hori, Y.; Kikuchi, K.; Suzuki, S. Production of CO and CH_4 in electrochemical reduction of CO_2 at metal electrodes in aqueous hydrogencarbonate solution. *Chem Lett* **1985**, *14* (11), 1695–1698. https://doi.org/10.1246/cl.1985.1695.

(72) Bagger, A.; Ju, W.; Varela, A. S.; Strasser, P.; Rossmeisl, J. Electrochemical CO2 Reduction: A Classification Problem. *ChemPhysChem* **2017**, *18* (22), 3266–3273. https://doi.org/10.1002/cphc.201700736.

(73) Poon, K. C.; Wan, W. Y.; Su, H.; Sato, H. A Review on Recent Advances in the Electrochemical Reduction of CO2 to CO with Nano-Electrocatalysts. *RSC Adv* **2022**, *12* (35), 22703–22721. https://doi.org/10.1039/D2RA03341K.

(74) Liu, Z.; Qian, J.; Zhang, G.; Zhang, B.; He, Y. Electrochemical CO2-to-CO Conversion: A Comprehensive Review of Recent Developments and Emerging Trends. *Sep Purif Technol* **2024**, *330*, 125177. https://doi.org/10.1016/j.seppur.2023.125177.

(75) Ji, Y.; Du, J.; Chen, A.; Gao, X.; Peng, M. Transition Metal-Nitrogen-Carbon Single-Atom Catalysts Enhanced CO2 Electroreduction Reaction: A Review. *ChemSusChem* **2024**, *n/a* (n/a), e202401557. https://doi.org/10.1002/cssc.202401557.

(76) Feaster, J. T.; Shi, C.; Cave, E. R.; Hatsukade, T.; Abram, D. N.; Kuhl, K. P.; Hahn, C.; Nørskov, J. K.; Jaramillo, T. F. Understanding Selectivity for the Electrochemical Reduction of Carbon Dioxide to Formic Acid and Carbon Monoxide on Metal Electrodes. *ACS Catal* **2017**, *7* (7), 4822–4827. https://doi.org/10.1021/acscatal.7b00687.

(77) Mistry, H.; Reske, R.; Zeng, Z.; Zhao, Z.-J.; Greeley, J.; Strasser, P.; Cuenya, B. R. Exceptional Size-Dependent Activity Enhancement in the Electroreduction of

CO2 over Au Nanoparticles. *J Am Chem Soc* **2014**, *136* (47), 16473–16476. https://doi.org/10.1021/ja508879j.

(78) Wang, H.; Fu, Y.; Chen, Z.-N.; Zhuang, W.; Cao, M.; Cao, R. Tunable CO2 Enrichment on Functionalized Au Surface for Enhanced CO2 Electroreduction. *Nano Res* **2023**, *16* (4), 4723–4728. https://doi.org/10.1007/s12274-022-5159-8.

(79) Zhu, W.; Michalsky, R.; Metin, Ö.; Lv, H.; Guo, S.; Wright, C. J.; Sun, X.; Peterson, A. A.; Sun, S. Monodisperse Au Nanoparticles for Selective Electrocatalytic Reduction of CO2 to CO. *J Am Chem Soc* **2013**, *135* (45), 16833–16836. https://doi.org/10.1021/ja409445p.

(80) Liu, J.; Wang, Y.; Jiang, H.; Jiang, H.; Zhou, X.; Li, Y.; Li, C. Ag@Au Core-Shell Nanowires for Nearly 100 % CO2-to-CO Electroreduction. *Chem Asian J* **2020**, *15* (3), 425–431. https://doi.org/10.1002/asia.201901550.

(81) Zhu, W.; Zhang, Y.-J.; Zhang, H.; Lv, H.; Li, Q.; Michalsky, R.; Peterson, A. A.; Sun, S. Active and Selective Conversion of CO2 to CO on Ultrathin Au Nanowires. *J Am Chem Soc* **2014**, *136* (46), 16132–16135. https://doi.org/10.1021/ja5095099.

(82) Zhu, W.; Zhang, Y.-J.; Zhang, H.; Lv, H.; Li, Q.; Michalsky, R.; Peterson, A. A.; Sun, S. Active and Selective Conversion of CO2 to CO on Ultrathin Au Nanowires. *J Am Chem Soc* **2014**, *136* (46), 16132–16135. https://doi.org/10.1021/ja5095099.

(83) Chen, C.; Zhang, B.; Zhong, J.; Cheng, Z. Selective Electrochemical CO2 Reduction over Highly Porous Gold Films. *J Mater Chem A Mater* **2017**, *5* (41), 21955–21964. https://doi.org/10.1039/C7TA04983H.

(84) Cho, K. M.; Jung, W.-B.; Kim, D.; Kim, J. Y.; Kim, Y.; Yun, G.-T.; Ryu, S.; Al-Saggaf, A.; Gereige, I.; Jung, H.-T. Confined Cavity on a Mass-Producible Wrinkle Film Promotes Selective CO2 Reduction. *J Mater Chem A Mater* **2020**, *8* (29), 14592–14599. https://doi.org/10.1039/D0TA03400B.

(85) Woldu, A. R.; Wang, Y.; Shah, A. H.; Zhang, X.; He, T. Efficient Reduction of CO2 to CO over Grain Boundary Rich Gold Film Reconstructed by O2 Plasma Treatment. *Appl Catal A Gen* **2021**, *625*, 118333. https://doi.org/10.1016/j.apcata.2021.118333.

(86) Zeng, M.; Liu, Y.; Hu, Y.; Zhang, X. High-Efficient CO2 Electrocatalysis over Nanoporous Au Film Enabled by a Combined Pore Engineering and Ionic Liquid-Mediated Approach. *Chemical Engineering Journal* **2021**, *425*, 131663. https://doi.org/10.1016/j.cej.2021.131663.

(87) Lu, X.; Yu, T.; Wang, H.; Qian, L.; Lei, P. Electrochemical Fabrication and Reactivation of Nanoporous Gold with Abundant Surface Steps for CO2 Reduction. *ACS Catal* **2020**, *10* (15), 8860–8869. https://doi.org/10.1021/acscatal.0c00627.

(88) Mahyoub, S. A.; Qaraah, F. A.; Chen, C.; Zhang, F.; Yan, S.; Cheng, Z. An Overview on the Recent Developments of Ag-Based Electrodes in the Electrochemical Reduction of CO2 to CO. *Sustain Energy Fuels* **2020**, *4* (1), 50–67. https://doi.org/10.1039/C9SE00594C.

(89) Sun, D.; Xu, X.; Qin, Y.; Jiang, S. P.; Shao, Z. Rational Design of Ag-Based Catalysts for the Electrochemical CO2 Reduction to CO: A Review. *ChemSusChem* **2020**, *13* (1), 39–58. https://doi.org/10.1002/cssc.201902061.

(90) Mattarozzi, F.; Visser, N.; de Rijk, J. W.; Ngene, P.; de Jongh, P. Ligand-Free Silver Nanoparticles for CO2 Electrocatalytic Reduction to CO. *Eur J Inorg Chem* **2022**, *2022* (29), e202200365. https://doi.org/10.1002/ejic.202200365.

(91) Salehi-Khojin, A.; Jhong, H.-R. M.; Rosen, B. A.; Zhu, W.; Ma, S.; Kenis, P. J. A.; Masel, R. I. Nanoparticle Silver Catalysts That Show Enhanced Activity for Carbon Dioxide Electrolysis. *The Journal of Physical Chemistry C* **2013**, *117* (4), 1627–1632. https://doi.org/10.1021/jp310509z.

(92) Mattarozzi, F.; van der Willige, N.; Gulino, V.; Keijzer, C.; van de Poll, R. C. J.; Hensen, E. J. M.; Ngene, P.; de Jongh, P. E. Oxide-Derived Silver Nanowires for CO2 Electrocatalytic Reduction to CO. *ChemCatChem* **2023**, *15* (22), e202300792. https://doi.org/10.1002/cctc.202300792.

(93) Xi, W.; Ma, R.; Wang, H.; Gao, Z.; Zhang, W.; Zhao, Y. Ultrathin Ag Nanowires Electrode for Electrochemical Syngas Production from Carbon Dioxide. *ACS Sustain Chem Eng* **2018**, *6* (6), 7687–7694. https://doi.org/10.1021/acssuschemeng.8b00527.

(94) Ye, K.; Liu, T.; Song, Y.; Wang, Q.; Wang, G. Tailoring the Interactions of Heterogeneous Ag2S/Ag Interface for Efficient CO2 Electroreduction. *Appl Catal B* **2021**, *296*, 120342. https://doi.org/10.1016/j.apcatb.2021.120342.

(95) Liu, S.; Tao, H.; Liu, Q.; Xu, Z.; Liu, Q.; Luo, J.-L. Rational Design of Silver Sulfide Nanowires for Efficient CO2 Electroreduction in Ionic Liquid. *ACS Catal* **2018**, *8* (2), 1469–1475. https://doi.org/10.1021/acscatal.7b03619.

(96) Jee, M. S.; Jeon, H. S.; Kim, C.; Lee, H.; Koh, J. H.; Cho, J.; Min, B. K.; Hwang, Y. J. Enhancement in Carbon Dioxide Activity and Stability on Nanostructured Silver Electrode and the Role of Oxygen. *Appl Catal B* **2016**, *180*, 372–378. https://doi.org/10.1016/j.apcatb.2015.06.046.

(97) Mistry, H.; Choi, Y.-W.; Bagger, A.; Scholten, F.; Bonifacio, C. S.; Sinev, I.; Divins, N. J.; Zegkinoglou, I.; Jeon, H. S.; Kisslinger, K.; Stach, E. A.; Yang, J. C.; Rossmeisl, J.; Roldan Cuenya, B. Enhanced Carbon Dioxide Electroreduction to Carbon Monoxide over Defect-Rich Plasma-Activated Silver Catalysts. *Angewandte Chemie International Edition* **2017**, *56* (38), 11394–11398. https://doi.org/10.1002/anie.201704613.

(98) Park, H.; Choi, J.; Kim, H.; Hwang, E.; Ha, D.-H.; Ahn, S. H.; Kim, S.-K. AgIn Dendrite Catalysts for Electrochemical Reduction of CO2 to CO. *Appl Catal B* **2017**, *219*, 123–131. https://doi.org/https://doi.org/10.1016/j.apcatb.2017.07.038.

(99) Zhang, W.; Zhu, N.; Ding, L.; Hu, Y.; Wu, Z. Efficacious CO2 Adsorption and Activation on Ag Nanoparticles/CuO Mesoporous Nanosheets Heterostructure for CO2 Electroreduction to CO. *Inorg Chem* **2021**, *60* (24), 19356–19364. https://doi.org/10.1021/acs.inorgchem.1c03183.

(100) Dai, S.; Huang, T.-H.; Liu, W.-I.; Hsu, C.-W.; Lee, S.-W.; Chen, T.-Y.; Wang, Y.-C.; Wang, J.-H.; Wang, K.-W. Enhanced CO2 Electrochemical Reduction Performance over Cu@AuCu Catalysts at High Noble Metal Utilization Efficiency. *Nano Lett* **2021**, *21* (21), 9293–9300. https://doi.org/10.1021/acs.nanolett.1c03483.

(101) Lamaison, S.; Wakerley, D.; Blanchard, J.; Montero, D.; Rousse, G.; Mercier, D.; Marcus, P.; Taverna, D.; Giaume, D.; Mougel, V.; Fontecave, M. High-Current-Density CO2-to-CO Electroreduction on Ag-Alloyed Zn Dendrites at Elevated Pressure. *Joule* **2020**, *4* (2), 395–406. https://doi.org/10.1016/j.joule.2019.11.014.

(102) Valenti, M.; Prasad, N. P.; Kas, R.; Bohra, D.; Ma, M.; Balasubramanian, V.; Chu, L.; Gimenez, S.; Bisquert, J.; Dam, B.; Smith, W. A. Suppressing H2 Evolution and Promoting Selective CO2 Electroreduction to CO at Low Overpotentials by Alloying Au with Pd. *ACS Catal* **2019**, *9* (4), 3527–3536. https://doi.org/10.1021/acscatal.8b04604.

(103) Xie, H.; Wan, Y.; Wang, X.; Liang, J.; Lu, G.; Wang, T.; Chai, G.; Adli, N. M.; Priest, C.; Huang, Y.; Wu, G.; Li, Q. Boosting Pd-Catalysis for Electrochemical CO2 Reduction to CO on Bi-Pd Single Atom Alloy Nanodendrites. *Appl Catal B* **2021**, *289*, 119783. https://doi.org/10.1016/j.apcatb.2020.119783.

(104) Wang, C.; Ren, H.; Wang, Z.; Guan, Q.; Liu, Y.; Li, W. A Promising Single-Atom Co-N-C Catalyst for Efficient CO2 Electroreduction and High-Current Solar Conversion of CO2 to CO. *Appl Catal B* **2022**, *304*, 120958. https://doi.org/10.1016/j.apcatb.2021.120958.

(105) Cheng, Y.-T.; Peng, J.-Z.; Lai, G.-T.; Yue, X.; Li, F.-Z.; Wang, Q.; Chen, L.-N.; Gu, J. Edge-Site Co–Nx Model Single-Atom Catalysts for CO2 Electroreduction. *ACS Catal* **2024**, *14* (11), 8446–8455. https://doi.org/10.1021/acscatal.4c02079.

(106) Chen, H.; Guo, X.; Kong, X.; Xing, Y.; Liu, Y.; Yu, B.; Li, Q.-X.; Geng, Z.; Si, R.; Zeng, J. Tuning the Coordination Number of Fe Single Atoms for the Efficient Reduction of CO2. *Green Chemistry* **2020**, *22* (21), 7529–7536. https://doi.org/10.1039/D0GC02689A.

(107) Ren, M.; Guo, X.; Huang, S. Coordination-Tuned Fe Single-Atom Catalyst for Efficient CO2 Electroreduction: The Power of B Atom. *Chemical Engineering Journal* **2022**, *433*, 134270. https://doi.org/10.1016/j.cej.2021.134270.

(108) Guo, Y.; Yao, S.; Xue, Y.; Hu, X.; Cui, H.; Zhou, Z. Nickel Single-Atom Catalysts Intrinsically Promoted by Fast Pyrolysis for Selective Electroreduction of CO2 into CO. *Appl Catal B* **2022**, *304*, 120997. https://doi.org/10.1016/j.apcatb.2021.120997.

(109) Zhang, J.; Cai, W.; Hu, F. X.; Yang, H.; Liu, B. Recent Advances in Single Atom Catalysts for the Electrochemical Carbon Dioxide Reduction Reaction. *Chem Sci* **2021**, *12* (20), 6800–6819. https://doi.org/10.1039/D1SC01375K.

(110) He, Q.; Lee, J. H.; Liu, D.; Liu, Y.; Lin, Z.; Xie, Z.; Hwang, S.; Kattel, S.; Song, L.; Chen, J. G. Accelerating CO2 Electroreduction to CO Over Pd Single-Atom Catalyst. *Adv Funct Mater* **2020**, *30* (17), 2000407. https://doi.org/10.1002/adfm.202000407.

(111) Liu, Z.; Cao, L.; Wang, M.; Zhao, Y.; Hou, M.; Shao, Z. A Robust Ni Single-Atom Catalyst for Industrial Current and Exceptional Selectivity in Electrochemical CO2 Reduction to CO. *J Mater Chem A Mater* **2024**, *12* (14), 8331–8339. https://doi.org/10.1039/D3TA07216A.

(112) Wang, J.; Zhu, Z.; Lin, Y.; Li, Z.; Tang, W.; Wang, J.; Chen, J. S.; Wu, R. Nano-Engineering in Zinc-Based Catalysts for CO2 Electroreduction: Advances and Challenges. *Carbon Neutralization* **2024**, *3* (3), 423–440. https://doi.org/10.1002/cnl2.131.

(113) Liu, Q.-W.; He, B.-L.; Zheng, D.-S.; Zhou, X.-Q.; Zhang, X.; Huang, J.-M.; Wang, Y.; Lai, W.-C.; Gu, Z.-Y. Delocalization State-Stabilized Znδ+ Active Sites for Highly Selective and Durable CO2 Electroreduction. *Small* **2024**, *20* (52), 2406604. https://doi.org/10.1002/smll.202406604.

(114) Han, N.; Ding, P.; He, L.; Li, Y.; Li, Y. Promises of Main Group Metal–Based Nanostructured Materials for Electrochemical CO2 Reduction to Formate. *Adv Energy Mater* **2020**, *10* (11), 1902338. https://doi.org/10.1002/aenm.201902338.

(115) Chen, Y.; Kanan, M. W. Tin Oxide Dependence of the CO2 Reduction Efficiency on Tin Electrodes and Enhanced Activity for Tin/Tin Oxide Thin-Film Catalysts. *J Am Chem Soc* **2012**, *134* (4), 1986–1989. https://doi.org/10.1021/ja2108799.

(116) Wang, T.; Chen, J.; Ren, X.; Zhang, J.; Ding, J.; Liu, Y.; Lim, K. H.; Wang, J.; Li, X.; Yang, H.; Huang, Y.; Kawi, S.; Liu, B. Halogen-Incorporated Sn Catalysts for Selective Electrochemical CO2 Reduction to Formate. *Angewandte Chemie International Edition* **2023**, *62* (10), e202211174. https://doi.org/10.1002/anie.202211174.

(117) Tian, B.; Wu, H.; Zhang, Y.; Chen, C.; Abdalla, K. K.; Sendeku, M. G.; Zhou, L.; Yu, J.; Wang, Y.; Kuang, Y.; Xu, H.; Li, J.; Sun, X. Cu-Induced Interfacial Water Engineering of SnO2 for Durable and Highly Selective CO2 Electroreduction. *ACS Catal* **2024**, *14* (14), 10904–10912. https://doi.org/10.1021/acscatal.4c01670.

(118) Li, K.; Xu, J.; Zheng, T.; Yuan, Y.; Liu, S.; Shen, C.; Jiang, T.; Sun, J.; Liu, Z.; Xu, Y.; Chuai, M.; Xia, C.; Chen, W. In Situ Dynamic Construction of a Copper Tin Sulfide Catalyst for High-Performance Electrochemical CO2 Conversion to Formate. *ACS Catal* **2022**, *12* (16), 9922–9932. https://doi.org/10.1021/acscatal.2c02627.

(119) Bai, X.; Chen, W.; Zhao, C.; Li, S.; Song, Y.; Ge, R.; Wei, W.; Sun, Y. Exclusive Formation of Formic Acid from CO2 Electroreduction by a Tunable Pd-Sn Alloy. *Angewandte Chemie International Edition* **2017**, *56* (40), 12219–12223. https://doi.org/10.1002/anie.201707098.

(120) Liu, H.; Li, B.; Liu, Z.; Liang, Z.; Chuai, H.; Wang, H.; Lou, S. N.; Su, Y.; Zhang, S.; Ma, X. Ceria -Mediated Dynamic Sn0/Snδ+ Redox Cycle for CO2 Electroreduction. *ACS Catal* **2023**, *13* (7), 5033–5042. https://doi.org/10.1021/acscatal.2c06135.

(121) Sabouhanian, N.; Lipkowski, J.; Chen, A. Unveiling the Potential of Bismuth-Based Catalysts for Electrochemical CO2 Reduction. *Industrial Chemistry & Materials* **2025**. https://doi.org/10.1039/D4IM00126E.

(122) Guan, Y.; Liu, M.; Rao, X.; Liu, Y.; Zhang, J. Electrochemical Reduction of Carbon Dioxide (CO2): Bismuth-Based Electrocatalysts. *J Mater Chem A Mater* **2021**, *9* (24), 13770–13803. https://doi.org/10.1039/D1TA01516H.

(123) Yang, Z.; Oropeza, F. E.; Zhang, K. H. L. P-Block Metal-Based (Sn, In, Bi, Pb) Electrocatalysts for Selective Reduction of CO2 to Formate. *APL Mater* **2020**, *8* (6), 060901. https://doi.org/10.1063/5.0004194.

(124) Zhang, X.; Sun, X.; Guo, S.-X.; Bond, A. M.; Zhang, J. Formation of Lattice-Dislocated Bismuth Nanowires on Copper Foam for Enhanced Electrocatalytic CO2 Reduction at Low Overpotential. *Energy Environ Sci* **2019**, *12* (4), 1334–1340. https://doi.org/10.1039/C9EE00018F.

(125) Zu, M. Y.; Zhang, L.; Wang, C.; Zheng, L. R.; Yang, H. G. Copper-Modulated Bismuth Nanocrystals Alter the Formate Formation Pathway to Achieve Highly Selective CO2 Electroreduction. *J Mater Chem A Mater* **2018**, *6* (35), 16804–16809. https://doi.org/10.1039/C8TA05355C.

(126) Yang, S.; Sun, Y.; Wang, C.; Lv, L.; Hu, M.; Jin, J.; Xie, H. One-Step Co-Electrodeposition of SnBi for Efficient Electrochemical Reduction of Carbon Dioxide to Formic Acid. *Catal Sci Technol* **2023**, *13* (3), 758–766. https://doi.org/10.1039/D2CY00859A.

(127) Ren, B.; Wen, G.; Gao, R.; Luo, D.; Zhang, Z.; Qiu, W.; Ma, Q.; Wang, X.; Cui, Y.; Ricardez–Sandoval, L.; Yu, A.; Chen, Z. Nano-Crumples Induced Sn-Bi Bimetallic Interface Pattern with Moderate Electron Bank for Highly Efficient CO2 Electroreduction. *Nat Commun* **2022**, *13* (1), 2486. https://doi.org/10.1038/s41467-022-29861-w.

(128) Detweiler, Z. M.; White, J. L.; Bernasek, S. L.; Bocarsly, A. B. Anodized Indium Metal Electrodes for Enhanced Carbon Dioxide Reduction in Aqueous Electrolyte. *Langmuir* **2014**, *30* (25), 7593–7600. https://doi.org/10.1021/la501245p.

(129) Ma, W.; Xie, S.; Zhang, X.-G.; Sun, F.; Kang, J.; Jiang, Z.; Zhang, Q.; Wu, D.-Y.; Wang, Y. Promoting Electrocatalytic CO2 Reduction to Formate via Sulfur-Boosting Water Activation on Indium Surfaces. *Nat Commun* **2019**, *10* (1), 892. https://doi.org/10.1038/s41467-019-08805-x.

(130) Nitopi, S.; Bertheussen, E.; Scott, S. B.; Liu, X.; Engstfeld, A. K.; Horch, S.; Seger, B.; Stephens, I. E. L.; Chan, K.; Hahn, C.; Nørskov, J. K.; Jaramillo, T. F.; Chorkendorff, I. Progress and Perspectives of Electrochemical CO2 Reduction on Copper in Aqueous Electrolyte. *Chem Rev* **2019**, *119* (12), 7610–7672. https://doi.org/10.1021/acs.chemrev.8b00705.

(131) Vasileff, A.; Xu, C.; Jiao, Y.; Zheng, Y.; Qiao, S.-Z. Surface and Interface Engineering in Copper-Based Bimetallic Materials for Selective CO_2 Electroreduction. *Chem* **2018**, *4* (8), 1809–1831. https://doi.org/10.1016/j.chempr.2018.05.001.

(132) Gao, D.; Arán-Ais, R. M.; Jeon, H. S.; Roldan Cuenya, B. Rational Catalyst and Electrolyte Design for CO2 Electroreduction towards Multicarbon Products. *Nat Catal* **2019**, *2* (3), 198–210. https://doi.org/10.1038/s41929-019-0235-5.

(133) Albo, J.; Sáez, A.; Solla-Gullón, J.; Montiel, V.; Irabien, A. Production of Methanol from CO2 Electroreduction at Cu2O and Cu2O/ZnO-Based Electrodes in Aqueous Solution. *Appl Catal B* **2015**, *176–177*, 709–717. https://doi.org/10.1016/j.apcatb.2015.04.055.

(134) Nie, X.; Luo, W.; Janik, M. J.; Asthagiri, A. Reaction Mechanisms of CO2 Electrochemical Reduction on Cu(111) Determined with Density Functional Theory. *J Catal* **2014**, *312*, 108–122. https://doi.org/10.1016/j.jcat.2014.01.013.

(135) Cai, J.; Zhao, Q.; Hsu, W.-Y.; Choi, C.; Liu, Y.; Martirez, J. M. P.; Chen, C.; Huang, J.; Carter, E. A.; Huang, Y. Highly Selective Electrochemical Reduction of CO2 into Methane on Nanotwinned Cu. *J Am Chem Soc* **2023**, *145* (16), 9136–9143. https://doi.org/10.1021/jacs.3c00847.

(136) Wang, X.; Klingan, K.; Klingenhof, M.; Möller, T.; Ferreira de Araújo, J.; Martens, I.; Bagger, A.; Jiang, S.; Rossmeisl, J.; Dau, H.; Strasser, P. Morphology and Mechanism of Highly Selective Cu(II) Oxide Nanosheet Catalysts for Carbon Dioxide Electroreduction. *Nat Commun* **2021**, *12* (1), 794. https://doi.org/10.1038/s41467-021-20961-7.

(137) Liu, W.; Zhai, P.; Li, A.; Wei, B.; Si, K.; Wei, Y.; Wang, X.; Zhu, G.; Chen, Q.; Gu, X.; Zhang, R.; Zhou, W.; Gong, Y. Electrochemical CO2 Reduction to Ethylene by Ultrathin CuO Nanoplate Arrays. *Nat Commun* **2022**, *13* (1), 1877. https://doi.org/10.1038/s41467-022-29428-9.

(138) Cheng, D.; Zhao, Z.-J.; Zhang, G.; Yang, P.; Li, L.; Gao, H.; Liu, S.; Chang, X.; Chen, S.; Wang, T.; Ozin, G. A.; Liu, Z.; Gong, J. The Nature of Active Sites for Carbon Dioxide Electroreduction over Oxide-Derived Copper Catalysts. *Nat Commun* **2021**, *12* (1), 395. https://doi.org/10.1038/s41467-020-20615-0.

(139) Wang, S.; Kou, T.; Baker, S. E.; Duoss, E. B.; Li, Y. Recent Progress in Electrochemical Reduction of CO2 by Oxide-Derived Copper Catalysts. *Mater Today Nano* **2020**, *12*, 100096. https://doi.org/10.1016/j.mtnano.2020.100096.

(140) Zhong, D.; Cheng, D.; Fang, Q.; Liu, Y.; Li, J.; Zhao, Q. Understanding the Restructuring and Degradation of Oxide-Derived Copper during Electrochemical CO2 Reduction. *Chemical Engineering Journal* **2023**, *470*, 143907. https://doi.org/10.1016/j.cej.2023.143907.

(141) Long, C.; Liu, X.; Wan, K.; Jiang, Y.; An, P.; Yang, C.; Wu, G.; Wang, W.; Guo, J.; Li, L.; Pang, K.; Li, Q.; Cui, C.; Liu, S.; Tan, T.; Tang, Z. Regulating Reconstruction of Oxide-Derived Cu for Electrochemical CO2 Reduction toward n-Propanol. *Sci Adv* **2025**, *9* (43), eadi6119. https://doi.org/10.1126/sciadv.adi6119.

(142) Dai, J.; Zhu, J.; Xu, Y.; Liu, X.; Zhu, D.; Xu, G.; Liu, H.; Li, G. Structural Regulating of Cu-Based Metallic Electrocatalysts for CO2 to C2+ Products Conversion. *ChemSusChem* **2024**, *n/a* (n/a), e202402184https://doi.org/10.1002/cssc.202402184.

(143) Zhang, Z.-Y.; Tian, H.; Bian, L.; Liu, S.-Z.; Liu, Y.; Wang, Z.-L. Cu-Zn-Based Alloy/Oxide Interfaces for Enhanced Electroreduction of CO2 to C2+ Products. *Journal of Energy Chemistry* **2023**, *83*, 90–97. https://doi.org/10.1016/j.jechem.2023.04.034.

(144) Guo, P.; Liu, K.; Liu, X.; Liu, R.; Yin, Z. Perspectives on Cu–Ag Bimetallic Catalysts for Electrochemical CO2 Reduction Reaction: A Mini-Review. *Energy & Fuels* **2024**, *38* (7), 5659–5675. https://doi.org/10.1021/acs.energyfuels.3c05194.

(145) Zhu, C.; Chen, A.; Mao, J.; Wu, G.; Li, S.; Dong, X.; Li, G.; Jiang, Z.; Song, Y.; Chen, W.; Wei, W. Cu–Pd Bimetallic Gas Diffusion Electrodes for Electrochemical Reduction of CO2 to C2+ Products. *Small Struct* **2023**, *4* (5), 2200328. https://doi.org/10.1002/sstr.202200328.

(146) Chen, C.; Li, Y.; Yu, S.; Louisia, S.; Jin, J.; Li, M.; Ross, M. B.; Yang, P. Cu-Ag Tandem Catalysts for High-Rate CO2 Electrolysis toward Multicarbons. *Joule* **2020**, *4* (8), 1688–1699. https://doi.org/10.1016/j.joule.2020.07.009.

(147) Varela, A. S. The Importance of PH in Controlling the Selectivity of the Electrochemical CO2 Reduction. *Curr Opin Green Sustain Chem* **2020**, *26*, 100371. https://doi.org/10.1016/j.cogsc.2020.100371.

(148) Moura de Salles Pupo, M.; Kortlever, R. Electrolyte Effects on the Electrochemical Reduction of CO2. *ChemPhysChem* **2019**, *20* (22), 2926–2935. https://doi.org/10.1002/cphc.201900680.

(149) Burgers, I.; Jónasson, J.; Goetheer, E.; Kortlever, R. The Effect of Electrolyte PH and Impurities on the Stability of Electrolytic Bicarbonate Conversion. *ChemSusChem* **2024**, *n/a* (n/a), e202401631. https://doi.org/10.1002/cssc.202401631.

(150) Hori, Y.; Takahashi, R.; Yoshinami, Y.; Murata, A. Electrochemical Reduction of CO at a Copper Electrode. *J Phys Chem B* **1997**, *101* (36), 7075–7081. https://doi.org/10.1021/jp970284i.

(151) Varela, A. S.; Kroschel, M.; Reier, T.; Strasser, P. Controlling the Selectivity of CO2 Electroreduction on Copper: The Effect of the Electrolyte Concentration and the Importance of the Local PH. *Catal Today* **2016**, *260*, 8–13. https://doi.org/10.1016/j.cattod.2015.06.009.

(152) Calle-Vallejo, F.; Koper, M. T. M. Theoretical Considerations on the Electroreduction of CO to C2 Species on Cu(100) Electrodes. *Angewandte Chemie International Edition* **2013**, *52* (28), 7282–7285. https://doi.org/10.1002/anie.201301470.

(153) Wu, J.; Li, W.; Liu, K.; Kucernak, A.; Liu, H.; Chai, L.; Liu, M. Cation Effects on Electrochemical CO2 Reduction Reaction. *Next Energy* **2023**, *1* (3), 100032. https://doi.org/10.1016/j.nxener.2023.100032.

(154) Murata, A.; Hori, Y. Product Selectivity Affected by Cationic Species in Electrochemical Reduction of CO2 and CO at a Cu Electrode. *Bull Chem Soc Jpn* **1991**, *64* (1), 123–127. https://doi.org/10.1246/bcsj.64.123.

(155) Singh, M. R.; Kwon, Y.; Lum, Y.; Ager, J. W. I. I. I.; Bell, A. T. Hydrolysis of Electrolyte Cations Enhances the Electrochemical Reduction of CO2 over Ag and Cu. *J Am Chem Soc* **2016**, *138* (39), 13006–13012. https://doi.org/10.1021/jacs.6b07612.

(156) Hori, Y.; Murata, A.; Takahashi, R. Formation of Hydrocarbons in the Electrochemical Reduction of Carbon Dioxide at a Copper Electrode in Aqueous Solution. *Journal of the Chemical Society, Faraday Transactions 1: Physical Chemistry in Condensed Phases* **1989**, *85* (8), 2309–2326. https://doi.org/10.1039/F19898502309.

(157) Hori, Y.; Murata, A.; Takahashi, R.; Suzuki, S. Enhanced Formation of Ethylene and Alcohols at Ambient Temperature and Pressure in Electrochemical Reduction of Carbon Dioxide at a Copper Electrode. *J Chem Soc Chem Commun* **1988**, No. 1, 17–19. https://doi.org/10.1039/C39880000017.

(158) Yoo, J. M.; Ingenmey, J.; Salanne, M.; Lukatskaya, M. R. Anion Effect in Electrochemical CO2 Reduction: From Spectators to Orchestrators. *J Am Chem Soc* **2024**, *146* (46), 31768–31777. https://doi.org/10.1021/jacs.4c10661.

(159) Overa, S.; Ko, B. H.; Zhao, Y.; Jiao, F. Electrochemical Approaches for CO2 Conversion to Chemicals: A Journey toward Practical Applications. *Acc Chem Res* **2022**, *55* (5), 638–648. https://doi.org/10.1021/acs.accounts.1c00674.

(160) Higgins, D.; Hahn, C.; Xiang, C.; Jaramillo, T. F.; Weber, A. Z. Gas-Diffusion Electrodes for Carbon Dioxide Reduction: A New Paradigm. *ACS Energy Lett* **2019**, *4* (1), 317–324. https://doi.org/10.1021/acsenergylett.8b02035.

(161) Lees, E. W.; Mowbray, B. A. W.; Parlane, F. G. L.; Berlinguette, C. P. Gas Diffusion Electrodes and Membranes for CO2 Reduction Electrolysers. *Nat Rev Mater* **2022**, *7* (1), 55–64. https://doi.org/10.1038/s41578-021-00356-2.

(162) Wakerley, D.; Lamaison, S.; Wicks, J.; Clemens, A.; Feaster, J.; Corral, D.; Jaffer, S. A.; Sarkar, A.; Fontecave, M.; Duoss, E. B.; Baker, S.; Sargent, E. H.; Jaramillo, T. F.; Hahn, C. Gas Diffusion Electrodes, Reactor Designs and Key Metrics of Low-Temperature CO2 Electrolysers. *Nat Energy* **2022**, *7* (2), 130–143. https://doi.org/10.1038/s41560-021-00973-9.

Chapter- 1.2

Investigation of CO_2 hydrogenation over NiPd/C_3N_4 catalyst

Summary:

Palladium-based catalysts have been widely investigated for the hydrogenation of CO_2 to formate. However, monometallic Pd catalysts typically require high metal loadings to achieve significant turnover numbers. To address this limitation, bimetallic catalysts have been developed to enhance catalytic performance while reducing Pd content. Herein, NiPd/C_3N_4 have been developed as an efficient catalyst for this reaction. In this catalyst, the synergistic interaction between the metal species and the support helps in achieving enhanced catalytic activity.

1.2.1. Introduction

The hydrogenation of CO_2 to formic acid is typically conducted in an aqueous medium under high pressure and temperature, with a base additive such as bicarbonate or carbonate. The use of an aqueous medium plays a pivotal role in lowering the Gibbs free energy to -4 kJ mol^{-1}, rendering the reaction thermodynamically spontaneous. In this medium, CO_2 exists in equilibrium with bicarbonate, which is a crucial intermediate for the conversion[1,2].

Monometallic palladium based catalyst has been extensively studied for the conversion of CO_2/bicarbonate to formate. In these catalysts, Pd functions as an active site for H_2 activation, leading to the formation of surface hydrides[3,4]. However, in these systems, higher Pd loading is required to achieve higher turnover numbers for formate formation[5–7]. As a noble metal, Pd is expensive, making these systems less cost-effective. Therefore, advancing catalyst design to reduce Pd loading while enhancing catalytic activity is essential for the broader application and economic feasibility of this process.

To overcome this limitation, bimetallic catalysts have been developed.[8–11] Among them, the PdAg system has emerged as a state-of-the-art catalyst exhibiting high turnover numbers (TON). However, Ag, being a noble metal, adds to the cost of the catalyst, necessitating its replacement with more affordable transition metals to improve economic feasibility.

Nickel-based catalysts have garnered attention for their ability to hydrogenate CO_2 into methane and other hydrocarbons[12,13]. The application of Ni for the direct conversion of CO_2 to formic acid was first reported by Farlow et al.[14], wherein Raney Ni was used as the catalyst. Density functional theory (DFT) calculations by Peng et al. further support the efficiency of Ni-based systems. Their findings indicate that the energy barrier for forming the formate ($HCOO^-$) intermediate is lower than that for forming the carboxyl intermediate, favoring a low-energy pathway for formic acid production on the Ni(111) surface[15]. Recently, Fu et al. developed a Ni@$Ni(OH)_2$ core-shell catalyst, where metallic Ni serves as the core and $Ni(OH)_2$ forms the shell. In this system, CO_2 or bicarbonate species adsorb onto the $Ni(OH)_2$ shell, while molecular hydrogen dissociatively adsorbs onto the metallic Ni core. The hydrogen atoms then spill over to the $Ni(OH)_2$ shell, reacting with the adsorbed CO_2 species to form formate. This catalyst shows that Ni is the active site for the activation of H_2 while $Ni(OH)_2$ is a potential catalytic site for the adsorption and activation of CO_2[16]. However, the low activity compared to Pd based systems could be attributed to the limited activation of H_2 on metallic Ni.

Bimetallic PdNi alloy supported on a carbon nanotube (CNT)-graphene composite has been studied for CO_2 hydrogenation to formate under base-free conditions. Herein, Ni acts as the active site for CO_2 activation, while Pd dissociatively adsorbs H_2 to form surface hydrides, facilitating formate formation. However, the observed TON for formate remained low[17]. This could be attributed to two factors: (1) the absence of a base additive, which limits CO_2 solubility in the reaction medium, and (2) the lack of a support material with basic functional groups to bring more CO_2 molecules closer to the active sites.

Recent studies have explored various N-functionalized supports, such as amine-functionalized silica, aminopolymers encapsulated in hollow mesoporous silica, as efficient catalytic supports[18,19]. In these reports, it was observed that the nitrogen functional groups help to capture and activate CO_2, ensuring its steady supply to the metal active sites. However, silica-based supports face a critical limitation due to their instability in basic media, which leads to their gradual dissolution over time[20–22]. To address this, alternative supports such as amine-functionalized mesoporous carbon and C_3N_4 have been developed[23–27]. These materials are stable under basic conditions and lead to superior performance. Integrating such supports into NiPd systems can address the challenges of CO_2 solubility and its proximity to active sites, thereby enhancing catalytic performance and developing cost-effective catalysts.

1.2.2. Scope of the Investigation

In this study, we present NiPd supported on g-C_3N_4 as an efficient catalyst for the hydrogenation of CO_2 to formic acid in the presence of a carbonate base. Our findings reveal that C_3N_4 plays a critical role in facilitating the adsorption of CO_2 molecules closer to the active site. At these sites, $Ni(OH)_2$ aids in CO_2 activation, which then reacts with hydrides present on the Pd surface to form formic acid. The catalyst demonstrates exceptional performance, achieving a high turnover number of 2432 over a reaction duration of 24 hours. Additionally, operando DRIFT spectroscopy has been employed to elucidate the reaction mechanism on the metal active site, providing insights into the catalytic process.

1.2.3. Experimental Section

1.2.3.1. Materials

Melamine, palladium chloride ($PdCl_2$), sodium borohydride ($NaBH_4$), silver nitrate ($AgNO_3$), dicyandiamide, and D_2O were purchased from Sigma Aldrich. Nickel chloride hexahydrate ($NiCl_2.6H_2O$), sodium carbonate (Na_2CO_3) were procured from Loba Chemie Pvt. Ltd. Copper chloride dihydrate ($CuCl_2. 2H_2O$), sodium hydroxide (NaOH) and boric Acid (H_3BO_3) were purchased from Merck Life Sciences Pvt. Ltd. Cobalt chloride hexahydrate ($CoCl_2. 6H_2O$), manganous chloride tetrahydrate ($MnCl_2.4H_2O$), activated charcoal and sodium bicarbonate ($NaHCO_3$) was purchased from SD fine Chem Ltd. Dimethyl sulphoxide (DMSO) was procured from Spectrochem. All the chemicals were used without further purification. Deionized (Milli-Q) water was used for all the synthesis and catalytic studies.

1.2.3.2. Characterization technique

The Powder X-Ray Diffraction (PXRD) patterns of the synthesized materials were acquired using a Rigaku diffractometer with Cu anode generating an X-ray of wavelength 1.54 Å. HRTEM (high resolution transmission electron microscopy) images were obtained using the JEOL JEM-2100 Plus electron microscope. HAADF- STEM images were obtained using the Thermofisher Talos F200S electron microscope. The samples for the TEM measurements were prepared by dropcasting the material dispersed in ethanol on Cu grid. X-ray Photoelectron Spectroscopy (XPS) measurements were performed using a Thermofisher K-Alpha spectrometer using a microfocused Al Kα monochromator. Inductively coupled plasma optical emission spectroscopy (ICP-OES) analyses were performed on the Perkin Elmer Optima 7000DV instrument to determine the Ni and Pd amount loaded on the support. XAS measurements were performed at PETRA III, beamline P64 in DESY, Germany. Measurements of Ni K-edge and Pd K-edges at ambient pressures were performed in both fluorescence and transmission modes using gas ionization chambers to monitor the incident and transmitted X-ray intensities. The samples for the XAS measurements were prepared by homogeneously mixing the material with cellulose and then pressed into a pellet. Temperature programmed desorption (TPD) with CO_2 as the probe molecule was performed using BelCat II instrument. Quantification of the formate obtained was performed using a Bruker 400 NMR spectrometer. The DRIFT measurements were carried out using Bruker Vertex 70v

FTIR spectrometer equipped with a Harrick DRIFTS cell. The spectra were recorded at a resolution of 4 cm^{-1}, and each spectrum averaged 32 times. The samples were heated to 348 K and maintained at the temperature to determine the intermediates formed on the surface. The sample was purged with CO_2-H_2 (1:1) gas mixture using mass flow controllers from Brooks instruments. A Carbolite Muffle furnace and an Elite tubular furnace were used to prepare the catalyst supports.

1.2.3.3. Synthesis of g-C_3N_4

g-C_3N_4 was synthesized by polycondensation of melamine reported in literature[28]. In a typical synthesis, 5g of melamine was taken in an alumina crucible and was heated to 550 ^{o}C in the muffle furnace at a heating rate of 2 ^{o}C/min and kept at 550 ^{o}C for 5 h to obtain a pale-yellow colored g-C_3N_4 material.

1.2.3.4. Synthesis of BCN

To synthesize Boron carbon nitride (BCN), 1 g of activated charcoal, 0.61 g of boric acid and 2.5 g of dicyandiamide were dispersed in 75 mL of water in a 100 mL beaker. The solution was heated at 75 ^{o}C until the water evaporated. The resultant black powder was collected, ground, and transferred into an alumina crucible. The crucible was placed in a tubular furnace and annealed at 900 ^{o}C for 10 h in the N_2 atmosphere, followed by heating at 930 ^{o}C in the NH_3 atmosphere for 3 h. The ramp rate was kept at 5 ^{o}C/min ramp rate for the heating and cooling steps[29].

1.2.3.5. Synthesis of N-doped Carbon

For the synthesis of N-doped carbon, 1 g of activated charcoal and 2.5 g of dicyandiamide were dispersed in 75 mL of water in a 100 ml beaker. The solution was heated at 75 ^{o}C until the water evaporated. The resultant black powder was collected, ground, and transferred into an alumina crucible. The crucible was placed in a tubular furnace and annealed at 930 ^{o}C in an NH_3 atmosphere for 3 h. The ramp rate was kept at 5 ^{o}C/min ramp rate for the heating and cooling steps.

1.2.3.6. Synthesis of NiPd/g-C_3N_4

NiPd/C_3N_4 was synthesized by $NaBH_4$ assisted reduction of metal precursors over g-C_3N_4 at room temperature[30]. In a typical synthesis, 200mg of C_3N_4 was dispersed in 25 mL water by sonication for 15 mins. To the dispersion, 0.188 mL of 0.1M H_2PdCl_4 solution and 0.341 mL of 0.1 M $NiCl_2.6H_2O$ solution were added. The mixture was stirred for 30 mins. Subsequently, 3 mL of 0.1 M $NaBH_4$ was added dropwise to the mixture and stirred for 30 mins. The sample was collected by centrifugation at 12000 rpm for 4 mins. The sample was washed twice with distilled water and once with ethanol to obtain the final catalyst. NiPd/C_3N_4 with varying Ni content was synthesized using the same method. Similarly, MnPd, CoPd, AgPd, CuPd, Ni, and Pd supported on C_3N_4 were prepared using $MnCl_2.4H_2O$, $CoCl_2.6H_2O$, $AgNO_3$, and $CuCl_2.2H_2O$ as precursors for Mn, Co, Ag, and Cu respectively. NiPd supported on N-doped Carbon and BCN were also synthesized for comparison.

1.2.3.7. Catalytic Hydrogenation of CO_2

CO_2 hydrogenation to formic acid was conducted with a batch type reactor *(Figure 1.2.1)*. The CO_2 hydrogenation reactions were carried out using a Parr Hastealloy 4790 pressure vessel of 50mL capacity. The autoclave consisted of a movable head with split ring closure. The head was fitted with a pressure gauge, rupture disk, J-type thermocouple, and gas inlet/outlet valve. For the reaction, 10 mL of 0.5 M Na_2CO_3 was taken in a glass cell. To this, 30 mg of the catalyst was added and dispersed by sonication. The glass cell was inserted in the autoclave. The system was then pressurized to 40 bar by adding 20 bar CO_2 and 20 bar H_2. The formic acid obtained was analyzed by Nuclear Magnetic Resonance Spectroscopy (NMR).

Figure 1.2.1: Parr autoclave used to study CO_2 hydrogenation (Parr Hastelloy 4790)

1.2.3.8. Sample preparation for quantification of formate

To prepare the solution for NMR analysis, the post reaction samples were filtered using 0.2 micron nylon filters to remove the solid catalyst. 480 µl of the sample was mixed with 100 µl D_2O (used as a solvent) and 20 µl DMSO (used as an internal standard). The resultant solution was transferred into an NMR tube. Solvent suppression was used to get a better resolution of the peak corresponding to the formate present in the aqueous medium. The catalytic activity was compared using the turnover number, which is the ratio of mmol of formate to mmol of Pd present in the catalyst.

$$\textbf{Turnover Number} = \frac{\boldsymbol{mmol\ of\ formate}}{\boldsymbol{mmol\ of\ Pd}}$$

1.2.3.9. Fitting of EXAFS data:

The EXAFS data are processed using Athena software, which is a part of the Demeter 0.9.26 software suite, following the standard background subtraction procedure[31]. The fitting of the EXAFS data was performed using Artemis software in the radial (R) space.

For Feff calculations of Ni K edge and Pd K edge, the standard Ni metal (ICSD 8688), $Ni(OH)_2$ (ICSD 24015), and Pd metal (PDF 9009820), $Pd(acac)_2$ (ICSD 251339) were used. The quick first shell (QFS) method was used to fit the Ni-Pd path of the NiPd bimetallic system.

1.2.4. Result and Discussion

CO_2 hydrogenation reaction was performed in a 50mL Parr reactor at a total pressure of 40 bar (H_2:CO_2 = 1:1) at 75 °C. The catalytic activity was analyzed by comparing the turnover number (TON) values which is a ratio of moles of formate produced per mole of Pd in the catalyst.

Initially, to determine the optimal metal content, the hydrogenation reaction was performed with varying Ni and Pd content *(Figure 1.2.2 a)*. It was observed that NiPd with 64 mol% of Ni and 36 mol% Pd on g-C_3N_4 (corresponding to 0.7 wt% Ni and 0.7 wt % Pd with respect to g-C_3N_4) gives the highest TON of 995 for a reaction duration of 1h. After determining the optimal ratio of Ni with respect to Pd, Ni was replaced with other elements, i.e., Mn, Co, Cu, and Ag, in the same proportion *(Figure 1.2.2 b)*. For a reaction duration of 1 h, NiPd supported on C_3N_4 showed exceptional activity, outperforming other metal combinations. Interestingly, Ni/C_3N_4 showed negligible activity, while Pd/C_3N_4 showed a TON of 600. Hence, NiPd/C_3N_4 was used for all further studies.

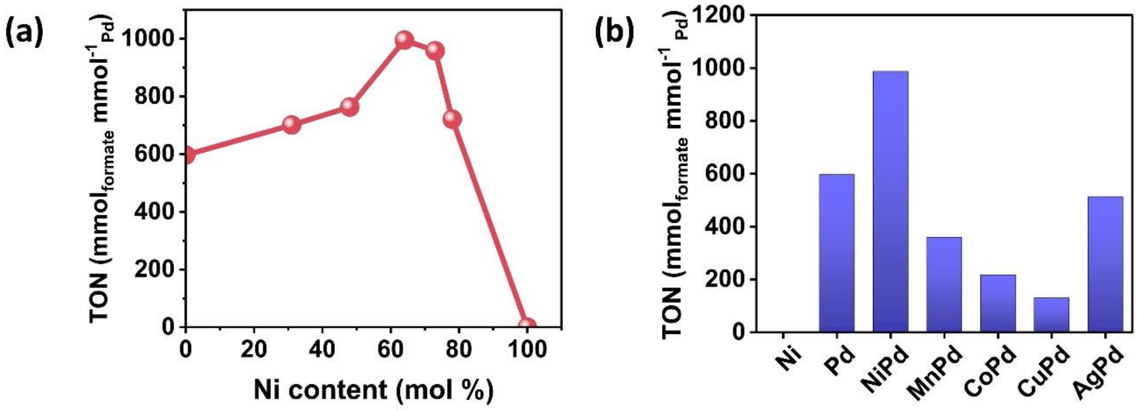

Figure 1.2.2 : (a) Dependence of TON on varying Ni and Pd content and **(b)** Catalytic activity with different metal combinations. The metal species were supported on C_3N_4. (Reaction conditions: 30 mg catalyst, 75 °C, 0.5 M Na_2CO_3, 40 bar H_2, 40 bar CO_2, 1h)

The choice of support plays a critical role in stabilizing nanoparticles and enhancing the catalytic activity. For CO_2 hydrogenation, nitrogen-containing supports are particularly effective, as they facilitate the proximity of CO_2 to the metal active sites. Additionally, supports with high surface areas expose more active sites to reactants, thereby improving catalytic performance. To explore this, the catalytic activity of NiPd (1:1) on various nitrogen-containing supports, including N-doped carbon and boron carbon nitride (BCN), was studied *(Figure 1.2.3 a)*. Among these, C_3N_4, with its higher nitrogen content compared to BCN and N-doped carbon, proved to be the most suitable support. Catalytic activity tests over 24 hrs using NiPd supported on activated charcoal showed no significant activity. Likewise, unsupported NiPd did not show any catalytic activity. These findings highlight the pivotal role of the N-functional group containing C_3N_4 in enhancing catalytic activity for CO_2 hydrogenation.

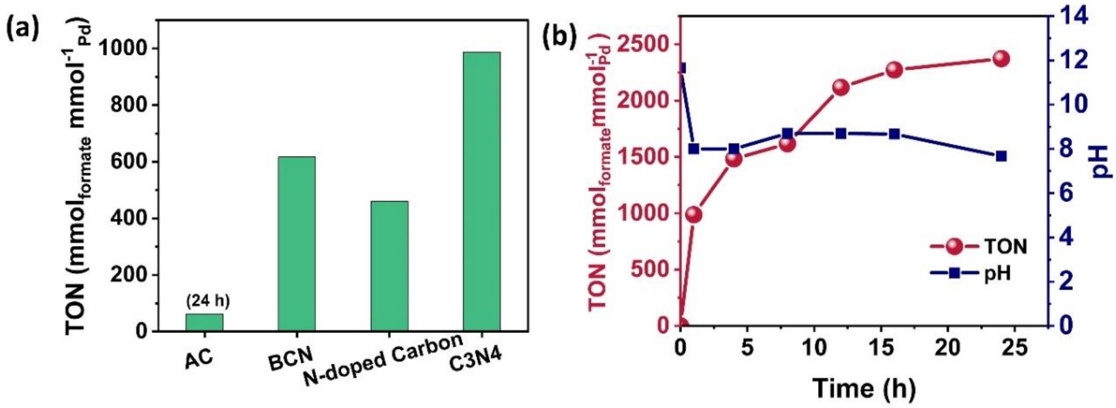

Figure 1.2.3: (a) Catalytic activity on NiPd on varying support (Reaction conditions: 30 mg catalyst, 75 °C, 0.5 M Na_2CO_3, 40 bar H_2, 40 bar CO_2, 1h) and **(b)** Variation in TON for the catalytic activity of NiPd/C_3N_4 with time and the corresponding changes in the pH. (Reaction conditions: 30 mg catalyst, 75 °C, 0.5 M Na_2CO_3, 40 bar H_2, 40 bar CO_2)

The variation in activity with the overall duration of the reaction was estimated to determine the maximum TON *(Figure 1.2.3 b)*. NiPd/C_3N_4 exhibited a maximum TON of 2432 for a reaction duration of 24 h. pH of the solution was also measured before and after the reaction. A decrease in pH from 11.4 to 7.7 is observed post reaction due to the dissolution of CO_2. This decrease in the pH results in limited solubility of CO_2, leading to a saturation in activity beyond 12 h.

The influence of the concentration of the base additive, i.e. carbonate, on the reaction rate was investigated, and the order of reaction with respect to base concentration was determined from the double logarithmic plot. It was observed that increasing the carbonate concentration enhanced the reaction rate for NiPd/C_3N_4, exhibiting a positive order of reaction, i.e., 0.225. In contrast, for Pd/C_3N_4, the reaction rate decreased with higher carbonate concentrations, resulting in a negative order of reaction, i.e., -0.275 *(Figure 1.2.4 a)*. This indicates that elevated carbonate concentrations poison the active sites, reducing the rate of the reaction for Pd/C_3N_4. However, the incorporation of Ni mitigates active site poisoning, thereby promoting the catalytic activity. The activation energy to drive CO_2 hydrogenation was determined from the Arrhenius plot. For Pd/C_3N_4, the activation energy was estimated to be 44.9 kJ mol^{-1}. Incorporation of Ni lowers the activation energy to 34.92 kJ mol^{-1} on NiPd/C_3N_4, indicating a faster reaction kinetics *(Figure 1.2.4 b)*.

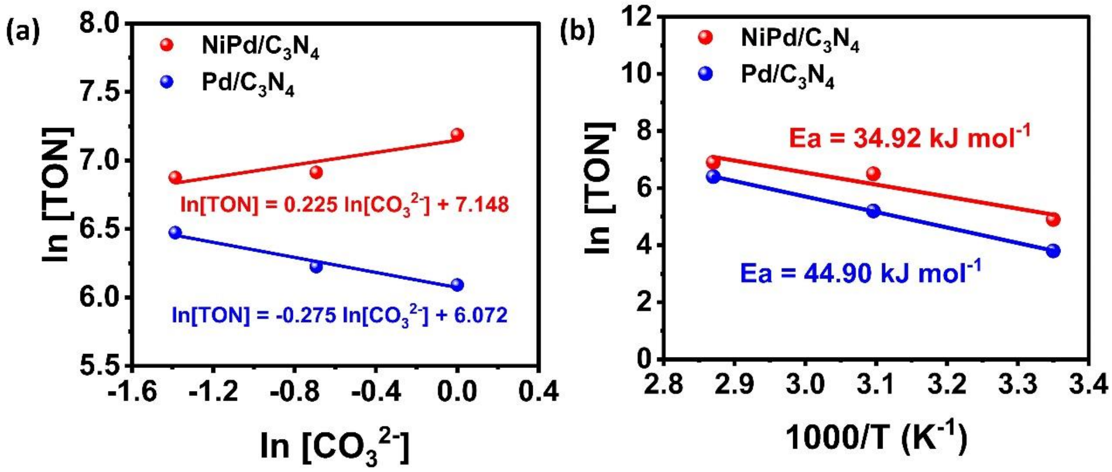

Figure 1.2.4: (a) Dependence of rate of reaction on carbonate concentration and **(b)** Determination of activation energy from Arrhenius plot. (Reaction conditions: 30 mg catalyst, 75 °C, 0.5 M Na_2CO_3, 40 bar H_2, 40 bar CO_2, 1h)

To elucidate the factors contributing to the observed catalytic activity, NiPd/C_3N_4 was further characterized. The PXRD pattern for NiPd/C_3N_4 *(Figure 1.2.5)* showed a pronounced diffraction peak for the (002) plane at 27.3° corresponding to periodic interplanar stacking of the graphitic sheets and a broad peak at 12.8° for (100) due to the intraplanar structural packing of the tri-s-triazine units[32]. No characteristic peaks corresponding to the metal species were observed. This could be attributed to the low loading of the metal nanoparticles on the C_3N_4 support. From ICP-OES analysis, the loading of Ni and Pd was estimated to be 0.67 wt% and 0.72 wt%, respectively with respect to C_3N_4. Likewise, the PXRD pattern for Ni/C_3N_4 and Pd/C_3N_4 showed the peaks corresponding to g-C_3N_4, and no peaks corresponding to the metal entities were observed.

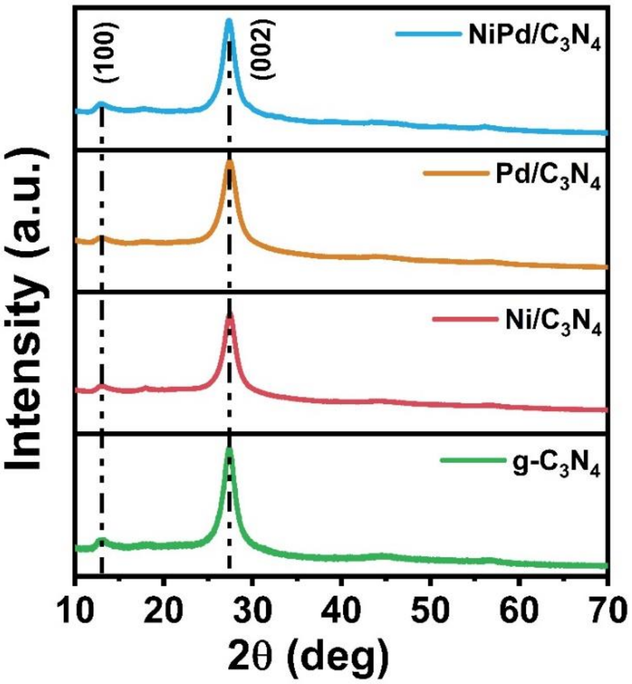

Figure 1.2.5 : Powder X-Ray Diffraction of NiPd/C_3N_4, Ni/C_3N_4, Pd/C_3N_4 and g-C_3N_4

To further understand the chemical state of Ni and Pd atoms in the catalyst, XPS and XAS measurements were performed. The Ni 2p XPS spectra *(Figure 1.2.6 a)* of NiPd/C_3N_4 and Ni/C_3N_4 show the existence of both Ni^0 and Ni^{2+} species. NiPd/C_3N_4 shows peaks corresponding to Ni^0 at 853.3 eV ($2p_{3/2}$) and 870.4 eV ($2p_{1/2}$) and for Ni^{2+} at 855.8 eV ($2p_{3/2}$) and 873.2 eV ($2p_{1/2}$). The Ni 2p XPS spectra of Ni/C_3N_4 show peaks at 853.0 eV ($2p_{3/2}$) and 870.2 eV ($2p_{1/2}$) for Ni^0, while the peaks at 855.6 eV ($2p_{3/2}$) and 873.4 eV ($2p_{1/2}$) correspond to Ni^{2+} [33,34]. Upon comparison, it can be observed that the $2p_{3/2}$ peaks for NiPd/C_3N_4 show a positive shift of 0.3 eV and 0.2 eV in the binding energy of Ni^0 and Ni^{2+}, respectively.

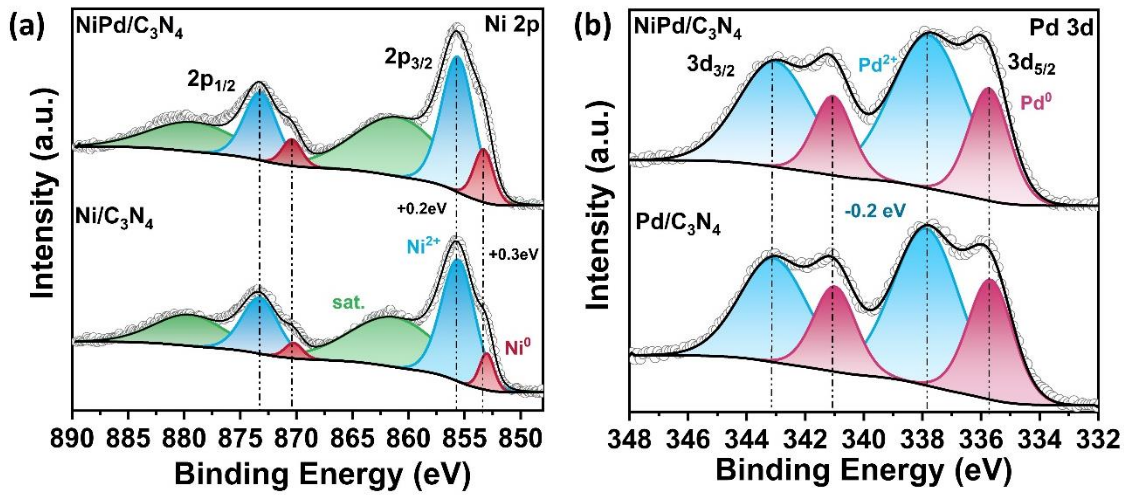

Figure 1.2.6 : X- Ray Photoelectron Spectroscopy **(a)** Ni 2p high resolution spectra comparing NiPd/C_3N_4 and Ni/C_3N_4 , **(b)** Pd 3d high resolution spectra comparing NiPd/C_3N_4 and Pd/C_3N_4

The Pd 3d XPS spectra of NiPd/C_3N_4 and Pd/C_3N_4 *(Figure 1.2.6 b)* also show the existence of both Pd^0 and Pd^{2+} species. Pd/C_3N_4 shows peaks at 335.7 eV ($3d_{5/2}$) and 341.0 eV ($3d_{3/2}$) for Pd^0, while the peaks at 337.9 eV ($3d_{5/2}$) and 343.2 eV ($3d_{3/2}$) correspond to Pd^{2+}. For NiPd/C_3N_4, peaks at 335.8 eV ($3d_{5/2}$) and 341.1 eV ($3d_{3/2}$) are attributed to Pd^0, while the peaks corresponding to Pd^{2+} appear at 337.7 eV ($3d_{5/2}$) and 343.1 eV ($3d_{3/2}$) [35–37]. A negative shift of 0.2 eV is observed in the binding energy for Pd^{2+} peaks in NiPd/C_3N_4 as compared to Pd/C_3N_4, while no significant shift in the binding energy is observed for the Pd^0 peaks. This negative shift in the binding energy of Pd^{2+} peaks suggests a charge transfer from Ni to Pd.

XAS studies were performed to further understand the oxidation states and the local coordination environment of Ni and Pd in the catalyst *(Figure 1.2.7)*. The spectra obtained were compared with the standard Ni foil, NiO, Pd foil and Pd(acac)$_2$. The Ni-K edge XANES spectra *(Figure 1.2.7 a)* for NiPd/C_3N_4 and Ni/C_3N_4 overlap with NiO, suggesting that in the catalyst, Ni is present predominantly in the +2 oxidation state as Ni(OH)$_2$. However, the Pd K edge XANES spectra *(Figure 1.2.7 b)* of NiPd/C_3N_4 and Pd/C_3N_4 lie in between that of Pd foil and Pd(acac)$_2$, suggesting the existence of Pd in a mixed oxidation state[38]. The Ni K edge EXAFS spectra show the presence of the Ni-O bond and the metallic Ni-Ni/Pd bond in NiPd/C_3N_4 and Ni/C_3N_4 *(Figure 1.2.7 c)*.

Likewise, Pd K edge EXAFS spectra show the presence of Pd-O and Pd-Pd/Ni bond in NiPd/C_3N_4 and Pd/C_3N_4 *(Figure 1.2.7 d)*.

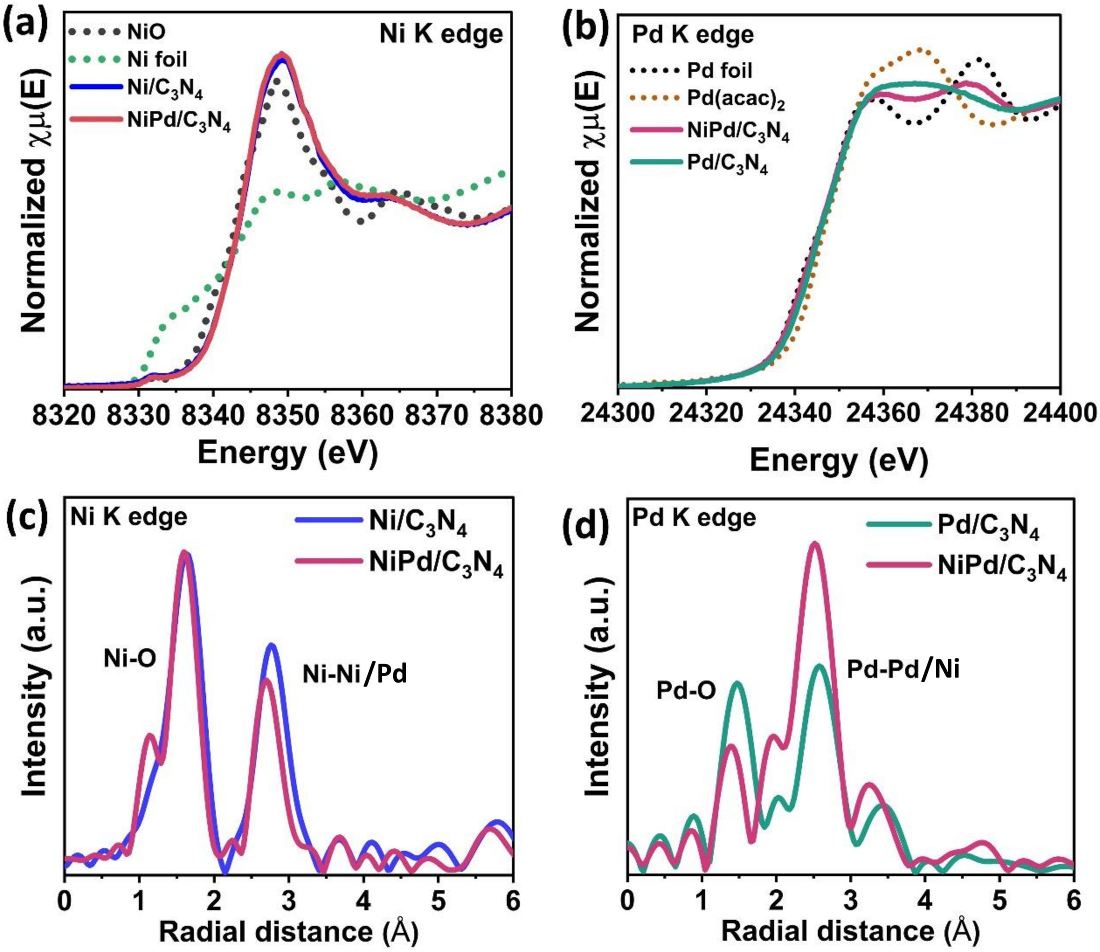

Figure 1.2.7: X-ray Absorption Spectroscopy **(a)** Ni K edge XANES spectra, **(b)** Pd K edge XANES spectra, **(c)** Ni K edge EXAFS spectra and **(d)** Pd K edge EXAFS spectra

Multishell fitting of the FT-EXAFS spectra of Ni K-edge and Pd K edge *(Figure 1.2.8 to Figure 1.2.10)* was performed to determine the bond length and the relative phases of the metal species in the catalyst. The estimated Ni-O, Ni-Ni, and Ni-Pd bond lengths are 2.04 Å, 2.45 Å, and 2.62 Å, respectively, for NiPd/C_3N_4. These values are comparable to the theoretical value for Ni-O (2.05 Å) from the $Ni(OH)_2$ phase, Ni-Ni (2.49 Å) from the Ni metal phase, and Ni-Pd (2.72 Å) from NiPd bimetallic phase[39–42] confirming the presence of both the oxide and metallic species of Ni *(Figure 1.2.8)*. Similarly, multishell fitting of the Pd K edge showed that the Pd-O, Pd-Pd and Pd-Ni bond lengths were estimated to be 1.98 Å, 2.75 Å and 2.62 Å, respectively. These values also matched well with the theoretical values for the Pd-O bond (2.047 Å) from the $Pd(acac)_2$ phase, Pd-Pd bond

(2.75 Å) from the Pd metal phase and the Pd-Ni bond (2.719 Å) from the NiPd bimetal phase supporting the presence of oxide and the metallic species within the catalyst *(Figure 1.2.9)*[35,42,43].

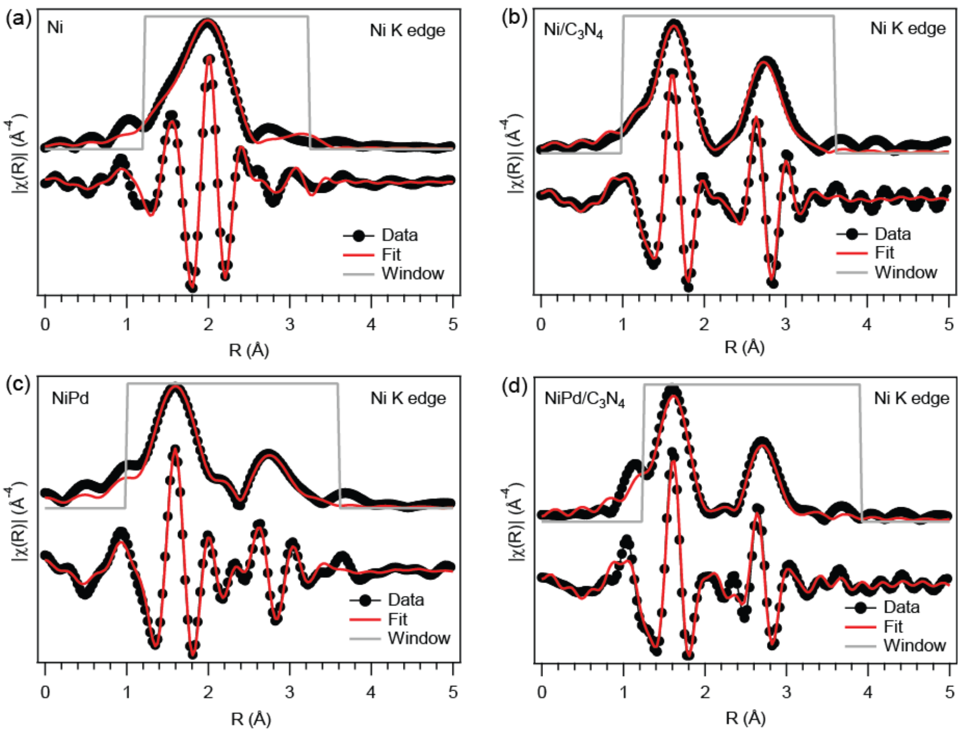

Figure 1.2.8: Multishell peak fitting for the Fourier transformed R-space plots of Ni K edge EXAFS spectra of **(a)** Ni$(OH)_2$, **(b)** Ni/C_3N_4, **(c)** NiPd and **(d)** NiPd/C_3N_4

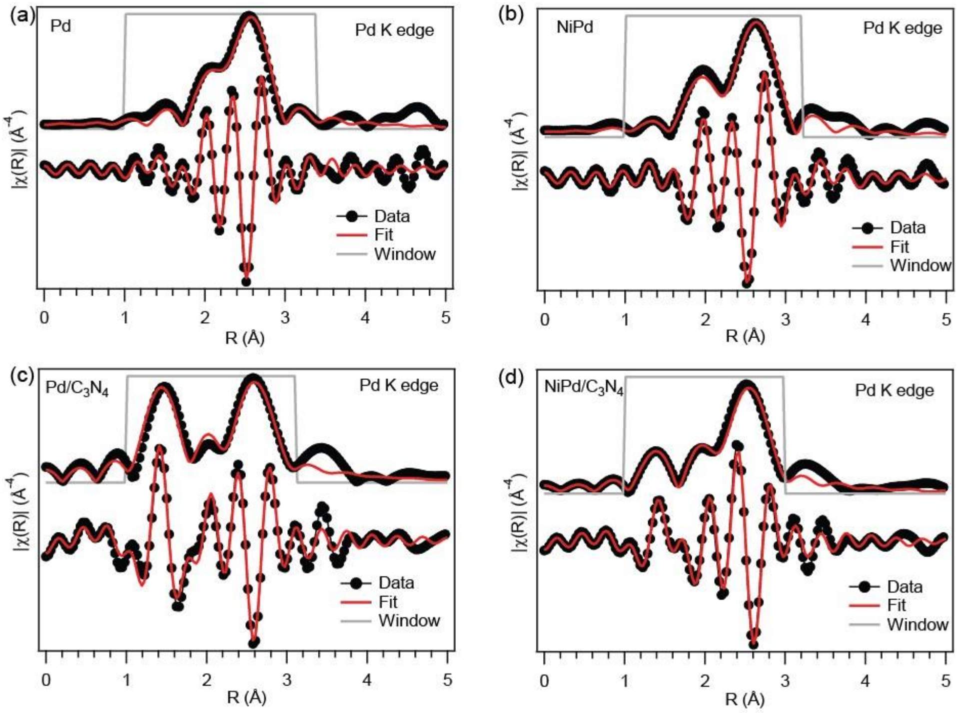

Figure 1.2.9: Multishell peak fitting for the Fourier transformed R-space plots of Pd K edge EXAFS spectra of **(a)** Pd, **(b)** NiPd, **(c)** Pd/C_3N_4 and **(d)** NiPd/C_3N_4

The analysis of the relative phases of the metal species revealed that, in NiPd/C_3N_4, Ni is primarily present as $Ni(OH)_2$ (97%), similar to its distribution in Ni/C_3N_4. In contrast, Pd exists in mixed oxidation states, with 53% as Pd^0 and 47% as Pd^{2+}. This differs from Pd/C_3N_4, where Pd predominantly exists as Pd^{2+} (70.5%). The bimetallic phases were relatively small compared to the Ni-Ni and Pd-Pd bonds and were, therefore, incorporated into the overall estimation of the metallic phase *(Figure 1.2.10)*. The fitting parameters of the EXAFS spectra are shown in *Table 1.2.1* and *Table 1.2.2*.

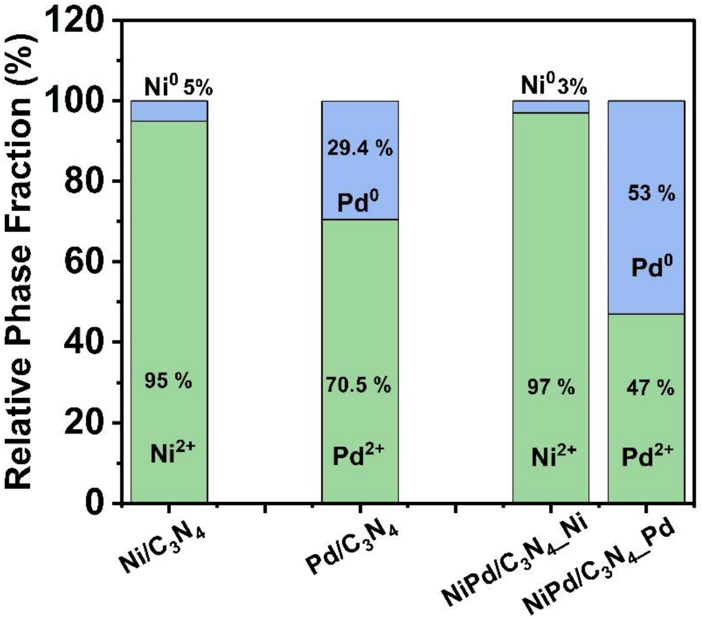

Figure 1.2.10: The relative phase fraction of Ni^{2+}, metallic Ni, $Pd^{2+,}$ and metallic Pd determined from the multi-shell fitting of Ni K edge and Pd K edge EXAFS of catalysts Pd/C_3N_4, Ni/C_3N_4, and NiPd/C_3N_4

Table 1.2.1: The Bond length (R) and Debye-Waller factor/Disorder (σ^2) derived from multishell peak fitting parameters for the R-space plots of Ni K edge for the catalysts Ni, Ni/C_3N_4, NiPd, and NiPd/C_3N_4.

Catalyst	**ΔE**	**Ni(OH)$_2$**				**Ni metal**				**NiPd bimetal**	
		Ni-O bond		**Ni-Ni bond**		**Ni-Ni$_1$ bond**		**Ni-Ni$_2$ bond**		**Ni-Pd$_1$ bond**	
		R (Å)	σ^2	R (Å)	σ^2	R (Å)	σ^2	R (Å)	σ^2	R (Å)	σ^2
Ni	-8.9 ± 0.9	2.05 ± 0.01	0.01 ± 0.003	3.08 ± 0.05	0.02 ± 0.001	2.48 ± 0.03	0.01 ± 0.001	3.48 ± 0.06	0.02 ± 0.01	-	-
Ni/C_3N_4	-5.7 ± 0.3	2.06 ± 0.01	0.01 ± 0.001	3.10 ± 0.01	0.01 ± 0.002	2.52 ± 0.008	0.01 ± 0.004	-	-	-	-

NiPd	-4.2 ± 0.6	2.04 ± 0.01	0.01 ± 0.001	3.06 ± 0.06	0.02 ± 0.004	2.49 ± 0.04	0.02 ± 0.01	3.51 ± 0.03	0.01 ± 0.008	2.60 ± 0.05	0.02 ± 0.01
NiPd/ C_3N_4	-6.3 ± 0.4	2.04 ± 0.01	0.01 ± 0.001	3.08 ± 0.01	0.01 ± 0.001	2.45 ± 0.02	0.02 ± 0.01	3.49 ± 0.02	0.01 ± 0.001	2.64 ± 0.03	0.02 ± 0.01

Table 1.2.2: The Bond length (R) and Debye-Waller factor/Disorder (σ^2) derived from multishell peak fitting parameters for the R-space plots of Pd K edge for the catalysts Pd, Pd/C_3N_4, NiPd, and NiPd/C_3N_4.

Catalyst	**ΔE**	**Pd- oxide**		**Pd metal**		**NiPd bimetal**	
		Pd-O bond		**Pd-Pd bond**		**Ni-Pd_1 bond**	
		R (Ȧ)	σ^2	R (Ȧ)	σ^2	R (Ȧ)	σ^2
Pd	3.17 ± 0.63	1.96 ± 0.01	0.02 ± 0.01	2.74 ± 0.10	0.01 ± 0.001	-	-
Pd/C_3N_4	0.55 ± 0.11	1.97 ± 0.02	0.01 ± 0.002	2.77 ± 0.02	0.01 ± 0.002	-	-
NiPd	4.47 ± 0.97	-	-	2.75 ± 0.02	0.01 ± 0.001	2.62 ± 0.05	0.05 ± 0.001
NiPd/C_3N_4	-5.18 ± 0.67	1.98 ± 0.01	0.01 ± 0.003	2.76 ± 0.03	0.01 ± 0.002	2.58 ± 0.09	0.04 ± 0.001

The interaction of the metal species with the support is crucial for enhanced catalytic activity. Hence, to understand the metal support interaction, the XPS spectra for N1s and C1s were analyzed *(Figure 1.2.11 to Figure 1.2.12)*. The N1s XPS spectrum of g-C_3N_4 displayed two prominent peaks corresponding to pyridinic nitrogen (C=N-C) and pyrrolic nitrogen (C-NH-C) at 398.2 eV and 400.2 eV, respectively, along with a minor peak for graphitic nitrogen (N-C_3) at 403.3 eV *(Figure 1.2.11a)*. In the case of NiPd/C_3N_4, a positive shift of 0.6 eV, 0.5 eV, and 0.5 eV was observed for the pyridinic nitrogen, pyrrolic nitrogen, and graphitic nitrogen, respectively[33,44]. This resulted in a binding energy value of 398.8 eV (C=N-C), 400.7 eV (C-NH-C), and 403.8 eV (N-C_3) *(Figure 1.2.11 b)*.

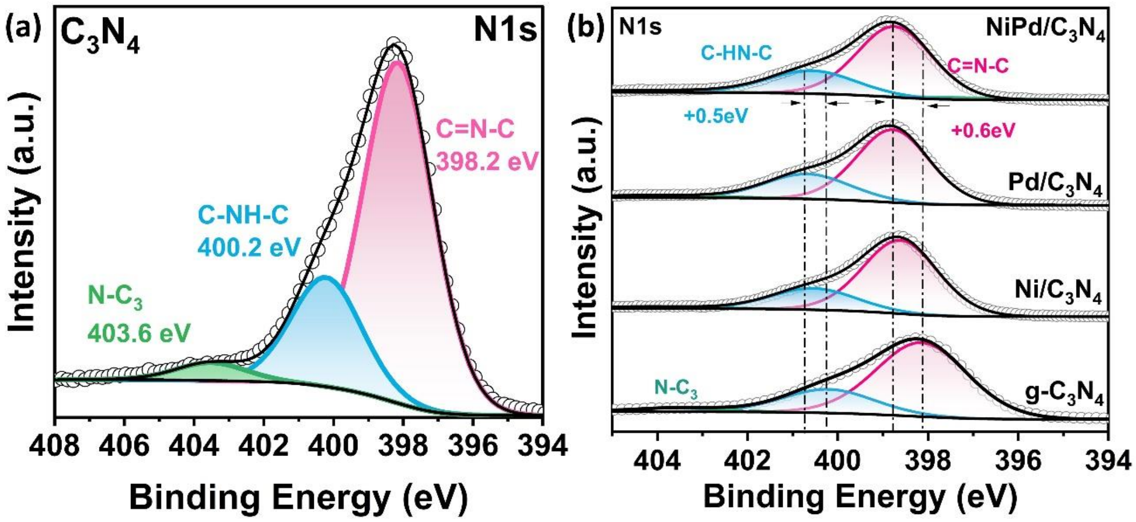

Figure 1.2.11: **(a)** N1s high resolution XPS spectrum of C_3N_4 and **(b)** comparison of N1s XPS spectra of NiPd/C_3N_4, Ni/C_3N_4, Pd/C_3N_4 and g-C_3N_4

The high-resolution C1s XPS spectra of g-C_3N_4 shows three prominent peaks at 284.8 eV, 286.2 eV, and 287.8 eV corresponding to C-C (adventitious carbon), C-NH, and C=N-C. In NiPd/C_3N_4, the peak for C=N-C appears at 288.1 eV, exhibiting a positive shift of 0.4 eV in the binding energy *(Figure 1.2.12)*[34,45]. This positive shift in the N1s and the C1s XPS spectra indicates a charge transfer from the support to the metal species due to the strong metal support interaction. Similarly, Ni/C_3N_4 and Pd/C_3N_4 also exhibit a positive shift in the N1s and C1s binding energy, indicating charge transfer from the support to the metal. The values for the binding energy for N1s and C1s spectra are reported in *Table 1.2.3* and *Table 1.2.4.*

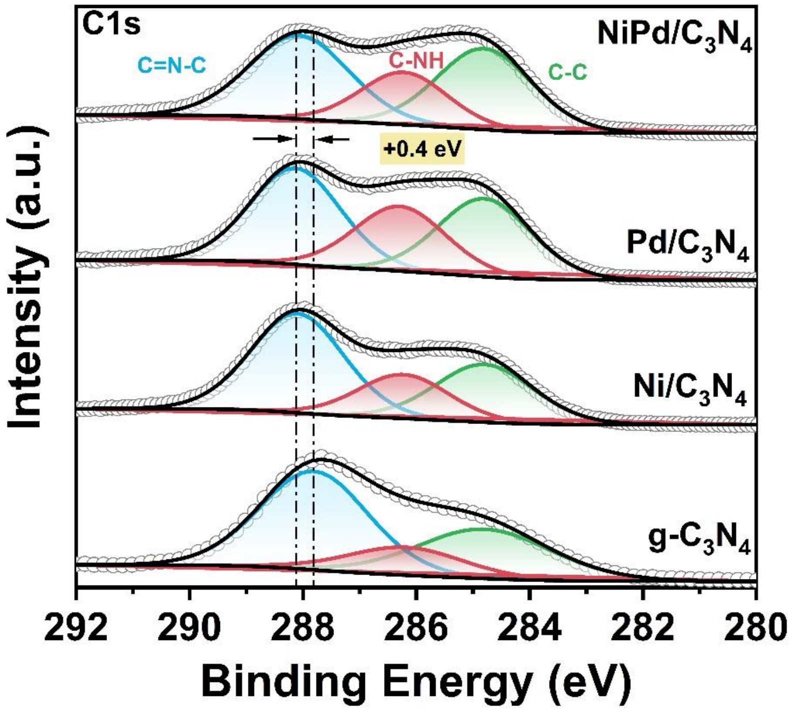

Figure 1.2.12: Comparison of C1s XPS spectra of NiPd/C_3N_4, Ni/C_3N_4, Pd/C_3N_4 and g-C_3N_4

Table 1.2.3: Peak positions of N obtained from the high resolution N 1s XPS spectra for g-C_3N_4, Pd/C_3N_4, Ni/C_3N_4 and NiPd/C_3N_4 (the peaks were obtained after carbon correction)

Catalyst	C-HN-C	C=N-C	N-C_3
g-C_3N_4	400.2 eV	398.2 eV	403.3 eV
Ni/C_3N_4	400.6 eV	398.7 eV	403.7 eV
Pd/C_3N_4	400.7 eV	398.8 eV	403.9 eV
NiPd/C_3N_4	400.7 eV	398.8 eV	403.8 eV

Table 1.2.4: Peak positions of C obtained from the high resolution C 1s XPS spectra for g-C_3N_4, Pd/C_3N_4, Ni/C_3N_4 and NiPd/C_3N_4 (the peaks were obtained after carbon correction)

Catalyst	C-HN-C	C=N-C	C-C (adventitious carbon)
g-C_3N_4	286.2 eV	287.8 eV	284.8 eV
Ni/C_3N_4	286.2 eV	288.1 eV	284.8 eV
Pd/C_3N_4	286.2 eV	288.1 eV	284.8 eV
NiPd/C_3N_4	286.2 eV	288.1 eV	284.8 eV

The TEM image of g-C_3N_4 reveals its characteristic 2D sheet-like morphology*(Figure 1.2.13 a)*. Ni/C_3N_4 also exhibits the sheet like morphology, and no Ni nanoparticles were observed *(Figure 1.2.13 b)*. In contrast, Pd/C_3N_4 exhibits uniformly distributed Pd nanoparticles *(Figure 1.2.13 c)* with an average size of 5–6 nm *(Figure 1.2.14 a)* on the C_3N_4 sheets. For NiPd/C_3N_4, a significant reduction in Pd nanoparticle size is observed, with dimensions ranging from approximately 1.5–2.5 nm *(Figure 1.2.13 d) and (Figure 1.2.14 b)*. Furthermore, HAADF-STEM imaging of NiPd/C_3N_4 reveals bright spots corresponding to Pd nanoparticles, uniformly dispersed across the C_3N_4 support*(Figure 1.2.15 a)*. Elemental mapping further confirms the homogeneous distribution of Ni and Pd throughout the g-C_3N_4 matrix *(Figure 1.2.15(b-f))*. This reduction in nanoparticle size and uniform dispersion, facilitated by the incorporation of Ni, improves atom utilization efficiency by increasing the number of exposed catalytically active sites.

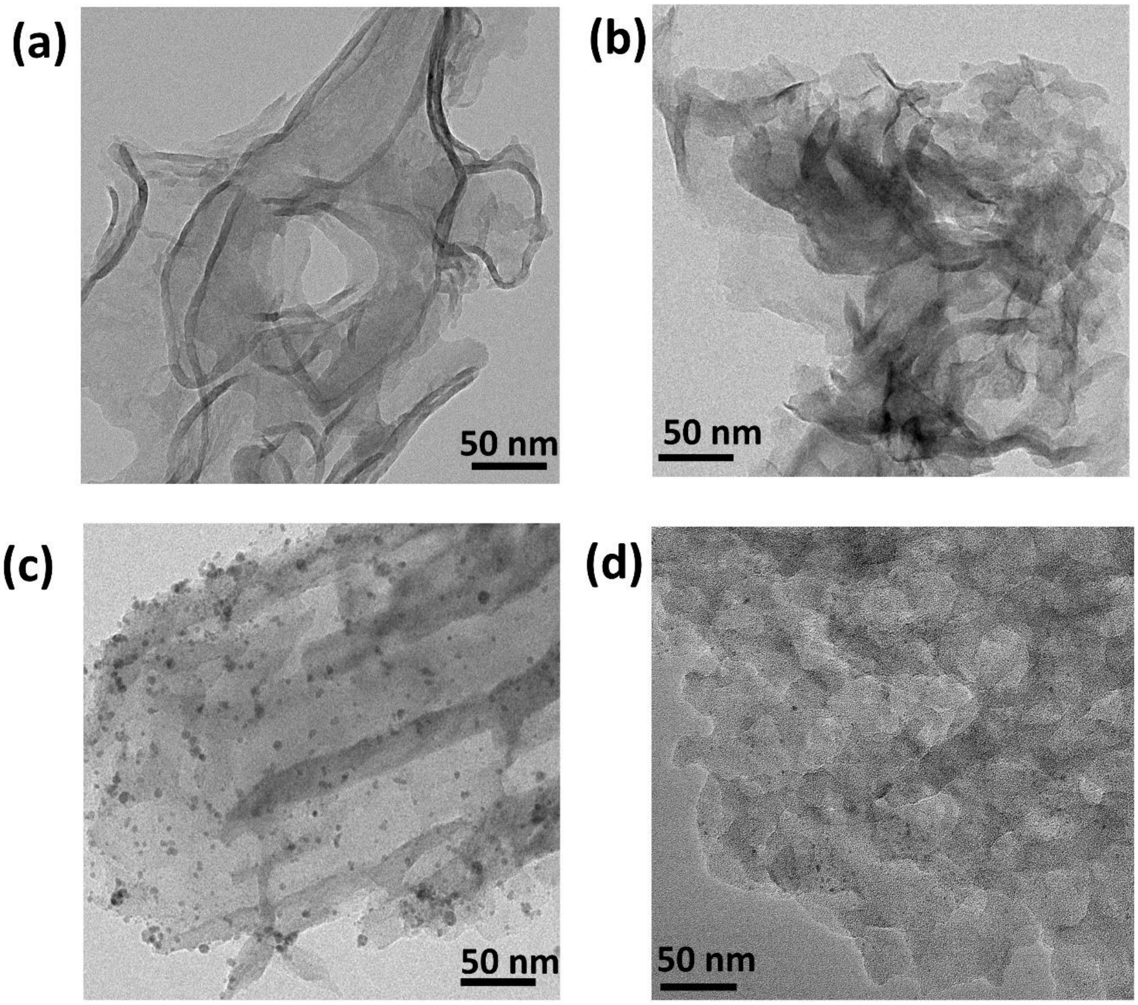

Figure 1.2.13: TEM image of **(a)** g-C_3N_4, **(b)** Ni/C_3N_4, **(c)** Pd/C_3N_4 and **(d)** NiPd/C_3N_4

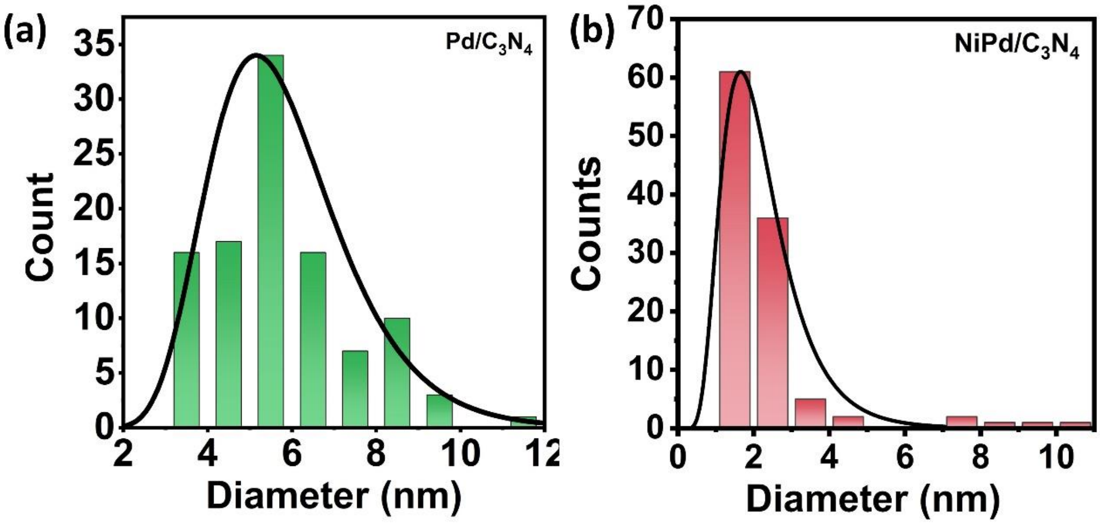

Figure 1.2.14: Particle size distribution of Pd nanoparticles in **(a)** Pd/C_3N_4 and **(b)** NiPd/C_3N_4

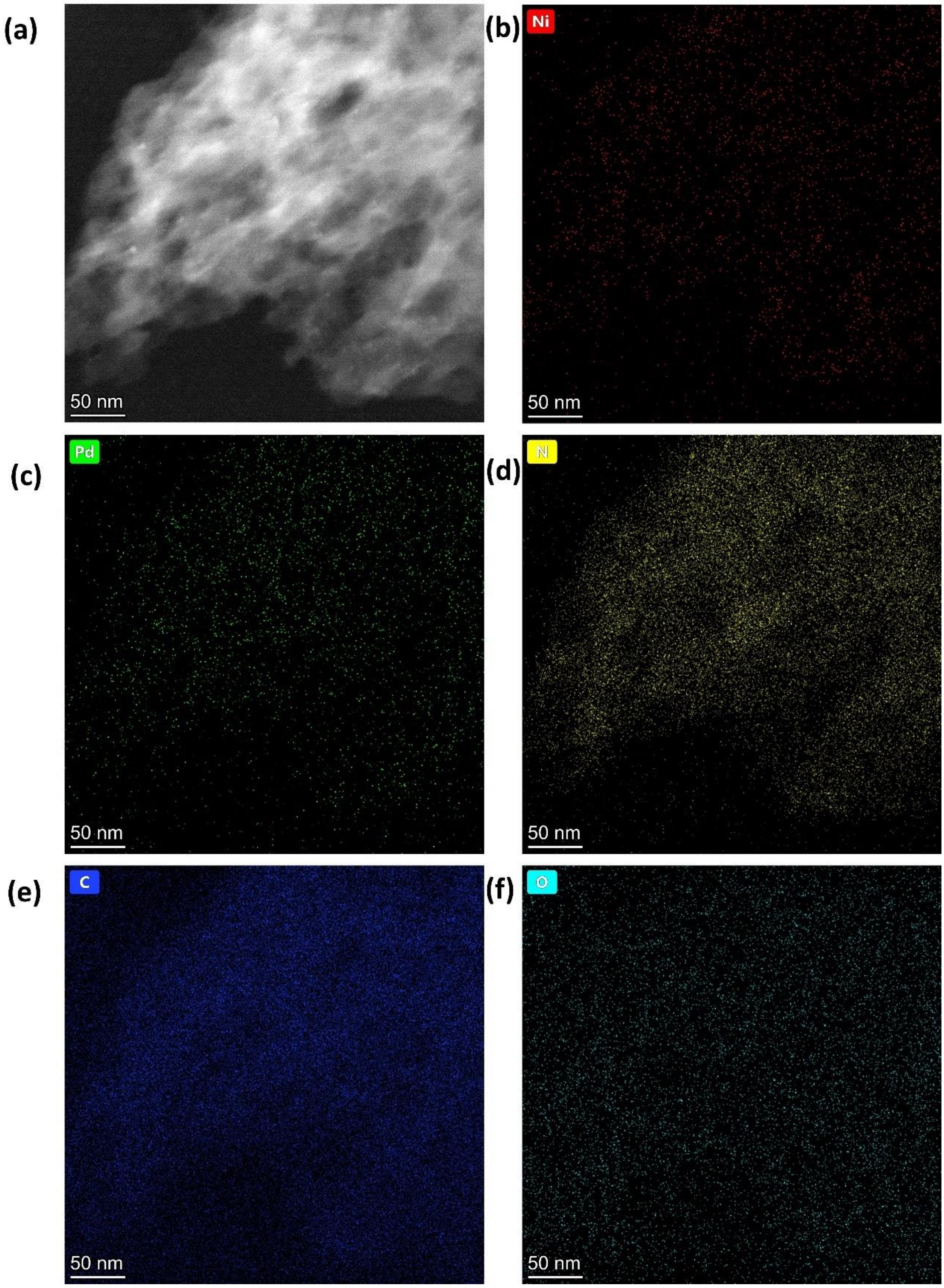

Figure 1.2.15: HAADF-STEM elemental mapping for NiPd/C_3N_4 **(a)** HAADF-STEM image and **(b)-(f)** Elemental mapping for Ni, Pd, N, C, and O

To further understand the mechanism and the contribution of each of the components of the catalyst, temperature programmed desorption (TPD) with CO_2 and Operando DRIFTS measurements were performed. TPD measurement for C_3N_4 shows only one CO_2 desorption peak at 140 ^oC *(Figure 1.2.16 a)*. This peak could be attributed to the CO_2 adsorbed on the N functional groups of C_3N_4. Ni/C_3N_4 shows an additional desorption peak at 330 ^oC along with a peak at 166 ^oC. This indicates that a new adsorption site is created in the presence of Ni, where the CO_2 is bound strongly *(Figure 1.2.16 b)*. In the case of Pd/C_3N_4, an increase in the desorption temperature to 162 ^oC was observed, indicating a stronger binding of the CO_2 molecule and no additional peaks at high temperatures were obtained *(Figure 1.2.16 c)*. This indicates that the CO_2 interacts strongly with the N functional groups of C_3N_4 in the presence of Pd. However, in the case of NiPd/C_3N_4, two desorption peaks are observed at 151 ^oC and 304 ^oC *(Figure 1.2.16 d)*, indicating CO_2 interaction with both C_3N_4 and the Ni site[46,47]. Compared to Ni/C_3N_4, the presence of Pd weakens the interaction of CO_2, resulting in the desorption peak at 304 ^oC. Thus, it can be concluded that the Ni sites are responsible predominantly for the activation of the CO_2 molecule, while Pd sites are responsible for the adsorption and activation of H_2.

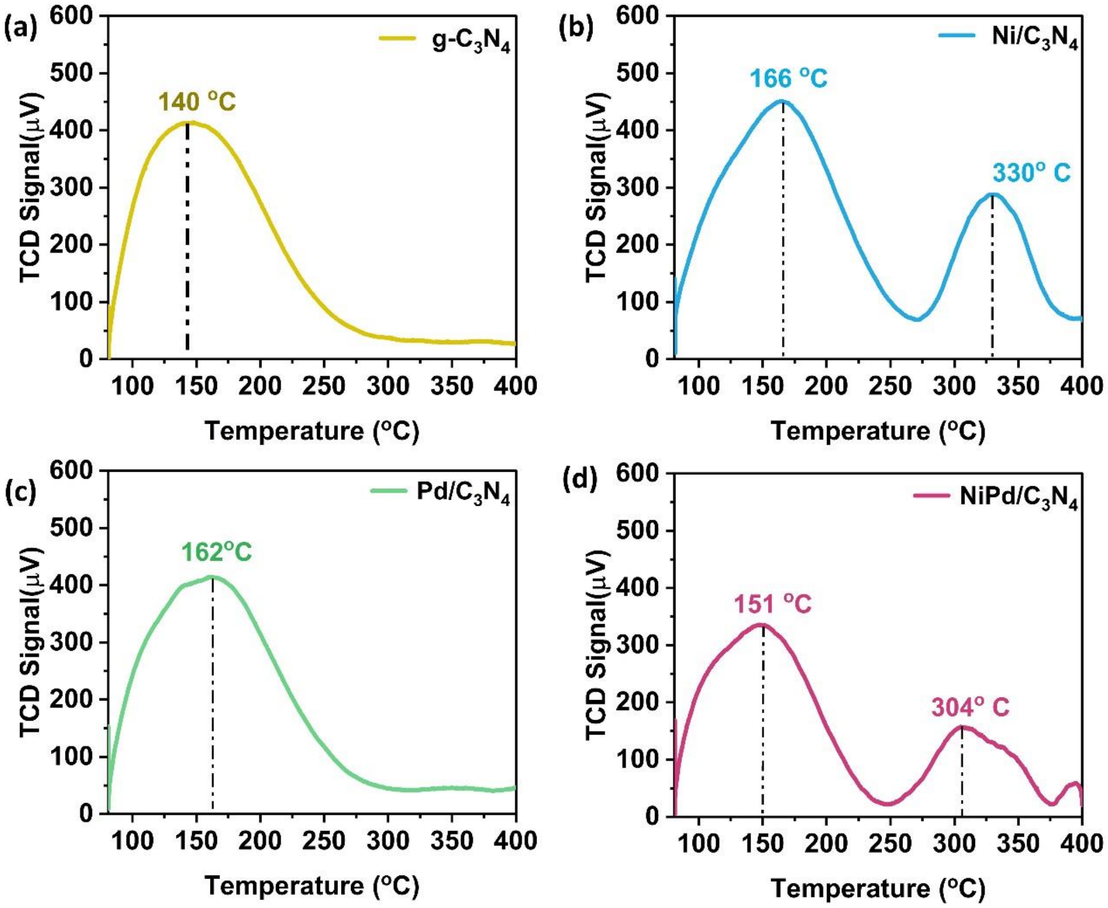

Figure 1.2.16: CO_2-temperature programmed desorption **(a)** g-C_3N_4**, (b)** Ni/ C_3N_4**, (c)** Pd/ C_3N_4 and **(d)** NiPd/C_3N_4

From the literature, it is established that on the surface of the metal, the CO_2 hydrogenation proceeds by the formation of bicarbonate. The bicarbonate bound to the metal site interacts with the surface hydride to form formate. Hence, to determine the intermediates formed during the reaction, the NiPd catalyst was synthesized without the g-C_3N_4 support. The operando DRIFT analysis *(Figure 1.2.17)* performed in the presence of CO_2 and H_2 in the gas phase shows the absorbance band for CO_3^{2-} at 1663 cm^{-1}, formed by the bidentate interaction of CO_2 with the metal species. The CO_3^{2-} interacts with the hydride formed on the adjacent Pd site to form the HCO_3^- intermediate, which shows an IR absorbance band at 1477 cm^{-1}. This converts to the $HCOO^-$ exhibiting an IR band at 1583 cm^{-1}. The continuous formation of these intermediates was observed for a reaction duration of 1h, as is evidenced from the IR absorbance bands[48,49].

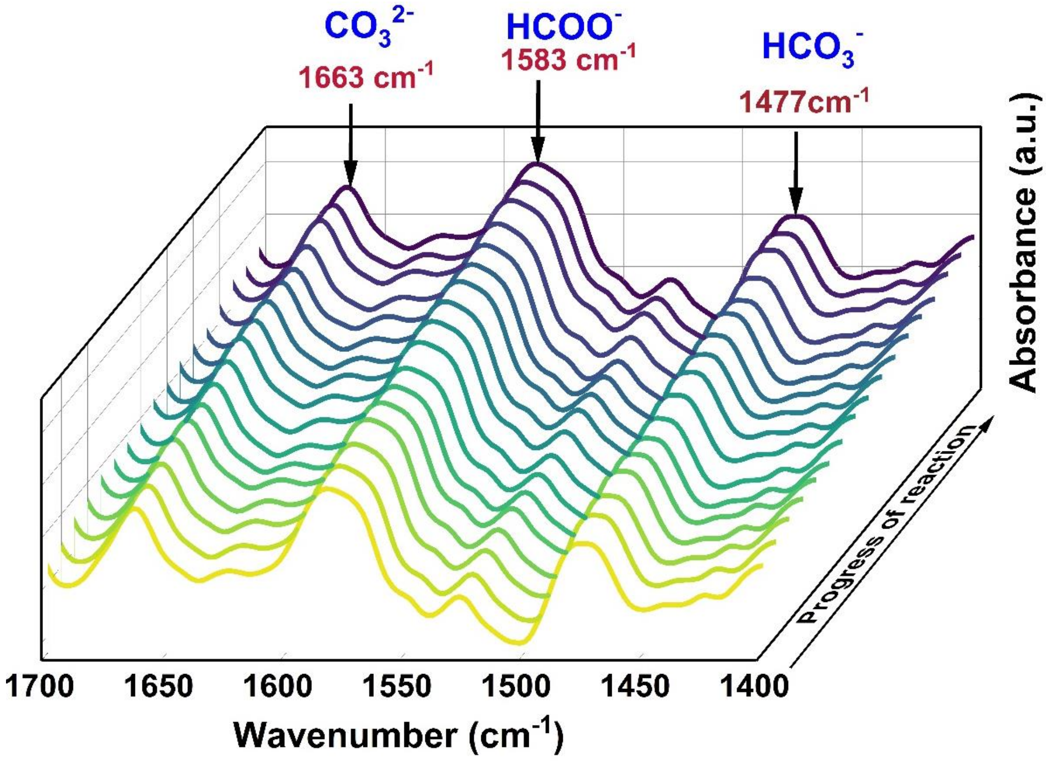

Figure 1.2.17: *Operando* DRIFT spectra of NiPd/C_3N_4

The catalyst and the solution were collected after the CO_2 hydrogenation reaction and were analyzed by TEM. The TEM of NiPd/C_3N_4 post reaction shows sheet like morphology with uniformly dispersed Pd nanoparticles. No severe agglomeration of the metal nanoparticles was observed. Interestingly, the TEM of the filtrate showed thin sheets of C_3N_4 containing metal nanoparticles *(Figure 1.2.18)*. This could be attributed to the exfoliation of C_3N_4 during the reaction. This results in the loss of the catalyst, which is responsible for the loss of catalytic activity in the subsequent cycles *(Figure 1.2.19)*. The TON decreases from 900 in the first cycle to 400 in the second cycle. Subsequently, the TON falls to 380 and 180 in the third and fourth cycle, respectively.

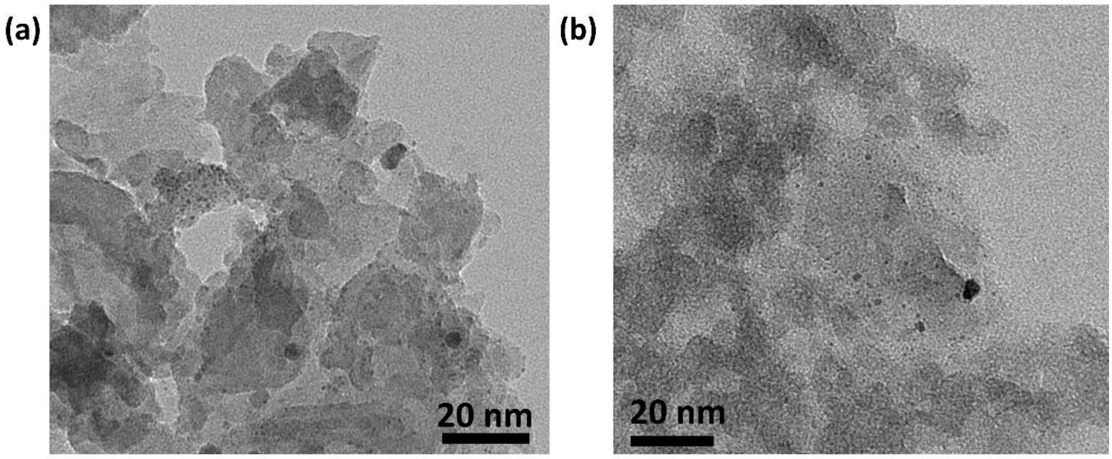

Figure 1.2.18: TEM image of $NiPd/C_3N_4$ post reaction **(a)** solid residue and **(b)** filtrate

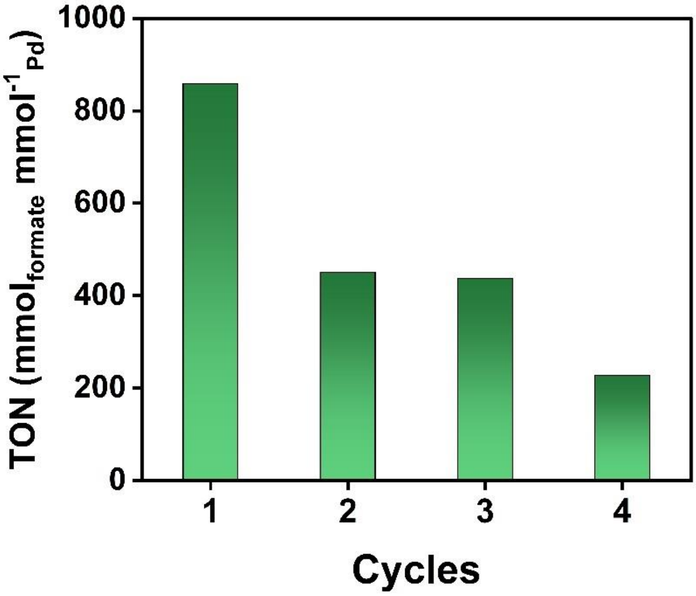

Figure 1.2.19: Cyclability study using $NiPd/C_3N_4$ catalyst. (Reaction conditions: 75 ^{o}C, 0.5 M Na_2CO_3, 40 bar H_2, 40 bar CO_2, 1h)

The XAS analysis was performed for NiPd/C_3N_4 post reaction *(Figure 1.2.20)*. The XANES *(Figure 1.2.20 a, b)* and EXAFS spectra *(Figure 1.2.20 c, d)* of Ni K edge and Pd K edge overlap with the spectra obtained before the reaction, indicating no change in the structure of the catalyst.

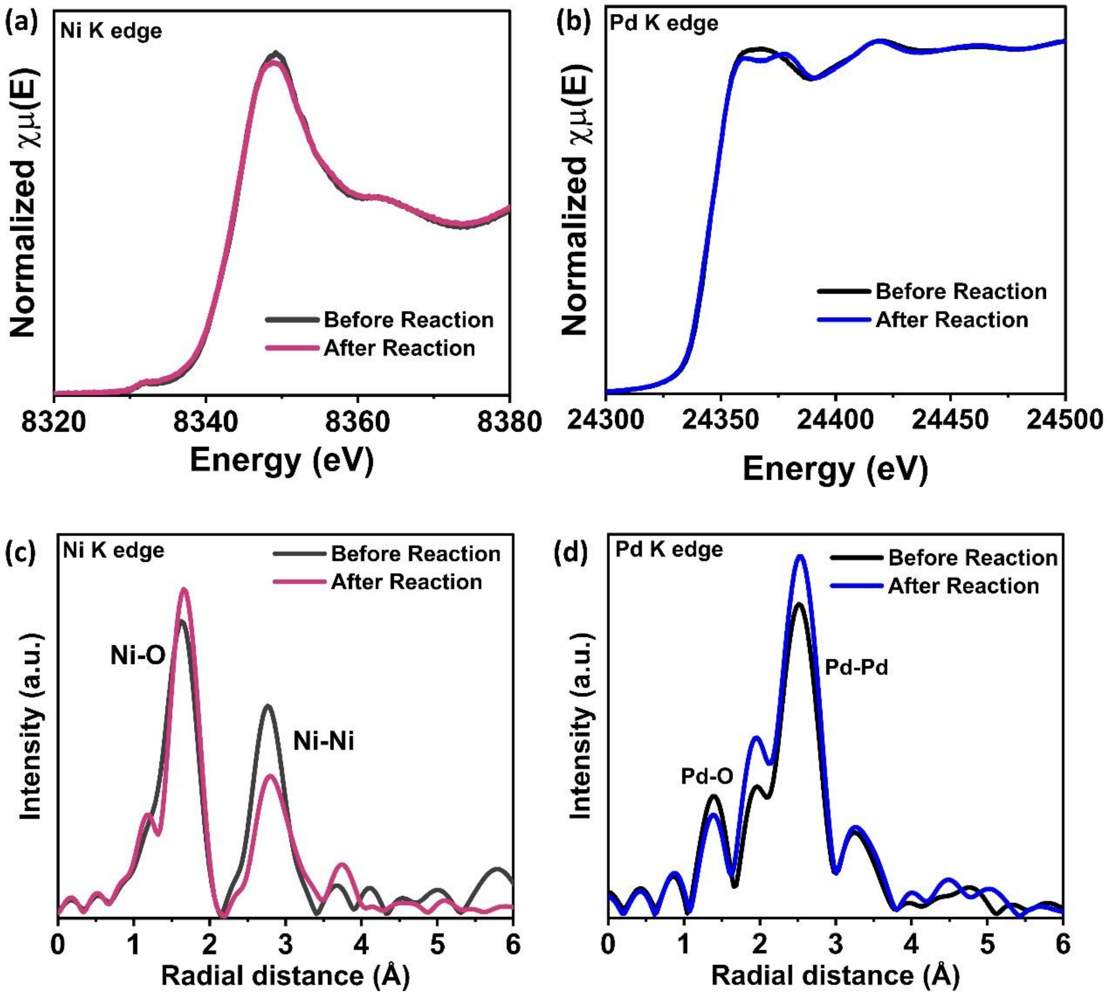

Figure 1.2.20: X-ray absorption spectroscopy of the catalyst post reaction **(a)** Ni K edge XANES spectra, **(b)** Pd K edge XANES spectra, **(c)** Ni K edge EXAFS spectra and **(d)** Pd K edge EXAFS spectra

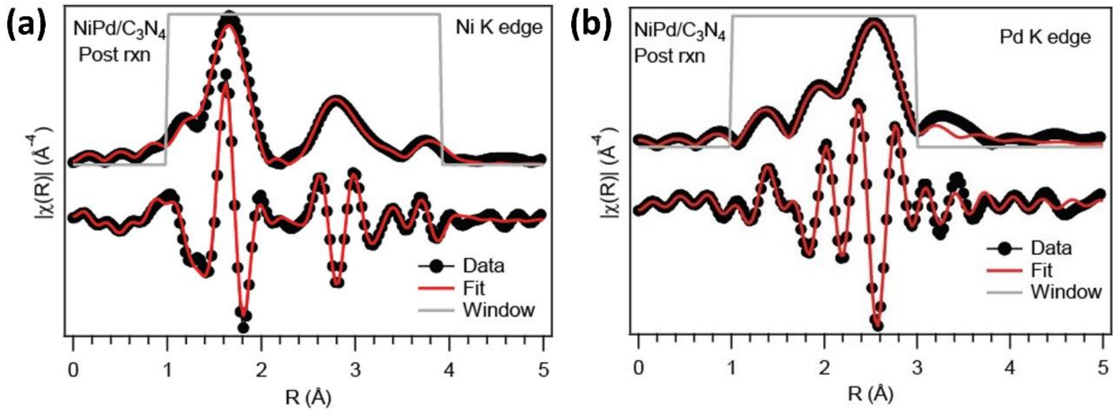

Figure 1.2.21: Multishell peak fitting for the Fourier transformed R-space plots of **(a)** Ni K edge EXAFS and **(b)** Pd K edge EXAFS of NiPd/C_3N_4

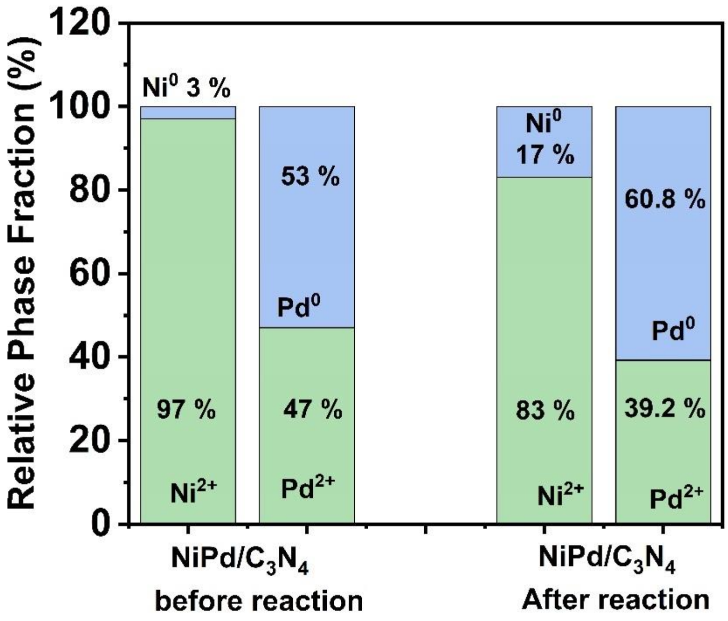

Figure 1.2.22: Comparison of the relative phase fraction of Ni^{2+}, metallic Ni, Pd^{2+}, and metallic Pd determined from the multi-shell fitting of Ni K edge and Pd K edge EXAFS of NiPd/C_3N_4 before and after the reaction

However, the relative phase fractions obtained from the multishell fitting of the FT-EXAFS spectra for the Ni K edge and the Pd K- edge *(Figure 1.2.21 to Figure 1.2.22)* shows an increase in the metallic Ni (17 %) and metallic Pd phase (60.8 %). This could be attributed to the reduction of the metal species under the reducing environment. The fitting parameters of the EXAFS spectra are shown in *Table 1.2.5* and *Table 1.2.6.*

Table 1.2.5: The Bond length (R) and Debye-Waller factor/Disorder (σ^2) derived from multishell peak fitting parameters for the R-space plots of Ni K edge for NiPd/C_3N_4 post reaction.

Sample	**ΔE**	**$Ni(OH)_2$**				**Ni metal**				**NiPd bimetal**	
		Ni-O bond		**Ni-Ni bond**		**$Ni\text{-}Ni_1$ bond**		**$Ni\text{-}Ni_2$ bond**		**$Ni\text{-}Pd_1$ bond**	
		R (Ȧ)	σ^2	R (Ȧ)	σ^2	R (Ȧ)	σ^2	R (Ȧ)	σ^2	R (Ȧ)	σ^2
NiPd/ C_3N_4 post rxn	-3.9 ± 0.8	2.07 ± 0.01	0.003 ± 0.001	3.07 ± 0.02	0.01 ± 0.003	2.60 ± 0.05	0.08 ± 0.01	3.45 ± 0.03	0.08 ± 0.01	2.67 ± 0.04	0.02 ± 0.004

Table 1.2.6: The Bond length (R) and Debye-Waller factor/Disorder (σ^2) derived from multishell peak fitting parameters for the R-space plots of Pd K edge for NiPd/C_3N_4 post reaction.

Sample	**ΔE**	**Pd- oxide**		**Pd metal**		**NiPd bimetal**	
		Ni-O bond		**$Ni\text{-}Ni_1$ bond**		**$Ni\text{-}Pd_1$ bond**	
		R (Ȧ)	σ^2	R (Ȧ)	σ^2	R (Ȧ)	σ^2
NiPd/C_3N_4 post rxn	-3.15 ± 0.81	1.98 ± 0.03	0.01 ± 0.007	2.75 ± 0.04	0.01 ± 0.001	2.53 ± 0.03	0.06 ± 0.002

1.2.5. Conclusion

In conclusion, we have synthesized NiPd/C_3N_4 by the $NaBH_4$ assisted reduction of the metal species over C_3N_4. The as synthesized catalyst shows exceptional activity with a high TON of 2432 towards CO_2 hydrogenation. The C_3N_4 support stabilizes the metal nanoparticles and helps bring the CO_2 molecules close to the metal active sites. The catalyst exhibits strong metal support interaction whereby the metal nanoparticles interact with the N functional groups in the support, as evidenced by the XPS measurement. Further, the kinetic analysis shows that the activation energy is significantly lowered for NiPd/C_3N_4 compared to Pd/C_3N_4. The in-situ DRIFT and TPD measurements were used to understand the mechanistic pathway, and it was observed that NiPd and C_3N_4 work in tandem to catalyze the hydrogenation of CO_2 to formate.

1.2.6. Reference

(1) Álvarez, A.; Bansode, A.; Urakawa, A.; Bavykina, A. V; Wezendonk, T. A.; Makkee, M.; Gascon, J.; Kapteijn, F. Challenges in the Greener Production of Formates/Formic Acid, Methanol, and DME by Heterogeneously Catalyzed CO2 Hydrogenation Processes. *Chem Rev* **2017**, *117* (14), 9804–9838. https://doi.org/10.1021/acs.chemrev.6b00816.

(2) Sun, R.; Liao, Y.; Bai, S.-T.; Zheng, M.; Zhou, C.; Zhang, T.; Sels, B. F. Heterogeneous Catalysts for CO2 Hydrogenation to Formic Acid/Formate: From Nanoscale to Single Atom. *Energy Environ Sci* **2021**, *14* (3), 1247–1285. https://doi.org/10.1039/D0EE03575K.

(3) Zhao, X.; Chang, Y.; Chen, W.-J.; Wu, Q.; Pan, X.; Chen, K.; Weng, B. Recent Progress in Pd-Based Nanocatalysts for Selective Hydrogenation. *ACS Omega* **2022**, *7* (1), 17–31. https://doi.org/10.1021/acsomega.1c06244.

(4) Zhang, L.; Zhou, M.; Wang, A.; Zhang, T. Selective Hydrogenation over Supported Metal Catalysts: From Nanoparticles to Single Atoms. *Chem Rev* **2020**, *120* (2), 683–733. https://doi.org/10.1021/acs.chemrev.9b00230.

(5) Lee, J. H.; Ryu, J.; Kim, J. Y.; Nam, S.-W.; Han, J. H.; Lim, T.-H.; Gautam, S.; Chae, K. H.; Yoon, C. W. Carbon Dioxide Mediated, Reversible Chemical Hydrogen Storage Using a Pd Nanocatalyst Supported on Mesoporous Graphitic Carbon Nitride. *J Mater Chem A Mater* **2014**, *2* (25), 9490–9495. https://doi.org/10.1039/C4TA01133C.

(6) Zhou, Y.; Huang, Y.; Jin, B.; Luo, X.; Liang, Z. Pd Nanoclusters-Based Catalysts with Schiff Base Modifying Carrier for Co2 Hydrogenation to Formic Acid. *Ind Eng Chem Res* **2019**, *58* (1), 44–52. https://doi.org/10.1021/acs.iecr.8b04047.

(7) Su, J.; Yang, L.; Lu, M.; Lin, H. Highly Efficient Hydrogen Storage System Based on Ammonium Bicarbonate/Formate Redox Equilibrium over Palladium Nanocatalysts. *ChemSusChem* **2015**, *8* (5), 813–816. https://doi.org/10.1002/cssc.201403251.

(8) Mori, K.; Sano, T.; Kobayashi, H.; Yamashita, H. Surface Engineering of a Supported PdAg Catalyst for Hydrogenation of CO2 to Formic Acid: Elucidating the Active Pd Atoms in Alloy Nanoparticles. *J Am Chem Soc* **2018**, *140* (28), 8902–8909. https://doi.org/10.1021/jacs.8b04852.

(9) Wang, Y.; Dong, M.; Li, S.; Chen, B.; Liu, H.; Han, B. The Superiority of Pd2+ in CO2 Hydrogenation to Formic Acid. *Chem Sci* **2024**, *15* (15), 5525–5530. https://doi.org/10.1039/D3SC06925G.

(10) Yang, G.; Kuwahara, Y.; Mori, K.; Louis, C.; Yamashita, H. Pd–Cu Alloy Nanoparticles Confined within Mesoporous Hollow Carbon Spheres for the Hydrogenation of CO2 to Formate. *The Journal of Physical Chemistry C* **2021**, *125* (7), 3961–3971. https://doi.org/10.1021/acs.jpcc.0c10962.

(11) Kuwahara, Y.; Fujie, Y.; Mihogi, T.; Yamashita, H. Hollow Mesoporous Organosilica Spheres Encapsulating PdAg Nanoparticles and Poly(Ethyleneimine) as Reusable Catalysts for CO2 Hydrogenation to Formate. *ACS Catal* **2020**, *10* (11), 6356–6366. https://doi.org/10.1021/acscatal.0c01505.

(12) Wang, W.; Duong-Viet, C.; Truong-Phuoc, L.; Nhut, J.-M.; Vidal, L.; Pham-Huu, C. Activated Carbon Supported Nickel Catalyst for Selective CO2 Hydrogenation to Synthetic Methane under Contactless Induction Heating. *Catal Today* **2023**, *418*, 114073. https://doi.org/10.1016/j.cattod.2023.114073.

(13) Ye, R.; Ma, L.; Hong, X.; Reina, T. R.; Luo, W.; Kang, L.; Feng, G.; Zhang, R.; Fan, M.; Zhang, R.; Liu, J. Boosting Low-Temperature CO2 Hydrogenation over Ni-Based Catalysts by Tuning Strong Metal-Support Interactions. *Angewandte Chemie International Edition* **2024**, *63* (3), e202317669. https://doi.org/10.1002/anie.202317669.

(14) Farlow, M. W.; Adkins, H. The Hydrogenation of Carbon Dioxide and a Correction of the Reported Synthesis of Urethans. *J Am Chem Soc* **1935**, *57* (11), 2222–2223. https://doi.org/10.1021/ja01314a054.

(15) Peng, G.; Sibener, S. J.; Schatz, G. C.; Ceyer, S. T.; Mavrikakis, M. CO2 Hydrogenation to Formic Acid on Ni(111). *The Journal of Physical Chemistry C* **2012**, *116* (4), 3001–3006. https://doi.org/10.1021/jp210408x.

(16) Fu, X.-P.; Peres, L.; Esvan, J.; Amiens, C.; Philippot, K.; Yan, N. An Air-Stable, Reusable Ni@Ni(OH)2 Nanocatalyst for CO2/Bicarbonate Hydrogenation to Formate. *Nanoscale* **2021**, *13* (19), 8931–8939. https://doi.org/10.1039/D1NR01054A.

(17) Nguyen, L. T. M.; Park, H.; Banu, M.; Kim, J. Y.; Youn, D. H.; Magesh, G.; Kim, W. Y.; Lee, J. S. Catalytic CO2 Hydrogenation to Formic Acid over Carbon Nanotube-Graphene Supported PdNi Alloy Catalysts. *RSC Adv* **2015**, *5* (128), 105560–105566. https://doi.org/10.1039/C5RA21017H.

(18) Mori, K.; Masuda, S.; Tanaka, H.; Yoshizawa, K.; Che, M.; Yamashita, H. Phenylamine-Functionalized Mesoporous Silica Supported PdAg Nanoparticles: A Dual Heterogeneous Catalyst for Formic Acid/CO2-Mediated Chemical Hydrogen Delivery/Storage. *Chemical Communications* **2017**, *53* (34), 4677–4680. https://doi.org/10.1039/C7CC00864C.

(19) Betsy, K. J.; Lazar, A.; Pavithran, A.; Vinod, C. P. CO2 Hydrogenation to Formate by Palladium Nanoparticles Supported on N-Incorporated Periodic Mesoporous Organosilica. *ACS Sustain Chem Eng* **2020**, *8* (39), 14765–14774. https://doi.org/10.1021/acssuschemeng.0c03860.

(20) Sjijberg, S. *Silica in Aqueous Environments*; 1996; Vol. 196.

(21) Spitzmüller, L.; Nitschke, F.; Rudolph, B.; Berson, J.; Schimmel, T.; Kohl, T. Dissolution Control and Stability Improvement of Silica Nanoparticles in Aqueous

Media. *Journal of Nanoparticle Research* **2023**, *25* (3), 40. https://doi.org/10.1007/s11051-023-05688-4.

(22) Pham, A. L.-T.; Sedlak, D. L.; Doyle, F. M. Dissolution of Mesoporous Silica Supports in Aqueous Solutions: Implications for Mesoporous Silica-Based Water Treatment Processes. *Appl Catal B* **2012**, *126*, 258–264. https://doi.org/10.1016/j.apcatb.2012.07.018.

(23) Masuda, S.; Mori, K.; Futamura, Y.; Yamashita, H. PdAg Nanoparticles Supported on Functionalized Mesoporous Carbon: Promotional Effect of Surface Amine Groups in Reversible Hydrogen Delivery/Storage Mediated by Formic Acid/CO2. *ACS Catal* **2018**, *8* (3), 2277–2285. https://doi.org/10.1021/acscatal.7b04099.

(24) Liu, Q.; Yang, X.; Li, L.; Miao, S.; Li, Y.; Li, Y.; Wang, X.; Huang, Y.; Zhang, T. Direct Catalytic Hydrogenation of CO2 to Formate over a Schiff-Base-Mediated Gold Nanocatalyst. *Nat Commun* **2017**, *8* (1), 1407. https://doi.org/10.1038/s41467-017-01673-3.

(25) Jaleel, A.; Haider, A.; Nguyen, C. Van; Lee, K. R.; Choung, S.; Han, J. W.; Baek, S.-H.; Shin, C.-H.; Jung, K.-D. Structural Effect of Nitrogen/Carbon on the Stability of Anchored Ru Catalysts for CO2 Hydrogenation to Formate. *Chemical Engineering Journal* **2022**, *433*, 133571. https://doi.org/10.1016/j.cej.2021.133571.

(26) Mondelli, C.; Puértolas, B.; Ackermann, M.; Chen, Z.; Pérez-Ramírez, J. Enhanced Base-Free Formic Acid Production from CO2 on Pd/g-C3N4 by Tuning of the Carrier Defects. *ChemSusChem* **2018**, *11* (17), 2859–2869. https://doi.org/10.1002/cssc.201801362.

(27) Kim, E. H.; Choi, Y. H.; Lee, M. H.; Kim, J.; Kim, H. Bin; Kim, K. Y.; Ra, E. C.; Lee, J. H.; Lee, J. S. Base-Free CO2 Hydrogenation to Formic Acid over Pd Supported on Defective Carbon Nitride Modified by Microwave and Acid Treatments. *J Catal* **2021**, *396*, 395–401. https://doi.org/10.1016/j.jcat.2021.03.016.

(28) Olufemi Oluwole, A.; Khoza, P.; Olatunji, O. S. Synthesis and Characterization of G-C3N4 Doped with Activated Carbon (AC) Prepared from Grape Leaf Litters for the Photocatalytic Degradation of Enrofloxacin in Aqueous Systems. *ChemistrySelect* **2022**, *7* (45), e202203601. https://doi.org/10.1002/slct.202203601.

(29) Ahamed, M.; Agarwal, S.; Singh, A. K.; Eswaramoorthy, M. Coke-Free Propane Dehydrogenation over Ultra-Stable Metal-Free BCN Catalyst. *Applied Catalysis B: Environment and Energy* **2025**, *365*, 124996. https://doi.org/10.1016/j.apcatb.2024.124996.

(30) Kumar, Y.; Rani, S.; Shabir, J.; Kumar, L. S. Nitrogen-Rich and Porous Graphitic Carbon Nitride Nanosheet-Immobilized Palladium Nanoparticles as Highly

Active and Recyclable Catalysts for the Reduction of Nitro Compounds and Degradation of Organic Dyes. *ACS Omega* **2020**, *5* (22), 13250–13258. https://doi.org/10.1021/acsomega.0c01280.

(31) Ravel, B. ; N. M. ATHENA, ARTEMIS, HEPHAESTUS: Data Analysis for X-Ray Absorption Spectroscopy Using IFEFFIT. *J. Synchrotron Radiat.* **2005**, *12*, 537–541. https://doi.org/10.1107/S0909049505012719.

(32) Miller, T. S.; Jorge, A. B.; Suter, T. M.; Sella, A.; Corà, F.; McMillan, P. F. Carbon Nitrides: Synthesis and Characterization of a New Class of Functional Materials. *Physical Chemistry Chemical Physics* **2017**, *19* (24), 15613–15638. https://doi.org/10.1039/C7CP02711G.

(33) Zhang, R.; Ran, T.; Cao, Y.; Ye, L.; Dong, F.; Zhang, Q.; Yuan, L.; Zhou, Y. Oxygen Activation of Noble-Metal-Free g-C3N4/α-Ni(OH)2 to Control the Toxic Byproduct of Photocatalytic Nitric Oxide Removal. *Chemical Engineering Journal* **2020**, *382*, 123029. https://doi.org/10.1016/j.cej.2019.123029.

(34) Zhang, J.; Li, Y.; Zhang, J.; Xu, W.; Yao, J.; Huang, B. Synthesis of Nanosheet-like α-Ni(OH)2/g-C3N4 Hybrid Anode Material with Enhanced Lithium Storage Performance. *Appl Surf Sci* **2024**, *664*, 160258. https://doi.org/10.1016/j.apsusc.2024.160258.

(35) Hu, Y.; Zhang, S.; Zhang, Z.; Zhou, H.; Li, B.; Sun, Z.; Hu, X.; Yang, W.; Li, X.; Wang, Y.; Liu, S.; Wang, D.; Lin, J.; Chen, W.; Wang, S. Enhancing Photocatalytic-Transfer Semi-Hydrogenation of Alkynes Over Pd/C3N4 Through Dual Regulation of Nitrogen Defects and the Mott–Schottky Effect. *Advanced Materials* **2023**, *35* (41), 2304130. https://doi.org/10.1002/adma.202304130.

(36) Yin, Z.; Tian, Y.; Gao, P.; Feng, L.; Liu, Y.; Du, Z.; Zhang, L. Photodegradation Mechanism and Genetic Toxicity of Bezafibrate by Pd/g-C3N4 Catalysts under Simulated Solar Light Irradiation: The Role of Active Species. *Chemical Engineering Journal* **2020**, *379*, 122294. https://doi.org/10.1016/j.cej.2019.122294.

(37) Wang, N.; Wang, J.; Hu, J.; Lu, X.; Sun, J.; Shi, F.; Liu, Z.-H.; Lei, Z.; Jiang, R. Design of Palladium-Doped g-C3N4 for Enhanced Photocatalytic Activity toward Hydrogen Evolution Reaction. *ACS Appl Energy Mater* **2018**, *1* (6), 2866–2873. https://doi.org/10.1021/acsaem.8b00526.

(38) Li, L.; Dai, X.; Lu, M.; Guo, C.; Wabaidur, S. M.; Wu, X.-L.; Lou, Z.; Zhong, Y.; Hu, Y. Electron-Enriched Single-Pd-Sites on g-C3N4 Nanosheets Achieved by in-Situ Anchoring Twinned Pd Nanoparticles for Efficient CO2 Photoreduction. *Advanced Powder Materials* **2024**, *3* (2), 100170. https://doi.org/10.1016/j.apmate.2024.100170.

(39) Yang, L.; Sivasankaran, R. P.; Song, M. K.; Pawar, A. U.; Lee, D. K.; Kang, Y. S. Highly Selective Solar CO2 Conversion into Formic Acid in Nickel-Perylene-

C3N4 Semiconductor Photocatalyst. *Adv Energy Mater* **2025**, *15* (3), 2402798. https://doi.org/10.1002/aenm.202402798.

(40) Chen, S.; Gong, B.; Gu, J.; Lin, Y.; Yang, B.; Gu, Q.; Jin, R.; Liu, Q.; Ying, W.; Shi, X.; Xu, W.; Cai, L.; Li, Y.; Sun, Z.; Wei, S.; Zhang, W.; Lu, J. Dehydrogenation of Ammonia Borane by Platinum-Nickel Dimers: Regulation of Heteroatom Interspace Boosts Bifunctional Synergetic Catalysis. *Angewandte Chemie International Edition* **2022**, *61* (41), e202211919. https://doi.org/10.1002/anie.202211919.

(41) Zhang, X.; Su, H.; Cui, P.; Cao, Y.; Teng, Z.; Zhang, Q.; Wang, Y.; Feng, Y.; Feng, R.; Hou, J.; Zhou, X.; Ma, P.; Hu, H.; Wang, K.; Wang, C.; Gan, L.; Zhao, Y.; Liu, Q.; Zhang, T.; Zheng, K. Developing Ni Single-Atom Sites in Carbon Nitride for Efficient Photocatalytic H2O2 Production. *Nat Commun* **2023**, *14* (1), 7115. https://doi.org/10.1038/s41467-023-42887-y.

(42) Huynh, T.-T.; Tsai, M.-C.; Pan, C.-J.; Su, W.-N.; Chan, T.-S.; Lee, J.-F.; Hwang, B.-J. Synergetic Electrocatalytic Activities towards Hydrogen Peroxide: Understanding the Ordered Structure of PdNi Bimetallic Nanocatalysts. *Electrochem commun* **2019**, *101*, 93–98. https://doi.org/10.1016/j.elecom.2019.02.009.

(43) Li, X.; Liu, J.; Wu, J.; Zhang, L.; Cao, D.; Cheng, D. Constructing a Highly Active Pd Atomically Dispersed Catalyst for Cinnamaldehyde Hydrogenation: Synergistic Catalysis between Pd–N3 Single Atoms and Fully Exposed Pd Clusters. *ACS Catal* **2024**, *14* (4), 2369–2379. https://doi.org/10.1021/acscatal.3c05883.

(44) Tonda, S.; Kumar, S.; Bhardwaj, M.; Yadav, P.; Ogale, S. G-C3N4/NiAl-LDH 2D/2D Hybrid Heterojunction for High-Performance Photocatalytic Reduction of CO2 into Renewable Fuels. *ACS Appl Mater Interfaces* **2018**, *10* (3), 2667–2678. https://doi.org/10.1021/acsami.7b18835.

(45) Zhang, L.; Ou, M.; Yao, H.; Li, Z.; Qu, D.; Liu, F.; Wang, J.; Wang, J.; Li, Z. Enhanced Supercapacitive Performance of Graphite-like C3N4 Assembled with NiAl-Layered Double Hydroxide. *Electrochim Acta* **2015**, *186*, 292–301. https://doi.org/10.1016/j.electacta.2015.10.192.

(46) Li, C.; Yang, J.; Zhang, C.; Wang, C.; Lyu, C.; Fan, K. Study on Catalytic Performance in CO2 Hydrogenation to Methanol over Au–Cu/C3N4 Catalysts. *Catalysts* **2024**, *14* (8). https://doi.org/10.3390/catal14080470.

(47) Jia, G.; Wang, Z.; Gong, M.; Wang, Y.; Li, L. H.; Dong, Y.; Liu, L.; Zhang, L.; Zhao, J.; Zheng, W.; Cui, X. Ultrathin Origami Accordion-like Structure of Vacancy-Rich Graphitized Carbon Nitride for Enhancing CO2 Photoreduction. *Carbon Energy* **2023**, *5* (4), e270. https://doi.org/https://doi.org/10.1002/cey2.270.

(48) Zhang, J.; Liao, W.; Zheng, H.; Zhang, Y.; Xia, L.; Teng, B.-T.; Lu, J.-Q.; Huang, W.; Zhang, Z. Morphology-Engineered Highly Active and Stable Pd/TiO2 Catalysts for CO2 Hydrogenation into Formate. *J Catal* **2022**, *405*, 152–163. https://doi.org/10.1016/j.jcat.2021.11.035.

(49) Zhang, Z.; Zhang, L.; Hülsey, M. J.; Yan, N. Zirconia Phase Effect in Pd/ZrO2 Catalyzed CO2 Hydrogenation into Formate. *Molecular Catalysis* **2019**, *475*, 110461. https://doi.org/10.1016/j.mcat.2019.110461.

\

Chapter- 1.3

Synergistic Effects of Bismuth on CO_2 electroreduction to formate in CuSn catalyst

Summary:

CuO_x-SnO_x interfaces have demonstrated high efficiency in CO_2 conversion to formate. However, under reduction conditions, they tend to transform into metallic Cu and Sn, leading to a loss of activity. To address this, in this work, Bi_2O_3 has been incorporated into the Cu-Sn catalyst. The synergistic interaction among the three metals helps stabilize the active sites, maintaining high Faradaic efficiency for formate production.

1.3.1 Introduction

Electroreduction of CO_2 to formate offers an energy-efficient pathway for transforming CO_2 into a valuable product. This approach is particularly advantageous as it can be performed under ambient conditions, making it a sustainable solution. The conversion of CO_2 to formic acid involves a two-electron transfer process:

$$CO_2 + 2H^+ + 2e^- \rightarrow HCOOH \qquad E^o = -0.61\ V$$

Sn-, Bi-, and In-based catalysts have been extensively investigated for the electrochemical conversion of CO_2 to formate[1–3]. In these metals, the active sites typically consist of MO_x species. Theoretical predictions using volcano plots identify Sn as the most effective metal catalyst, offering optimal binding energy for the *OCHO intermediate, which is a crucial step in formate production. Consequently, Sn-based catalysts have garnered significant attention for this reaction[4,5].

However, two primary challenges limit the performance of Sn-based catalysts. First, Sn often exhibits selectivity toward CO formation, resulting in low Faradaic efficiencies for formate. Second, the reduction of SnO_x active sites during the reaction leads to decreased electrochemical activity towards CO_2 conversion. Hence, there is a need to modify Sn-based catalysts to enhance their selectivity for formate and ensure the long-term stability of the active sites[6,7]. Several strategies have been explored to stabilize SnO_x sites, such as the formation of heterojunctions, introducing oxygen vacancies, morphology tuning, and incorporating elements with higher electronegativity or reduction potential than SnO_x[8–13]. These approaches aim to maintain Sn in a higher oxidation state, thereby preserving its electrocatalytic activity.

Bimetallic Cu-Sn catalysts have been extensively studied for CO_2 electroreduction to formate[12,14,15]. In these systems, Cu and Sn exhibit higher oxidation states, forming CuO-SnO_2 interfaces[16]. This interface has proven effective in optimizing the *OCHO binding energy. Additionally, it aids in retaining Sn in the higher oxidation state owing to the higher reduction potential of the CuO, resulting in higher Faradaic efficiencies for formate. The electrochemical redox potential for Cu^{2+}/ Cu, Cu^+/ Cu and SnO_2/Sn are as follows:

$Cu^{2+} + 2e^- \leftrightarrow Cu$ $E^o = 0.34$ V

$Cu^+ + e^- \leftrightarrow Cu$ $E^o = 0.520$ V

$Sn^{4+} + 2e^- \leftrightarrow Sn^{2+}$ $E^o = 0.151$ V

$Sn^{2+} + 2e^- \leftrightarrow Sn$ $E^o = -0.13$ V

However, when the cathodic potential is applied, CuO_x and SnO_x undergo reduction forming monometallic species[6,17]. This leads to increased selectivity towards hydrogen evolution reaction, thereby reducing the efficiency of CO_2 conversion. Thus, the major challenge faced in this bimetallic catalyst is retaining the CuO_x-SnO_x interfaces to ensure durable electrochemical activity.

1.3.2 Scope of the investigation

In this study, a CuSnBi trimetallic catalyst has been synthesized to enhance CO_2 electroreduction to formate. The synergistic interaction among Cu, Sn, and Bi facilitates the formation of an increased number of CuO_x-SnO_x interfaces. Additionally, incorporating Bi_2O_3 contributes to lowering the overpotential and achieving a Faradaic efficiency of 80% for the formate, along with stable electrochemical performance for upto 6 hours. Operando ATR-FTIR spectroscopy was used to identify the formation of the intermediates to gain mechanistic insights into the CO_2 electroreduction process.

1.3.3 Experimental Section

1.3.3.1 Materials

Sodium borohydride ($NaBH_4$), copper chloride ($CuCl_2.2H_2O$), and sodium bicarbonate ($NaHCO_3$) were purchased from Sigma Aldrich. Tin chloride ($SnCl_2.2H_2O$) and bismuth nitrate ($Bi(NO_3)_3.5H_2O$) were obtained from Loba Chemie Pvt. Ltd. Isopropyl alcohol (IPA) was purchased from Merck Life Sciences Pvt. Ltd. Ethanol was procured from Hayman. Nafion-117 membrane was procured from the Fuel Cell store. Tin oxide (SnO_2) and Toray Carbon paper (with a thickness of ~0.4mm) were obtained from Alfa Aesar. Tedlar gas bags were obtained from Techinstro. HPLC vials were procured from Agilent. All the chemicals obtained were used without further purification. Deionized (Milli-Q) water was used for all the syntheses and catalytic studies.

1.3.3.2 Characterization technique

The PXRD patterns of the synthesized material were acquired using a Rigaku diffractometer with Cu anode generating an X-ray of wavelength 1.54 Å. HRTEM images were obtained using the JEOL JEM-2100 Plus electron microscope. HAADF-STEM-EDS-Elemental mapping measurement was performed using a Thermofisher Talos F200S electron microscope. The samples for the TEM measurements were prepared by dropcasting the material dispersed in ethanol on Cu grid. XPS measurements were performed using a Thermofisher K-Alpha spectrometer using a microfocused Al Kα monochromator. The spectra was collected before and after etching with Ar sputtering for 2.5 mins to remove the surface oxides. ICP-OES analyses were performed on the Perkin Elmer Optima 7000DV instrument to determine the Sn and Bi loading. The in-situ IR study was carried out using a Bruker 70v vertex FTIR spectrometer equipped with a mid-band MCT detector. The electrochemical studies were performed using Biologic potentiostat. The flow of CO_2/N_2 was controlled using Horiba mass flow controller. To monitor the flow rate of the gas, Agilent ADM gas flow meter was used. The gaseous products were determined using Agilent 7890B gas chromatograph, and liquid products were determined using Agilent HPLC.

1.3.3.3 Synthesis of CuSnBi nanostructures

CuSnBi was synthesized using the $NaBH_4$ assisted reduction method at room temperature. In a typical synthesis, 7.9 mL of 0.1 M $CuCl_2.2H_2O$ solution, 2.1 mL of 0.1 M $SnCl_2.2H_2O$ solution, and 120 µL of 0.04 M $Bi(NO_3)_3.6H_2O$ solution were mixed and stirred in a beaker for 30 mins. The resultant solution was added into a 250 mL beaker containing 50 mL of 0.1 M $NaBH_4$ solution under vigorous stirring. The resultant solution was stirred for 20 min. CuSnBi precipitates as a black colored compound. The black compound was collected by centrifugation and washed thrice with water and once with ethanol. The solution was kept for drying at 40 ^{o}C overnight. CuSn and Cu nanostructures were also synthesized following the above procedure

1.3.3.4 Preparation of working electrode

To prepare the coating ink, 2 mg of the prepared catalyst was dispersed in 1 mL of isopropyl alcohol. The mixture was sonicated for 1 h. 40 µL of 5 wt% Nafion solution was added to the ink and sonicated for another hour. 200 µL of the as prepared coating ink was drop casted on Toray carbon paper of area 1 cm^2 to maintain a mass loading of 0.4 mg cm^{-2}. The electrodes were then dried overnight.

1.3.3.5 CO_2 electroreduction studies

The electrochemical reactions were carried out in a three-electrode configuration *(Figure 1.3.1)* in an H-cell. CuSnBi coated C-paper was used as the working electrode. Ag/AgCl and graphite rod were used as the reference and counter electrodes, respectively. The anodic and cathodic chamber was filled with 30 mL, 0.5 M $KHCO_3$ electrolyte. The solution was purged with CO_2 at a flow rate of 30 mL/min for 1 h before reaction. CO_2 was passed through a humidifier containing milliQ water before passing it into the electrolyte. The reference electrodes were calibrated before the experiment. The obtained potential (vs. Ag/AgCl) was converted into a reversible hydrogen electrode (RHE) scale using the Nernst equation:

$$\mathbf{E_{RHE} = E_{Ag/AgCl} + 0.059\ pH + E^{o}_{Ag/AgCl}}$$

Here $E_{Ag/AgCl}$ is the potential measured vs Ag/AgCl electrode in volts. The pH of the solution is 7.8, and $E^{o}_{Ag/AgCl}$ is the standard potential for Ag/AgCl electrode in 0.5 M $KHCO_3$.

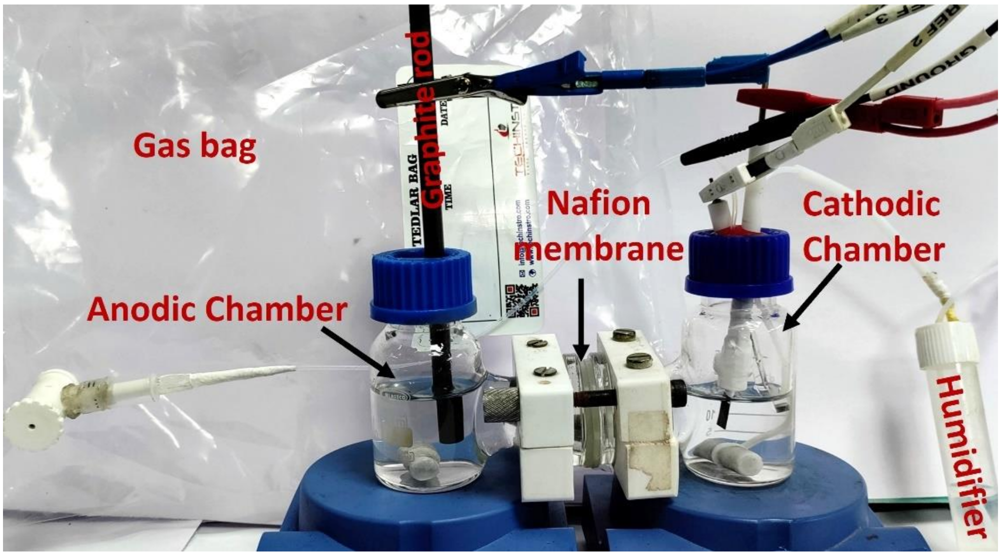

Figure 1.3.1: H-cell setup used to study the electrochemical reduction of CO_2

Linear sweep voltammetry (LSV) was performed in the potential range of -0.5 V (vs. Ag/AgCl) to -2.2 V (vs. Ag/AgCl) with a scan rate of 10 mV s^{-1} with and without 85% iR compensation. Chronoamperometric (CA) i-t measurement was performed without iR compensation at different potentials. The current density for LSV and CA was normalized with respect to the geometrical surface area of 1 cm^2. The CO_2 flow was maintained at 30 mL/min during the reaction. The gaseous products were collected during the reaction in the Tedlar gas bag and analyzed by gas chromatography (GC). The liquid products were collected post chronoamperometry and analyzed by high performance liquid chromatography (HPLC). The Faradaic efficiency for formate was determined using the formula[18,19]:

$$\textbf{Faradaic efficiency} = \frac{\mathbf{C \times n \times V \times F \times 100}}{\mathbf{Q}}$$

Here, C stands for the concentration of formate in moles, V stands for the volume of electrolyte, n stands for no. of electrons required per CO_2 molecule to form formate, and Q stands for the total charge calculated from the chronoamperometry.

The Faradaic efficiency for CO and H_2 is calculated using the formula[18,19]:

$$\textbf{Faradaic efficiency} = \frac{\mathbf{C \times flow\ rate \times \left(\frac{n \times P \times F}{R \times T}\right) \times 100}}{\mathbf{Q}}$$

Here, C stands for the concentration of gas detected from GC, the flow rate for CO_2 is 30 mL/min, P is the pressure (1.013 bar), F is the Faraday constant (96500), R is the gas constant, T is the temperature and n stands for no. of electrons required per CO_2 molecule to form CO/ no. of electron required to produce H_2 and Q stands for the total charge calculated from the chronoamperometric measurement.

Reusability study

The CO_2 electrode was used for five consecutive cycles. The electrode was collected after every cycle and rinsed with Milli-Q water. The liquid product was collected and analyzed after each measurement. The electrolyte was refreshed for each cycle.

1.3.3.6 Product estimation

Gaseous product

Gas Chromatography was utilized to analyze the gaseous products. The gas chromatograph used was equipped with an HP-Plot Q capillary column, HP-Molsieve capillary column, Hysep Q-packed column, TCD (thermal conductivity detector), methanizer and FID (flame ionization detector). The TCD was connected to a methanizer. The outlet of the methanizer was connected to the FID. The methanizer was used to detect the CO in low concentrations. FID was used to detect C_2H_6, C_2H_4, CH_4, and CO, while TCD was used to detect permanent gases such as H_2. For quantifying the products, a 5-point calibration plot was prepared using calibration gas of concentrations 20 ppm, 100 ppm, 500 ppm, 1000 ppm, and 3000 ppm. An average peak area value for 5 injections was considered for the plot. For the product analysis, the gaseous products were collected in a Tedlar gas bag and injected manually into the GC at a constant flow rate of 5 mL/min *(Figure 1.3.2)*.

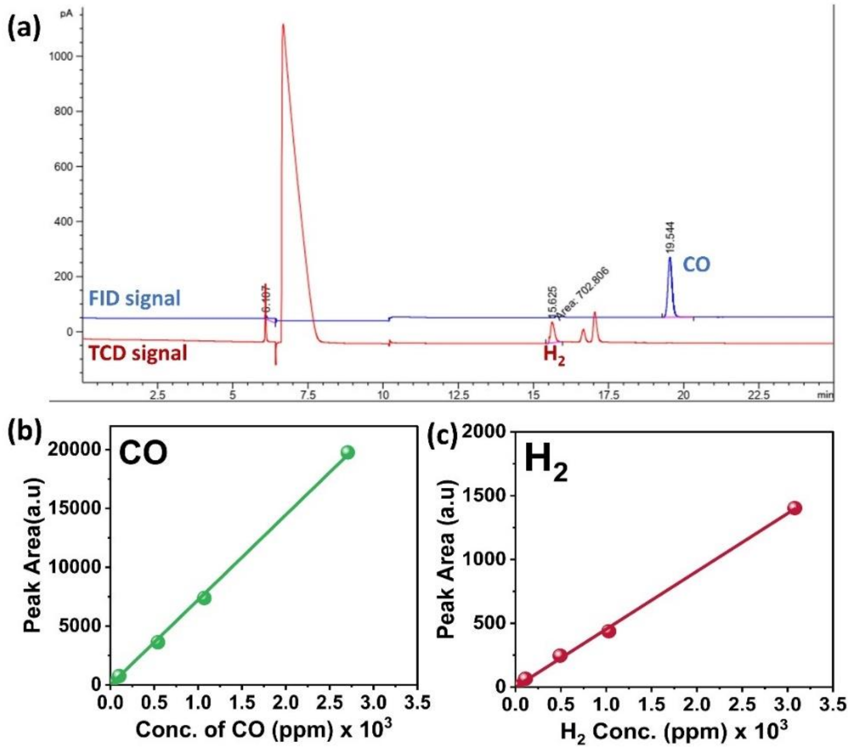

Figure 1.3.2: Gas chromatography for product estimation **(a)** Chromatogram obtained for product analyses showing signals obtained from TCD and FID, **(b)** Calibration plot for CO, and **(c)** Calibration plot for H_2

Liquid product

High performance liquid chromatography (HPLC) was used to analyse the liquid products. The HPLC was equipped with a Hi Plex-H column and a refractive index detector (RID) for the formate analysis. In an HPLC vial, 1.5 mL of the electrolyte was collected after the reaction and taken for the analyses. To quantify the products, a 5-point calibration plot was prepared with varying concentrations of sodium formate *(Figure 1.3.3).*

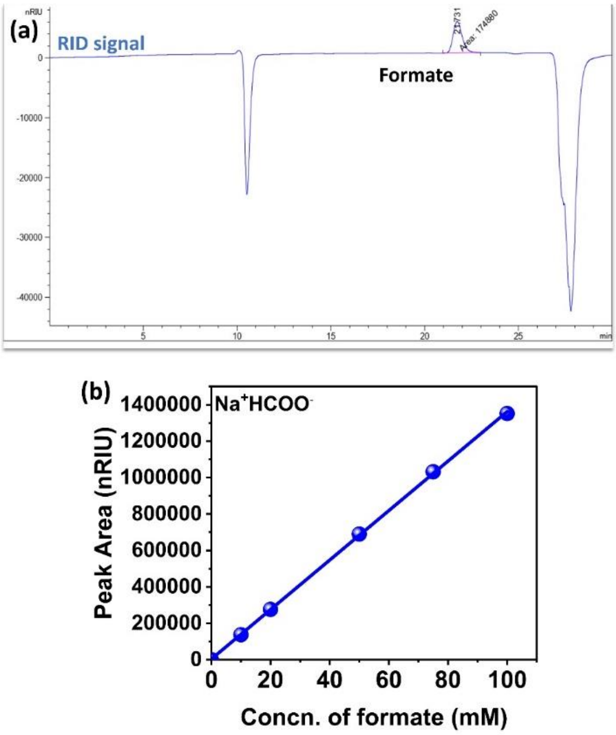

Figure 1.3.3: High performance liquid chromatography for product estimation **(a)** chromatogram obtained for product analysis showing signals obtained from RID and **(b)** calibration plot for formate

1.3.3.7 Operando Infrared Spectroscopy (ATR-FTIR)

For the in-situ IR study, the electrochemical cell was connected to a Si hemispherical window. Carbon paper coated with the catalyst attached to a graphite rod using silver paste was used as the working electrode. The Hg/HgO electrode and Pt coil were used as the reference and the counter electrodes, respectively. For the electrolyte, 15 mL, 0.5M $KHCO_3$ solution was used. The working electrode was placed close to the Si hemispherical window for the attenuated total reflection- Fourier transform infrared spectroscopy study (ATR-FTIR). At the beginning of the experiment, background spectra were collected with the electrolyte in the cell. The background spectra were subtracted from all the subsequent spectra to remove the contribution of the electrolyte towards the measurement. The scan resolution was set at 4 cm^{-1}. For studying the time dependent evolution of the intermediates, chronoamperometry at different potentials was performed. The IR measurement was performed simultaneously. The total number of IR measurements at each potential was set at 50. Each measurement was an average of 128 scans. Between each measurement, a rest time of 60 sec was given. The spectra were analyzed by the OPUS software and plotted directly as a function of potential and time.

1.3.4 Result and Discussion

CuSnBi nanostructures were prepared by the simultaneous reduction of the mixture of metal solutions by $NaBH_4$. The PXRD pattern *(Figure 1.3.4)* of the as prepared catalyst showed the characteristic peak of CuO predominantly. The peaks at 2θ 32.7^o, 35.7^o, 38.9^o, 48.9^o, 58.2^o, 61.7^o, 68^o, 72.3^o, and 75.2^o correspond to CuO planes (110), (11-1), (200), (20-2), (202), (11-3), (310), (220), (311) and (22-2) respectively. The peaks at 2θ 42.8^o, 53.7^o, 83.2^o, and 89.8^o belong to metallic Cu (211), Bi_2O_3 (112), SnO_2 (222), and SnO_2 (411), respectively. The PXRD peaks were matched with the database PDF card No.: 9016326 for CuO, PDF card No.: 1534785 for SnO_2 and PDF card No. 1537328 for Bi_2O_3. From ICP-OES analysis, the loading of Sn and Bi was estimated to be 30 wt% and 3.5 wt%, respectively.

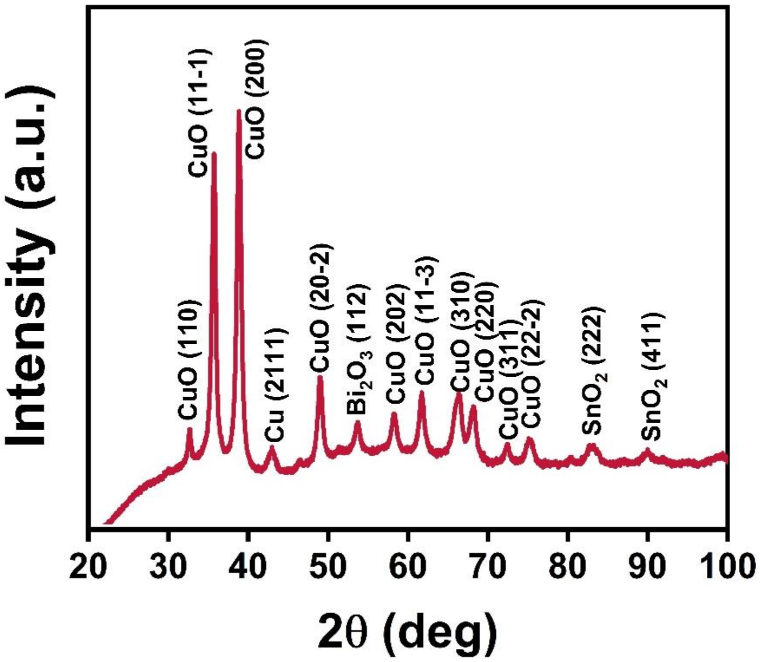

Figure 1.3.4: Powder X-ray diffraction pattern for CuSnBi nanostructures

TEM analysis showed nanostructures of CuSnBi with CuO-SnO interfaces *(Figure 1.3.5)*. HAADF STEM elemental mapping of CuSnBi showed a uniform distribution of Cu, Sn, Bi, and O *(Figure 1.3.6).*

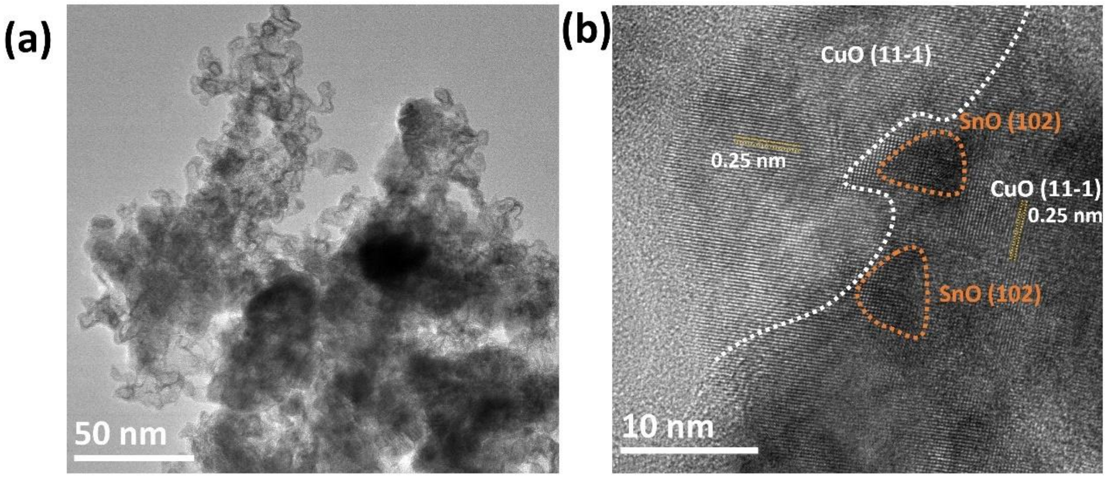

Figure 1.3.5 : (a) HRTEM image of CuSnBi nanostructures and **(b)** CuO_x-SnO_x interface

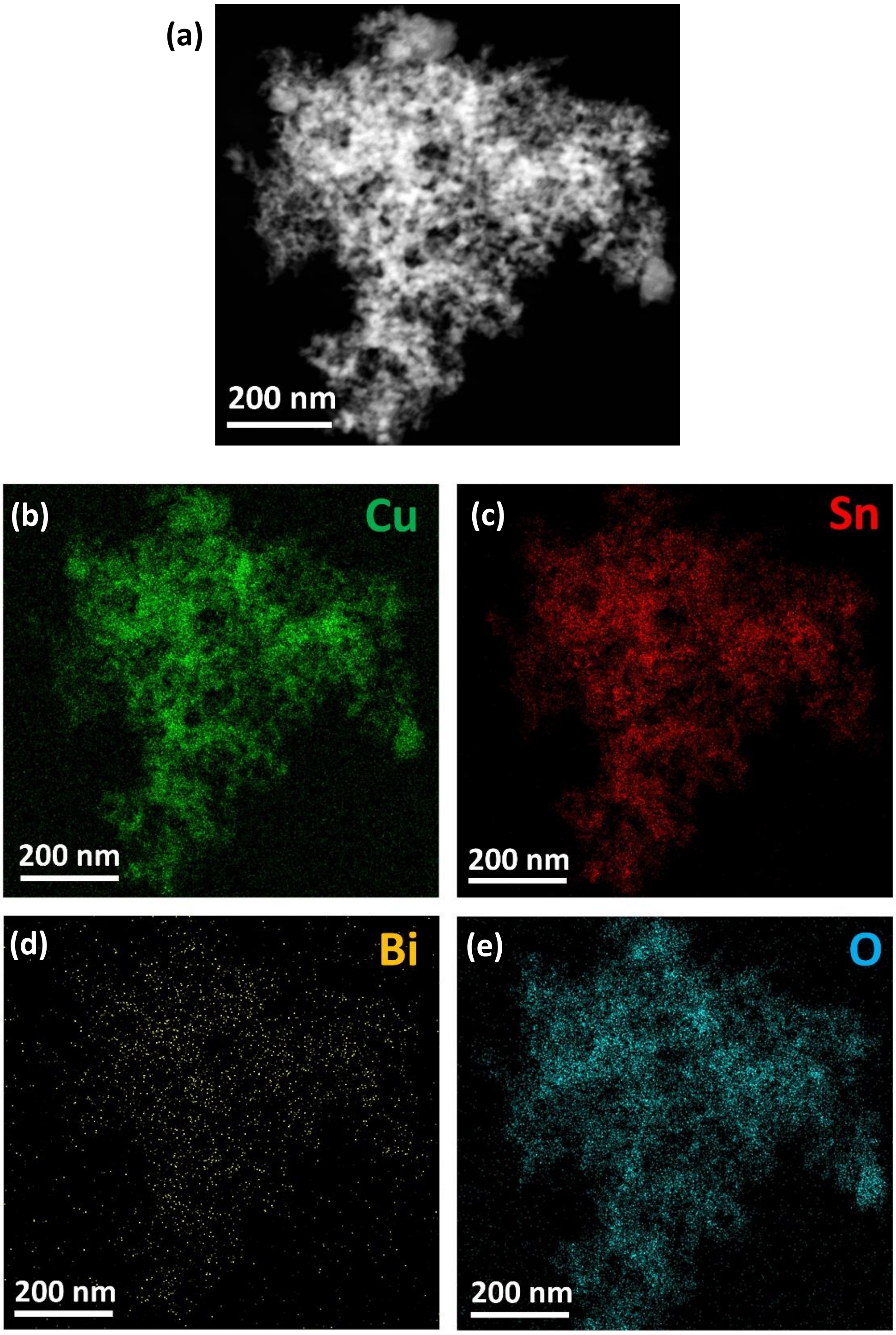

Figure 1.3.6: HAADF-STEM-Elemental Mapping **(a)** HAADF-STEM image of CuSnBi nanostructures, **(b)-(e)** Elemental mapping for Cu, Sn, Bi, and O.

XPS was performed to determine the valence state of the metal species in the catalyst. XPS of CuSnBi nanostructures were compared with CuSn nanostructures to understand the effect of Bi addition on the catalyst. The high resolution Sn3d XPS spectra of CuSnBi coated on carbon paper showed peaks at 487.5 eV ($3d_{5/2}$) and 495.9 eV ($3d_{3/2}$) for Sn^{2+} while the peaks at 488.7 eV ($3d_{5/2}$) and 497.0 eV ($3d_{3/2}$) correspond to Sn^{4+}. The Sn 3d

XPS spectra for CuSn nanostructures show peaks at 486.8 eV ($3d_{5/2}$) and 495.2 eV ($3d_{3/2}$) for Sn^{2+}. The peaks at 485.3 eV ($3d_{5/2}$) and 493.8 eV ($3d_{3/2}$) correspond to Sn^0, while the peaks for Sn^{4+} appears at 488.2 eV ($3d_{5/2}$) and 496.5 eV ($3d_{3/2}$) [20,21]. Upon comparison, it can be observed that in CuSnBi, Sn^{2+} shows a positive shift in binding energy by 0.6 eV, while Sn^{4+} shows a positive shift of 0.4 eV. This positive shift in the binding energy could be attributed to the charge transfer from Sn to Cu and Bi *(Figure 1.3.7)*[22]. The high resolution XPS spectra for Bi 4f show characteristic peaks for Bi^0 at 159.3 eV ($4f_{7/2}$) and 163.3 eV ($4f_{5/2}$), while the peaks at 160.4 eV ($4f_{7/2}$) and 165.3 eV ($4f_{5/2}$) correspond to Bi^{3+} *(Figure 1.3.8)*[23,24].

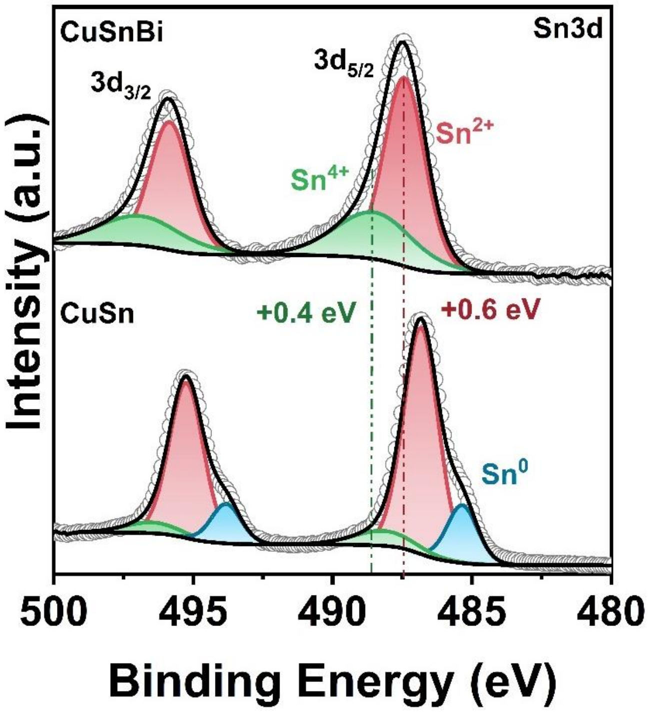

Figure 1.3.7: High resolution Sn 3d XPS spectra of CuSnBi and CuSn (spectra collected after Ar sputtering for 2.5 min)

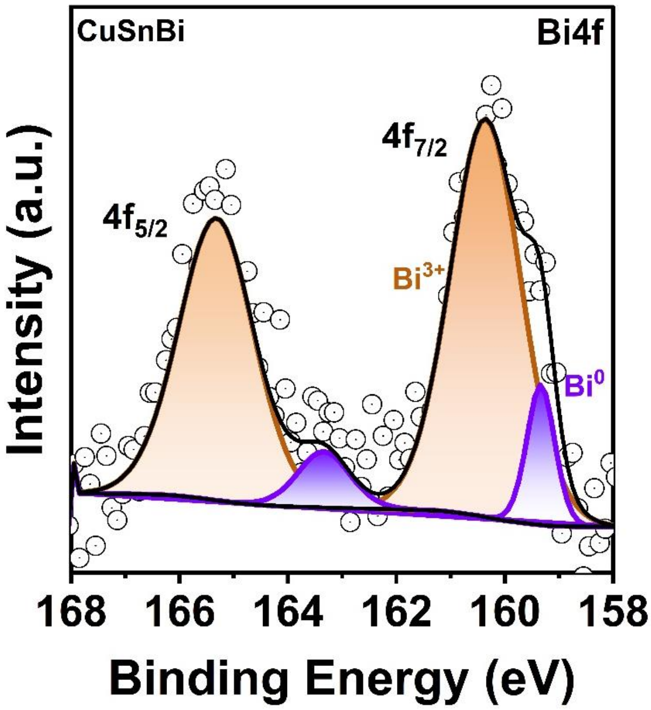

Figure 1.3.8: High resolution Bi 4f XPS spectra of CuSnBi and CuSn (spectra collected after Ar sputtering)

The Cu LMM Auger spectra of both CuSnBi and CuSn showed that Cu exists as CuO, Cu_2O, and metallic Cu *(Figure 1.3.9)*. CuSnBi shows peaks for kinetic energy at 916.8 eV, 915.4 eV, and 918.5 eV, corresponding to CuO, Cu_2O, and metallic Cu, respectively. The Cu LMM Auger spectra for CuSn show peaks at 918.1 eV, 916.5 eV, and 918.6 eV for CuO, Cu_2O, and metallic Cu. Upon comparison, it was observed that CuSnBi showed a negative shift of 1.3 eV for CuO and 1.1 eV for Cu_2O in kinetic energy in comparison to CuSn[25–27]. The negative shift in binding energy could be attributed to the charge transfer from Sn to Cu[28,29].

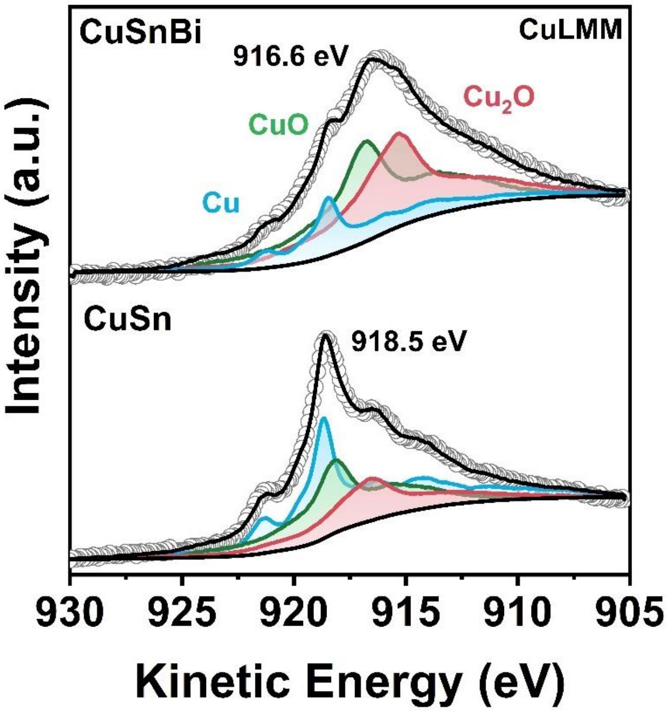

Figure 1.3.9: Cu LMM Auger spectra of CuSnBi and CuSn (spectra collected after Ar sputtering)

It is also observed that the intensity of the metallic Cu, Sn, and Bi is less in comparison to the corresponding oxides. This indicates that the metal species exist predominantly in the higher oxidation states in the catalyst. The different valence states of the metal species were quantified from the fitting of the XPS spectra, as shown in *Figure 1.3.10*. From the quantification of the Sn 3d XPS spectra, it is observed that in the case of CuSn nanostructures, 80 % of the Sn is present as SnO_x (SnO + SnO_2), while 20% is present as metallic Sn. Upon the addition of Bi, all the Sn in the catalyst is converted into SnO_x in CuSnBi. The quantification of the Cu species was performed using the Cu LMM Auger spectra. It is observed that in CuSn nanostructures, 52% of the Cu is present as CuO_x (CuO+Cu_2O), while 48% is present as metallic Cu. The incorporation of Bi increases the oxide content to 80%, and the metallic content is reduced to 20%. This shows that in the presence of Bi_2O_3, a greater number of CuO_x-SnO_x interfaces are generated, which are responsible for the enhanced activity.

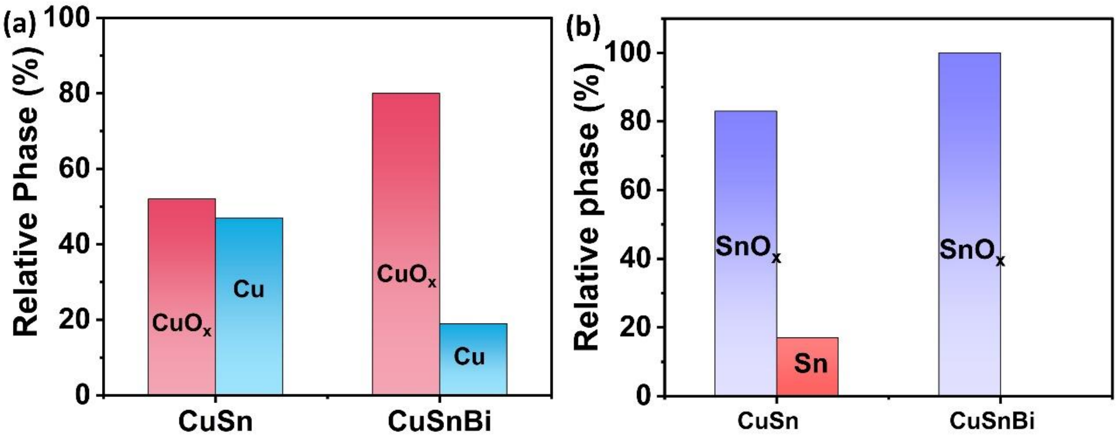

Figure 1.3.10: Quantification of the different valence states in CuSnBi and CuSn nanostructures obtained from fitting the XPS spectra **(a)** Cu and CuO_x, **(b)** Sn and SnO_x.

Evaluation of CO_2 electroreduction

Linear sweep voltammograms of CuSnBi, CuSn, Cu, and SnO_2 (commercial) were obtained in a CO_2 saturated, 0.5 M $KHCO_3$ solution. It was observed that the CuSnBi exhibited a maximum current density of -200 mA cm^{-2} at -1.5 V_{RHE}. CuSn showed a maximum current density of 180 mA cm^{-2} at -1.5 V_{RHE}, while the LSV for Cu nanostructures overlapped with that of CuSnBi *(Figure 1.3.11(a))*. In comparison, SnO_2 exhibits a higher overpotential for electrochemical CO_2 reduction. *Figure 1.3.11(b)* compares overpotentials at -10 mA cm^{-2}, -50 mA cm^{-2} and -100 mA cm^{-2} for CuSnBi, CuSn and SnO_2. It is observed that at all the current densities, the overpotential for electrochemical CO_2 reduction on the CuSnBi catalyst is significantly reduced. LSV for CuSnBi was also performed in the N_2 saturated electrolyte. The polarization curve overlapped with the curve obtained in the CO_2 saturated electrolyte. The increased current density of the catalyst in the absence of CO_2 could be attributed to the hydrogen evolution reaction *(Figure 1.3.12 a)*. The linear sweep voltammograms were also obtained without iR compensation. In comparison to the iR compensated voltammogram, it showed a maximum current density of -100 mA cm^{-2} at -1.5 V_{RHE} *(Figure 1.3.12(b))*.

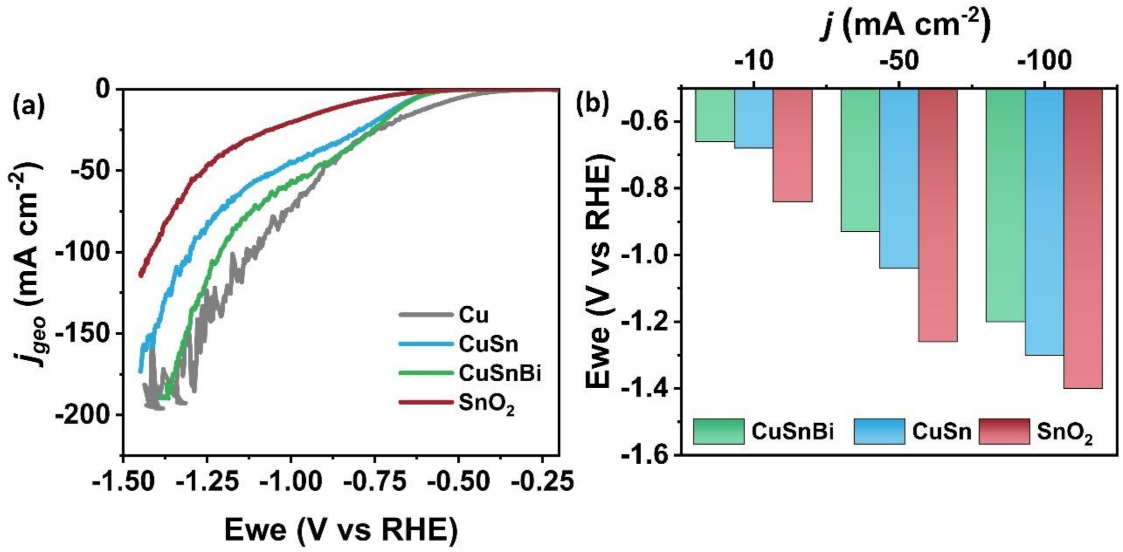

Figure 1.3.11: (a) Linear sweep voltammogram for CO_2ER in CO_2 saturated 0.5 M $KHCO_3$ for CuSnBi, CuSn, SnO_2, and Cu, **(b)** comparison of overpotential at -10 mA cm^{-2}, 50 mA cm^{-2} and -100 mA cm^{-2} for CuSnBi, CuSn and SnO_2

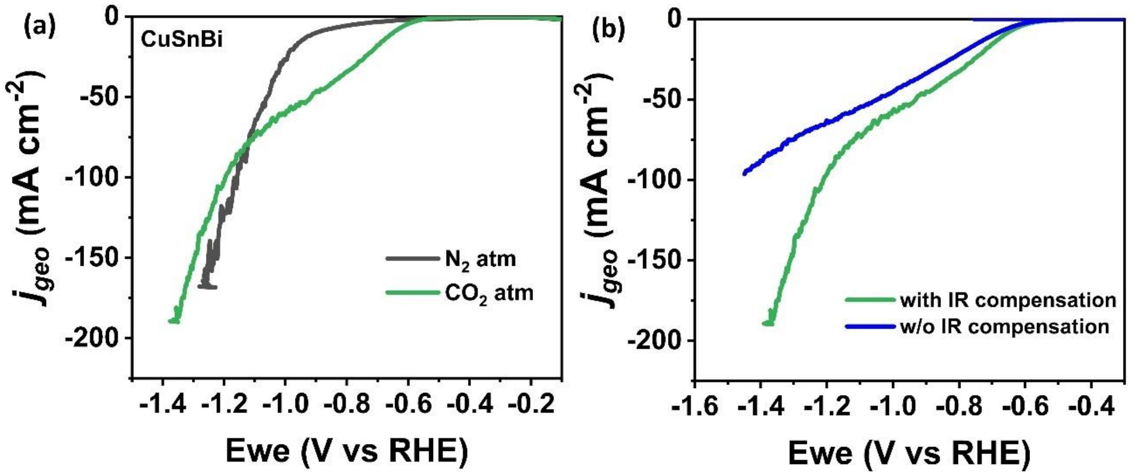

Figure 1.3.12: (a) Comparison of Linear sweep voltammogram for CuSnBi in 0.5 M $KHCO_3$ saturated with CO_2 and N_2 and **(b)** Comparison of Linear sweep voltammogram for CO_2ER in CO_2 saturated 0.5 M $KHCO_3$ for CuSnBi with and without iR compensation

Chronoamperometry was performed to determine the products formed at -1.05 V_{RHE}, -1.25 V_{RHE}, and -1.45 V_{RHE} without iR compensation *(Figure 1.3.13 a)*. The Faradaic efficiency plot for the products formed is shown in *Figure 1.3.13 (b)*. It is observed that the CuSnBi exhibits selectivity towards formate. Maximum Faradaic efficiency of 80 % for formate, 4 % for CO, and 18 % for H_2 was obtained at -1.45 V_{RHE}. The chronoamperometry was also performed in a solution purged with N_2. H_2 was formed as the major product, and negligible amounts of formate were obtained.

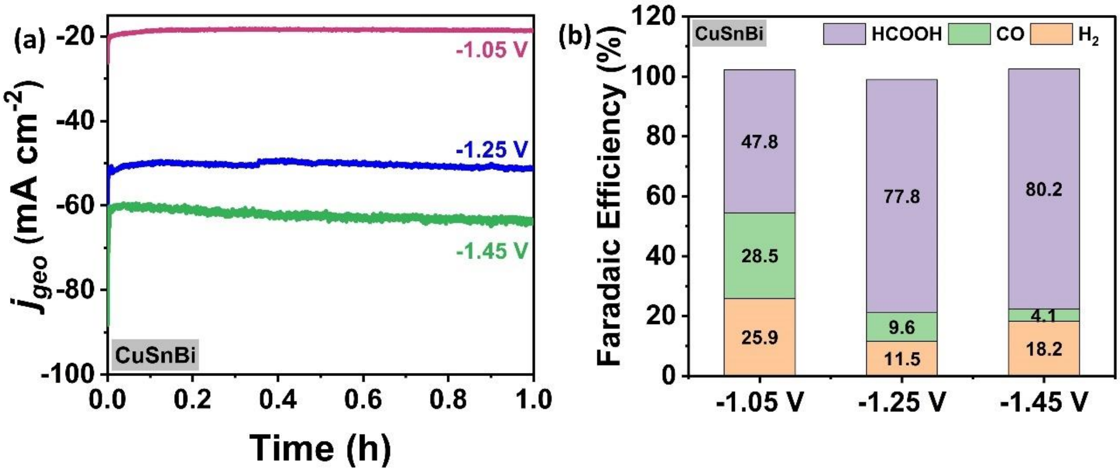

Figure 1.3.13: (a) Chronoamperometry obtained at -1.05 V_{RHE}, -1.25 V_{RHE}, and -1.45 V_{RHE} for CuSnBi in CO_2 saturated 0.5 M $KHCO_3$ and **(b)** Comparison of Faradaic efficiency of formate, CO and H_2 obtained after chronoamperometry at -1.05 V, -1.25 V and -1.45 V

The formate Faradaic efficiency was compared for CuSnBi, CuSn, Cu, and SnO_2 at -1.25 $V_{RHE,}$ as shown in *Figure 1.3.14 (a)*. Faradaic efficiency of 10 %, 60%, 58 %, and 78% were obtained for Cu, SnO_2, CuSn, and CuSnBi, respectively. This indicates that the synergistic effect between Cu, Sn, and Bi enhances the CO_2ER electrochemical activity. Furthermore, CuSnBi shows a long-term stability of 6 h at a potential of -1.05 V_{RHE} with a current density of 20 mA cm^{-2} *(Figure 1.3.14 b)*. The formate Faradaic efficiency obtained after 6 h of continuous operation was estimated to be 35 %.

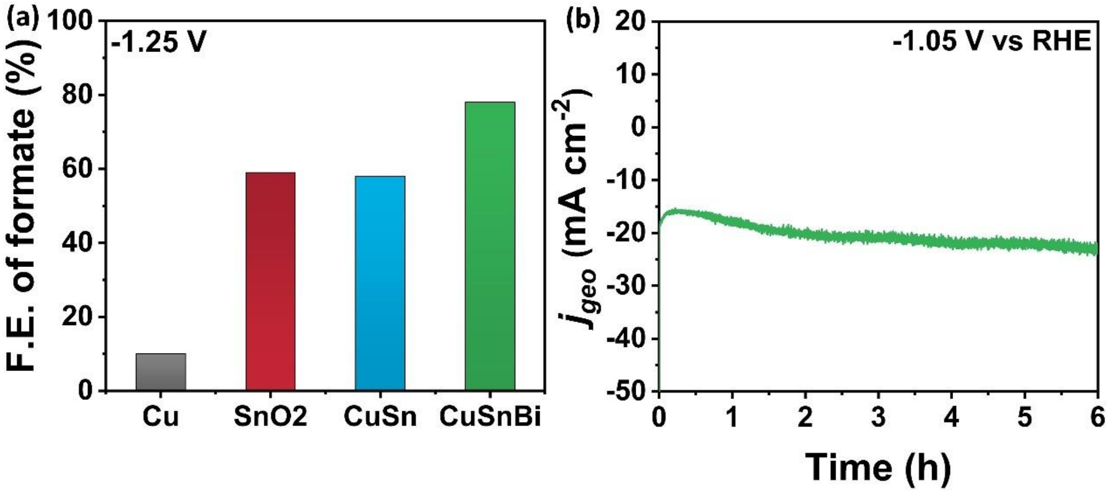

Figure 1.3.14: (a) Comparison of formate Faradaic efficiency of CuSnBi, CuSn, SnO_2, and Cu after chronoamperometry for 1 h at -1.25 V_{RHE} and **(b)** Chronoamperometric stability study of CO_2 ER by CuSnBi for 6 h.

Recyclability studies were performed for CuSnBi at -1.05 V_{RHE}, and the Faradaic efficiency of formate was compared *(Figure 1.3.15)*. It was observed that the catalyst shows a Faradaic efficiency of 51.4 % for formate in the first cycle. In the second cycle, a 10% decrease in the Faradaic efficiency is observed, resulting in 40.2 % for formate. In the subsequent cycles, CuSnBi shows a stable performance, exhibiting a Faradaic efficiency close to 40 %.

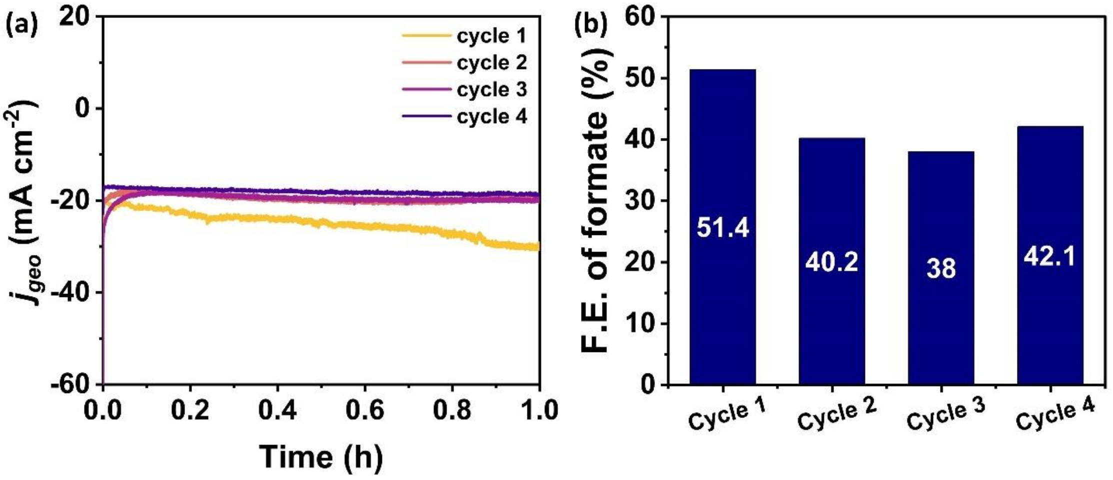

Figure 1.3.15: (a) Chronoamperometric recyclability study for CO_2ER by CuSnBi at -1.05 V_{RHE} and **(b)** Faradaic efficiency of formate obtained after each cycle

Post reaction Characterization

Post reaction characterization was performed using XPS and FESEM after chronoamperometry for 1 h at -1.25 V_{RHE}. The XPS spectra obtained after the reaction were compared with the spectra obtained before the reaction. Sn 3d XPS spectra of CuSnBi show peaks at 487.1 eV ($3d_{5/2}$) and 495.5 eV ($3d_{3/2}$) for Sn^{2+}, while the peaks at 487.9 eV ($3d_{5/2}$) and 496.5 eV ($3d_{3/2}$) belong to Sn^{4+}. Additionally, small peaks at 485.4 eV ($3d_{5/2}$) and 494.0 eV ($3d_{3/2}$) were observed for Sn^0. The Sn 3d XPS spectra show an increase in the intensity of the Sn^{4+} peak and a decrease in the intensity of the Sn^{2+} peak *(Figure 1.3.17)*[30].

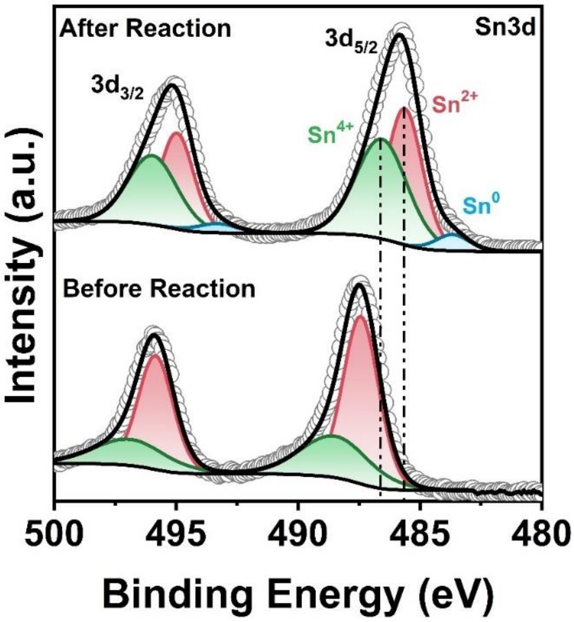

Figure 1.3.17: Comparison of high resolution Sn 3d XPS spectra of CuSnBi before and after reaction. The spectra were collected after Ar sputtering for 2.5 mins.

The Cu LMM Auger spectra for CuSnBi show peaks at kinetic energy 917.6 eV, 916.0 eV, and 918.7 eV for CuO, Cu_2O, and metallic Cu, respectively *(Figure 1.3.18)*. An increase in the intensity of the metallic Cu peak was observed. The high resolution Bi 4f XPS spectra show peaks at 160.8 eV ($4f_{7/2}$) and 165.9 eV ($4f_{5/2}$) for Bi^{3+}, while the peaks at 159.8 eV ($4f_{7/2}$) and 165.0 eV ($4f_{5/2}$) belongs to Bi^0. The intensity of the peak corresponding to Bi^0 shows an increase with a corresponding decrease in the intensity of Bi^{3+} *(Figure 1.3.19)*. The increase in the intensity of the metallic Cu and Bi peaks indicates that under the reduction potential, some of the Cu and Bi oxide species have undergone reduction.

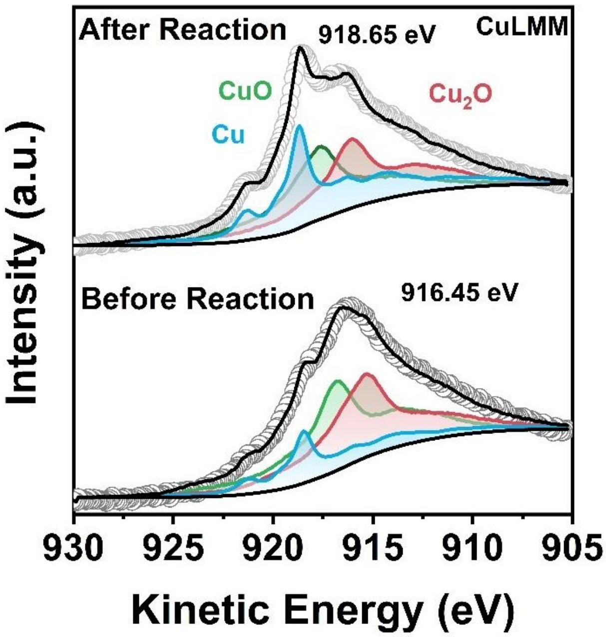

Figure 1.3.18: Comparison of high resolution Cu LMM Auger spectra of CuSnBi before and after reaction. The spectra were collected after Ar sputtering for 2.5 mins.

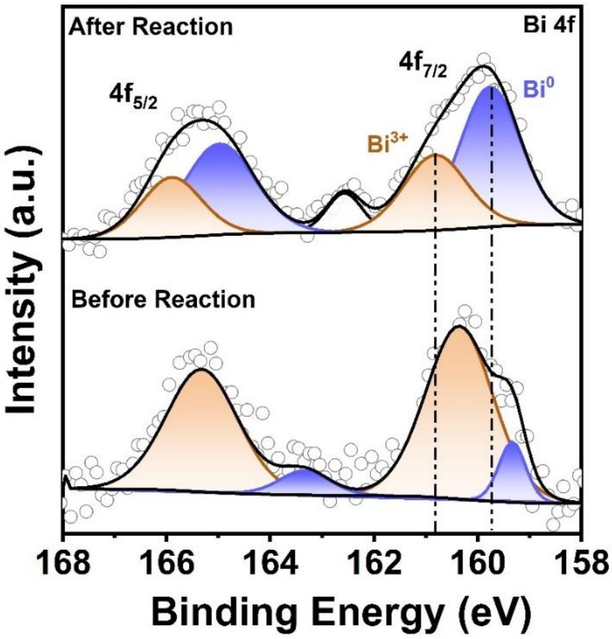

Figure 1.3.19: Comparison of high resolution Bi 4f XPS spectra of CuSnBi before and after reaction. The spectra were collected after Ar sputtering for 2.5 mins.

Quantitative analysis of the fitted XPS spectra for various metallic species in CuSnBi reveals a notable post-reaction shift in the oxidation states *(Figure 1.3.20)*. The total concentration of metallic species increases while that of MO_x species decreases. For Cu, 64% exists as CuO_x and 36% as metallic Cu. Sn exhibits a minor reduction in total oxide content, with 95% present as SnO_x and 5% as metallic Sn. In contrast, Bi shows a distribution where 64% is in the metallic Bi state, and 36% is present as Bi^{3+}. This indicates that in the presence of Bi, most of the CuO_x-SnO_x interfaces are retained.

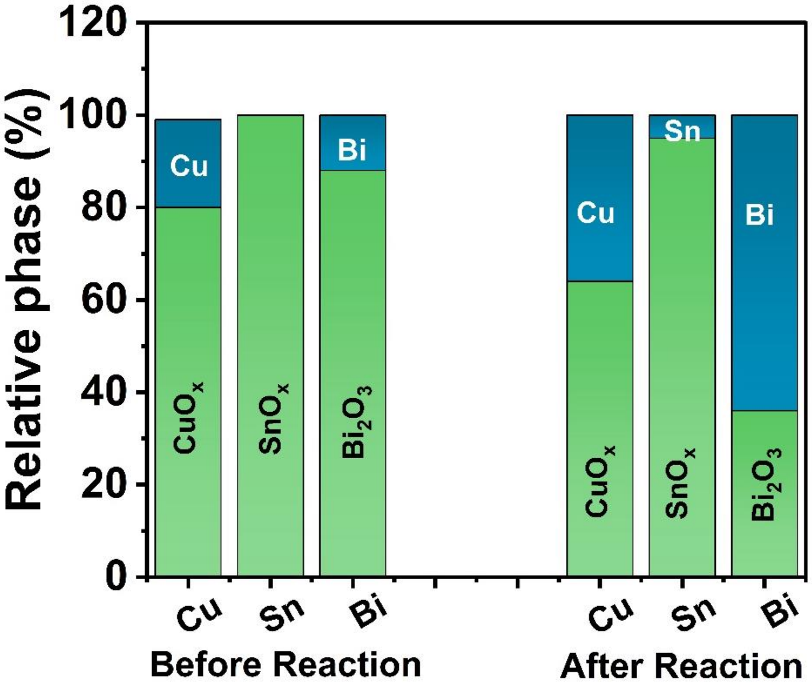

Figure 1.3.20: Comparison of different valence states of the metal species before and after reaction in CuSnBi nanostructures.

FESEM-elemental mapping confirms the presence of all elements on the electrode, indicating their retention and uniform distribution across the electrode surface *(Figures 1.3.21 and 1.3.22).*

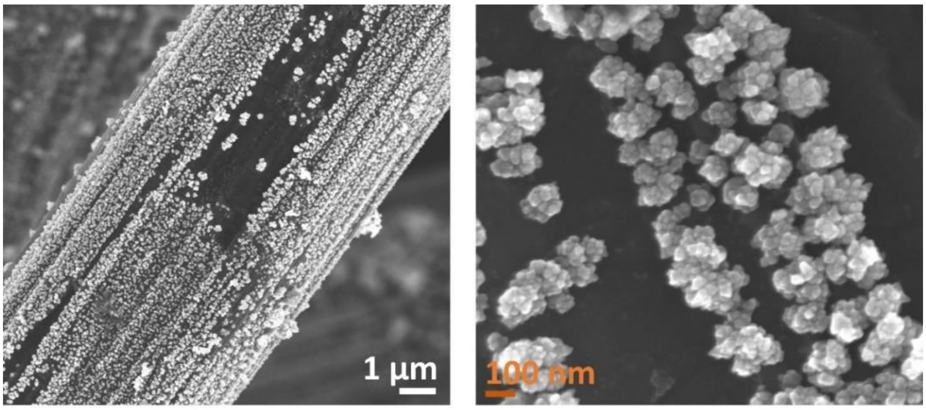

Figure 1.3.21: FESEM of CuSnBi coated carbon paper obtained after chronoamperometry at -1.25 V for 1h

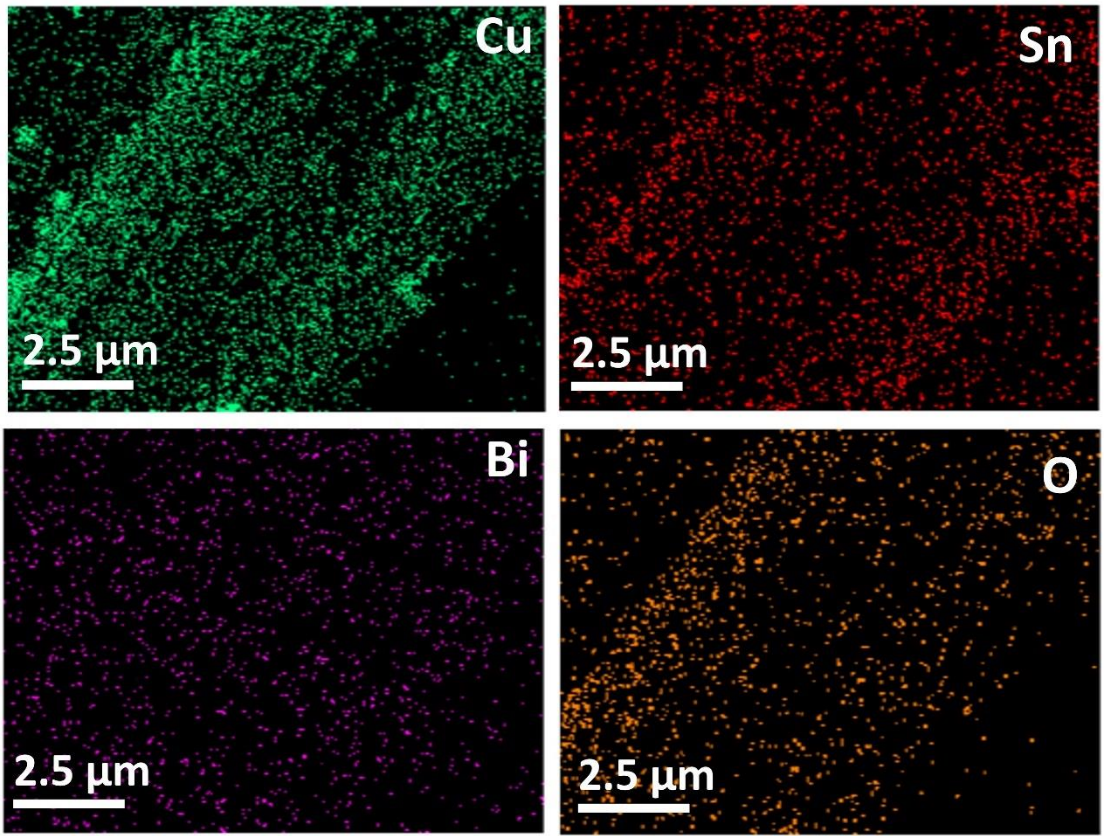

Figure 1.3.22: FESEM-Elemental mapping of CuSnBi coated carbon paper obtained after chronoamperometry at -1.25 V for 1h

Operando ATR-FTIR

To determine the mechanism for CO_2 electroreduction on CuSnBi, operando ATR-FTIR spectroscopy was performed. From the product analyses, it is observed that $HCOO^-$ is the major product obtained from CO_2 electroreduction. CO_2 can bind to the catalyst either through C or O, resulting in *COOH or *OCHO intermediate, respectively. The formation of the *OCHO intermediate results in formate as the major product[22].

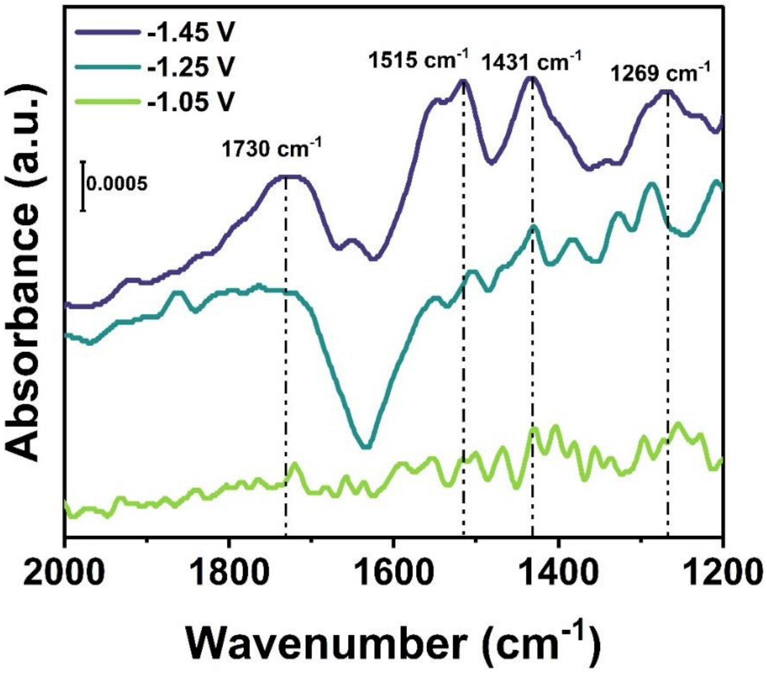

Figure 1.3.23: Potential dependant *operando* ATR-FTIR spectra at -1.05 V, -1.25 V, and -1.45 V obtained in CO_2 saturated 0.5 M $KHCO_3$ solution

The potential dependent IR spectra *(Figure 1.3.22)* show absorbance bands at 1269 cm^{-1} and 1431 cm^{-1} for the $*CO_2^-$ and *OCHO intermediate respectively[14,31]. The IR bands at 1515 cm^{-1} correspond to surface bound $*CO_3^-$, while the band at 1730 cm^{-1} is due to the *H-O-H bending of water[32–34]. It is observed that with an increase in the applied reduction potential, the intensity of the absorbance band is found to increase. This is attributed to the increase in the reduction of CO_2 resulting in an increase in the products formed. Time dependent in situ IR spectra *(Figure 1.3.23)* were obtained by conducting chronoamperometry at -1.45 V for a duration of 1 h. A gradual increase in the intensity of the absorbance bands was observed, indicating the continuous reduction of CO_2 and the simultaneous formation of formate.

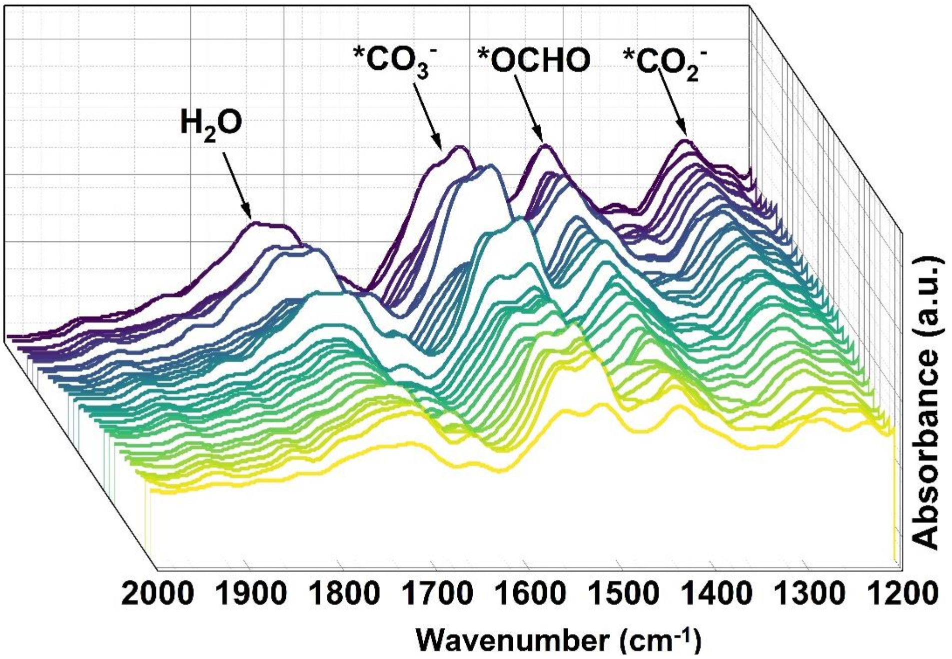

Figure 1.3.23: Time dependant *operando* ATR-FTIR spectra at -1.45 V obtained in CO_2 saturated 0.5 M $KHCO_3$ solution

1.3.5 Conclusion

CuSnBi nanostructures have been synthesized by $NaBH_4$ assisted reduction at room temperature. Herein, incorporating Bi_2O_3 in CuSn helps enhance the formation of CuO_x-SnO_x interfaces, which has proven effective for CO_2 electroreduction to formate. This could be attributed to the high electronegativity of Bi, which results in charge transfer to Bi. Compared to SnO_2 and CuSn, CuSnBi shows a reduction in the overpotential for CO_2 reduction, and a maximum formate Faradaic efficiency of 80% was obtained at -1.45 V_{RHE}. Operando ATR-FTIR spectroscopy shows the formation of the key intermediate *OCHO required for the formation of formate.

1.3.6 Reference

(1) Yang, Z.; Oropeza, F. E.; Zhang, K. H. L. P-Block Metal-Based (Sn, In, Bi, Pb) Electrocatalysts for Selective Reduction of CO2 to Formate. *APL Mater* **2020**, *8* (6), 060901. https://doi.org/10.1063/5.0004194.

(2) Ren, T.; Miao, Z.; Ren, L.; Xie, H.; Li, Q.; Xia, C. Nanostructure Engineering of Sn-Based Catalysts for Efficient Electrochemical CO2 Reduction. *Small* **2023**, *19* (2), 2205168. https://doi.org/10.1002/smll.202205168.

(3) Guan, Y.; Liu, M.; Rao, X.; Liu, Y.; Zhang, J. Electrochemical Reduction of Carbon Dioxide (CO2): Bismuth-Based Electrocatalysts. *J Mater Chem A Mater* **2021**, *9* (24), 13770–13803. https://doi.org/10.1039/D1TA01516H.

(4) Feaster, J. T.; Shi, C.; Cave, E. R.; Hatsukade, T.; Abram, D. N.; Kuhl, K. P.; Hahn, C.; Nørskov, J. K.; Jaramillo, T. F. Understanding Selectivity for the Electrochemical Reduction of Carbon Dioxide to Formic Acid and Carbon Monoxide on Metal Electrodes. *ACS Catal* **2017**, *7* (7), 4822–4827. https://doi.org/10.1021/acscatal.7b00687.

(5) Bagger, A.; Ju, W.; Varela, A. S.; Strasser, P.; Rossmeisl, J. Electrochemical CO2 Reduction: A Classification Problem. *ChemPhysChem* **2017**, *18* (22), 3266–3273. https://doi.org/10.1002/cphc.201700736.

(6) Van Daele, K.; De Mot, B.; Pupo, M.; Daems, N.; Pant, D.; Kortlever, R.; Breugelmans, T. Sn-Based Electrocatalyst Stability: A Crucial Piece to the Puzzle for the Electrochemical CO2 Reduction toward Formic Acid. *ACS Energy Lett* **2021**, *6* (12), 4317–4327. https://doi.org/10.1021/acsenergylett.1c02049.

(7) Dutta, A.; Kuzume, A.; Rahaman, M.; Vesztergom, S.; Broekmann, P. Monitoring the Chemical State of Catalysts for CO2 Electroreduction: An In Operando Study. *ACS Catal* **2015**, *5* (12), 7498–7502. https://doi.org/10.1021/acscatal.5b02322.

(8) Wang, T.; Chen, J.; Ren, X.; Zhang, J.; Ding, J.; Liu, Y.; Lim, K. H.; Wang, J.; Li, X.; Yang, H.; Huang, Y.; Kawi, S.; Liu, B. Halogen-Incorporated Sn Catalysts for Selective Electrochemical CO2 Reduction to Formate. *Angewandte Chemie International Edition* **2023**, *62* (10), e202211174. https://doi.org/10.1002/anie.202211174.

(9) Bai, X.; Chen, W.; Zhao, C.; Li, S.; Song, Y.; Ge, R.; Wei, W.; Sun, Y. Exclusive Formation of Formic Acid from CO2 Electroreduction by a Tunable Pd-Sn Alloy. *Angewandte Chemie International Edition* **2017**, *56* (40), 12219–12223. https://doi.org/10.1002/anie.201707098.

(10) Liu, H.; Li, B.; Liu, Z.; Liang, Z.; Chuai, H.; Wang, H.; Lou, S. N.; Su, Y.; Zhang, S.; Ma, X. Ceria -Mediated Dynamic Sn0/Snδ+ Redox Cycle for CO2 Electroreduction. *ACS Catal* **2023**, *13* (7), 5033–5042. https://doi.org/10.1021/acscatal.2c06135.

(11) Ren, B.; Wen, G.; Gao, R.; Luo, D.; Zhang, Z.; Qiu, W.; Ma, Q.; Wang, X.; Cui, Y.; Ricardez–Sandoval, L.; Yu, A.; Chen, Z. Nano-Crumples Induced Sn-Bi Bimetallic Interface Pattern with Moderate Electron Bank for Highly Efficient CO2 Electroreduction. *Nat Commun* **2022**, *13* (1), 2486. https://doi.org/10.1038/s41467-022-29861-w.

(12) Tian, B.; Wu, H.; Zhang, Y.; Chen, C.; Abdalla, K. K.; Sendeku, M. G.; Zhou, L.; Yu, J.; Wang, Y.; Kuang, Y.; Xu, H.; Li, J.; Sun, X. Cu-Induced Interfacial Water Engineering of SnO2 for Durable and Highly Selective CO2 Electroreduction. *ACS Catal* **2024**, *14* (14), 10904–10912. https://doi.org/10.1021/acscatal.4c01670.

(13) Tu, X.; Liu, X.; Zhang, Y.; Zhu, J.; Jiang, H. Advances in Sn-Based Oxide Catalysts for the Electroreduction of CO2 to Formate. *Green Carbon* **2024**, *2* (2), 131–148. https://doi.org/10.1016/j.greenca.2024.03.006.

(14) Shi, Y.; Wang, Y.; Yu, J.; Chen, Y.; Fang, C.; Jiang, D.; Zhang, Q.; Gu, L.; Yu, X.; Li, X.; Liu, H.; Zhou, W. Superscalar Phase Boundaries Derived Multiple Active Sites in SnO2/Cu6Sn5/CuO for Tandem Electroreduction of CO2 to Formic Acid. *Adv Energy Mater* **2023**, *13* (13), 2203506. https://doi.org/10.1002/aenm.202203506.

(15) Jiang, Y.; Shan, J.; Wang, P.; Huang, L.; Zheng, Y.; Qiao, S.-Z. Stabilizing Oxidation State of SnO2 for Highly Selective CO2 Electroreduction to Formate at Large Current Densities. *ACS Catal* **2023**, *13* (5), 3101–3108. https://doi.org/10.1021/acscatal.3c00123.

(16) Ning, B.; Chang, W.; Liu, M.; Jiang, H.; Li, C. Derived CuSn Alloys from Heterointerfaces in Bimetallic Oxides Promote the CO2 Electroreduction to Formate. *ChemElectroChem* **2021**, *8* (6), 1150–1155. https://doi.org/10.1002/celc.202100013.

(17) Popović, S.; Smiljanić, M.; Jovanovič, P.; Vavra, J.; Buonsanti, R.; Hodnik, N. Stability and Degradation Mechanisms of Copper-Based Catalysts for Electrochemical CO2 Reduction. *Angewandte Chemie International Edition* **2020**, *59* (35), 14736–14746. https://doi.org/10.1002/anie.202000617.

(18) Chakraborty, S.; Kalita, D.; Agarwal, S.; Vashishth, S.; Mathew, N.; Maity, S.; Goud, D.; Rao, A.; Peter, S. C.; Singh, A. K.; Eswaramoorthy, M. Tuning the Electrocatalytic Activity of Pd Nanocatalyst toward Hydrogen Evolution and Carbon Dioxide Reduction Reactions by Nickel Incorporation. *Chemistry of Materials* **2024**, *36* (13), 6547–6557. https://doi.org/10.1021/acs.chemmater.4c00809.

(19) Dutta, N.; Bagchi, D.; Chawla, G.; Peter, S. C. A Guideline to Determine Faradaic Efficiency in Electrochemical CO2 Reduction. *ACS Energy Lett* **2024**, *9* (1), 323–328. https://doi.org/10.1021/acsenergylett.3c02362.

(20) Cho, J. S.; Kang, Y. C. Nanofibers Comprising Yolk–Shell Sn@void@SnO/SnO2 and Hollow SnO/SnO2 and SnO2 Nanospheres via the Kirkendall Diffusion Effect and Their Electrochemical Properties. *Small* **2015**, *11* (36), 4673–4681. https://doi.org/10.1002/smll.201500940.

(21) Kamboj, N.; Debnath, B.; Bhardwaj, S.; Paul, T.; Kumar, N.; Ogale, S.; Roy, K.; Dey, R. S. Ultrafine Mix-Phase SnO-SnO2 Nanoparticles Anchored on Reduced Graphene Oxide Boost Reversible Li-Ion Storage Capacity beyond Theoretical Limit. *ACS Nano* **2022**, *16* (9), 15358–15368. https://doi.org/10.1021/acsnano.2c07008.

(22) Ren, B.; Wen, G.; Gao, R.; Luo, D.; Zhang, Z.; Qiu, W.; Ma, Q.; Wang, X.; Cui, Y.; Ricardez–Sandoval, L.; Yu, A.; Chen, Z. Nano-Crumples Induced Sn-Bi Bimetallic Interface Pattern with Moderate Electron Bank for Highly Efficient CO2 Electroreduction. *Nat Commun* **2022**, *13* (1), 2486. https://doi.org/10.1038/s41467-022-29861-w.

(23) Wei, Y.; Zhang, P.; Zhou, S.; Tian, X.; Soomro, R. A.; Liu, H.; Du, H.; Xu, B. Encapsulating Bi Nanoparticles in Reduced Graphene Oxide with Strong Interfacial Bonding toward Advanced Potassium Storage. *Small* **2024**, *20* (30), 2306541. https://doi.org/10.1002/smll.202306541.

(24) Yan, X.; Yu, G.; Xing, C.; Hu, Y.; Liu, H.; Li, X. Schottky Junction with Bi/Bi2O3 Core–Shell Nanoparticle Modified g-C3N4 for Boosting Photocatalytic H2O2 Evolution from Pure Water. *Catal Sci Technol* **2023**, *13* (10), 3094–3105. https://doi.org/10.1039/D3CY00235G.

(25) Jiang, Z.-T.; Thurgate, S. M.; Wilkie, P. Line Structure in Photoelectron and Auger Electron Spectra of CuO/Cu and Cu by Auger Photoelectron Coincidence Spectroscopy (APECS). *Surface and Interface Analysis* **2001**, *31* (4), 287–290. https://doi.org/10.1002/sia.990.

(26) Timmermans, B.; Reniers, F.; Hubin, A.; Buess-Herman, C. Chemical Effects in the Auger Spectrum of Copper–Oxygen Compounds. *Appl Surf Sci* **1999**, *144–145*, 54–58. https://doi.org/10.1016/S0169-4332(98)00764-8.

(27) Espinós, J. P.; Morales, J.; Barranco, A.; Caballero, A.; Holgado, J. P.; González-Elipe, A. R. Interface Effects for Cu, CuO, and Cu2O Deposited on SiO2 and ZrO2. XPS Determination of the Valence State of Copper in Cu/SiO2 and Cu/ZrO2 Catalysts. *J Phys Chem B* **2002**, *106* (27), 6921–6929. https://doi.org/10.1021/jp014618m.

(28) Dou, T.; He, J.; Diao, S.; Wang, Y.; Zhao, X.; Zhang, F.; Lei, X. Dynamic Reconstructuring of CuS/SnO2-S for Promoting CO2 Electroreduction to Formate. *Journal of Energy Chemistry* **2023**, *82*, 497–506. https://doi.org/10.1016/j.jechem.2023.03.016.

(29) Shi, Y.; Wang, Y.; Yu, J.; Chen, Y.; Fang, C.; Jiang, D.; Zhang, Q.; Gu, L.; Yu, X.; Li, X.; Liu, H.; Zhou, W. Superscalar Phase Boundaries Derived Multiple

Active Sites in SnO2/Cu6Sn5/CuO for Tandem Electroreduction of CO2 to Formic Acid. *Adv Energy Mater* **2023**, *13* (13), 2203506. https://doi.org/10.1002/aenm.202203506.

(30) Tian, B.; Wu, H.; Zhang, Y.; Chen, C.; Abdalla, K. K.; Sendeku, M. G.; Zhou, L.; Yu, J.; Wang, Y.; Kuang, Y.; Xu, H.; Li, J.; Sun, X. Cu-Induced Interfacial Water Engineering of SnO2 for Durable and Highly Selective CO2 Electroreduction. *ACS Catal* **2024**, *14* (14), 10904–10912. https://doi.org/10.1021/acscatal.4c01670.

(31) Tian, B.; Wu, H.; Zhang, Y.; Chen, C.; Abdalla, K. K.; Sendeku, M. G.; Zhou, L.; Yu, J.; Wang, Y.; Kuang, Y.; Xu, H.; Li, J.; Sun, X. Cu-Induced Interfacial Water Engineering of SnO2 for Durable and Highly Selective CO2 Electroreduction. *ACS Catal* **2024**, *14* (14), 10904–10912. https://doi.org/10.1021/acscatal.4c01670.

(32) Li, J.; Li, J.; Liu, X.; Chen, J.; Tian, P.; Dai, S.; Zhu, M.; Han, Y.-F. Probing the Role of Surface Hydroxyls for Bi, Sn and In Catalysts during CO2 Reduction. *Appl Catal B* **2021**, *298*, 120581. https://doi.org/10.1016/j.apcatb.2021.120581.

(33) Baruch, M. F.; Pander, J. E. I. I. I.; White, J. L.; Bocarsly, A. B. Mechanistic Insights into the Reduction of CO2 on Tin Electrodes Using in Situ ATR-IR Spectroscopy. *ACS Catal* **2015**, *5* (5), 3148–3156. https://doi.org/10.1021/acscatal.5b00402.

(34) Fan, T.; Zhang, J.; Zhang, X.; Wang, M.; Yi, X.; Lum, Y.; Chen, Z. Interface-Stabilized High-Valent Sn Enables Efficient CO2 Electroreduction to Formate/Formic Acid across the Full PH Range. *Nano Energy* **2024**, *130*, 110135. https://doi.org/10.1016/j.nanoen.2024.110135.

PART 2

Chapter 2.1. Introduction to electrochemical urea oxidation

Chapter 2.2. Improvement in overall performance for electrochemical urea oxidation by introduction of Pd in $Ni(OH)_2$

Chapter 2.3. Elucidating the urea electrooxidation pathway on Ni_3N

Chapter- 2.1

Introduction to Electrochemical Urea Oxidation

Summary:

A transition to a hydrogen-based economy offers a sustainable approach to energy production. However, the primary challenge lies in hydrogen generation. Electrochemical water splitting is an environmentally friendly method for hydrogen production, but its widespread adoption is hindered by high overpotentials. Urea-assisted water electrolysis emerges as an energy efficient alternative. The overall potential required for this process is 0.37 V, which is 860 mV less than the conventional water splitting. This chapter provides a comprehensive overview of the urea electrooxidation process, discussing its challenges, advancements in catalyst development, and the analytical tools used to elucidate its reaction mechanism.

2.1.1 Hydrogen Economy

The rise in greenhouse gas emissions, driven by burning fossil fuels and other human activities, emphasizes the urgent need for alternative energy sources. These alternatives must be efficient and environmentally friendly, ensuring that their use does not contribute to further emissions. Thus, a hydrogen-based economy offers a sustainable approach to energy production.

Hydrogen stands out as a clean-burning fuel, producing only water as a byproduct when utilized for energy generation. In addition to being lightweight, hydrogen has a remarkable gravimetric energy density of 142 MJ/kg, which is three times greater than that of gasoline[1,2]. Compared to other energy storage materials, hydrogen's superior gravimetric energy density makes it an exceptional choice, positioning it as a vital energy source for a sustainable future.

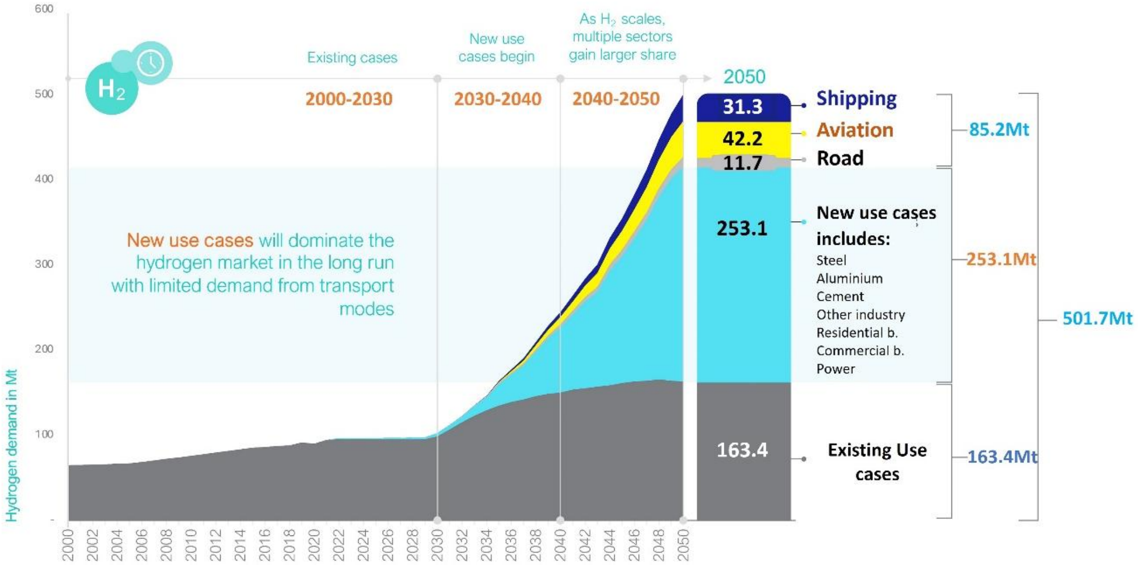

Figure 2.1.1: Assessment of Hydrogen demand by 2050 in different sectors. (This image is adapted from the report by The International Chamber of Shipping published in July 2024)

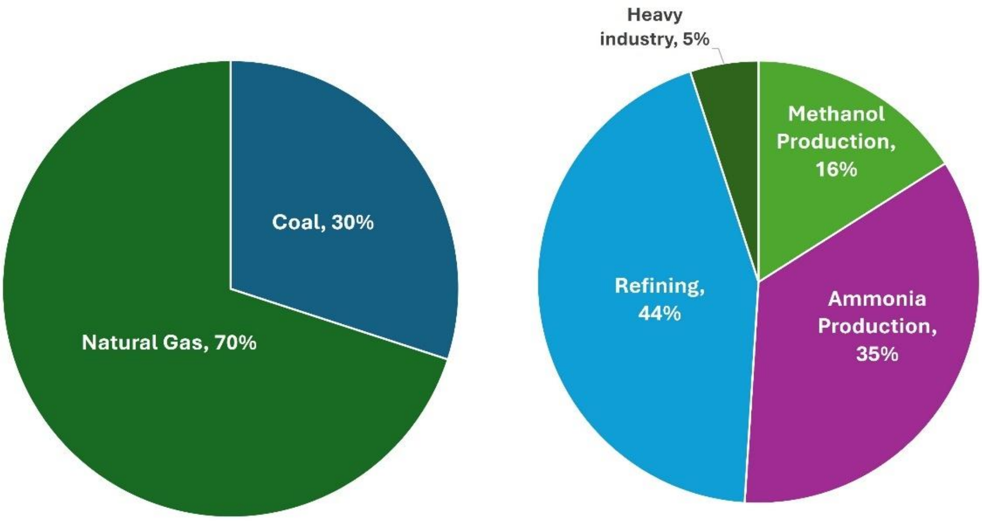

Figure 2.1.2 : (a) Current sources of H_2, (b) hydrogen demand in various industries. (This image is adapted from reference (3))

The current demand for hydrogen stands at ~ 95 Mt and is expected to increase to > 400 Mt by 2050, as shown in *Figure 2.1.1*[1,2]. Traditionally, hydrogen is produced from fossil fuel by steam methane reforming and coal gasification, as shown in *Figure 2.1.2 (a)*. It is majorly consumed in the refining sector (~44%) and in ammonia production (35%), as shown in *Figure 2.1.2 (b)*[3]. In recent years, the drive to decarbonize the energy sector has brought hydrogen into the spotlight as a low-emission alternative, particularly in the transportation sector. This shift has been accompanied by growing interest in fuel cell-powered vehicles. As a result, meeting the rising demand for hydrogen has become quintessential for enabling this transition to cleaner energy solutions.

Hydrogen can be produced/obtained by various methods. Based on the source/technology and its environmental impact, it is colour coded into 8 different categories[3]:

1. **Black and Brown Hydrogen**: This refers to the production of H_2 by coal gasification. This is the most environmentally damaging process, wherein huge amounts of greenhouse gasses are released into the atmosphere. This process contributes to over 30% of the hydrogen obtained worldwide.

2. **Grey Hydrogen**: This is the conventional way of producing H_2. This consists of steam methane reforming at a high temperature of 800-900 ^{o}C and 20-30 bar pressures. CO/CO_2 is emitted as the byproduct. At present, 70% of hydrogen gas is obtained through this process.

3. **Blue Hydrogen**: This refers to the hydrogen obtained from the steam reforming of the natural gas at high temperatures. CO_2 is emitted as the byproduct in the process. However, combining this process with carbon capture and storage technology helps in reducing emissions.

4. **Turquoise Hydrogen**: This process of hydrogen generation involves methane pyrolysis. Herein, methane obtained from natural gas is split into hydrogen and solid carbon, making it a low emission hydrogen generation process.

5. **Green Hydrogen**: It refers to the hydrogen obtained by water splitting. This process is driven by the electricity produced from renewable energy sources.

6. **Pink Hydrogen**: This refers to the hydrogen generated by electrolysis, using the electricity produced by nuclear energy.

7. **Yellow Hydrogen**: It is the hydrogen produced by electrolysis powered by solar energy

8. **White Hydrogen**: This refers to the naturally occurring hydrogen found in the underground deposits. This hydrogen is extracted by fracking, wherein a pressurized liquid consisting of water, sand, and chemicals is forced into a drilled well to release the gas from the rocks.

Out of the processes mentioned above, green hydrogen produced by electrolysis has emerged as a promising approach. This may be attributed to the following reasons: (i) the fall in the cost of electrolyzers and renewable power technologies[1,4], (ii) negligible greenhouse gas emissions, (iii) production of H_2 under ambient conditions, and (iv) the abundant supply of water as feedstock.

2.1.2 Electrochemical water splitting

In this process, electrical energy is applied to split water into hydrogen and oxygen[5,6]. The device used to perform the water splitting is termed an electrolyser[7]. The electrolyzer consists of three major components: cathode, anode, and membrane. At the cathode, water is reduced to produce H_2, while at the anode, water is oxidized to produce oxygen. The two chambers are separated by an ion exchange membrane, which prevents the mixing of the products formed during electrolysis, as shown in *Figure 2.1.3*. The thermodynamic potential required for driving this reaction is 1.23 V vs RHE.

H_2O (l) → H_2 + ½ O_2 (g) $\Delta G^o = 237$ kJ mol^{-1}, $\Delta E^o = 1.23$ V_{RHE}

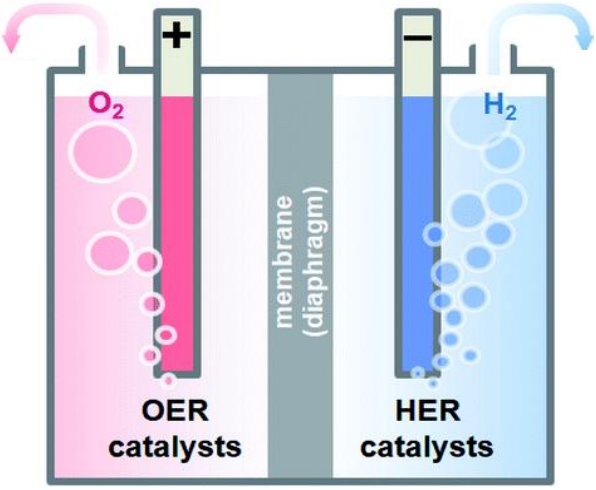

Figure 2.1.3: Schematic of an electrolyzer used for water splitting. Reproduced with permission from reference (7)

Due to the poor ionic conductivity of pure water, sulphuric acid, potassium hydroxide, or phosphate buffer is added to increase its conductivity. The addition of these substances alters the pH of the solution, thus making the electrolyte acidic, basic, and neutral, respectively. The pH dependence of water splitting can be understood by the Pourbaix diagram[8] shown *in Figure 2.1.4*. The Pourbaix diagram is divided into three regions by lines (a) and (b). The lines have a slope of -0.0591 and represent the equilibrium condition. The region below line (a) represents the region where water can be reduced to H_2, while the region above line (b) represents the region where water can be oxidized to O_2. In the region between the two lines, water is thermodynamically stable and does not undergo any reaction.

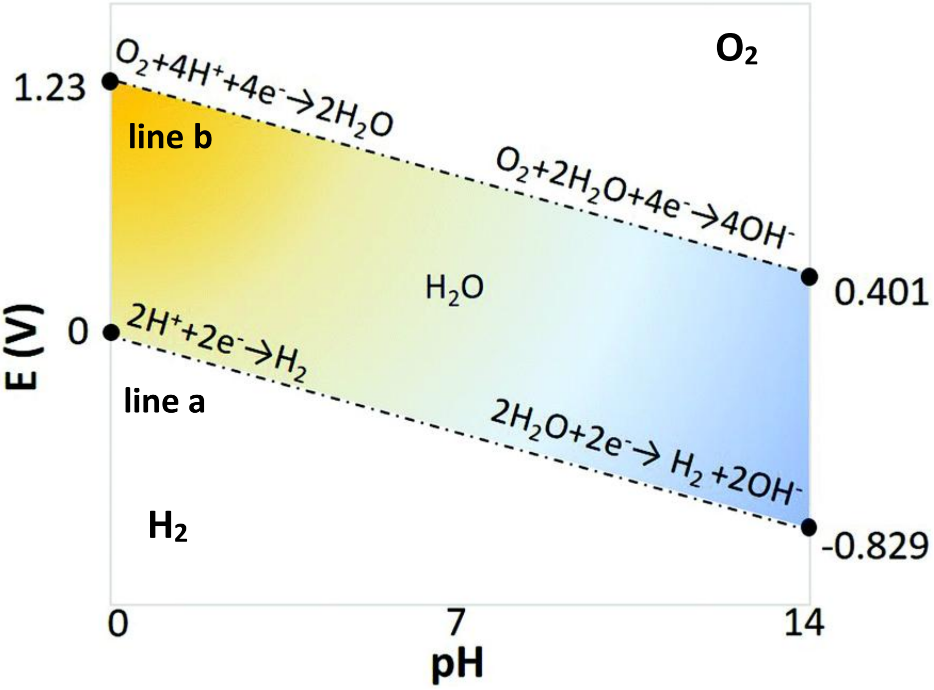

Figure 2.1.4: Pourbaix diagram showing the pH dependence of water splitting on potential. Reproduced with permission from reference (8)

Depending on the electrolyte used, water splitting can be performed in different mediums. The cathodic and the anodic half reactions in the three mediums can be represented as follows[5]:

Acidic Medium:

Anode: $2H_2O \rightarrow O_2 + 4H^+ + 4\,e^-$ $E^o = 1.23$ V

Cathode: $4H^+ + 4\,e^- \rightarrow 2H_2$ $E^o = 0$ V

Alkaline Medium:

Anode: $4OH^- \rightarrow O_2 + 2H_2O + 4\,e^-$ $E^o = 0.401$ V

Cathode: $4H_2O + 4\,e^- \rightarrow 2H_2 + 4\,OH^-$ $E^o = -0.83$ V

Neutral Medium:

Anode: $2H_2O \rightarrow O_2 + 4H^+ + 4\,e^-$ $E^o = 0.82$ V

Cathode: $4H_2O + 4\,e^- \rightarrow 2H_2 + 4\,OH^-$ $E^o = 0.413$ V

From the above equations, it can be observed that HER is a 2 electron process and OER is a 4 electron process. The sluggish kinetics associated with the 4 electron transfer process results in a high overpotential of $\geq \mathbf{200\ mV}$ for OER. Therefore, a key determining factor for improving the energy efficiency of the water splitting process is improving the kinetics of the oxygen evolution reaction. Furthermore, water splitting cannot be performed in a single compartment setup because of the explosive nature of the H_2/O_2 gaseous mixture. Hence, the use of an appropriate membrane is essential. These membranes are prone to degradation with time, which results in device failure. A potential strategy to overcome the mentioned limitation is the substitution of OER with oxidation of readily oxidizable organic molecules such as glucose, formaldehyde, benzyl alcohol, urea, etc, resulting in hybrid water electrolysis.

2.1.3. Hybrid water electrolysis

The thermodynamic potential for the oxidation of these organic molecules is low in comparison to the oxygen evolution reaction, as shown in *Figure 2.1.5*. Thus, the process becomes more energy efficient. This kind of water electrolysis is termed hybrid water electrolysis.[9–11]

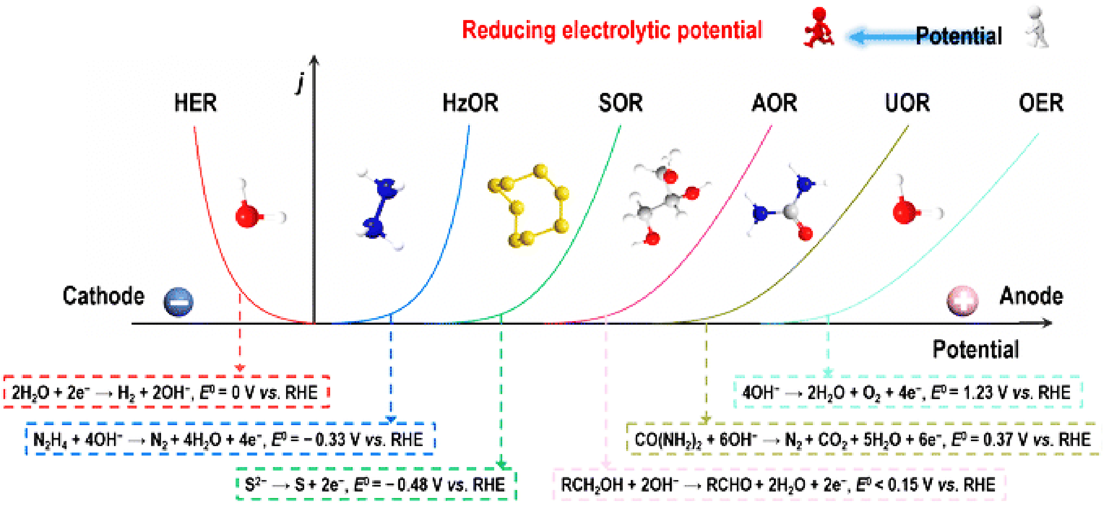

Figure 2.1.5: Comparison of standard potential for the oxidation of organic molecules with respect to OER. (Reproduced with permission from reference (11))

Oxygen Evolution: $4OH^- \rightarrow O_2 + 2H_2O + 4\ e^-$ **$E^o = -1.23\ V_{RHE}$**

Hydrazine Oxidation: $N_2H_4 + 4OH^- \rightarrow N_2 + 4H_2O + 4\ e^-$ **$E^o = -0.33V_{RHE}$**

Sulfide Oxidation: $S^{2-} \rightarrow S + 2e^-$ **$E^o = -0.48\ V_{RHE}$**

Alcohol Oxidation: $RCH_2OH + 2OH^- \rightarrow RCHO + 2H_2O + 2e^-$ **$E^o = 0.41\ V_{RHE}$**

Urea Oxidation: $CO(NH_2)_2 + 6\ OH^- \rightarrow N_2\ (g) + 5H_2\ (g) + CO_2 + 6e^-$ **$E^o = 0.37\ V_{RHE}$**

Apart from being energy efficient, the oxidation of these organic molecules provides distinct advantages. Firstly, organic molecules such as urea, hydrazine, ammonia, etc., are major pollutants that get consumed. This helps in overcoming the cost incurred in the separation and removal of waste substances from water and makes the process environment friendly. Secondly, organic molecules such as glycerol, glucose, benzyl alcohol, etc., can be oxidized to produce value added products, which can be further used as industrial feedstocks for synthesizing essential chemicals.

2.1.4. Electrochemical Urea Oxidation (UOR)

In nature, the hydrolysis of the urea molecule is facilitated by the urease enzyme. It consists of two Ni (II) sites attached to water molecules and a bridging hydroxide group *(Figure 2.1.6 a)*. The hydroxide and the Ni^{2+} sites form the active site for urea dissociation. During the process, one of the Ni sites gets attached to the carbonyl oxygen of the urea, making the carbon susceptible to nucleophilic attack. Subsequently, the amine group of the urea molecule binds with the second Ni site, resulting in a bidentate bond formation. This facilitates the nucleophilic attack by the bridging hydroxide on the carbonyl carbon, forming a tetrahedral intermediate that dissociates to form carbamate and ammonia *(Figure 2.1.6 b)*.[12–15]

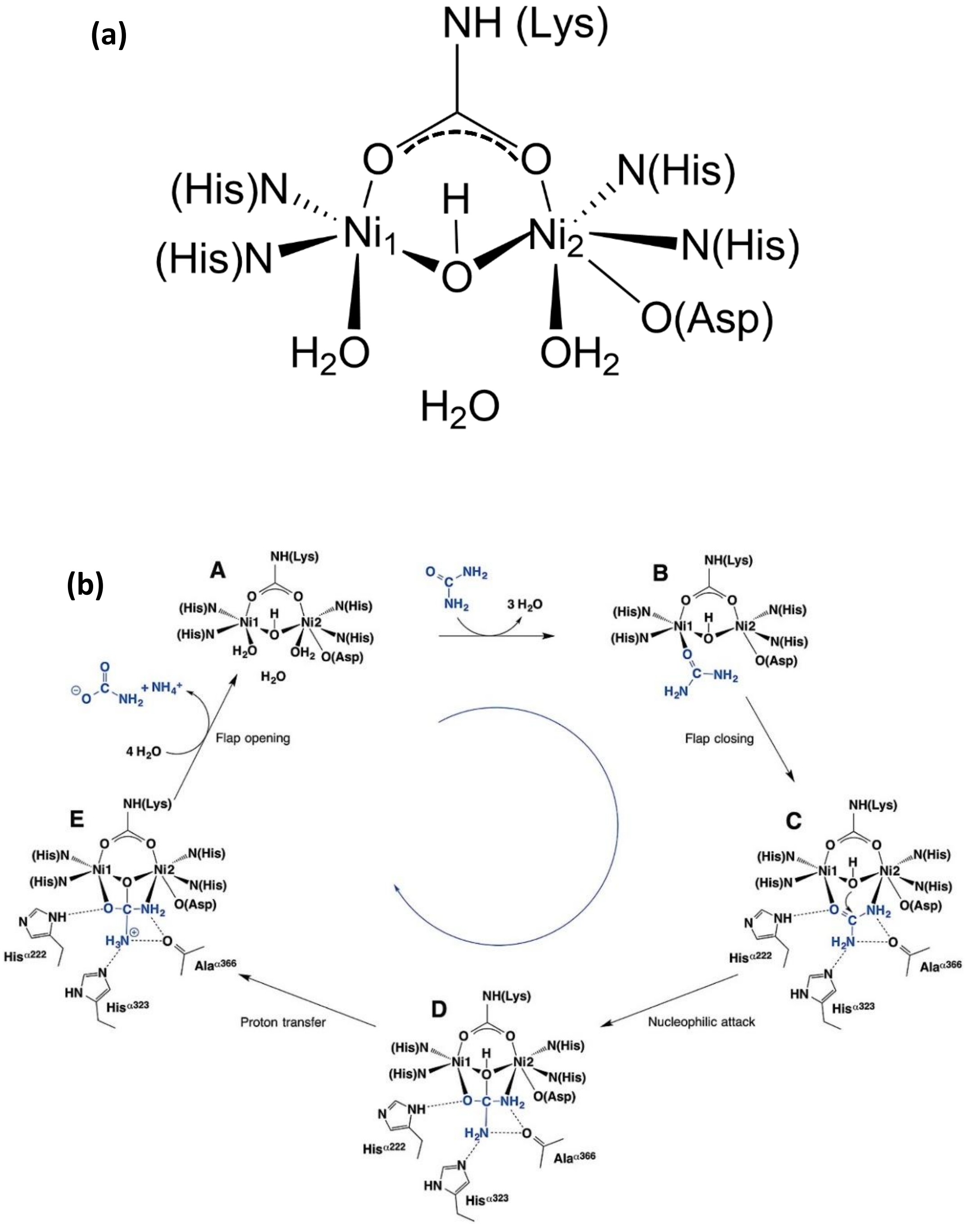

Figure 2.1.6: (a) Structure of the active site of urease enzyme**, (b)** Mechanism of urea hydrolysis on urease enzyme. Reproduced with permission from references (14,15)

Inspired by the urease enzyme, in 2009, Botte et al. [16] reported for the first time the electrooxidation of urea in the alkaline medium by $Ni(OH)_2$. The experiment was performed in a solution containing 1 M KOH and 0.33 M urea. The concentration of urea taken is equivalent to the concentration of urea in human urine. It was observed that during the electrooxidation, $Ni(OH)_2$ gets oxidized to Ni(OOH), which acts as the active site for the oxidation of urea to N_2, CO_2, and H_2.

At anode:

Reaction 1: Oxidation of $Ni(OH)_2$

$Ni(OH)_2\ (s) + OH^- \rightarrow NiOOH\ (s) + H_2O\ (l) + e^-$ $E^o = 0.49\ V_{SHE}$

Reaction 2: Oxidation of Urea

$CO(NH_2)_2\ (aq) + 6OH^- \rightarrow N_2\ (g) + 5H_2O\ (l) + CO_2\ (g) + 6e^-$ $E^o = -0.46V_{SHE}$

At Cathode: Hydrogen Evolution Reaction

$6H_2O\ (l) + 6e^- \rightarrow 3H_2\ (g) + 6OH^-$ $E^o = -0.83\ V_{SHE}$

Overall : $CO(NH_2)_2 + H_2O(l) \rightarrow N_2\ (g) + 3H_2\ (g) + CO_2\ (g)$ $E^o = -0.37\ V$

At the anode, two reactions take place. First is the generation of the active site by the oxidation of $Ni(OH)_2$ to NiOOH, followed by the oxidation of urea. At the cathode, the reduction of water takes place. In comparison, the potential required for urea assisted water electrolysis is 860 mV less than that required for conventional water electrolysis. Thus, making the process energy efficient.

Botte et al. [17,18] suggested two possible pathways for urea electrooxidation on Ni(OOH), namely the direct and indirect urea electrooxidation.

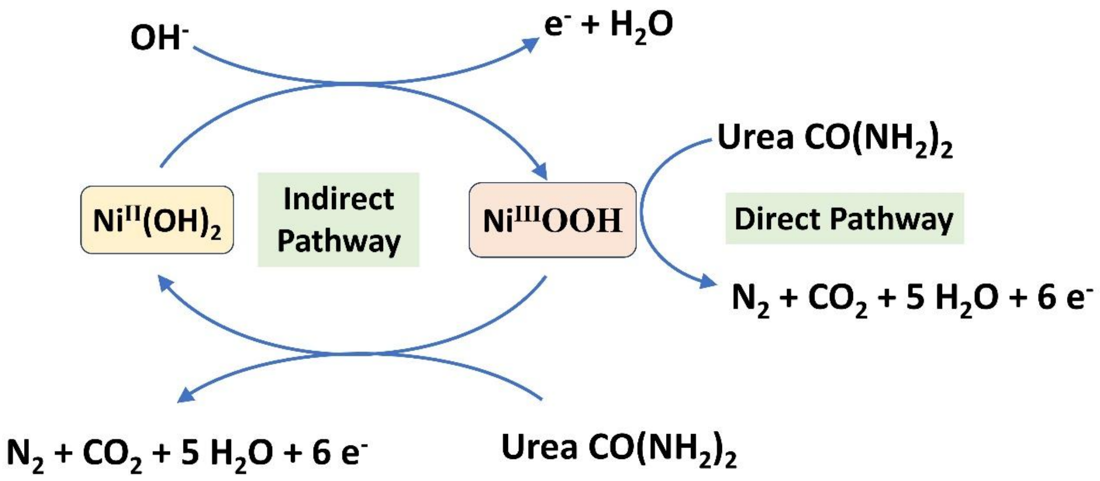

Figure 2.1.7: Indirect pathway and direct pathway for electrooxidation

Indirect urea electrooxidation mechanism: this mechanism is also termed as electrochemical-chemical (E-C) oxidation mechanism *(Figure 2.1.7)*. It consists of two steps. In the first step, electrochemical oxidation of $Ni(OH)_2$ to NiOOH occurs. This is followed by the OH^- assisted chemical oxidation of urea to N_2, CO_2, and H_2O on the NiOOH, with the simultaneous reduction of Ni(OOH) to $Ni(OH)_2$.

Electrochemical : $Ni(OH)_2\ (s) + OH^- \leftrightarrow NiOOH\ (s) + H_2O\ (l) + e^-$

Chemical : $CO(NH_2)_2\ (aq) + 6OH^- \rightarrow N_2\ (g) + 5H_2O\ (l) + CO_2\ (g) + 6e^-$

EC Pathway:

$$CO(NH_2)_2 + H_2O(l) + NiOOH\ (s) \rightarrow N_2\ (g) + 3H_2\ (g) + CO_2\ (g) + Ni(OH)_2\ (s)$$

Direct Urea electrooxidation Mechanism: In this mechanism, NiOOH is formed by the electrochemical oxidation of $Ni(OH)_2$. It is followed by the electrooxidation of urea to N_2, CO_2, and H_2O over the formed NiOOH *(Figure 2.1.7)*. Unlike the EC mechanism, NiOOH sites are retained following the urea oxidation.

$$Ni(OH)_2\ (s) + OH^- \leftrightarrow NiOOH\ (s) + H_2O\ (l) + e^-$$

$$CO(NH_2)_2\ (aq) + 6OH^- \rightarrow N_2\ (g) + 5H_2O\ (l) + CO_2\ (g) + 6e^-$$

Once the urea is adsorbed on NiOOH, its dissociation is facilitated by the hydroxide ions present in the medium. DFT analysis by Botte et al. revealed that the urea dissociation pathway on NiOOH leads to the formation of N_2 and CO_2, as shown in *Table 2.1.1*.[18] The authors proposed that the first step involves the adsorption of urea on NiOOH. The hydroxide ion present in the medium then attacks the adsorbed urea molecule and extracts the proton from the amine groups of the urea molecule.

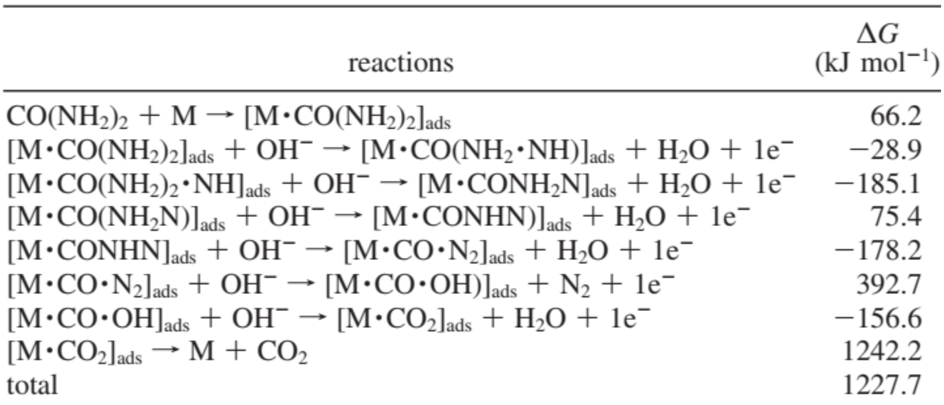

reactions	ΔG (kJ mol^{-1})
$CO(NH_2)_2 + M \rightarrow [M\cdot CO(NH_2)_2]_{ads}$	66.2
$[M\cdot CO(NH_2)_2]_{ads} + OH^- \rightarrow [M\cdot CO(NH_2\cdot NH)]_{ads} + H_2O + 1e^-$	−28.9
$[M\cdot CO(NH_2)_2\cdot NH]_{ads} + OH^- \rightarrow [M\cdot CONH_2N]_{ads} + H_2O + 1e^-$	−185.1
$[M\cdot CO(NH_2N)]_{ads} + OH^- \rightarrow [M\cdot CONHN)]_{ads} + H_2O + 1e^-$	75.4
$[M\cdot CONHN]_{ads} + OH^- \rightarrow [M\cdot CO\cdot N_2]_{ads} + H_2O + 1e^-$	−178.2
$[M\cdot CO\cdot N_2]_{ads} + OH^- \rightarrow [M\cdot CO\cdot OH)]_{ads} + N_2 + 1e^-$	392.7
$[M\cdot CO\cdot OH]_{ads} + OH^- \rightarrow [M\cdot CO_2]_{ads} + H_2O + 1e^-$	−156.6
$[M\cdot CO_2]_{ads} \rightarrow M + CO_2$	1242.2
total	1227.7

Table 2.1.1: Sum of free energies for all intermediates on NiOOH. Reproduced with permission from reference (18)

The N-moieties present on the surface then react to form N_2 (N-N coupling) and *CO. Subsequently, the N_2 formed is released, and the CO is oxidized to CO_2, which is desorbed from the catalyst surface. The calculations show that the rate determining step is the desorption of CO_2 from the surface attributed to the large positive Gibbs free energy value of 1227.7 kJ mol^{-1}. This makes the desorption non-spontaneous.

2.1.4.1. Formation of byproducts

Formation of Nitrates

As proposed by Yang's group[19] and Klinkova's group[20], there is a possibility of the overoxidation of the N-moieties to form NO_x^- species. During the electrooxidation, if the C-N cleavage is simultaneously followed by N-N coupling, it results in the formation of N_2 and CO_2 as the product.

However, if during the C-N cleavage, OH^- attacks the carbon center of the urea molecule, *$NHCO(NH_2)OH$ is formed. The adsorbed urea molecule is cleaved to form *NH_2 and *COONH intermediate. The adsorbed NH_2 then undergoes intermolecular N-N coupling by reaction with the surrounding urea molecule to form N_2 and N_2O. It can also react with the OH^- in the medium to form *NO_2^- which further gets oxidized to NO_3^- or gets reduced to N_2O by selective catalytic reduction, as shown in *Figure 2.1.8*. The overall reaction is as follows:

$$CO(NH_2)_2\ (aq) + 16OH^- \rightarrow 2NO_2^-\ (g) + 10H_2O\ (l) + CO_3^{2-}\ (g) + 12e^-$$

The nitrates thus formed are not environment friendly. Thus, a catalyst needs to be designed to inhibit the formation of these species.

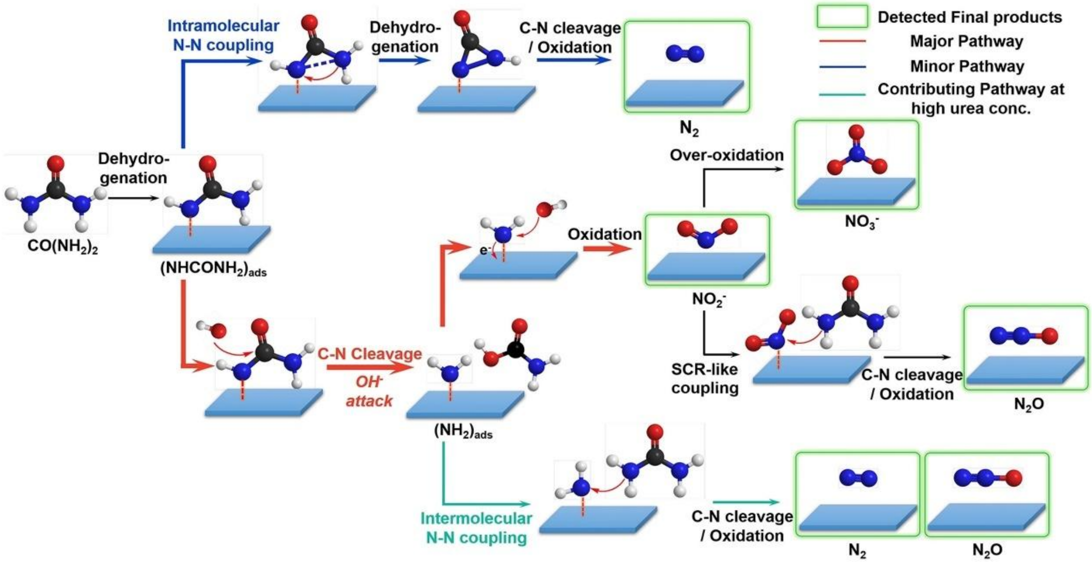

Figure 2.1.8: Pathway for overoxidation of urea to form NO_x^-. Reproduced with permission from reference (19)

Formation of Cyanates

During the urea electrooxidation, cyanate species can be formed as a byproduct. There are two possible pathways for the formation of cyanate. The first pathway involves the intermolecular interaction of the urea molecule to form N_2, which leads to isocyanic acid being the byproduct *(Figure 2.1.9)*. This gets deprotonated to form cyanate in the alkaline medium. [21]

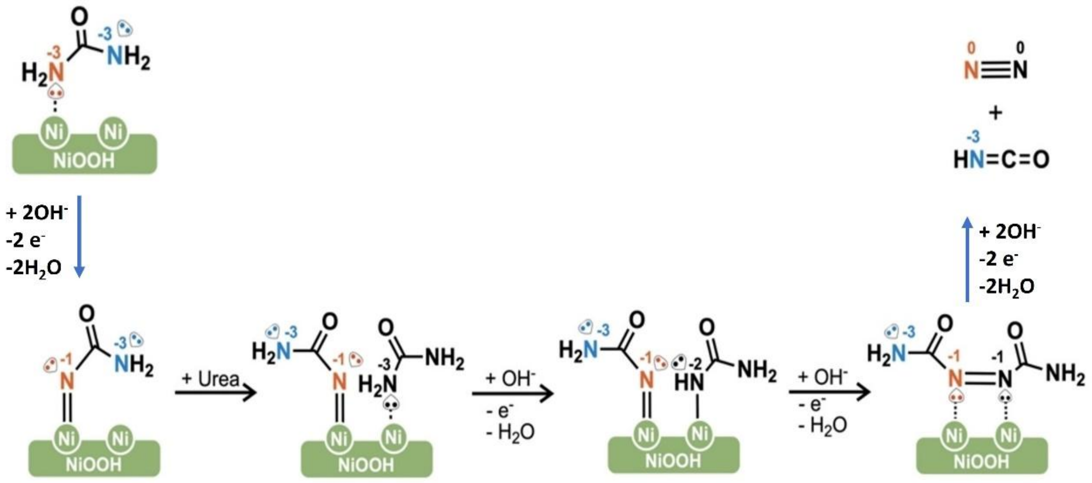

Figure 2.1.9: Formation of cyanate by the intermolecular interaction of urea. Reproduced with permission from reference (21)

In the second pathway, isocyanic acid is formed by the deprotonation of the unoxidized NH_2 group of the urea molecule by the OH^- in the medium, while the partially oxidized N species are left on the surface of NiOOH. The isocyanic acid undergoes deprotonation to form cyanate *(Figure 2.1.10)*. The partially oxidized nitrogen can undergo further oxidation to form NO_x^- species. However, the kinetics for this oxidation is slower in comparison to the oxidation to N_2.[21]

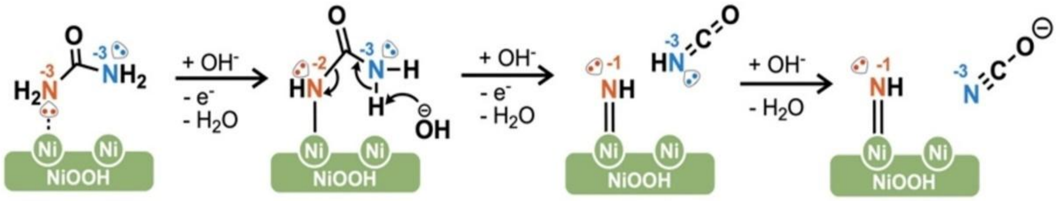

Figure 2.1.10: Formation of cyanate by deprotonation of the unoxidized NH_2 group by OH^- . Reproduced with permission from reference (21)

2.1.5. Operando spectroscopy for mechanistic investigation

The dynamic nature of the electrochemical urea oxidation can be tracked by operando Raman spectroscopy, operando Infrared spectroscopy, and Potentiostatic electrochemical impedance spectroscopy.

2.1.5.1 Raman Spectroscopy

In situ Raman spectroscopy can be used to identify the evolution of the active site during the reaction. As reported by Botte et al. [22], operando Raman spectroscopy was used to identify the reaction mechanism for the electrooxidation of urea in the alkaline medium on $Ni(OH)_2$ catalyst. Initially, the broad hump observed between 200-600cm^{-1} was assigned to $Ni(OH)_2$. Upon applying the oxidation potential, the $Ni(OH)_2$ gets converted to NiOOH *(Figure 2.1.11a)*. This is evident from the evolution of two strong peaks at 479 cm^{-1} and 559 cm^{-1}, corresponding to the Eg bending and A1g stretching vibrations of the Ni-O bond in Ni-OOH, respectively. In the absence of urea, the intensity of this peak remains constant from 1.2V to 1.5V vs RHE. When urea is present along with KOH, these peaks shift to 476 and 558 cm^{-1}, respectively *(Figure 2.1.11b)*. Moreover, the intensity of this peak diminishes and eventually disappears. The peak corresponding to the C-N stretch of urea is also observed at 1003 cm^{-1}. The intensity of this peak is also found to decrease as the applied potential increases. Furthermore, a peak at 1062 cm^{-1} was assigned to the symmetric stretch of CO_3^{2-} formed by the reaction of evolved CO_2 with hydroxide in the medium.

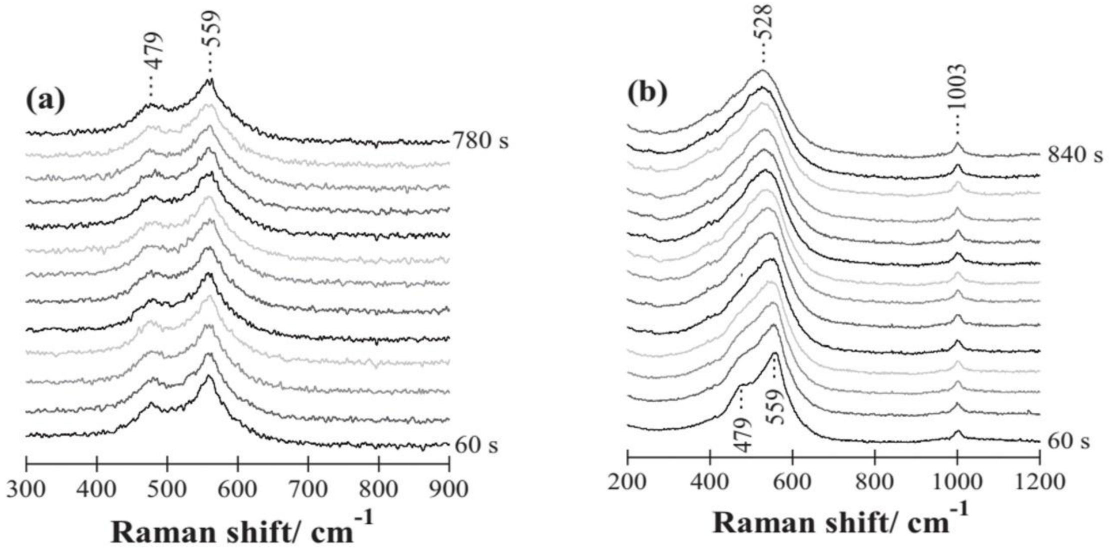

Figure 2.1.11: Urea electrooxidation of $Ni(OH)_2$ as monitored by Raman spectroscopy (a) in the absence of urea and (b) in the presence of urea. Reproduced with permission from reference (22)

Likewise, operando Raman spectroscopy was used to study the urea electrooxidation in the bimetallic system, such as NiCo hydroxides [23] and Mo doped NiS.[24] In case of NiCo hydroxide[23], it was observed that in addition to the oxidation of $Ni(OH)_2$ to NiOOH, $Co(OH)_2$ was also converted to CoOOH and CoO_2. This change in the oxidation state of Co was identified by the appearance of the additional broad peak centered at 573 cm^{-1} corresponding to CoOOH and CoO_2. The as formed active site consisting of Ni^{III}-Co^{III}-Co^{IV} has a higher electrooxidation ability to split urea.

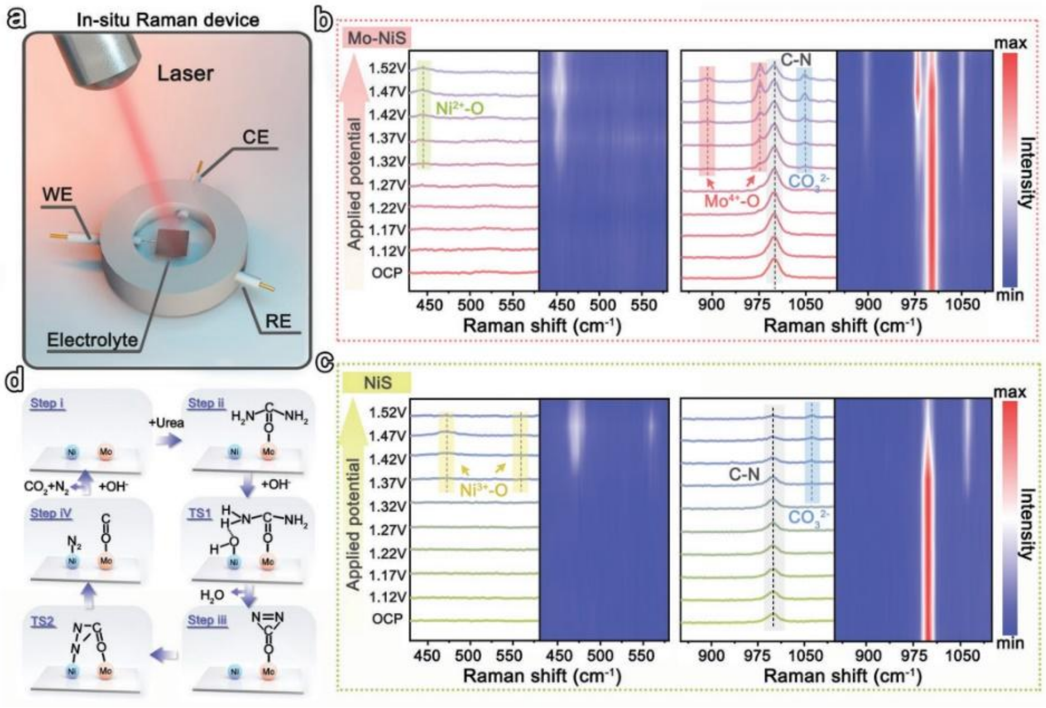

Figure 2.1.12: Urea electrooxidation on Mo doped NiS. Reproduced with permission from reference (24)

In another example, Mo^{4+} was the active site for UOR in Mo doped NiS[24], as shown in *Figure 2.1.12*. Herein, the interaction of urea with Mo was identified by the appearance of peaks at 896 cm^{-1} and 976 cm^{-1}, which corresponds to Mo^{4+}-O bond between the Mo site and the O atom of the adsorbed urea.

2.1.5.2 Infrared Spectroscopy

Operando IR spectroscopy can be used to identify the characteristic intermediates formed on the catalyst surface during the urea electrooxidation reaction[25]. Two characteristic peaks are generally studied to identify the reaction pathway: A peak at ~2169 cm^{-1} characteristic of CNO^- intermediate and a peak at ~1381 cm^{-1} corresponding to the formation of CO_3^{2-}. The appearance of the peak corresponding to CNO^- indicates the incomplete oxidation of the urea molecule. While the appearance of the peak corresponding to CO_3^{2-} indicates complete oxidation of the urea molecule. The intensity of the cyanate and the carbonate bands is used as an indicator of the oxidation of urea. An increase in the intensity of the cyanate IR band indicates that an incomplete oxidation pathway is preferred. An increase in the intensity of the carbonate band with a minimal change in the intensity of the cyanate band indicates that the complete oxidation of urea is preferred. Apart from this, IR peaks with negative absorbance are also observed at 3300 cm^{-1}, which is attributed to the consumption of hydroxide present in the medium. Similarly, the peaks at 1669 cm^{-1}, 1610 cm^{-1}, and 1470 cm^{-1} are characteristic of the C=O, N-H, and C-N bonds of urea, respectively *(Figure 2.1.13)*. The negative absorbance is attributed to the consumption of urea in the medium.

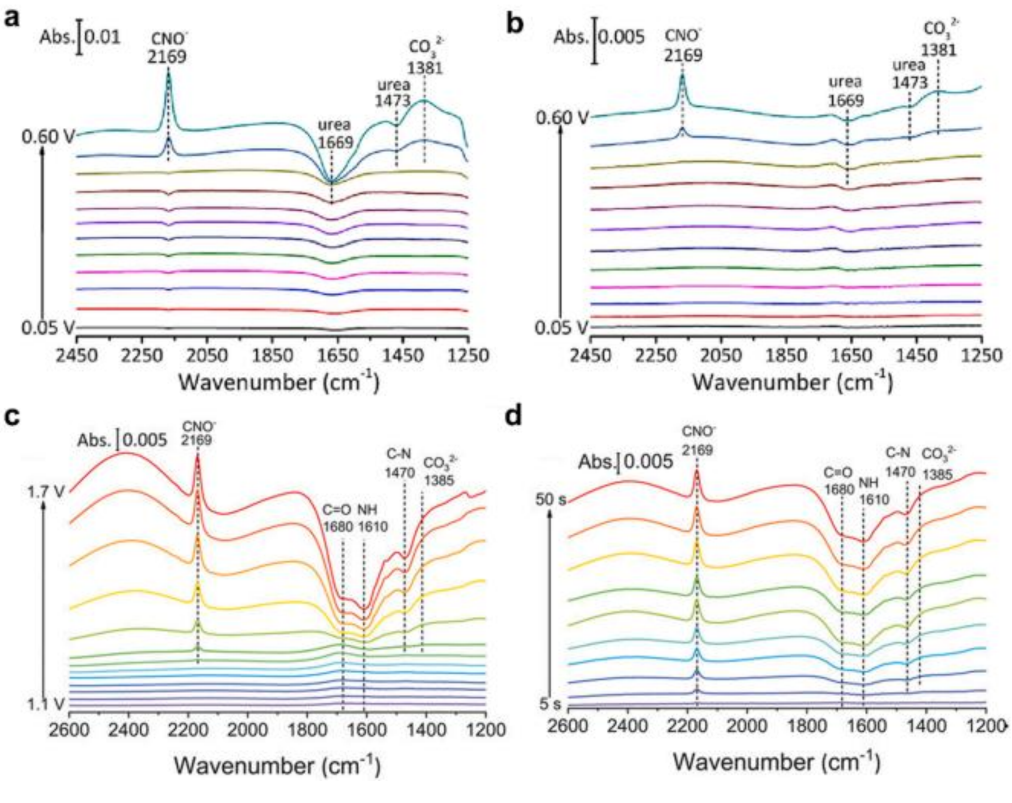

Figure 2.1.13: The operando FTIR spectra of urea electrooxidation on **(a), (b)** $NiWO_4$ (Reproduced with permission from references (25, 26)) and **(c), (d)** $FeCo_{0.85}$ Se/FeCo LDH. Reproduced with permission from references (25, 27)

For instance, operando studies on amorphous and crystalline $NiWO_4$[26] predicted two pathways. The FTIR spectra show the presence of CNO^- and CO_3^{2-} in both amorphous and crystalline $NiWO_4$ *(Figure 2.1.13 a, b)*. However, in amorphous $NiWO_4$, the area of the peak corresponding to CO_3^{2-} was much higher than the peak corresponding to CNO^-, implying the preference for a complete oxidation pathway. In contrast, the partial oxidation of urea was favored over crystalline $NiWO_4$. Likewise, in the case of $FeCo_{0.85}$ Se/FeCo LDH[27], the formation of NCO^- intermediate was observed *(Figure 2.1.13 c, d)*. It was observed that the intensity of the peak at 2169 cm^{-1} increases significantly with time. However, the vibrational band corresponding to the CO_3^{2-} was weak. This implies that urea undergoes incomplete oxidation over the catalyst.

2.1.5.3 Electrochemical Impedance spectroscopy

This technique is used to determine the urea electrooxidation pathway and the charge transfer resistance associated with it. Two types of plots, namely the Nyquist plot and the Bode plot can be obtained from potentiostatic impedance spectroscopy.

A Bode plot is a plot of log (-frequency) vs -phase angle. From the Bode plot[28–30], the urea electrooxidation pathway followed by the catalyst can be determined. If the urea electrooxidation occurs by the direct pathway, only one peak in the low frequency region is observed. However, if the urea electrooxidation follows both the direct and indirect pathway, two peaks are observed. The peak in the low frequency region corresponds to the direct pathway, while the peak in the high frequency region corresponds to the indirect pathway (*Figure 2.1.14 b, d*).

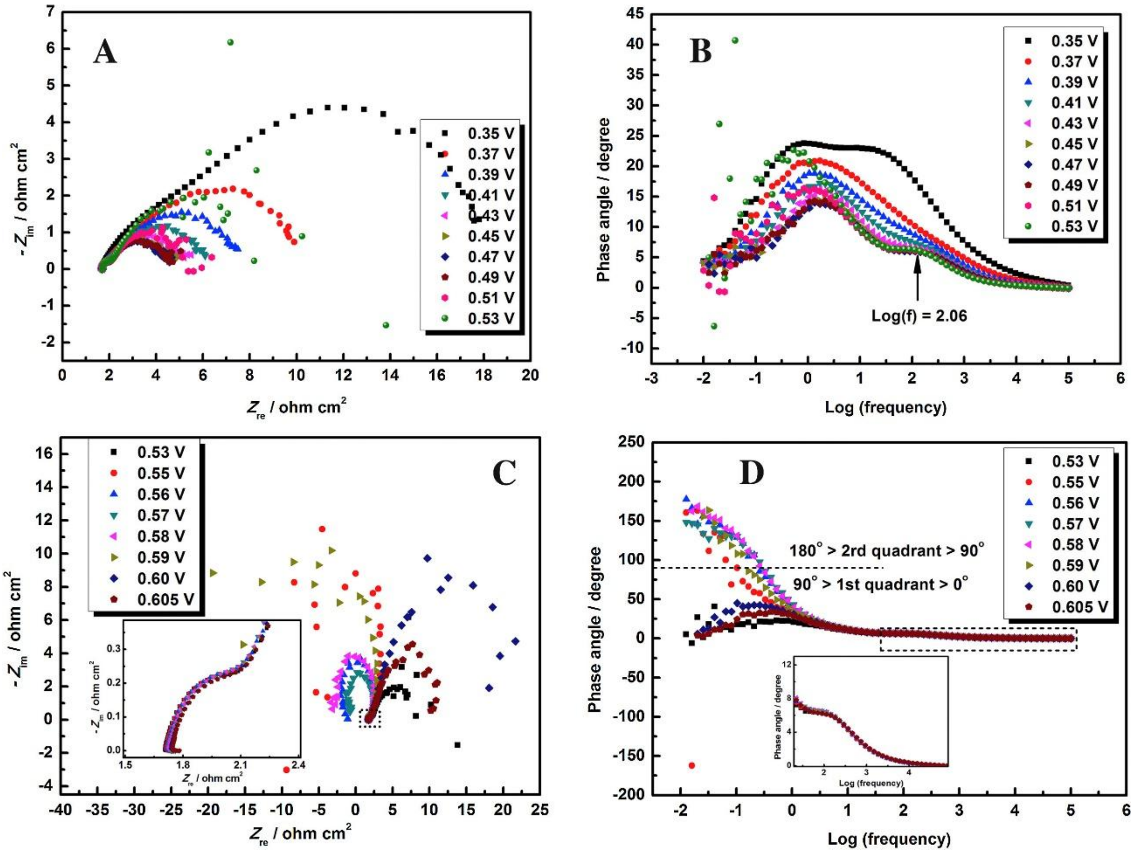

Figure 2.1.14: (a), (c) Nyquist plot and **(b), (d)** corresponding Bode plot for urea electrooxidation on the Ni catalyst. Reproduced with permission from reference (28)

The charge transfer resistance associated with each pathway is determined from the Nyquist plot. The Nyquist plot is a plot of -Im (Z) vs Re(Z). For the urea electrooxidation proceeding by a combination of direct and indirect pathways, two semicircles are observed. The first semicircle corresponds to the charge transfer resistance for the electrochemical oxidation of $Ni(OH)_2$ to NiOOH in the indirect pathway, while the second semicircle corresponds to the charge transfer resistance for the electrooxidation of urea over NiOOH in the direct pathway. Nyquist plot can also be used to determine the rate determining step. The occurrence of the negative real impedance (*Figure 2.1.14 c*) indicates that the desorption of CO_x species is the rate determining step. On the contrary, the occurrence of positive impedance (*Figure 2.1.14 a, c*) implies that the formation of CO_x is the rate-determining step[28,30].

2.1.6 Electrochemical parameters to evaluate the catalytic activity

Overpotential: It is a measure of the potential required over the thermodynamic potential to drive the electrolytic process. The sluggish kinetics of the 6 e^- transfer results in the requirement of higher potentials. Hence, for UOR, one of the main aims is to reduce the overpotential. The overpotential is determined by the following formula:

$$\eta = E_{RHE} - 0.37\text{V}$$

Current Density: It represents the rate of the reaction for any electrochemical reaction. A suitable catalyst should be able to achieve higher current densities at lower potentials, thus making the process energy efficient.

Stability: It is measured generally by chronoamperometry or chronopotentiometry, where a constant potential or constant current is applied, respectively. Corresponding current density/potential response is recorded. A stable catalyst shows minimal change in the current density/potential. This parameter measures how long the catalyst can retain its activity without any degradation.

Tafel slope: The Tafel equation is derived from the Butler Volmer equation, and it connects the rate of the reaction with the overpotential[31]. It measures how fast the overpotential changes as the current density increases by a factor of ten. The Tafel relation holds only in the absence of mass transfer limitations. It shows a linear behaviour when the electrode kinetics are sluggish resulting in significant activation polarisation.

For a reaction, O + e^-↔ R, the Tafel equation for the forward reaction (cathodic process) is given by

$$\eta = -\frac{2.303RT}{\alpha F}\log i + \frac{2.303RT}{\alpha F}\log i_o$$

While the Tafel equation for the backward reaction (anodic process) is given by

$$\eta = \frac{2.303RT}{(1-\alpha)F}\log i - \frac{2.303RT}{(1-\alpha)F}\log i_o$$

Here, η stands for overpotential, i stands for current density, i_o stands for exchange current density, α stands for transfer coefficient, F stands for Faraday constant, R stands for universal gas constant and T stands for temperature. The Tafel plot is a plot of log *i* vs η as shown in *Figure 2.1.15.* At high overpotentials, the plot shows a linear behaviour. However, as the η approaches zero, the plot deviates from linearity as the backward reaction is no longer negligible.

The slope of the linear region, also called the Tafel slope, can be used to determine the transfer coefficient (α). It is a measure of the fraction of the applied energy that is required to drive the redox reaction. The Tafel slope is inversely proportional to the value of the transfer coefficient. Hence, lower the Tafel slope value, the higher the value of the transfer coefficient indicating faster reaction kinetics.

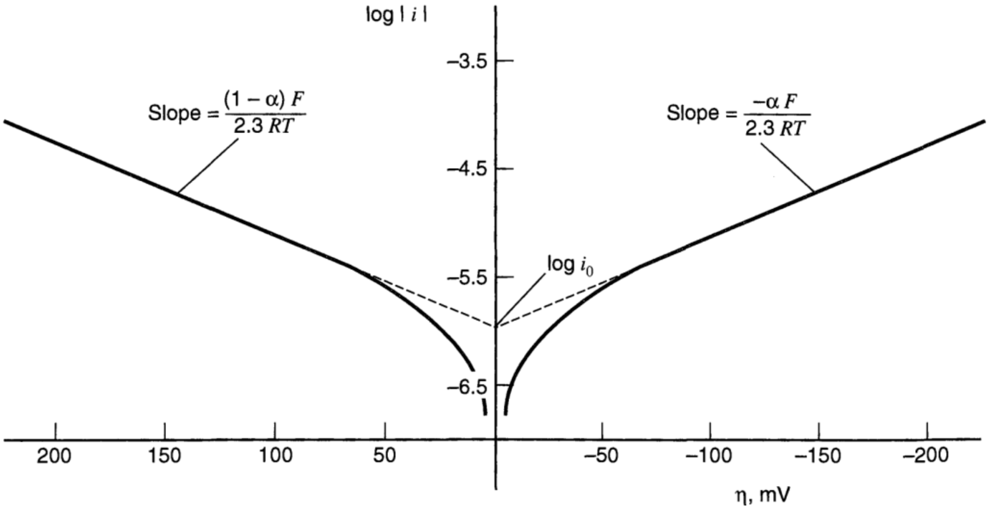

Figure 2.1.15: Tafel plots for anodic and cathodic reactions for the reaction O + e^-↔ R with $\alpha = 0.5$ at T = 298 K and $j_o = 10^{-6}$ A/cm^2. Reproduced with permission from reference (31)

From, the intercept of the Tafel plot, the value of the exchange current density (i_o) can be determined. The exchange current density indicates the current flowing in both the anodic and cathodic directions at equilibrium. The higher the value of i_o the faster is the exchange of the ions and charge across the electrode/electrolyte interface.

Electrochemically active surface area (ECSA): It is a measure of the effective area of the electrode, which is responsible for the electrochemical reaction. The higher the ECSA, the higher the number of the catalytically active site.

2.1.7 Strategies for designing UOR electrocatalysts

The major challenges that need to be addressed while designing a catalyst for urea electrooxidation are:

1. Rapid formation of active NiOOH species, thereby improving the kinetics of the reaction

2. Inhibiting the poisoning of the active site by the adsorption of CO_x species on the catalyst surface

3. Regulating the adsorption and activation of the urea molecule to reduce the overpotential

Ni in the form of oxides, hydroxides, and metallic Ni has proven to be an active catalyst for UOR. However, it lacks long term stability owing to the poisoning of the active site and high overpotential for the electrochemical oxidation of $Ni(OH)_2$ to NiOOH. To address these challenges, $Ni(OH)_2$ is modified by introducing other transition metals or non-metals such as Mo[32,33], Mn[34], Co[35], S[36], B[37], F[38], etc. This provides an additional site for urea adsorption, prevents the poisoning of the active site, and enhances the urea electrooxidation kinetics by introducing defects or the creation of efficient heterojunctions.

2.1.7.1. Creation of an additional adsorption site

Xiao et al. synthesized $MnO_2/MnCo_2O_4/Ni$ heterostructures[34], wherein $MnCo_2O_4$ forms the core, and MnO_2 forms the shell. The presence of Co^{2+}/Co^{3+} and $Mn^{2+}/Mn^{3+}/Mn^{4+}$ provides a surface rich in electroactive species. Further, the synergistic interaction betweenMnCo₂O₄ core and MnO_2 shell results in optimum adsorption of the urea molecule. In another report by Song et al., Mn was found to be the active site in $NiS_2@MnO_x$[39]. It was observed that urea gets adsorbed onto the Mn^{4+} site, reducing it to Mn^{2+}. The Ni site adjacent to the Mn site is converted to Ni^{3+} and promotes N-N coupling *(Figure 2.1.16 a, b)*.

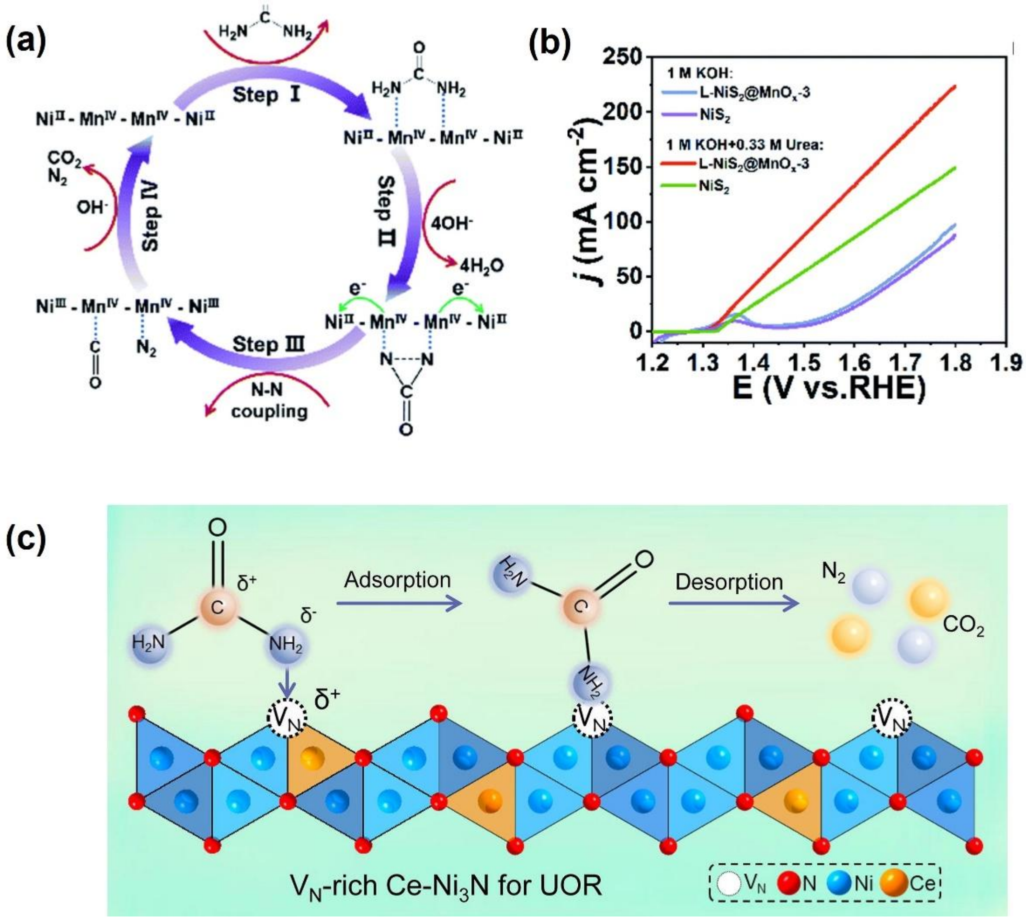

Figure 2.1.16 : (a), (b) Urea electrooxidation on NiS_2@MnO_2. Reproduced with permission from reference (39) and **(c)** Urea electrooxidation of N vacancy-rich Ce doped Ni_3N. Reproduced with permission from reference (40)

In another example, Ce doped Ni_3N^{40} is a potential catalyst for urea electrooxidation. Here, the high electronegativity of Ni pulls the electrons towards itself, resulting in a higher oxidation state for Ce. The electron withdrawing C=O group of the urea molecule is attracted to the Ni site, while the electron donating NH_2 group is attracted towards the Ce, promoting urea oxidation. The introduction of Ce also helps in the formation of N vacancies which is responsible for the enhancement in the kinetics of the reaction *(Figure 2.1.16 c)*. Co and V co-doped NiS_2^{35} is a potential catalyst for UOR. The synergistic interaction between Ni, Co, V, and S proves to be efficient for the electrooxidation activity. The V element helps to improve the activity of Ni and Co elements and enhance the electron transfer ability between Ni and S. The Ni-Co sites synergistically catalyzed the urea electrooxidation. Herein, Co with high oxygen affinity stabilized the carbonyl group while the highly active Ni interacts with the N functional group of urea. The introduction of V reduced the electron density of Co and Ni and thereby reduced the energy barriers of N-H bond breakage.

2.1.7.2.Formation of active sites

The higher oxidation state of Mo[32,41], W[33], and Ce[42] also plays a critical role in enhancing the UOR activity. For instance, in the case of NiMoO[32], the presence of Mo as Mo^{6+} helps in oxidizing Ni^{2+} to Ni^{3+}, thereby creating more active sites. Likewise, nickel molybdate hydrate nanorods ($NiMoO_4. xH_2O$)[41] act as a precatalyst. Herein, the nickel molybdate hydrate nanorods undergo exfoliation to form nanosheets of amorphous nickel hydroxide. This lowers the potential for the oxidation of $Ni(OH)_2$ to NiOOH. The resultant catalyst also exhibits higher current density and a higher turnover frequency in comparison to $Ni(OH)_2$. In the case of W doped NiS_2 /MoO_2[33], the electron transfer takes place across the heterogeneous interface from NiS_2 to more electronegative MoO_2. Doping with W helps improve the catalytic activity by tuning the d-band center, resulting in the enhancement of the activity by increasing the number of exposed active sites. Ce doped α-$Ni(OH)_2$[42] exhibits excellent catalytic activity towards UOR. Herein, the Ce is present in a mixed oxidation state consisting of Ce^{3+} and Ce^{4+}. The strong interaction between Ce and Ni results in a positive shift in the binding energy of Ni. This interaction helps in creating a greater number of high valence catalytically active sites responsible for UOR.

Nickel borides (NiB_x) is another class of compound that has proven to be efficient for this reaction [37]. In this catalyst, metaborates, i.e., BO_2^- are formed, which promotes the formation of NiOOH. Moreover, the presence of these borates provides an optimum adsorption strength for urea, thereby ensuring high electrooxidation activity. Nickel sulfides have been extensively studied for the electrooxidation reactions. Ni_xS_y are non-layered sulfides[43], and their conducting nature depends on their composition. For instance, NiS_2 is insulating while Ni_3S_2 shows a metallic behavior. In these systems, the metal atoms are the actual active site, while S plays a crucial role in determining the catalytic activity. The delocalized electron on the S atom promotes the -OOH intermediate formation on the metal surface. In a recent report, X. Zhuo et al. have shown the activity of Ni_3S_2/Ni heterostructure nanobelt arrays[44] as bifunctional catalysts for urea assisted water electrolysis. The strong interaction between Ni_3S_2 and Ni results in the formation of electron poor Ni species. This accelerates the formation of NiOOH required for urea oxidation. Transition metal selenides[45] are another class of compounds that have properties similar to sulfides. The increased metallic character of selenides is due to the efficient bonding of the 3d orbitals of Se with the metals 3s and 3p orbitals, which result in higher conductivity and lower band gaps. This is responsible for the enhanced catalytic activity of these compounds. For instance, Ni_3Se_4[46] nanorod arrays have proven to be efficient for UOR, wherein the formation of the Ni-Se bond improves the intrinsic activity of the catalyst.

Transition metal nitrides are interstitial alloys where the N atoms are present at the interstitial sites. The presence of these nitrogen atoms helps in improving the conductivity and chemical stability of the catalyst [47,48]. Ni_3N has been studied for the urea electrooxidation activity wherein the presence of the more electronegative N atom enables the formation of high valence Ni sites responsible for the catalytic activity [49].

2.1.7.3.Creation of heterojunctions

Fe-$Co_{0.85}$Se/FeCo LDH nanosheet array has proven to be an efficient UOR catalyst. Herein, the electron transfer occurs from the FeCoLDH side to the Fe-$Co_{0.85}$ Se region, resulting in strong electronic interaction between the two phases. This, in turn, provides optimum adsorption of the intermediates, resulting in enhanced UOR activity[27]. Likewise, in NiF_3/Ni_2P heterojunction, the electron flows from the electron rich NiF_3 site to the electron deficient Ni_2P site. The carbonyl group binds on the NiF_3 site, while the amino group is bound to the Ni_2P site, thereby promoting the decomposition of the urea molecule. [38]

Mott Schottky heterojunctions are formed when a metal comes in contact with the semiconductor. As a result, the semiconductor band bends to match the work function of the metal (i.e., the minimum energy required to extract the electron from the electronic ground state of the metal). This results in the flow of the electron across the heterointerface *(Figure 2.1.17 a, b)*. The creation of such heterojunctions enhances the catalytic performance of the material by creating more active sites, efficient charge transfer, and optimum adsorption of the intermediates.[50,51]

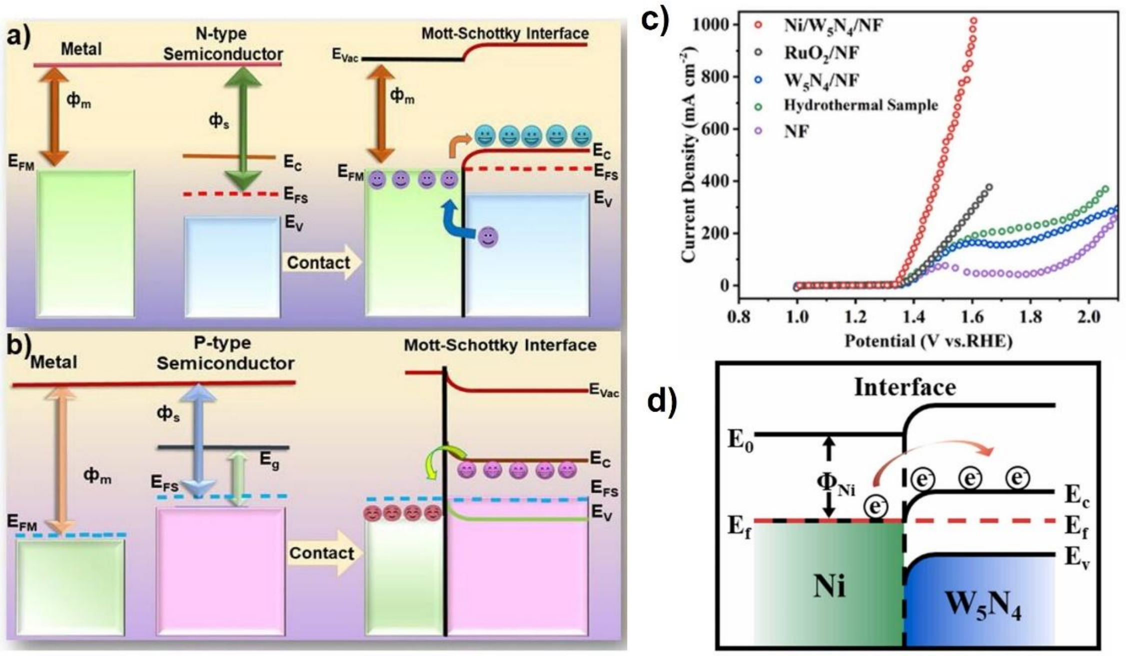

Figure 2.1.17: (a), (b) Schematic of a Mott Schottky heterojunction. Reproduced with permission from reference (51), **(c)** Urea electrooxidation on Mott Schottky catalyst Ni/W_5N_4 supported on Ni foam and **(d)** Ni/W_5N_4 heterojunction. Reproduced with permission from reference (52).

For instance, Ni/W_5N_4 supported on Ni foam[52] is an efficient Mott- Schottky heterojunction. Herein, the electron transfer occurs from metallic Ni to the W_5N_4 phase *(Figure 2.1.17 c, d)*. The surface of the catalyst undergoes reconstruction to form nickel tungsten hydroxide, which is the catalytically active phase and results in enhanced UOR activity. In NiS/Ni_3S_2[36], the electron moves from the Ni_3S_2 to NiS, resulting in charge redistribution at the interface, creating an electric field beneficial for electron transfer. This favors the formation of NiOOH sites at lower potential and provides optimal adsorption for the urea molecule. In the case of CoS_2- MoS_2 Schottky catalyst[53], the electron transfer between CoS_2 and MoS_2 results in the electrophilic CoS_2 surface and nucleophilic MoS_2 surface. During urea electrooxidation, the carbonyl group of the urea is adsorbed on the MoS_2 side while the amino group is absorbed on the CoS_2 site. This facilitates the C-N bond cleavage and promotes the decomposition of urea.

2.1.8 Conclusion

This chapter explores the critical role of hydrogen in shaping a sustainable energy future, highlighting its sources, applications, and the growing importance of the hydrogen economy. A key focus is on electrochemical water splitting, a promising and energy-efficient approach to hydrogen production. However, the main bottleneck in this process is the sluggish kinetics associated with the oxygen evolution reaction, which limits its commercial viability. Replacing OER with the electrooxidation of readily oxidizable molecules for hybrid water electrolysis is a promising strategy. In this context, urea electrooxidation emerges as a viable alternative, enabling water electrolysis at a potential of 0.37 V, which is much lower than the potential required for conventional water electrolysis. This chapter discusses the major limitations, and the mechanistic pathways associated with UOR. Furthermore, the different analytical techniques used to study urea electrooxidation have been discussed in detail. Lastly, different strategies to modify the electrocatalyst to enhance the electrochemical activity have been reviewed.

2.1.9 References

(1) World Energy Council. Working_Paper_-_Hydrogen_Demand_And_Cost_Dynamics_-_September_2021. 2021.

(2) *Turning Hydrogen Demand Into Reality: Which Sectors Come First? Chair of the Task Force Renewables of Energy Traders Europe 2 Turning Hydrogen Demand Into Reality: Which Sectors Come First?*; 2024. https://www.ics-shipping.org/wp-content/uploads/2024/07/Turning-Hydrogen-Demand-Into-Reality-Which-Sectors-Come-First.pdf

(3) Hydrogen _ Understand Energy Learning Hub. Stanford Energy. https://understand-energy.stanford.edu/energy-currencies/hydrogen

(4) Renewable Energy Agency, I. *Renewable power generation costs in 2022*; 2023.

(5) Raveendran, A.; Chandran, M.; Dhanusuraman, R. A Comprehensive Review on the Electrochemical Parameters and Recent Material Development of Electrochemical Water Splitting Electrocatalysts. *RSC Adv* 2023, *13* (6), 3843–3876. https://doi.org/10.1039/D2RA07642J.

(6) Anantharaj, S.; Ede, S. R.; Sakthikumar, K.; Karthick, K.; Mishra, S.; Kundu, S. Recent Trends and Perspectives in Electrochemical Water Splitting with an Emphasis on Sulfide, Selenide, and Phosphide Catalysts of Fe, Co, and Ni: A Review. *ACS Catal* 2016, *6* (12), 8069–8097. https://doi.org/10.1021/acscatal.6b02479.

(7) Shang, X.; Tang, J.-H.; Dong, B.; Sun, Y. Recent Advances of Nonprecious and Bifunctional Electrocatalysts for Overall Water Splitting. *Sustain Energy Fuels* 2020, *4* (7), 3211–3228. https://doi.org/10.1039/D0SE00466A.

(8) Sharifian, R.; Wagterveld, R. M.; Digdaya, I. A.; Xiang, C.; Vermaas, D. A. Electrochemical Carbon Dioxide Capture to Close the Carbon Cycle. *Energy Environ Sci* 2021, *14* (2), 781–814. https://doi.org/10.1039/D0EE03382K.

(9) Yao, D.; Zhang, Y.; Zhang, S.; Wan, J.; Yu, H.; Jin, H. Hybrid Water Electrolysis with Integrated and Cascading Reactions Using Two-Dimensional Electrocatalysts. *J Mater Chem A Mater* 2023, *11* (31), 16433–16457. https://doi.org/10.1039/D3TA01931D.

(10) Roh, H.; Oh, S.; Lim, C.; Yong, K. Recent Progress and Challenges in Hybrid Water Electrolysis through Economic Evaluation. *ACS Mater Lett* 2024, *6* (7), 3080–3089. https://doi.org/10.1021/acsmaterialslett.4c00676.

(11) Ren, J.-T.; Chen, L.; Wang, H.-Y.; Tian, W.-W.; Yuan, Z.-Y. Water Electrolysis for Hydrogen Production: From Hybrid Systems to Self-Powered/Catalyzed Devices. *Energy Environ Sci* 2024, *17* (1), 49–113. https://doi.org/10.1039/D3EE02467A.

(12) Estiu, G.; Merz, K. M. Enzymatic Catalysis of Urea Decomposition: Elimination or Hydrolysis? *J Am Chem Soc* 2004, *126* (38), 11832–11842. https://doi.org/10.1021/ja047934y.

(13) Estiu, G.; Merz, K. M. The Hydrolysis of Urea and the Proficiency of Urease. *J Am Chem Soc* 2004, *126* (22), 6932–6944. https://doi.org/10.1021/ja049327g.

(14) Kappaun, K.; Piovesan, A. R.; Carlini, C. R.; Ligabue-Braun, R. Ureases: Historical Aspects, Catalytic, and Non-Catalytic Properties – A Review. *J Adv Res* 2018, *13*, 3–17. https://doi.org/10.1016/j.jare.2018.05.010.

(15) Mazzei, L.; Musiani, F.; Ciurli, S. Urease. In *The Biological Chemistry of Nickel*; Zamble, D., Rowińska-Żyrek, M., Kozlowski, H., Eds.; The Royal Society of Chemistry, 2017; p 0. https://doi.org/10.1039/9781788010580-00060.

(16) Boggs, B. K.; King, R. L.; Botte, G. G. Urea Electrolysis: Direct Hydrogen Production from Urine. *Chemical Communications* 2009, No. 32, 4859–4861. https://doi.org/10.1039/B905974A.

(17) Vedharathinam, V.; Botte, G. G. Understanding the Electro-Catalytic Oxidation Mechanism of Urea on Nickel Electrodes in Alkaline Medium. *Electrochim Acta* 2012, *81*, 292–300. https://doi.org/10.1016/j.electacta.2012.07.007.

(18) Daramola, D. A.; Singh, D.; Botte, G. G. Dissociation Rates of Urea in the Presence of NiOOH Catalyst: A DFT Analysis. *J Phys Chem A* 2010, *114* (43), 11513–11521. https://doi.org/10.1021/jp105159t.

(19) Li, J.; Li, J.; Liu, T.; Chen, L.; Li, Y.; Wang, H.; Chen, X.; Gong, M.; Liu, Z. P.; Yang, X. Deciphering and Suppressing Over-Oxidized Nitrogen in Nickel-Catalyzed Urea Electrolysis. *Angewandte Chemie - International Edition* 2021, *60* (51), 26656–26662. https://doi.org/10.1002/anie.202107886.

(20) Tatarchuk, S. W.; Medvedev, J. J.; Li, F.; Tobolovskaya, Y.; Klinkova, A. Nickel-Catalyzed Urea Electrolysis: From Nitrite and Cyanate as Major Products to Nitrogen Evolution. *Angewandte Chemie International Edition* 2022, *61* (39), e202209839. https://doi.org/10.1002/anie.202209839.

(21) Medvedev, J. J.; Delva, N. H.; Klinkova, A. Mechanistic Analysis of Urea Electrooxidation Pathways: Key to Rational Catalyst Design. *Chempluschem* 2024, *89* (6), e202300739. https://doi.org/10.1002/cplu.202300739.

(22) Vedharathinam, V.; Botte, G. G. Direct Evidence of the Mechanism for the Electro-Oxidation of Urea on Ni(OH)2 Catalyst in Alkaline Medium. *Electrochim Acta* 2013, *108*, 660–665. https://doi.org/10.1016/j.electacta.2013.06.137.

(23) Yang, X.; Zhang, H.; Yu, B.; Liu, Y.; Xu, W.; Wu, Z. An Unveiled Electrocatalysis Essence of NiCo Hydroxides through in Situ Raman Spectroscopy for Urea Oxidation. *Energy Technology* 2022, *10* (5), 2101010. https://doi.org/10.1002/ente.202101010.

(24) Zhou, Y.; Wang, Y.; Kong, D.; Zhao, Q.; Zhao, L.; Zhang, J.; Chen, X.; Li, Y.; Xu, Y.; Meng, C. Revealing the Reactant Mediation Role of Low-Valence Mo for Accelerated Urea-Assisted Water Splitting. *Adv Funct Mater* 2023, *33* (8), 2210656. https://doi.org/10.1002/adfm.202210656.

(25) Ge, J.; Kuang, J.; Xiao, Y.; Guan, M.; Yang, C. Recent Development of Nickel-Based Catalysts and in Situ Characterization Techniques for Mechanism Understanding of the Urea Oxidation Reaction. *Surfaces and Interfaces* 2023, *41*, 103230. https://doi.org/10.1016/j.surfin.2023.103230.

(26) Wang, L.; Zhu, S.; Wang, Y.; Liu, Z.; Liu, Y.; Wang, Q.; Gu, M.; Li, K.; Sun, X.; Yang, L.; Shao, M. Amorphous Nickel Tungstate Nanocatalyst Boosts Urea Electrooxidation. *Chemical Engineering Journal* 2023, *460*, 141826. https://doi.org/10.1016/j.cej.2023.141826.

(27) Yu, H.; Zhu, S.; Hao, Y.; Chang, Y.-M.; Li, L.; Ma, J.; Chen, H.-Y.; Shao, M.; Peng, S. Modulating Local Interfacial Bonding Environment of Heterostructures for Energy-Saving Hydrogen Production at High Current Densities. *Adv Funct Mater* 2023, *33* (12), 2212811. https://doi.org/10.1002/adfm.202212811.

(28) Guo, F.; Ye, K.; Du, M.; Huang, X.; Cheng, K.; Wang, G.; Cao, D. Electrochemical Impedance Analysis of Urea Electro-Oxidation Mechanism on Nickel Catalyst in Alkaline Medium. *Electrochim Acta* 2016, *210*, 474–482. https://doi.org/10.1016/j.electacta.2016.05.149.

(29) Chen, W.; Xu, L.; Zhu, X.; Huang, Y.-C.; Zhou, W.; Wang, D.; Zhou, Y.; Du, S.; Li, Q.; Xie, C.; Tao, L.; Dong, C.-L.; Liu, J.; Wang, Y.; Chen, R.; Su, H.; Chen, C.; Zou, Y.; Li, Y.; Liu, Q.; Wang, S. Unveiling the Electrooxidation of Urea: Intramolecular Coupling of the N−N Bond. *Angewandte Chemie International Edition* 2021, *60* (13), 7297–7307. https://doi.org/10.1002/anie.202015773.

(30) Safeer N. K., M.; Alex, C.; Jana, R.; Datta, A.; John, N. S. Remarkable COx Tolerance of Ni3+ Active Species in a Ni2O3 Catalyst for Sustained Electrochemical Urea Oxidation. *J Mater Chem A Mater* 2022, *10* (8), 4209–4221. https://doi.org/10.1039/D1TA05753G.

(31) Allen J. Bard, L. R. F. Electrochemical Methods: Fundamentals and Applications. 2001.

(32) Yu, Z.-Y.; Lang, C.-C.; Gao, M.-R.; Chen, Y.; Fu, Q.-Q.; Duan, Y.; Yu, S.-H. Ni–Mo–O Nanorod-Derived Composite Catalysts for Efficient Alkaline Water-to-Hydrogen Conversion via Urea Electrolysis. *Energy Environ Sci* 2018, *11* (7), 1890–1897. https://doi.org/10.1039/C8EE00521D.

(33) Ligani Fereja, S.; Li, P.; Zhang, Z.; Guo, J.; Fang, Z.; Li, Z.; He, S.; Chen, W. W-Doping Induced Abundant Active Sites in a 3D NiS2/MoO2 Heterostructure as an Efficient Electrocatalyst for Urea Oxidation and Hydrogen Evolution Reaction.

Chemical Engineering Journal 2022, *432*, 134274. https://doi.org/10.1016/j.cej.2021.134274.

(34) Xiao, C.; Li, S.; Zhang, X.; MacFarlane, D. R. MnO2/MnCo2O4/Ni Heterostructure with Quadruple Hierarchy: A Bifunctional Electrode Architecture for Overall Urea Oxidation. *J Mater Chem A Mater* 2017, *5* (17), 7825–7832. https://doi.org/10.1039/C7TA00980A.

(35) Ji, Z.; Song, Y.; Zhao, S.; Li, Y.; Liu, J.; Hu, W. Pathway Manipulation via Ni, Co, and V Ternary Synergism to Realize High Efficiency for Urea Electrocatalytic Oxidation. *ACS Catal* 2022, *12* (1), 569–579. https://doi.org/10.1021/acscatal.1c05190.

(36) Guo, X.; Li, Y.; Xu, Z.; Liu, D.; Kong, A.; Liu, R. Interface Electron Transfer Direction-Tuned Urea Electrooxidation Over Multi-Interface Nickel Sulfide Heterojunctions. *Small* 2024, *n/a* (n/a), 2408908. https://doi.org/10.1002/smll.202408908.

(37) Hu, Y.; Shao, L.; Jiang, Z.; Shi, L.; Li, Q.; Shu, K.; Chen, H.; Li, G.; Dong, Y.; Wang, T.; Li, J.; Jiao, L.; Deng, Y. Unveiling the Role of Boron on Nickel-Based Catalyst for Efficient Urea Oxidation Assisted Hydrogen Production. *Adv Funct Mater* 2024, *34* (52), 2411011. https://doi.org/10.1002/adfm.202411011.

(38) Wang, K.; Huang, W.; Cao, Q.; Zhao, Y.; Sun, X.; Ding, R.; Lin, W.; Liu, E.; Gao, P. Engineering NiF3/Ni2P Heterojunction as Efficient Electrocatalysts for Urea Oxidation and Splitting. *Chemical Engineering Journal* 2022, *427*, 130865. https://doi.org/10.1016/j.cej.2021.130865.

(39) Song, Y.; Ji, Z.; Zhao, S.; Wang, T.; Liu, J.; Hu, W. Reaction Site Exchange in Hierarchical Bimetallic Mn/Ni Catalysts Triggered by the Electron Pump Effect to Boost Urea Electrocatalytic Oxidation. *J Mater Chem A Mater* 2022, *10* (19), 10417–10426. https://doi.org/10.1039/D2TA01318E.

(40) Li, M.; Wu, X.; Liu, K.; Zhang, Y.; Jiang, X.; Sun, D.; Tang, Y.; Huang, K.; Fu, G. Nitrogen Vacancies Enriched Ce-Doped Ni3N Hierarchical Nanosheets Triggering Highly-Efficient Urea Oxidation Reaction in Urea-Assisted Energy-Saving Electrolysis. *Journal of Energy Chemistry* 2022, *69*, 506–515. https://doi.org/10.1016/j.jechem.2022.01.031.

(41) Zhu, Y.; Liu, C.; Cui, S.; Lu, Z.; Ye, J.; Wen, Y.; Shi, W.; Huang, X.; Xue, L.; Bian, J.; Li, Y.; Xu, Y.; Zhang, B. Multistep Dissolution of Lamellar Crystals Generates Superthin Amorphous Ni(OH)2 Catalyst for UOR. *Advanced Materials* 2023, *35* (24), 2301549. https://doi.org/10.1002/adma.202301549.

(42) Xie, J.; Liu, W.; Zhang, X.; Guo, Y.; Gao, L.; Lei, F.; Tang, B.; Xie, Y. Constructing Hierarchical Wire-on-Sheet Nanoarrays in Phase-Regulated Cerium-Doped Nickel Hydroxide for Promoted Urea Electro-Oxidation. *ACS Mater Lett* 2019, *1* (1), 103–110. https://doi.org/10.1021/acsmaterialslett.9b00124.

(43) Wang, M.; Zhang, L.; He, Y.; Zhu, H. Recent Advances in Transition-Metal-Sulfide-Based Bifunctional Electrocatalysts for Overall Water Splitting. *J Mater Chem A Mater* 2021, *9* (9), 5320–5363. https://doi.org/10.1039/D0TA12152E.

(44) Zhuo, X.; Jiang, W.; Qian, G.; Chen, J.; Yu, T.; Luo, L.; Lu, L.; Chen, Y.; Yin, S. Ni3S2/Ni Heterostructure Nanobelt Arrays as Bifunctional Catalysts for Urea-Rich Wastewater Degradation. *ACS Appl Mater Interfaces* 2021, *13* (30), 35709–35718. https://doi.org/10.1021/acsami.1c08148.

(45) Xia, X.; Wang, L.; Sui, N.; Colvin, V. L.; Yu, W. W. Recent Progress in Transition Metal Selenide Electrocatalysts for Water Splitting. *Nanoscale* 2020, *12* (23), 12249–12262. https://doi.org/10.1039/D0NR02939D.

(46) Zhang, J.-Y.; Tian, X.; He, T.; Zaman, S.; Miao, M.; Yan, Y.; Qi, K.; Dong, Z.; Liu, H.; Xia, B. Y. In Situ Formation of Ni3Se4 Nanorod Arrays as Versatile Electrocatalysts for Electrochemical Oxidation Reactions in Hybrid Water Electrolysis. *J Mater Chem A Mater* 2018, *6* (32), 15653–15658. https://doi.org/10.1039/C8TA06361C.

(47) Wang, H.; Li, J.; Li, K.; Lin, Y.; Chen, J.; Gao, L.; Nicolosi, V.; Xiao, X.; Lee, J. M. Transition Metal Nitrides for Electrochemical Energy Applications. *Chemical Society Reviews*. Royal Society of Chemistry January 21, 2021, pp 1354–1390. https://doi.org/10.1039/d0cs00415d.

(48) Chen, P.; Ye, J.; Wang, H.; Ouyang, L.; Zhu, M. Recent Progress of Transition Metal Carbides/Nitrides for Electrocatalytic Water Splitting. *Journal of Alloys and Compounds*. Elsevier Ltd November 25, 2021. https://doi.org/10.1016/j.jallcom.2021.160833.

(49) Hu, S.; Feng, C.; Wang, S.; Liu, J.; Wu, H.; Zhang, L.; Zhang, J. Ni 3 N/NF as Bifunctional Catalysts for Both Hydrogen Generation and Urea Decomposition. *ACS Appl Mater Interfaces* 2019, *11* (14), 13168–13175. https://doi.org/10.1021/acsami.8b19052.

(50) Zhang, H.; Li, R.; Humayun, M.; Huang, Z.; Fu, Y.; Cao, Y.; Duan, J.; Attia, Y. A.; Wang, C. Recent Progress in Mott–Schottky Junction Electrocatalysts for the PH-Universal Hydrogen Evolution Reaction. *Mater Chem Front* 2024, *8* (17), 2811–2835. https://doi.org/10.1039/D4QM00312H.

(51) Krishnamachari, M.; Lenus, S.; Pradeeswari, K.; Arun pandian, R.; Kumar, M.; Chang, J.-H.; Muthu, S. pandian; Perumalsamy, R.; Dai, Z.; Vijayakumar, P. Review of Mott–Schottky-Based Nanoscale Catalysts for Electrochemical Water Splitting. *ACS Appl Nano Mater* 2023, *6* (18), 16106–16139. https://doi.org/10.1021/acsanm.3c02677.

(52) Zhou, Y.; Chu, B.; Sun, Z.; Dong, L.; Wang, F.; Li, B.; Fan, M.; Chen, Z. Surface Reconstruction and Charge Distribution Enabling Ni/W5N4 Mott-Schottky Heterojunction Bifunctional Electrocatalyst for Efficient Urea-Assisted Water

Electrolysis at a Large Current Density. *Appl Catal B* 2023, *323*, 122168. https://doi.org/10.1016/j.apcatb.2022.122168.

(53) Li, C.; Liu, Y.; Zhuo, Z.; Ju, H.; Li, D.; Guo, Y.; Wu, X.; Li, H.; Zhai, T. Local Charge Distribution Engineered by Schottky Heterojunctions toward Urea Electrolysis. *Adv Energy Mater* 2018, *8* (27), 1801775. https://doi.org/10.1002/aenm.201801775.

Chapter- 2.2

Improvement in overall performance for electrochemical urea oxidation by introduction of Pd in $Ni(OH)_2$

Summary:

The modification of $Ni(OH)_2$ by incorporating other transition metals helps enhance the stability and the kinetics for urea electrooxidation reaction. In this work, $Pd/Ni(OH)_2$ was developed as an efficient catalyst for the process. The incorporation of Pd effectively mitigated rapid poisoning of the active sites, ensuring a remarkable stability of 300 hrs. Furthermore, a significant reduction in overpotential and charge transfer resistance was achieved. Operando Raman and ATR-FTIR spectroscopy was used to gain mechanistic insights into the reaction

2.2.1. Introduction

The hydrogen production by electrochemical water splitting can be made more energy efficient by replacing OER with the electrochemical oxidation of urea (UOR). $Ni(OH)_2$ is the primary catalyst investigated for urea electrooxidation. However, its major challenges include sluggish kinetics associated with the 6 electron transfer process and limited stability, primarily due to active site poisoning by the strong adsorption of CO_2[1].

Efforts have been made to improve the stability and overall electrooxidation performance by introducing heteroatoms such as Rh, Ru, Mo, Co, etc, with $Ni(OH)_2$[2–6]. Incorporation of the heteroatoms improves the electrocatalytic performance by providing optimal interaction of the urea molecule with the active site. However, further improvement in this direction is required for the large-scale application of this process.

Noble metals like Au and Pd have been employed to mitigate poisoning in electrocatalytic reactions. Their incorporation weakens the binding strength of CO_x species to active sites, enhancing catalyst tolerance. This improved resistance is attributed to their weak adsorption properties, electronic modifications, and lattice effects that prevent strong CO attachment[7,8]. Hence, the use of these metals could be extended to address the CO_2 poisoning in urea electrooxidation.

The synergy between Ni and Pd has been shown to enhance electrochemical activity by facilitating the optimal adsorption and activation of organic molecules. Thus, the PdNi catalysts have been extensively studied for electrocatalytic reactions such as HER[9–11], ORR[12], formic acid oxidation[13], hydrazine oxidation reaction[14], alcohol oxidation[15] UOR[16] etc. For example, in the PdNi catalyst, galvanic replacement of electrodeposited Ni with Pd enhances electrochemical hydrogen evolution and formic acid oxidation. This was attributed to two factors: the lattice contraction due to the dissolution of Ni atoms and the charge transfer from Ni to Pd, leading to the downshift of the Pd *d*-band center. These effects weaken the interaction strength between adsorbates and the Pd surface, leading to enhanced catalytic activity [10]. In another study, G. Liu et al. reported a Pd/NiFeLDH catalyst for hydrazine oxidation. The incorporation of Pd onto NiFe LDH enhances the electron density of the surrounding environment through electron transfer from Pd to the support, resulting in Pd adopting a positive valence state. This strengthens its interaction with hydrazine molecules, facilitating their complete electrooxidation to nitrogen. [14].

Similarly, NiPd bimetallic catalysts supported on ordered mesoporous carbon have been explored for urea electrooxidation. Their enhanced efficiency is primarily due to the interaction between Ni and Pd, which optimizes urea adsorption and activation, along with the high surface area and conductivity of the OMC support[16]. However, the major limitations of this catalyst include its high Pd content and limited stability, highlighting the need for further improvements.

2.2.2. Scope of the present investigation

In the present work, Pd/$Ni(OH)_2$ has been studied as an efficient catalyst for electrochemical urea oxidation. Herein, Pd helps improve the adsorption and activation of the urea molecule, resulting in enhanced reaction kinetics. This leads to a lowering of the overpotential and an increase in the overall current density (380 mA cm^{-2} at 1.5 V_{RHE}) in comparison to $Ni(OH)_2$. Additionally, the presence of Pd prevents the poisoning of the active site, resulting in a substantial improvement in stability of upto 300 h with negligible decay. Furthermore, operando spectroscopic studies were performed to understand the mechanism of the reaction

2.2.3. Experimental Section

2.2.3.1. Materials

Palladium chloride ($PdCl_2$), sodium borohydride ($NaBH_4$), and 5 wt% Nafion solution were purchased from Sigma Aldrich. Nickel chloride hexahydrate ($NiCl_2.6H_2O$) was procured from Loba Chemie Pvt. Ltd. Potassium hydroxide (KOH) and isopropyl alcohol (IPA) were purchased from Merck Life Sciences Pvt. Ltd. Ethanol was procured from Hayman. Toray Carbon paper (with a thickness of ~0.4mm) was obtained from Alfa Aesar. All the chemicals obtained were used without further purification. Deionized water with a resistivity of 18.2 MΩ cm (MilliQ water) was used for all the synthesis and catalytic studies.

2.2.3.2. Characterization technique

Powder X-ray diffraction (PXRD) patterns of the synthesized materials were acquired by a Rigaku diffractometer with copper anode generating X-ray of wavelength 1.54 Å. High-resolution transmission electron microscopy (HRTEM) images of the samples were obtained on the JEOL JEM 2100 Plus electron microscope. The samples for the TEM studies were prepared by stripping the catalyst from the carbon paper by sonication in ethanol. The as prepared dispersion was dropcasted on the Cu grid. Zeiss Gemini FESEM 500 was used to acquire FESEM images. X-ray photoelectron spectroscopy (XPS) measurements were carried out using a Thermo K-alpha spectrometer using micro focused and monochromated AlKα radiation. Inductively coupled plasma optical emission spectroscopy (ICP-OES) analyses were performed on the Perkin Elmer Optima 7000DV instrument to determine the Pd loading. XAS measurements were performed at PETRA III, beamline P64, DESY, Germany. Measurements of Ni K-edge and Pd K-edges at ambient pressures were performed in both fluorescence and transmission modes using gas ionization chambers to monitor the incident and transmitted X-ray intensities. The in-situ IR study was carried out using a Bruker 70v vertex FTIR spectrometer equipped with a mid-band MCT detector. The operando Raman spectroscopy was performed using the Renishaw inVia Raman spectrometer. Temperature programmed desorption with CO_2 as the probe molecule was performed using the Belcat II TPx instrument. The electrochemical studies were performed using Biologic potentiostat.

2.2.3.3. Synthesis of Ni(OH)$_2$

Ni(OH)$_2$ was synthesized by $NaBH_4$ assisted reduction method at room temperature[17]. In a typical synthesis, 17 mL of 0.1 M $NiCl_2.6H_2O$ solution was added into a 250 mL beaker containing 85 mL of 0.1 M $NaBH_4$ solution under vigorous stirring. The resultant solution was stirred for 20 min. Ni(OH)$_2$ precipitates as a black colored compound. The black compound was collected by centrifugation and washed thrice with water and once with ethanol. The black compound collected after centrifugation was kept for drying at 40 °C overnight.

2.2.3.4. Preparation of working electrode

To prepare the coating ink, 2 mg of as prepared Ni(OH)$_2$ was dispersed in 1 mL of isopropyl alcohol. The mixture was sonicated for 1 h. 20 µL of 5 wt% Nafion solution was added to the ink and sonicated for another hour. 200 µL of the as prepared coating ink was drop casted on Toray carbon paper of area 0.25 cm^2 to maintain a mass loading of 1.6 mg cm^{-2}. The electrodes were then dried overnight.

2.2.3.5. Electrodeposition of Pd on $Ni(OH)_2$

Pd was electrodeposited onto the $Ni(OH)_2$ coated C-paper by a reported method [18]. For the electrodeposition, 250 µM H_2PdCl_4 in 15 mL, 1M KOH was taken as the electrolyte. The electrodeposition was performed in a standard three electrode system. $Ni(OH)_2$ coated carbon paper connected to a Pt electrode holder was used as the working electrode. Hg/HgO and graphite rod were used as the reference and the counter electrode, respectively. The electrodeposition was performed using the linear sweep voltammetry method. The cathodic deposition was carried out from 0.2 V vs. Hg/HgO to -0.4 V vs Hg/HgO with a scan rate of 5 mV s^{-1}. The linear sweep voltammetry was repeated 50 times. After the deposition, the electrodes were washed thoroughly with Milli-Q water and directly used for urea electrooxidation studies.

2.2.3.6.Urea electrooxidation studies

The electrochemical reactions were carried out in a three-electrode configuration in a single cell, as shown in *Figure 2.2.1*. As prepared, Pd/$Ni(OH)_2$_C-paper was used as the working electrode. Hg/HgO and Pt coil were used as the reference and counter electrodes, respectively. 0.33M urea dissolved in 80 mL, 1M KOH was used as the electrolyte. The reference electrodes were calibrated before the experiment. The obtained potential (vs. Hg/HgO) was converted into a reversible hydrogen electrode (RHE) scale using the Nernst equation:

$$\mathbf{E_{RHE} = E_{Hg/HgO} + 0.059\ pH + E^{o}_{Hg/HgO}}$$

Here, $E_{Hg/HgO}$ is the potential measured vs Hg/HgO in volts. The pH of the solution is ~14, and $E^{o}_{Hg/HgO}$ is the standard potential for Hg/HgO electrode in 1M NaOH.

The overpotential was calculated by the following equation:

$$\boldsymbol{\eta} = \mathbf{E_{RHE} - 0.37V}$$

Linear sweep voltammetry (LSV), cyclic voltammetry (CV), chronoamperometry (CA), and potentiostatic electrochemical impedance spectroscopy (PEIS) were the electrochemical techniques used to study the urea electrooxidation activity. Linear sweep voltammetry (LSV) was performed in the potential range of 0.2 V (vs. Hg/HgO) to 0.6 V (vs. Hg/HgO) with a scan rate of 5 mV s^{-1} with 85% iR compensation.

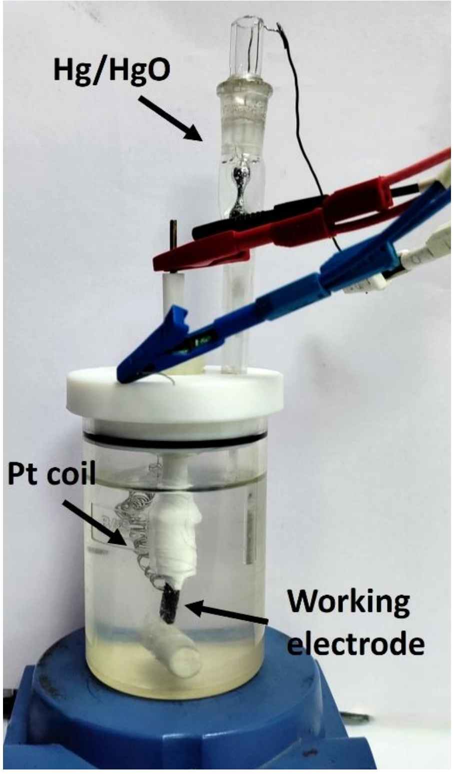

Figure 2.2.1: Electrochemical Cell used to study Urea Electrooxidation

The electrochemical impedance spectroscopy was conducted potentiostatically in the frequency range from 10^6 Hz to 0.1 Hz at different potentials. Chronoamperometric (CA) i-t measurement was performed with 85% iR compensation. The current density for LSV and CA was normalized with respect to the geometrical surface area of 0.25 cm^2.

To determine the electrochemically active surface area (ECSA), CV was performed in the non-faradaic region at different scan rates to calculate the electrochemical double layer capacitance (EDLC). ECSA was calculated by the following formula:

$$\text{ECSA} = \frac{C_{dl}}{C_s}$$

Here, C_{dl} stands for double layer capacitance, and C_s stands for specific capacitance for a smooth surface (40 µF cm^{-2}). To compare the intrinsic activity, ECSA normalized polarization curves were plotted.

Turnover frequency values at 1.5V vs. RHE were determined to compare the intrinsic activity using the following formula[19]:

$$\text{TOF} = \frac{j \times A}{n \times F \times \tau}$$

Here, *j* stands for current density at 1.5V vs RHE, A stands for the area of the electrode, n stands for the number of electrons involved in the urea electrooxidation reaction, F stands for Faraday's constant, and τ stands for the number of moles of Ni loaded on the substrate.

2.2.3.7. Operando infrared spectroscopy (ATR-FTIR)

For the in-situ IR study, the electrochemical cell was connected to a CaF_2 hemispherical window. Carbon paper coated with the catalyst attached to a graphite rod was used as the working electrode. The Hg/HgO electrode and Pt coil were used as the reference and the counter electrode, respectively. 0.1M KOH solution containing 0.33M urea was used as the electrolyte. The working electrode was placed close to the CaF_2 hemispherical window for the attenuated total reflection- Fourier transform infrared spectroscopy study (ATR-FTIR). At the beginning of the experiment, background spectra were collected with the electrolyte in the cell. The background spectra were subtracted from all the subsequent spectra to remove the contribution of the electrolyte towards the measurement. The scan resolution was set at 4 cm^{-1}. For studying the time dependent evolution of the intermediates, chronoamperometry at different potentials was performed. The IR measurement was performed simultaneously. The total number of IR measurements at each potential was set at 50. Each measurement was an average of 128 scans. Between each measurement, a rest time of 60 sec was given. The spectra were analyzed by the OPUS software and plotted directly as a function of potential and time.

2.2.3.8. Operando Raman Spectroscopy

The operando Raman spectroscopy was performed in a custom-made cell, as shown in *Figure 2.2.2*. Ni foam was used as the substrate for the measurement. $Pd/Ni(OH)_2$ coated Ni foam was prepared by electrodepositing Pd onto $Ni(OH)_2$ coated Ni foam by the above-mentioned procedure. The as prepared $Pd/Ni(OH)_2$_ Ni foam was used as the working electrode. Pt coil and Hg/HgO electrode were used as the counter and reference electrode, respectively. Raman spectra were recorded in 1M KOH in the presence and absence of urea (0.33 M). For the potential dependent study, the Raman spectra were collected immediately after chronoamperometry for 1 min at different potentials. For the time dependent measurement, chronoamperometry was performed for 15 mins at 1.5 V vs RHE. The Raman spectra were recorded during chronoamperometry every 2 mins. A laser of wavelength 532 nm was used. The laser power was set at 50%, and exposure time of the laser was set at 10 sec. The obtained spectra were processed using the WiRE software.

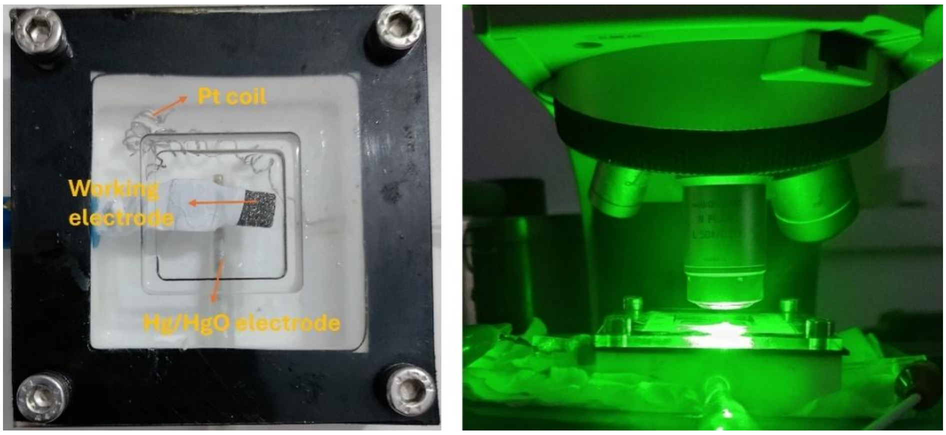

Figure 2.2.2 : (a) Custom-made Raman Cell and **(b)** The working electrode irradiated with the laser during reaction

2.2.3.9. Temperature Programmed Desorption (TPD)

For the TPD measurement, CO_2 was used as the probe molecule. Ni(OH)$_2$, Pd, and Pd/Ni(OH)$_2$ (with Pd loading = 1.57 wt%) were synthesized by $NaBH_4$ assisted reduction for the measurement. Thirty-four milligrams of the as prepared catalyst were taken in the sample cell. The sample was pretreated in an Ar atmosphere for 1h at 50 ^{o}C. This was followed by cooling the sample to 35 ^{o}C under an Ar atmosphere. CO_2 was then passed through the sample at 30 sccm for 1h. The excess CO_2 was removed by purging the sample cell with Ar for 30 mins at a flow rate of 30 sccm at 35 ^{o}C. The temperature was then raised from 35 ^{o}C to 800 ^{o}C at a heating rate of 10 ^{o}C/min. The data was recorded simultaneously at different temperatures.

2.2.3.9. Linear Sweep voltammetry with CO_2 purging

For studying the effect of CO_2 on the electrocatalytic activity, the electrochemical reaction was carried out in a three-electrode configuration in a single cell. As prepared, Pd/Ni(OH)$_2$_carbon paper or Ni(OH)$_2$_carbon paper was used as the working electrode. The Hg/HgO and Pt coil were used as the reference and counter electrodes, respectively. A solution of 0.33M urea dissolved in 80 mL of 1M KOH was used as the electrolyte. The LSV was first recorded prior to CO_2 purging. Subsequently, CO_2 was purged through the electrolyte close to the working electrode for different durations. Linear sweep voltammetry was performed in the range 0.2 V (vs. Hg/HgO) to 0.6 V (vs. Hg/HgO) with a scan rate of 5 mV s^{-1} with 85% iR compensation. The measurement was performed after every 5 mins of CO_2 purging.

2.2.3.10. EXAFS Calculation

The EXAFS data were processed[15,20,21] using the Athena software, part of the Demeter 0.9.26 suite, following standard background subtraction procedures. The EXAFS data was fitted in radial (R) space using the Artemis software. For Feff calculations, standard references were used: Ni metal (ICSD 8688), $Ni(OH)_2$ (ICSD 24015), Pd metal (PDF Card No.:9009820), and $Pd(acac)_2$ (ICSD 251339).

2.2.4. Result and Discussion

$Pd/Ni(OH)_2$ was synthesized by a two-step method wherein Pd was electrodeposited onto $Ni(OH)_2$, which was prepared by $NaBH_4$ assisted reduction. The PXRD of the synthesized $Ni(OH)_2$ (*Figure 2.2.3 a*) showed characteristic peaks at 2θ 34° and 60.5° for the (100) and (003) planes, respectively. Additionally, a broad peak at 45.75° due to the (111) plane of metallic Ni was also observed. The broadness of this peak could be attributed to the small size of the Ni nanoparticles dispersed on $Ni(OH)_2$. FESEM and TEM analysis of $Ni(OH)_2$ showed a spongy morphology (*Figure 2.2.4*).

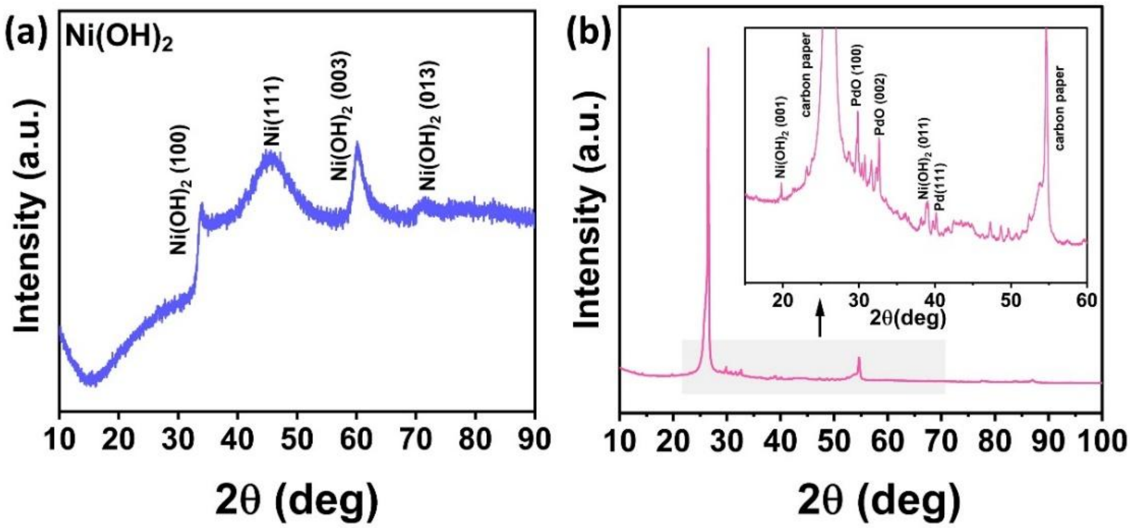

Figure 2.2.3: Powder X Ray diffraction pattern of **(a)** $Ni(OH)_2$ and **(b)** $Pd/Ni(OH)_2$ on carbon paper

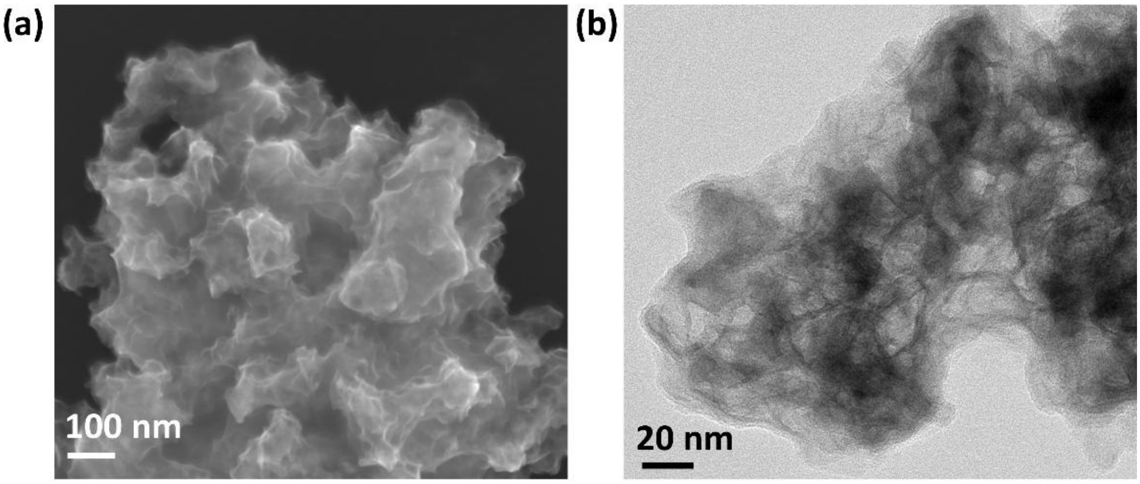

Figure 2.2.4: (a) FESEM and **(b)** TEM image of $Ni(OH)_2$

The as prepared $Ni(OH)_2$ was coated onto carbon paper to maintain a mass loading of 1.6 mg/cm^2. Pd was electrodeposited onto the $Ni(OH)_2$ coated substrate by a previously reported method. The PXRD pattern of Pd/$Ni(OH)_2$ on carbon paper (*Figure 2.2.1 b*) showed characteristic peaks of $Ni(OH)_2$ (001), PdO (100), PdO (002), $Ni(OH)_2$ (011) and Pd(111) at 19.2°, 29.8°, 32.65°, 38.93° and 40.23° respectively along with the peaks corresponding to the carbon substrate. The peaks were matched with the XRD database PDF Card No.: 1009031 (PdO), 1011104 (Pd), and 1011134 ($Ni(OH)_2$). Low-intensity peaks corresponding to KOx were also observed. These peaks may be attributed to the oxidation of K^+ ions intercalated into the carbon paper during electrodeposition. These peaks were matched with the XRD database: PDF Card No. 9009055 (K_2O), 1518207(KO_3), 1537125 (KO_2), 1536941($K_2O_{2.5}$). FESEM- elemental mapping analysis of the Pd/$Ni(OH)_2$_carbon paper after electrodeposition shows a uniform dispersion of Pd and Ni onto the substrate (*Figure 2.2.5)*. To estimate the Pd loading, the ICP- OES analysis was performed. The analysis showed that the Pd loading on carbon paper coated with $Ni(OH)_2$ was 1.57 wt%. From the TEM imaging *(Figure 2.2.6)*, Pd nanoparticles of size 2-3 nm well dispersed on $Ni(OH)_2$ were observed.

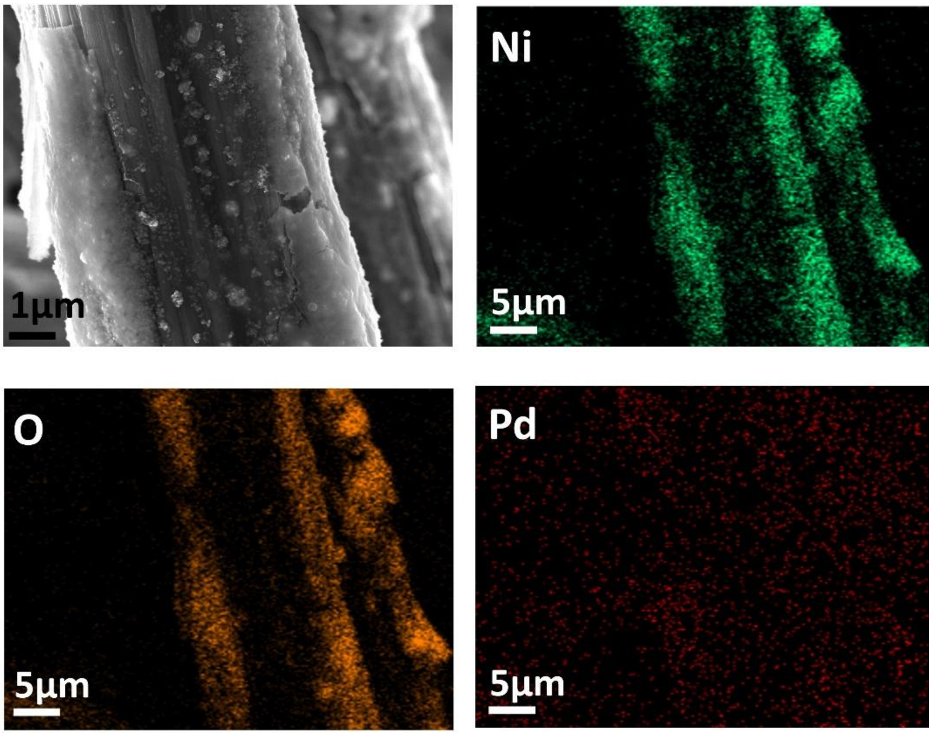

Figure 2.2.5: FESEM image and elemental mapping of Pd/ $Ni(OH)_2$ on carbon paper

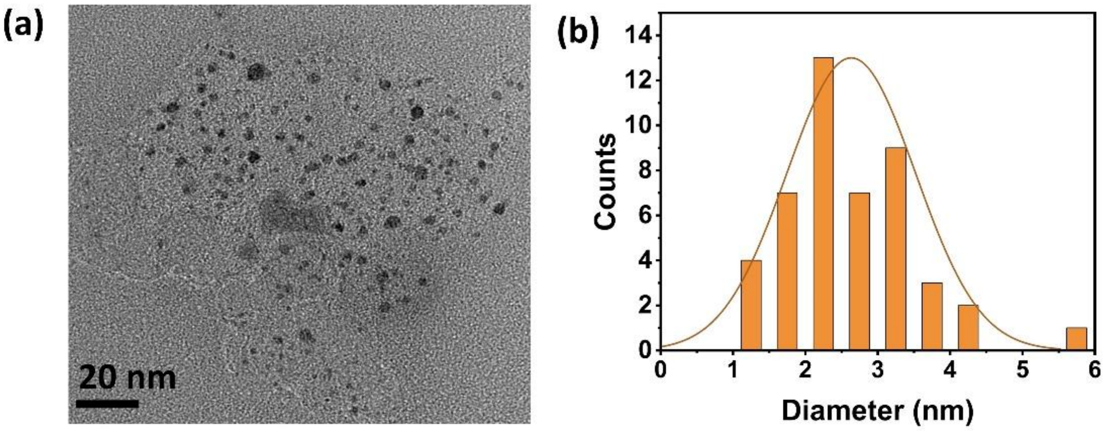

Figure 2.2.6: (a) TEM image of Pd/ $Ni(OH)_2$ (sample prepared by stripping the catalyst off the carbon paper by sonication) and **(b)** Particle size distribution for Pd nanoparticles

XPS and XAS measurements were performed to determine the valence state of the metal species in the catalyst. The Ni2p XPS spectra *(Figure 2.2.7 a)* of $Ni(OH)_2$ coated on carbon paper show peaks at 858.6 ($2p_{3/2}$) and 876.6 eV ($2p_{1/2}$) corresponding to Ni^{2+} and the small peaks at 854.2 eV ($2p_{3/2}$) and 870.7 eV ($2p_{1/2}$) corresponding to Ni metal[12,22]. The Ni 2p XPS spectra *(Figure 2.2.7 a)* of Pd/$Ni(OH)_2$ showed peaks at 853.7 eV ($2p_{3/2}$) and 870.9 eV($2p_{1/2}$) for Ni^0, while the peaks at 857.9 eV ($2p_{3/2}$) and 876.0 ($2p_{1/2}$) correspond to Ni^{2+}. When compared with the Ni 2p XPS spectra of $Ni(OH)_2$, the $2p_{3/2}$

peak shows a negative shift of 0.5 eV and 0.6 eV in the binding energy for Ni^0 and Ni$^{2+,}$ respectively. The high resolution Pd 3d XPS spectra for Pd/Ni(OH)$_2$ *(Figure 2.2.7 b)* showed peaks at 336.5 eV (3d$_{5/2}$) and 341.6 eV (3d$_{3/2}$) for Pd^0, while the peaks at 338.2 eV(3d$_{5/2}$) and 342.4 eV (3d$_{3/2}$) correspond to the Pd^{2+} state[23]. When compared with Pd 3d XPS spectra of Pd electrodeposited onto blank carbon paper, a positive shift of 1.2 eV was observed. This positive shift in the binding energy indicates a charge transfer from Pd to Ni[14,24].

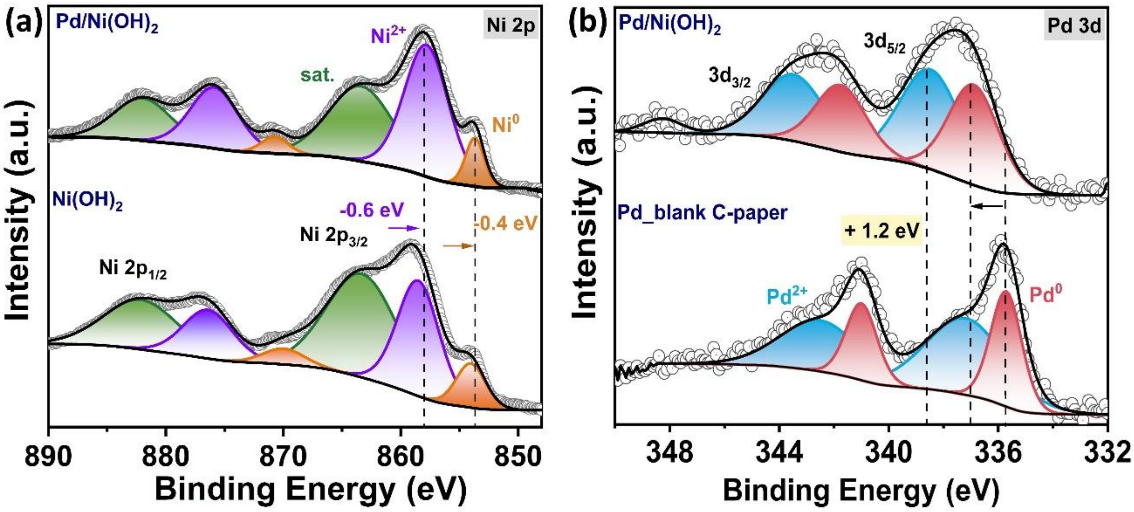

Figure 2.2.7: (a) High resolution Ni 2p XPS spectra of Ni(OH)$_2$ and Pd/Ni(OH)$_2$ on carbon paper and (b) High resolution Pd 3d XPS spectra comparing Pd/Ni(OH)$_2$ on carbon paper and Pd electrodeposited on blank carbon paper

X-ray absorption spectroscopy was used to determine the valency, local atomic structure, and the relative phase fraction of the oxides and the metallic phases in the catalyst. The Ni K edge XANES spectra *(Figure 2.2.8 a)* of Ni(OH)$_2$ and Pd/Ni(OH)$_2$ lie between that of Ni foil and NiO, suggesting the existence of a mixed oxidation state in the catalyst. Likewise, Pd K edge XANES spectra *(Figure 2.2.8 b)* show that the Pd spectra lie between that of metallic Pd foil and Pd(acac)$_2$, suggesting the existence of a mixed oxidation state for Pd as well. The Ni K edge EXAFS spectra show the existence of Ni-O and Ni-Ni bonds in the Ni(OH)$_2$ and Pd/Ni(OH)$_2$ *(Figure 2.2.8 c)*. Likewise, the Pd K-edge EXAFS spectra for Pd/Ni(OH)$_2$ show the existence of Pd-O and Pd-Pd bonds *(Figure 2.2.8 d).*

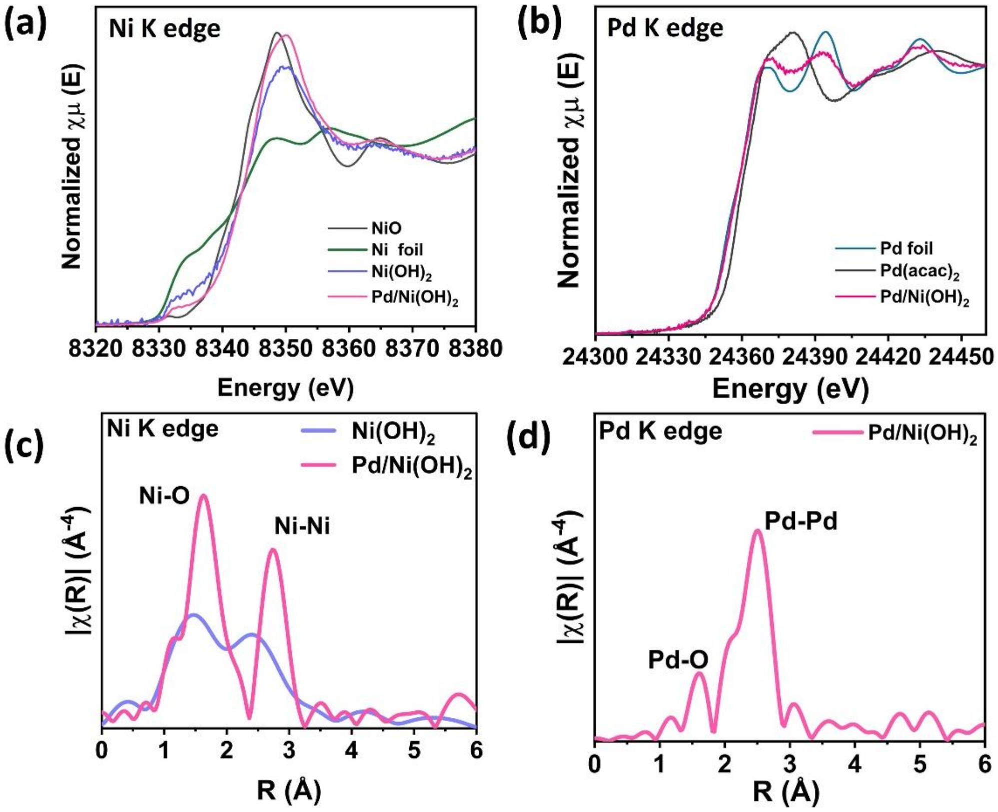

Figure 2.2.8: X-Ray Absorption Spectroscopy **(a)** XANES spectra for Ni K edge, **(b)** XANES spectra for Pd K edge, **(c)** EXAFS spectra for Ni K edge, and **(d)** EXAFS spectra for Pd K edge

Multi-shell fitting of the FT- EXAFS spectra of Ni K edge and Pd K edge was performed to determine the bond lengths and the disorder of the oxides and the metallic species, as shown in *(Figure 2.2.9)*. The values for ΔE, R, and σ^2 obtained after the fitting are tabulated in *Table 2.2.1 and Table 2.2.2.* The estimated Ni-O bond length is 2.05 Å, and the Ni-Ni bond length is 2.5 Å for Pd/Ni(OH)$_2$. These values were found to be close to the theoretical values for Ni-O (2.05 Å) from the Ni(OH)$_2$ phase and Ni-Ni (2.49 Å) bond from the Ni metal phase. These results support the presence of both Ni(OH)$_2$ and metallic Ni in the catalyst. Similarly, multi-shell fitting of the Pd K edge EXAFS spectra shows that the Pd-O bond length is 1.97 (± 0.01 Å) and the Pd-Pd bond length is 2.73 (± 0.01 Å). These values match with the theoretical values of Pd-O (2.05 Å) and Pd-Pd (2.75 Å) from the Pd metal phase, confirming the presence of both these phases in the catalyst. The relative phase fraction of the different species present in the catalyst was also quantified. The analysis showed that in Ni(OH)$_2$, 78.7% of Ni is present as Ni^{2+} and 21.3% is present as Ni^0. Upon electrodeposition, an increase in the percentage of Ni^{2+} state of upto 84 % was observed. This could be attributed to the further conversion of Ni nanoparticles present in the Ni(OH)$_2$ to Ni(OH)$_2$ in an alkaline medium. Likewise, the relative phase fractions of Pd species were also determined. The analysis showed that in Pd/Ni(OH)$_2$, 68.5% of Pd is present as Pd^{2+} and 31.5% is present as Pd^0. The XAS analysis does not show the formation of the Ni-Pd bond, indicating the absence of any alloy formation. However, the significant positive shift in the binding energy in XPS indicates the strong charge transfer interaction of Pd nanoparticles with Ni(OH)$_2$.

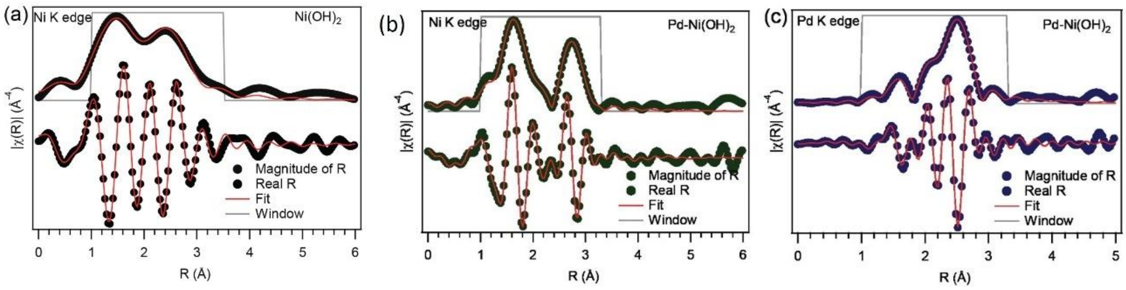

Figure 2.2.9: Multishell fitting of FT- EXAFS spectra of **(a)** Ni K edge for Ni(OH)$_2$, **(b)** Ni K edge for Pd/Ni(OH)$_2$, **(c)** Pd K edge for Pd/Ni(OH)$_2$

Table 2.2.1. The Bond length (R) and Debye-Waller factor/Disorder (σ^2) derived from multishell peak fitting parameters for the R-space plots of Ni K edge for the Ni(OH)$_2$ and Pd-Ni(OH)$_2$ catalysts before reaction. (Amplitude = 0.73, R factor= 0.009)

Ni K edge Sample	**ΔE**	**S_0^2**	**Ni(OH)$_2$**				**Ni metal**	
			Ni-O bond (CN=6)		Ni-Ni bond (CN=6)		Ni-Ni bond (CN=12)	
			R (Ȧ)	σ^2	R (Ȧ)	σ^2	R (Ȧ)	σ^2
Ni(OH)$_2$	-8.91 ± 0.87	0.78	2.025 ± 0.008	0.013 ± 0.002	2.996 ± 0.010	0.014 ± 0.009	2.523 ± 0.034	0.018 ± 0.010
Pd-Ni(OH)$_2$	-3.64 ± 0.53	0.95	2.054 ± 0.008	0.003 ± 0.001	3.104 ± 0.011	0.008 ± 0.001	2.501 ± 0.018	0.009 ± 0.003

Table 2.2.2. The Bond length (R) and Debye-Waller factor/Disorder (σ2) derived from multishell peak fitting parameters for the R-space plots of Pd K edge for the catalysts Pd-$Ni(OH)_2$ catalyst before reaction. (Amplitude = 0.71, R factor= 0.007)

Pd K edge Sample	**ΔE**	**S_0^2**	**Pd oxide**		**Pd metal**	
			Pd-O bond (CN=4)		Pd-Pd bond (CN=12)	
			R (Å)	σ^2	R (Å)	σ^2
Pd-$Ni(OH)_2$	1.55 ± 0.44	0.81	1.971 ± 0.017	0.002 ± 0.001	2.734 ± 0.005	0.007 ± 0.001

Evaluation of electrochemical oxidation of urea

The as prepared Pd/$Ni(OH)_2$ was used as the working electrode to study urea electrooxidation in the alkaline medium. $Ni(OH)_2$ loading on the carbon paper was maintained at 1.6 mg cm^{-2} for all the electrochemical studies. Performance metrics used to evaluate the catalyst are overpotential at 10mA cm^{-2} (η_{10}) and at 100mA cm^{-2} (η_{100}), stability, Tafel slope, and charge transfer resistance from electrochemical impedance spectroscopy. Urea electrooxidation was performed in the alkaline medium consisting of 1 M KOH and 0.33 M urea. Linear sweep voltammetry was recorded for Pd/$Ni(OH)_2$, $Ni(OH)_2$, and Pd_ blank carbon paper in 1 M KOH, both in the presence and absence of urea, to compare the UOR and OER performance of the catalyst *(Figure 2.2.10).*

In the presence of urea, $Ni(OH)_2$ exhibited a maximum current density of 180 mA cm^{-2} at 1.5 V_{RHE} and an overpotential of 970 mV and 1040 mV for 10 mA cm^{-2} and 100 mA $cm^{-2,}$ respectively. Upon incorporation of Pd, an increase in the overall current density was observed, resulting in a maximum current density of 380 mA cm^{-2} at 1.5 V_{RHE}. The overpotentials at 10 mA cm^{-2} and 100 mA cm^{-2} were 930 mV and 980 mV, respectively, which are lower than those observed for $Ni(OH)_2$. Interestingly, Pd electrodeposited on blank carbon paper did not show any urea electrooxidation activity*(Figure 2.2.10 a)*. This confirms that the active site for urea oxidation is $Ni(OH)_2$.

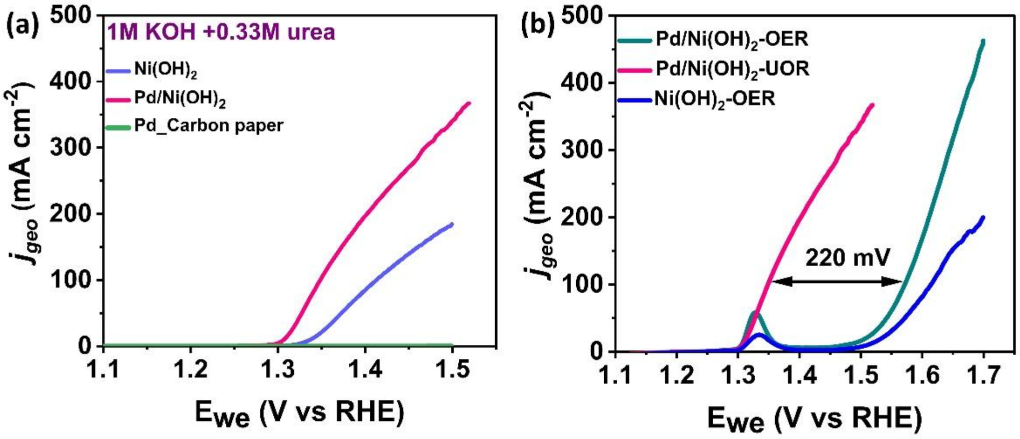

Figure 2.2.10: (a) Linear Sweep voltammetry plot for Ni(OH)$_2$ and Pd/Ni(OH)$_2$ in 1 M KOH containing 0.33 M urea, **(b)** Comparison of linear sweep voltammetry plots obtained in the presence and absence of urea

The polarization curve recorded in 1M KOH in the absence of urea demonstrates the electrochemical activity of the catalysts for the oxygen evolution reaction (OER). The onset potentials for OER over Ni(OH)$_2$ and Pd/Ni(OH)$_2$ were 1.52 V and 1.48 V, respectively *(Figure 2.2.10 b)*. Furthermore, peaks corresponding to the oxidation of Ni(OH)$_2$ to NiOOH were observed at 1.34V and 1.33V over Ni(OH)$_2$ and Pd/Ni(OH)$_2$, respectively. A decrease in the potential of upto 10 mV (from 1.34V to 1.33V) was observed for this oxidation upon incorporation of Pd *(Figure 2.2.11 a)*. Additionally, Pd/Ni(OH)$_2$ exhibited a twofold increase in the area under the curve, suggesting an increased formation of NiOOH in the presence of Pd. Upon comparing the OER and UOR polarization curves, urea assisted water electrolysis takes place at a potential which is 220 mV less than that for conventional water electrolysis. Moreover, the onset of urea electrooxidation is exactly at the position where Ni(OH)$_2$ undergoes oxidation to NiOOH. This suggests that for the electrochemical oxidation of urea, the formation of NiOOH is essential.

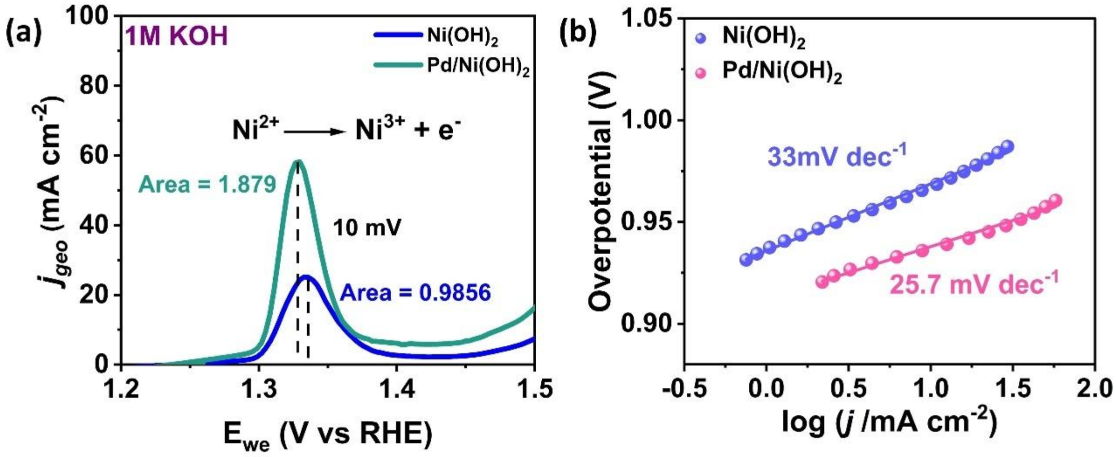

Figure 2.2.11: (a) Linear Sweep voltammetry plot for $Ni(OH)_2$ and $Pd/Ni(OH)_2$ in 1 M KOH showing the peak corresponding to the oxidation of $Ni(OH)_2$ to NiOOH, **(b)** Tafel plot for $Ni(OH)_2$ and $Pd/Ni(OH)_2$ in the electrolyte containing 1M KOH and 0.33 M urea.

The Tafel slope is an indicator of the rate of reaction. A decrease in the Tafel slope value indicates a faster rate of the reaction. From the Tafel plot *(Figure 2.2.11 b)*, it can be concluded that the addition of Pd to $Ni(OH)_2$ causes a significant decrease in Tafel slope value from 33 mV dec^{-1} for $Ni(OH)_2$ to 25.7 mV dec^{-1} for $Pd/NiOH_2$. This further confirms that the reaction becomes more facile in the presence of Pd.

To determine the electrochemically active surface area, electrochemical double layer capacitance measurement was performed *(Figure 2.2.12 a, b)*. The electrochemical double layer capacitance value was estimated to be 0.44 mF cm^{-2} for $Ni(OH)_2$ and 0.7 mF cm^{-2} for $Pd/Ni(OH)_2$. The corresponding ECSA values were estimated to be 11 cm^2 for $Ni(OH)_2$ and 17.8 cm^2 for $Pd/Ni(OH)_2$. This indicates that the incorporation of Pd enhances the electrochemically active surface area *(Figure 2.2.12 c)*. The increase in the surface area increases the current density, suggesting an enhancement in the intrinsic activity of the catalyst, as is evidenced by the ECSA normalized polarization curve*(Figure 2.2.12 d)*. To further compare the improvement in the intrinsic activity, the turnover frequency (TOF) value was estimated from the number of moles of Ni loaded on the substrate. The TOF value for $Pd/Ni(OH)_2$ at 1.5V vs RHE is 6.07×10^{-3} s^{-1}, which is about two times higher than that for $Ni(OH)_2$ at 1.5V (2.87×10^{-3} s^{-1}) which implies that the number of urea molecules oxidized per unit time for the loaded Ni sites is enhanced upon incorporating Pd.

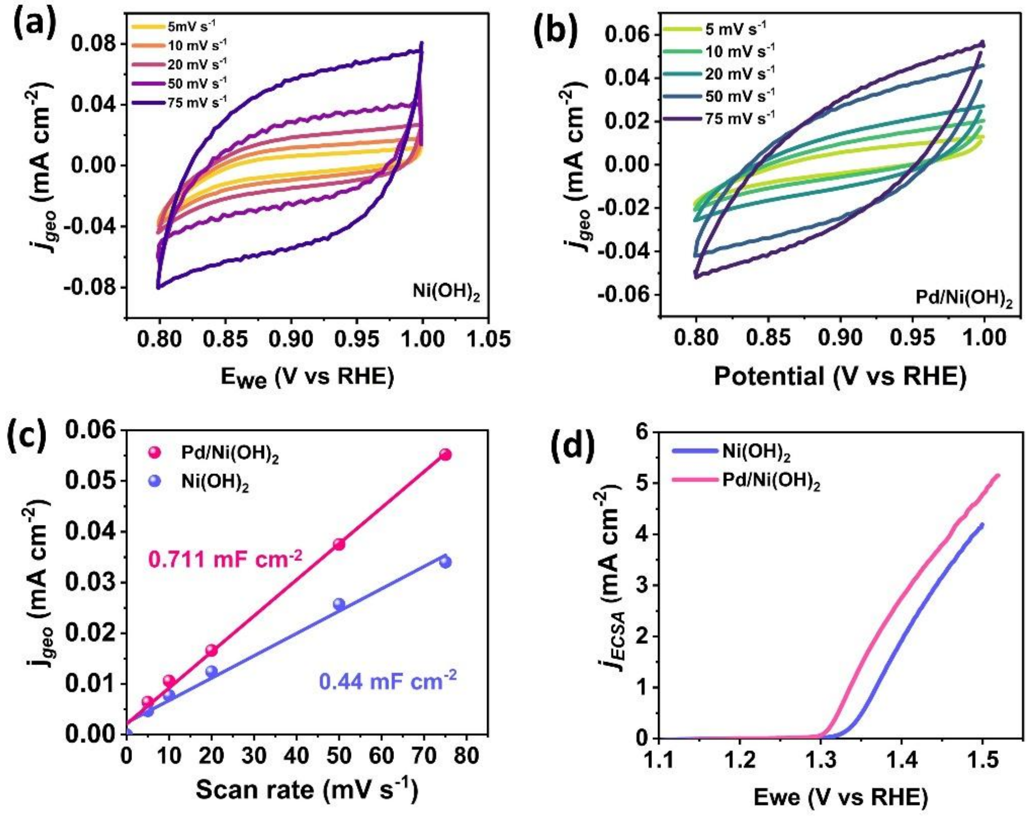

Figure 2.2.12: (a) Cyclic voltammetry plot for Ni(OH)$_2$ in the non-faradaic region, **(b)** cyclic voltammetry plot for Pd/Ni(OH)$_2$ in the non-faradaic region, **(c)** plot of scan rate vs current density to determine the electrochemical double layer capacitance and **(d)** ECSA normalized linear sweep voltammetry plot

Chronoamperometry was performed to study the electrochemical stability of the catalyst. Pd/Ni(OH)$_2$ showed an exceptional stability of upto 300 h at a current density of 20 mA cm^{-2} *(Figure 2.2.13 a)*. In comparison, Ni(OH)$_2$ shows a 20% decrease in the current density within 150 h. Moreover, the chronoamperometric measurement performed at 100 mA cm^{-2} shows a stability of upto 40 h for Pd/Ni(OH)$_2$ *(Figure 2.2.13 b)*.

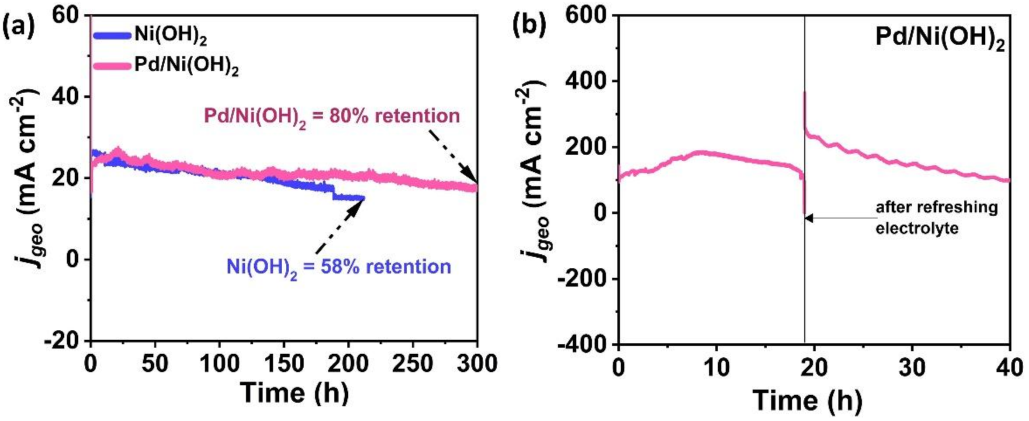

Figure 2.2.13: (a) Chronoamperometry plot for Pd/Ni(OH)$_2$ and Ni(OH)$_2$ at a current density of 20 mA cm^{-2}, **(b)** Chronoamperometry plot at a current density of 100 mA cm^{-2} for Pd/ Ni(OH)$_2$.

To determine the charge transfer resistance and the reaction pathway followed by the catalyst, potentiostatic electrochemical impedance spectroscopy (PEIS) measurement was performed at different potentials. The Nyquist plot exhibited a decrease in the charge transfer resistance for Pd/Ni(OH)$_2$ in comparison to Ni(OH)$_2$, confirming an enhancement in the charge transfer kinetics in the presence of Pd *(Figure 2.2.14 a)*.

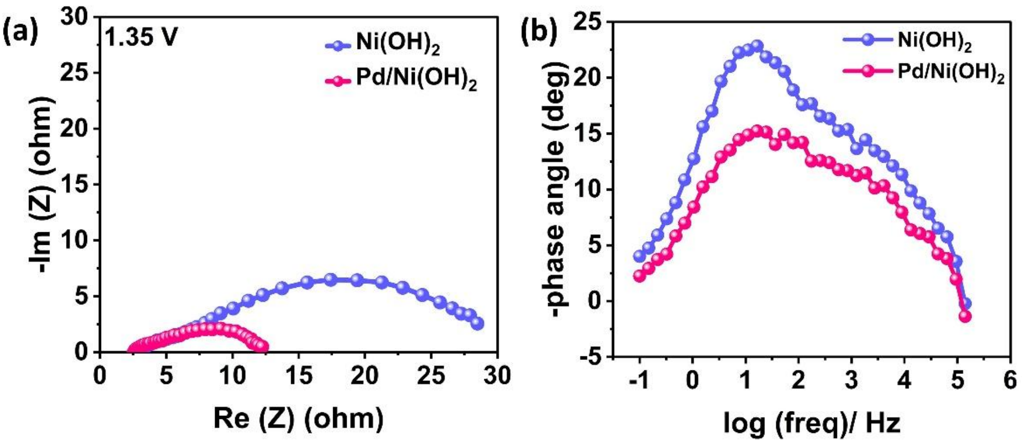

Figure 2.2.14: (a) Nyquist plot comparing the impedance for Ni(OH)$_2$ and Pd/Ni(OH)$_2$ and **(b)** Bode plot for Ni(OH)$_2$ and Pd/Ni(OH)$_2$

As discussed in Chapter 2.1, in the case of urea electrooxidation, there are two possible pathways, namely the indirect pathway and the direct pathway. The first step in both pathways is the formation of NiOOH. In the indirect pathway, the oxidation of urea results in a simultaneous reduction of NiOOH to Ni(OH)$_2$, while in the direct pathway, the NiOOH site is retained. The two pathways can be distinguished using the Bode plot, which is a plot of log (freq) vs -phase angle *(Figure 2.2.14 b)*. The Bode plot for both catalysts exhibits a peak in the low frequency region followed by a broadening in the high frequency region. The peak in the low frequency region indicates a direct pathway, and the broadening in the high frequency region indicates an indirect pathway. These observations suggest that both Ni(OH)$_2$ and Pd/Ni(OH)$_2$ follow direct and indirect pathways.

The charge transfer associated with each pathway is obtained by fitting the Nyquist plot using the equivalent circuit *(Figure 2.2.15 a, b)*. The equivalent circuit used to fit the Nyquist plot is shown in *Figure 2.2.15 (c).* The equivalent circuit consists of solution resistance (Rs), which is in series with the parallel connections between charge transfer resistance (R1 and R2) and constant phase elements (Q1 and Q2). The constant phase elements represent the double layer capacitance due to the formation of the electrochemical double layer by the adsorption of the reaction intermediates. The parallel circuit R1/Q1 represents the charge transfer associated with the indirect pathway, while R2/Q2 respresnts the charge transfer associated with the direct pathway[25–27]. The charge transfer resistance values for each pathway are compared in *(Figure 2.2.15 d).* The R1 and R2 denote the charge transfer resistance associated with the indirect pathway and the direct pathway, respectively. It can be observed that the incorporation of Pd results in a significant decrease in the charge transfer resistance for both pathways.

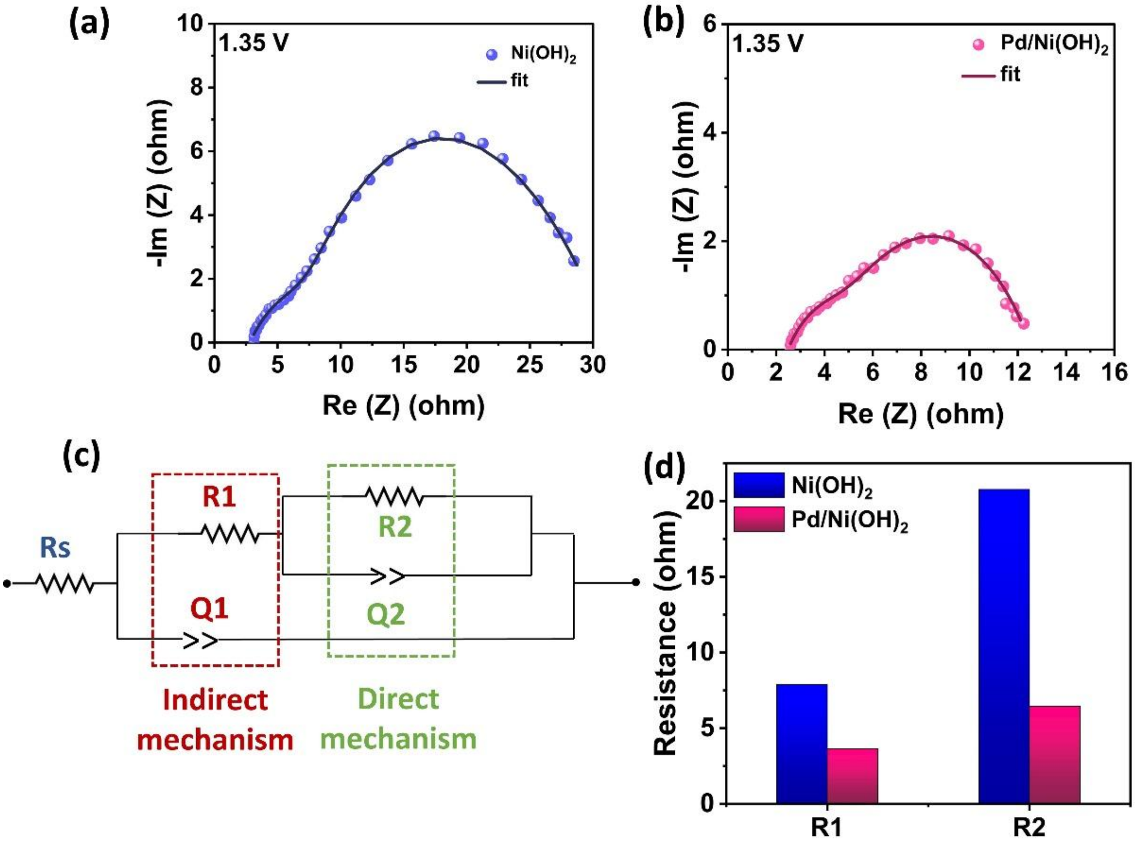

Figure 2.2.15: (a) Nyquist plot for $Ni(OH)_2$ fitted using the equivalent circuit, **(b)** Nyquist plot for $Pd/Ni(OH)_2$ fitted using the equivalent circuit, **(c)** Equivalent circuit used to fit the Nyquist plots and **(d)** Charge transfer resistance value obtained for each pathway.

To understand the mechanism of reaction during urea electrooxidation, operando Raman spectroscopy and ATR-FTIR spectroscopy were performed for $Pd/Ni(OH)_2$. The operando Raman spectroscopy *(Figure 2.2.16 a)* was performed in 1 M KOH medium with and without urea. The working electrode was prepared by electrodepositing Pd on $Ni(OH)_2$ coated Ni foam. In 1 M KOH, in the absence of urea, no prominent peaks were observed before the reaction. The Raman spectra were then collected after chronoamperometry for 2 mins under varying potentials. Upon applying potential (from 1.2 V_{RHE} to 1.5V_{RHE}), the oxidation of $Ni(OH)_2$ to NiOOH occurs, resulting in two prominent peaks at 472.7 cm^{-1} and 555 cm^{-1}. These peaks may be attributed to the Eg bending and A1g stretching modes of the Ni-O bond in NiOOH, respectively. An increase in the applied potential results in an increased intensity of the two peaks due to the increase in the number of NiOOH sites. Additionally, a broad hump at 802 cm^{-1} due to the O-O^- species in NiOOH was also observed[28–30].

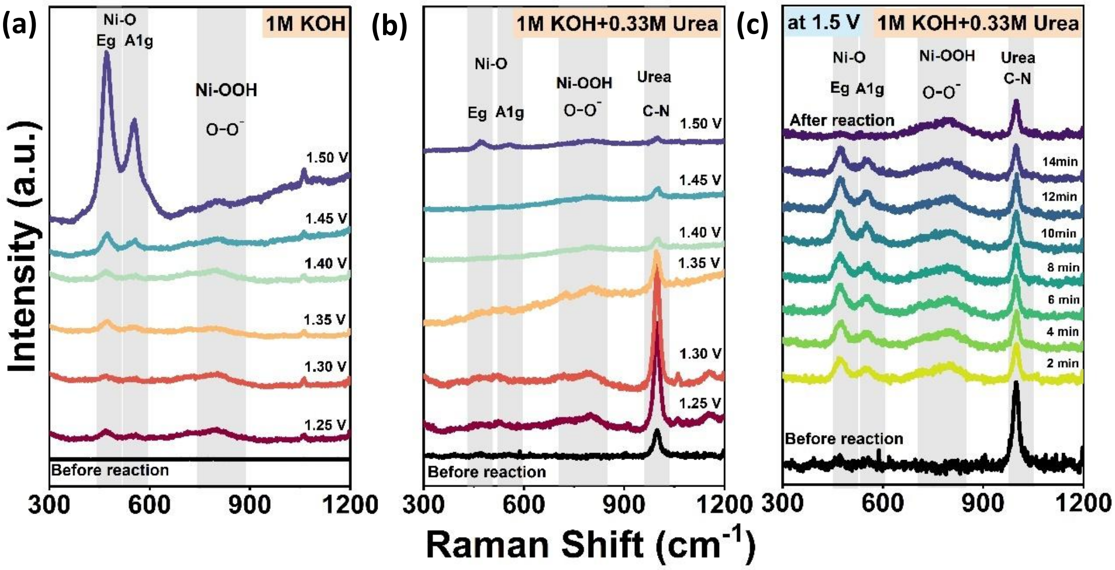

Figure 2.2.16: Operando Raman spectra for Pd/Ni(OH)$_2$ **(a)** in 1 M KOH obtained after chronoamperometry at varying potential, **(b)** in 1 M KOH + 0.33 M urea obtained after chronoamperometry, and **(c)** in 1 M KOH + 0.33 M urea at 1.5 V at different time intervals.

When 0.33M urea was added to the medium, the Raman spectra showed an additional peak at 1001 cm^{-1} corresponding to the C-N stretching of the urea molecule *(Figure 2.2.16 b)*. Before the reaction, no other peaks were observed. The Raman spectra were then collected post chronoamperometry at different potentials. It was observed that when the applied potential is below 1.35 V, i.e., in the non-faradaic region, the intensity of the peak at 1001 cm^{-1} was high. However, as the applied potential increased beyond 1.35 V, the intensity of this peak decreased. This is attributed to the consumption of urea during the electrooxidation process. Additionally, the intensity of the peak corresponding to NiOOH also decreases. This is attributed to the reduction of NiOOH to Ni(OH)$_2$ with the simultaneous oxidation of urea to N$_2$ and CO$_2$. Time dependent Raman spectra were obtained at a potential of 1.5 V$_{RHE}$ *(Figure 2.2.16 c)*. The spectra were collected every 2 mins during a chronoamperometric run of 15 mins. The peaks corresponding to Ni-O vibration modes (Eg and A1g) and O-O$^-$ species were distinctly visible, indicating the formation of the active site during the reaction. The intensity of these peaks decreased significantly post reaction indicating the reduction of NiOOH.

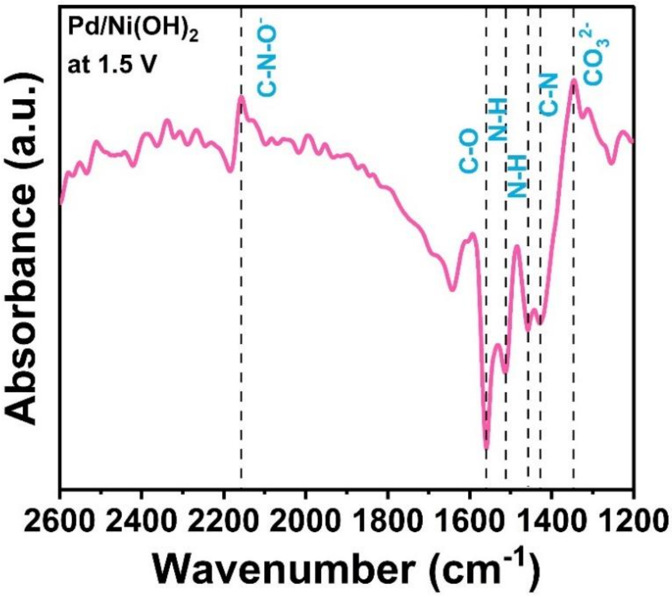

Figure 2.2.17: Operando ATR-FTIR spectra for $Pd/Ni(OH)_2$

To gain deeper insight into the intermediates adsorbed on the $Pd/Ni(OH)_2$ surface during urea electrooxidation, operando ATR-FTIR studies were conducted. Negative absorbance peaks were observed for the urea molecule at 1557 cm^{-1} (C=O stretching), 1518 cm^{-1} and 1460 cm^{-1} (N–H vibrational modes), and 1427 cm^{-1} (C–N stretching) *(Figure 2.2.17)*. The negative absorbance is attributed to the consumption of the urea molecules. (Note: The negative absorbance occurs due to the subtraction of the obtained spectrum from the background spectrum, which is collected before the reaction. Compared to the background, a decrease in the number of urea molecules leads to the observed negative absorbance). A peak at 2154 cm^{-1} arises due to the formation of $C–N–O^-$ intermediate species, indicating incomplete urea oxidation. Additionally, a peak at 1344 cm^{-1} was observed, which corresponded to CO_3^{2-}, formed by the reaction of CO_2 with OH^- in the electrolyte[31–34]. The presence of the carbonate band confirms the complete oxidation of urea to CO_2. Notably, peaks associated with overoxidized nitrogen species, such as nitrates or nitrites, were absent, indicating that overoxidation products were not formed during the urea electrooxidation process[35].

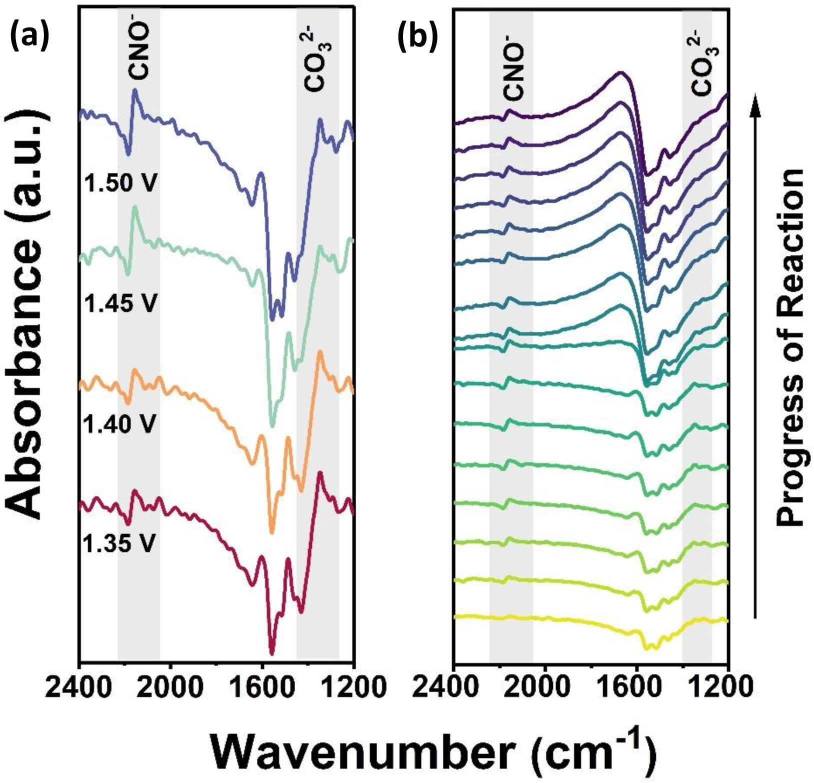

Figure 2.2.18: Operando ATR-FTIR spectra for Pd/Ni(OH)$_2$ with **(a)** varying potential and **(b)** varying time at 1.5 V$_{RHE}$.

A potential-dependent study *(Figure 2.2.18 a)*, carried out between 1.35 V and 1.50 V vs. RHE, revealed that with increasing potential, the intensity of the C–N–O$^-$ intermediate and the CO_3^{2-} absorbance band both increased. This suggests enhanced urea oxidation at higher potentials. A time-dependent study *(Figure 2.2.18 b)* conducted at 1.50 V vs. RHE, with spectra recorded at 2 minute intervals, demonstrated a negligible change in the intensity of the C–N–O$^-$ absorbance band over time, accompanied by an increase in the CO_3^{2-} absorbance band. This observation is attributed to the progressive oxidation of urea to CO_2 over time.

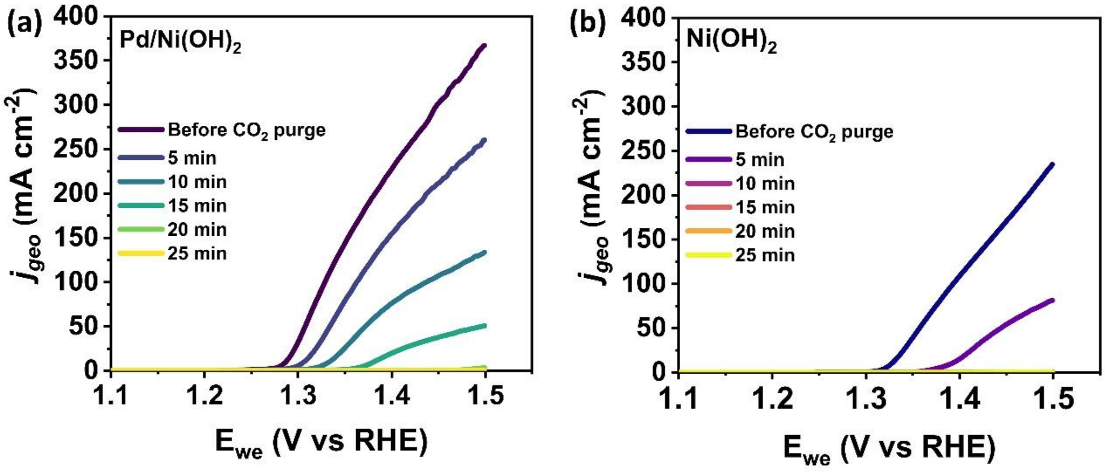

Figure 2.2.19: Linear sweep voltammetry plot after CO_2 purge for different durations for **(a)** Pd/Ni$(OH)_2$ and **(b)** Ni$(OH)_2$

To investigate CO_2 adsorption on the catalyst, linear sweep voltammetry plots were recorded after varying durations of CO_2 purging *(Figure 2.2.19)*. For Pd/Ni$(OH)_2$, the current density decreased noticeably after 25 minutes of CO_2 purging *(Figure 2.2.19 a)*. In contrast, Ni$(OH)_2$ exhibited a significant drop in current density within just 10 minutes of CO_2 purging, indicating faster poisoning of Ni$(OH)_2$ in the absence of Pd *(Figure 2.2.19 b)*.

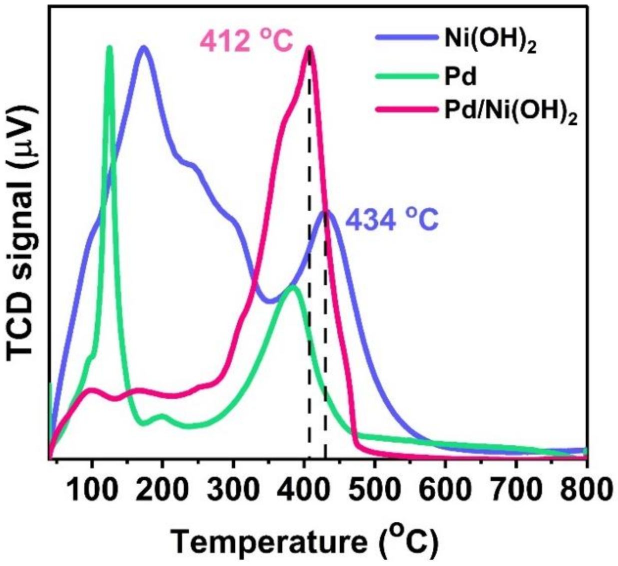

Figure 2.2.20: CO_2 Temperature programmed desorption for Ni$(OH)_2$, Pd and Pd/Ni$(OH)_2$

Temperature-Programmed Desorption (CO_2 TPD) was conducted using CO_2 as the probe molecule to analyze the interaction of CO_2 with the catalyst (*Figure 2.2.20*). $Ni(OH)_2$ displayed two prominent desorption peaks at 182.6 °C and 434.2 °C, while Pd exhibited peaks at 125 °C and 383 °C. The higher-temperature desorption peak for Pd was approximately 50 °C lower than for $Ni(OH)_2$, suggesting differences in CO_2 binding strength. In contrast, Pd/$Ni(OH)_2$ synthesized via $NaBH_4$ reduction showed no desorption peak at lower temperatures but exhibited a strong desorption peak at 412 °C suggesting a strong binding affinity for CO_2 binding affinity by Pd/$Ni(OH)_2$. The comparison of the desorption peak at high temperatures for Pd/$Ni(OH)_2$ and $Ni(OH)_2$ suggest that incorporation of Pd weakens the interaction of CO_2, thereby ensuring the stability of the catalyst.

2.2.5. Conclusion

In this study, we have demonstrated that Pd incorporated $Ni(OH)_2$ is a highly efficient catalyst for urea electrooxidation, positioning it as a promising candidate for energy-efficient hydrogen generation. Electrochemical analysis showed that incorporating Pd significantly enhances the catalyst's stability, maintaining performance for up to 300 hrs, compared to the shorter stability of $Ni(OH)_2$ alone. The improved reaction kinetics enabled the catalyst to achieve a maximum current density of 380 mA cm^{-2} at 1.5 V. Additionally, our findings revealed that Pd plays a critical role in enhancing the intrinsic activity of the catalyst and in protecting the Ni active sites from strong CO_2 adsorption. These results underscore the potential of Pd/$Ni(OH)_2$ as an advanced catalyst for energy-efficient hydrogen production.

2.2.6. Reference

(1) Daramola, D. A.; Singh, D.; Botte, G. G. Dissociation Rates of Urea in the Presence of NiOOH Catalyst: A DFT Analysis. *J Phys Chem A* **2010**, *114* (43), 11513–11521. https://doi.org/10.1021/jp105159t.

(2) Kang, W.; Wu, S.; Li, Z.; Li, Z.; Li, K.; Wang, H. Highly Stable Urea Oxidation Electrolysis via Rh Nanoparticles Residing in the Porous LaNiO3 Nanocubes. *Int J Hydrogen Energy* **2024**, *56*, 16–26. https://doi.org/10.1016/j.ijhydene.2023.11.297.

(3) Zheng, X.; Yang, J.; Li, P.; Jiang, Z.; Zhu, P.; Wang, Q.; Wu, J.; Zhang, E.; Sun, W.; Dou, S.; Wang, D.; Li, Y. Dual-Atom Support Boosts Nickel-Catalyzed Urea Electrooxidation. *Angewandte Chemie International Edition* **2023**, *62* (22), e202217449. https://doi.org/10.1002/anie.202217449.

(4) Xu, H.; Liao, Y.; Gao, Z.; Qing, Y.; Wu, Y.; Xia, L. A Branch-like Mo-Doped Ni3S2 Nanoforest as a High-Efficiency and Durable Catalyst for Overall Urea Electrolysis. *J Mater Chem A Mater* **2021**, *9* (6), 3418–3426. https://doi.org/10.1039/D0TA09423D.

(5) Wang, J.; Mo, F.; Fei, J.; Ling, W.; Cui, M.; Lei, H.; Jiang, L.; Huang, Y. Insights into the Synergistic Effect between Nickel and Molybdenum for Catalyzing Urea Electrooxidation. *Carbon Neutralization* **2022**, *1* (3), 267–276. https://doi.org/10.1002/cnl2.27.

(6) Liu, X.; Qin, H.; Wang, G.; Li, Q.; Huang, Q.; Wen, Z.; Mao, S. Co-Doped Ni–Mo Oxides: Highly Efficient and Robust Electrocatalysts for Urea Electrooxidation Assisted Hydrogen Production. *J Mater Chem A Mater* **2022**, *10* (32), 16825–16833. https://doi.org/10.1039/D2TA04728D.

(7) Chen, X.; Granda-Marulanda, L. P.; McCrum, I. T.; Koper, M. T. M. How Palladium Inhibits CO Poisoning during Electrocatalytic Formic Acid Oxidation and Carbon Dioxide Reduction. *Nat Commun* **2022**, *13* (1), 38. https://doi.org/10.1038/s41467-021-27793-5.

(8) Basu, D.; Basu, S. Performance Studies of Pd–Pt and Pt–Pd–Au Catalyst for Electro-Oxidation of Glucose in Direct Glucose Fuel Cell. *Int J Hydrogen Energy* **2012**, *37* (5), 4678–4684. https://doi.org/10.1016/j.ijhydene.2011.04.158.

(9) Liu, H.; Shang, J.; Zeng, L.; Cao, B.; Geng, H.; Lang, J.; Cao, X.; Gu, H. A Setaria-Shaped Pd/Ni-NC Electrocatalyst for High Efficient Hydrogen Evolution Reaction. *Chemical Engineering Journal Advances* **2021**, *6*, 100101. https://doi.org/10.1016/j.ceja.2021.100101.

(10) Rasouli, H.; Tabaian, S. H.; Rezaei, M. Galvanic Replacement of Electrodeposited Nickel by Palladium and Investigation of the Electrocatalytic Activity of Synthesized Pd/(Ni) for Hydrogen Evolution and Formic Acid Oxidation. *RSC Adv* **2016**, *6* (27), 22500–22510. https://doi.org/10.1039/C5RA27219J.

(11) Li, J.; Zhou, P.; Li, F.; Ren, R.; Liu, Y.; Niu, J.; Ma, J.; Zhang, X.; Tian, M.; Jin, J.; Ma, J. Ni@Pd/PEI–RGO Stack Structures with Controllable Pd Shell Thickness as Advanced Electrodes for Efficient Hydrogen Evolution. *J Mater Chem A Mater* **2015**, *3* (21), 11261–11268. https://doi.org/10.1039/C5TA01805F.

(12) Sahoo, L.; Garg, R.; Kaur, K.; Vinod, C. P.; Gautam, U. K. Ultrathin Twisty PdNi Alloy Nanowires as Highly Active ORR Electrocatalysts Exhibiting Morphology-Induced Durability over 200 K Cycles. *Nano Lett* **2022**, *22* (1), 246–254. https://doi.org/10.1021/acs.nanolett.1c03704.

(13) Li, X.; Zhang, J.; Dou, J.; Li, M.; Feng, X.; Liu, G. Precisely Tuning the Surface Nanostructure of Ni@Pd Nanocatalysts for Enhanced Formic Acid Oxidation. *ChemCatChem* **2022**, *14* (17), e202200599. https://doi.org/10.1002/cctc.202200599.

(14) Liu, G.; Nie, T.; Wang, H.; Shen, T.; Sun, X.; Bai, S.; Zheng, L.; Song, Y.-F. Size Sensitivity of Supported Palladium Species on Layered Double Hydroxides for the Electro-Oxidation Dehydrogenation of Hydrazine: From Nanoparticles to Nanoclusters and Single Atoms. *ACS Catal* **2022**, *12* (17), 10711–10717. https://doi.org/10.1021/acscatal.2c02628.

(15) Huang, W.; Ma, X.-Y.; Wang, H.; Feng, R.; Zhou, J.; Duchesne, P. N.; Zhang, P.; Chen, F.; Han, N.; Zhao, F.; Zhou, J.; Cai, W.-B.; Li, Y. Promoting Effect of Ni(OH)2 on Palladium Nanocrystals Leads to Greatly Improved Operation Durability for Electrocatalytic Ethanol Oxidation in Alkaline Solution. *Advanced Materials* **2017**, *29* (37), 1703057. https://doi.org/10.1002/adma.201703057.

(16) Muthuchamy, N.; Jang, S.; Park, J. C.; Park, S.; Park, K. H. Bimetallic NiPd Nanoparticle-Incorporated Ordered Mesoporous Carbon as Highly Efficient Electrocatalysts for Hydrogen Production via Overall Urea Electrolysis. *ACS Sustain Chem Eng* **2019**, *7* (18), 15526–15536. https://doi.org/10.1021/acssuschemeng.9b03275.

(17) Maity, S.; Harish, S.; Eswaramoorthy, M. Controlled Galvanic Replacement of Ni in Ni(OH)2 by Pd: A Method to Quantify Metallic Ni and to Synthesize Bimetallic Catalysts for Methanol Oxidation. *Mater Chem Phys* **2019**, *221*, 377–381. https://doi.org/10.1016/j.matchemphys.2018.09.071.

(18) Zhang, Z.; Feng, C.; Liu, C.; Zuo, M.; Qin, L.; Yan, X.; Xing, Y.; Li, H.; Si, R.; Zhou, S.; Zeng, J. Electrochemical Deposition as a Universal Route for Fabricating Single-Atom Catalysts. *Nat Commun* **2020**, *11* (1), 1215. https://doi.org/10.1038/s41467-020-14917-6.

(19) Rao, N. N.; Alex, C.; Mukherjee, M.; Roy, S.; Tayal, A.; Datta, A.; John, N. S. Evidence for Exclusive Direct Mechanism of Urea Electro-Oxidation Driven by In Situ-Generated Resilient Active Species on a Rare-Earth Nickelate. *ACS Catal* **2024**, *14* (2), 981–993. https://doi.org/10.1021/acscatal.3c04967.

(20) Caliebe, W. A.; Murzin, V.; Kalinko, A.; Görlitz, M. High-Flux XAFS-Beamline P64 at PETRA III. In *AIP Conference Proceedings*; American Institute of Physics Inc., 2019; Vol. 2054. https://doi.org/10.1063/1.5084662.

(21) Ravel, B.; Newville, M. ATHENA, ARTEMIS, HEPHAESTUS: Data Analysis for X-Ray Absorption Spectroscopy Using IFEFFIT. *J Synchrotron Radiat* **2005**, *12* (4), 537–541. https://doi.org/10.1107/S0909049505012719.

(22) Grosvenor, A. P.; Biesinger, M. C.; Smart, R. S. C.; McIntyre, N. S. New Interpretations of XPS Spectra of Nickel Metal and Oxides. *Surf Sci* **2006**, *600* (9), 1771–1779. https://doi.org/10.1016/j.susc.2006.01.041.

(23) Brun, * M; Berthet, A.; Bertolini, J. C. *XPS, AES and Auger Parameter of Pd and PdO*; 1999; Vol. 104.

(24) Liu, G.; Nie, T.; Song, Z.; Sun, X.; Shen, T.; Bai, S.; Zheng, L.; Song, Y. F. Pd Loaded NiCo Hydroxides for Biomass Electrooxidation: Understanding the Synergistic Effect of Proton Deintercalation and Adsorption Kinetics. *Angewandte Chemie - International Edition* **2023**, *62* (45). https://doi.org/10.1002/anie.202311696.

(25) Guo, F.; Ye, K.; Du, M.; Huang, X.; Cheng, K.; Wang, G.; Cao, D. Electrochemical Impedance Analysis of Urea Electro-Oxidation Mechanism on Nickel Catalyst in Alkaline Medium. *Electrochim Acta* **2016**, *210*, 474–482. https://doi.org/10.1016/j.electacta.2016.05.149.

(26) Mohamed, I. M. A.; Kanagaraj, P.; Yasin, A. S.; Iqbal, W.; Liu, C. Electrochemical Impedance Investigation of Urea Oxidation in Alkaline Media Based on Electrospun Nanofibers towards the Technology of Direct-Urea Fuel Cells. *J Alloys Compd* **2020**, *816*. https://doi.org/10.1016/j.jallcom.2019.152513.

(27) Chen, W.; Xu, L.; Zhu, X.; Huang, Y. C.; Zhou, W.; Wang, D.; Zhou, Y.; Du, S.; Li, Q.; Xie, C.; Tao, L.; Dong, C. L.; Liu, J.; Wang, Y.; Chen, R.; Su, H.; Chen, C.; Zou, Y.; Li, Y.; Liu, Q.; Wang, S. Unveiling the Electrooxidation of Urea: Intramolecular Coupling of the N−N Bond. *Angewandte Chemie - International Edition* **2021**, *60* (13), 7297–7307. https://doi.org/10.1002/anie.202015773.

(28) Vedharathinam, V.; Botte, G. G. Direct Evidence of the Mechanism for the Electro-Oxidation of Urea on Ni(OH)2 Catalyst in Alkaline Medium. *Electrochim Acta* **2013**, *108*, 660–665. https://doi.org/10.1016/j.electacta.2013.06.137.

(29) Yang, X.; Zhang, H.; Yu, B.; Liu, Y.; Xu, W.; Wu, Z. An Unveiled Electrocatalysis Essence of NiCo Hydroxides through in Situ Raman Spectroscopy for Urea Oxidation. *Energy Technology* **2022**, *10* (5). https://doi.org/10.1002/ente.202101010.

(30) Yang, X.; Zhang, H.; Xu, W.; Yu, B.; Liu, Y.; Wu, Z. A Doping Element Improving the Properties of Catalysis: In Situ Raman Spectroscopy Insights into Mn-Doped NiMn Layered Double Hydroxide for the Urea Oxidation Reaction. *Catal Sci Technol* **2022**, *12* (14), 4471–4485. https://doi.org/10.1039/d2cy00308b.

(31) Han, W.-K.; Wei, J.-X.; Xiao, K.; Ouyang, T.; Peng, X.; Zhao, S.; Liu, Z.-Q. Activating Lattice Oxygen in Layered Lithium Oxides through Cation Vacancies for Enhanced Urea Electrolysis. *Angewandte Chemie International Edition* **2022**, *61* (31), e202206050. https://doi.org/10.1002/anie.202206050.

(32) Yu, H.; Zhu, S.; Hao, Y.; Chang, Y.-M.; Li, L.; Ma, J.; Chen, H.-Y.; Shao, M.; Peng, S. Modulating Local Interfacial Bonding Environment of Heterostructures for Energy-Saving Hydrogen Production at High Current Densities. *Adv Funct Mater* **2023**, *33* (12), 2212811. https://doi.org/10.1002/adfm.202212811.

(33) Wang, L.; Zhu, S.; Marinkovic, N.; Kattel, S.; Shao, M.; Yang, B.; Chen, J. G. Insight into the Synergistic Effect between Nickel and Tungsten Carbide for Catalyzing Urea Electrooxidation in Alkaline Electrolyte. *Appl Catal B* **2018**, *232*, 365–370. https://doi.org/10.1016/j.apcatb.2018.03.064.

(34) Wang, L.; Zhu, S.; Wang, Y.; Liu, Z.; Liu, Y.; Wang, Q.; Gu, M.; Li, K.; Sun, X.; Yang, L.; Shao, M. Amorphous Nickel Tungstate Nanocatalyst Boosts Urea Electrooxidation. *Chemical Engineering Journal* **2023**, *460*, 141826. https://doi.org/10.1016/j.cej.2023.141826.

(35) Wang, P.; Bai, X.; Jin, H.; Gao, X.; Davey, K.; Zheng, Y.; Jiao, Y.; Qiao, S.-Z. Directed Urea-to-Nitrite Electrooxidation via Tuning Intermediate Adsorption on Co, Ge Co-Doped Ni Sites. *Adv Funct Mater* **2023**, *33* (25), 2300687. https://doi.org/10.1002/adfm.202300687.

Chapter- 2.3

Elucidating the urea electrooxidation pathway on Ni_3N

Summary:

Transition metal nitrides have been widely investigated for electrochemical water splitting and, more recently, for urea electrooxidation. While Ni_3N shows promise as a catalyst, its performance can still be enhanced. Additionally, the precise electrooxidation pathway of Ni_3N remains unclear, emphasizing the need for further research to improve its efficiency and mechanistic understanding.

2.3.1. Introduction

Transition metal nitrides are a type of interstitial alloy. Herein the metal atoms form the lattices of face-centred cubic (fcc), simple hexagonal, and hexagonal closed packed (hcp) structures. The N atoms occupy the interstitial sites between these metal atoms. In the case of fcc and hcp, the N atoms are present at the octahedral sites while they occupy the trigonal prismatic sites in the simple hexagonal structures[1–3], as shown in *Figure 2.3.1*.

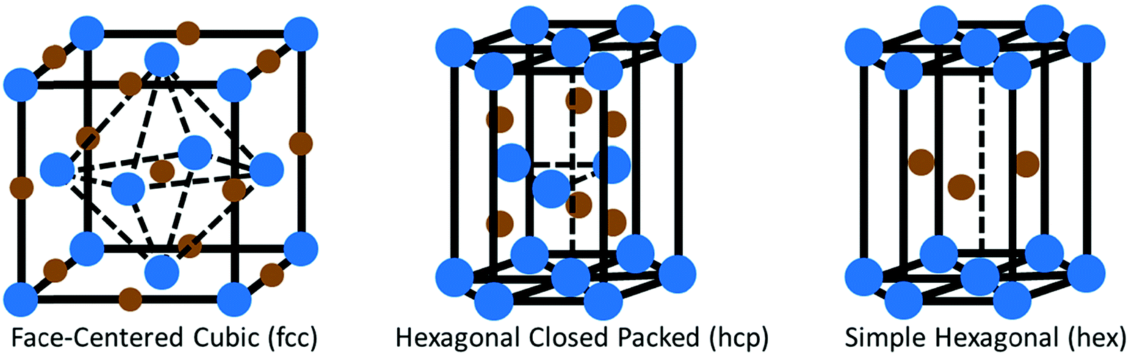

Figure 2.3.1: Different structures of transition metal nitrides. Reproduced with permission from reference (1)

The bonding in transition metal nitrides (TMNs) is a unique combination of metallic, covalent, and ionic characteristics. The metallic bonding is attributed to the metal-metal bonds. The covalent contribution is due to the covalent bond formation between the metal and the N atoms, while the ionic character arises from the charge transfer from the metal to the N atom. The incorporation of nitrogen atoms induces structural changes in the metal lattice. The formation of metal-nitrogen (M-N) bonds expands the parent metal lattice, increasing the metal-metal bond distance. This expansion leads to the contraction of the metal d-band, resulting in an increased density of states near the Fermi level compared to the original metal. These changes impart noble metal-like behavior to the TMNs, enhancing their conductivity and electrochemical stability. Additionally, the electronic properties of TMNs can be fine-tuned by adjusting the nitrogen-to-metal (N/M) ratio[3,4]. This versatility, combined with their exceptional properties, has made TMNs based on group IVB-IB metals (such as Ti, Mo, Mn, W, Co, Fe, Ni, and Cu) promising candidates for various electrocatalytic applications[2].

Ni_3N has been extensively studied for electrochemical water splitting. It adopts a simple hexagonal structure. During electrooxidation, the presence of nitrogen atoms facilitates charge transfer from the nickel to nitrogen. This charge redistribution enhances the formation of *OOH intermediates on the surface of nickel atoms. The in situ formed NiOOH serves as the active site for the OER. The enhanced formation of NiOOH has broadened the application of Ni_3N to the electrooxidation of various organic molecules, including ethanol, methanol, glucose, hydrazine, and urea[5–9].

In the case of urea electrooxidation, Ni_3N significantly improves electrochemical activity compared to $Ni(OH)_2$ by lowering the overpotential and enhancing the reaction kinetics. Modification of Ni_3N by the introduction of nitrogen vacancies and creation of heterojunctions have further helped in enhancing the catalytic activity[10–13]. However, despite these developments, there remains room for improvement in the electrocatalytic performance of Ni_3N. Additionally, the precise electrooxidation pathway for Ni_3N is not yet fully understood, underscoring the need for further investigation into this promising catalyst.

2.3.2. Scope of the investigation

This work focuses on the development of a free-standing, binder-free activated Ni_3N (A-Ni_3N) electrode for urea electrooxidation. Herein, the activation performed by chronopotentiometry led to a transformation in morphology, resulting in dodecahedral structures that enhanced the catalytic performance and ensured long-term stability of upto 300 h at a current density of 100 mA cm^{-2}. Potentiostatic impedance spectroscopy revealed that A-Ni_3N operates via a direct electrooxidation pathway, unlike $Ni(OH)_2$, which utilizes both direct and indirect pathways. Operando Raman spectroscopy provided further insights into the reaction mechanism.

2.3.3. Experimental Section

2.3.3.1. Materials

Sodium borohydride ($NaBH_4$) and 5 wt% Nafion solution were purchased from Sigma Aldrich. Nickel nitrate hexahydrate ($Ni(NO_3)_2.6H_2O$) was purchased from Thomas Baker. Nickel chloride hexahydrate ($NiCl_2.6H_2O$) was procured from Loba Chemie Pvt. Ltd. Potassium hydroxide (KOH) and isopropyl alcohol (IPA) were purchased from Merck Life Sciences Pvt. Ltd. Ethanol was procured from Hayman. Ni foam was purchased from the Electrode Store. All the chemicals obtained used without further purification. Deionized water with a resistivity of 18.2 MΩ cm (MilliQ water) was used for all the synthesis and catalytic studies.

2.3.3.2.Characterization technique

Powder X-ray diffraction (PXRD) patterns of the synthesized materials were acquired using a Rigaku diffractometer with copper anode generating X-ray of wavelength 1.54 Å. Zeiss Gemini FESEM 500 was used to acquire Field emission scanning electron microscopy (FESEM) images. X-ray photoelectron spectroscopy (XPS) measurements were carried out using a Thermo K-alpha spectrometer using micro focused and monochromated AlKα radiation. The operando Raman spectroscopy was performed using the Renishaw inVia Raman spectrometer. The electrochemical studies were performed using Biologic potentiostat.

2.3.3.3.Synthesis of $Ni(OH)_2$ by $NaBH_4$ assisted reduction

$Ni(OH)_2$ was synthesized by $NaBH_4$ assisted reduction method at room temperature[14]. In a typical synthesis, 17 mL of 0.1 M $NiCl_2.6H_2O$ solution was added into a 250 mL beaker containing 85 mL of 0.1 M $NaBH_4$ solution under vigorous stirring. The resultant solution was stirred for 20 min. $Ni(OH)_2$ precipitates as a black colored compound. The black compound was collected by centrifugation and washed thrice with water and once with ethanol. The as obtained $Ni(OH)_2$ precipitate was kept for drying at 40 °C overnight. The coating ink was prepared by dispersing 2 mg of the as prepared $Ni(OH)_2$ in 1 mL IPA. 800 µL of the coating ink was dropcasted on a Ni foam of 1 cm^2 area to maintain a loading of 1.6 mg cm^{-2}.

2.3.3.4. Synthesis of $Ni(OH)_2$ by solvothermal route

The solvothermal synthesis of $Ni(OH)_2$ was performed by a previously reported method[13]. In a 100 mL beaker, 0.931 g $Ni(NO_3)_2$. $6H_2O$, 0.971 g urea, 0.237 g NH_4F were taken. These were dissolved in 80 mL H_2O and stirred for 20 mins. The solution was then transferred into a 100 mL Teflon lined autoclave. A clean Ni foam of dimension 1.5 cm^2 was then put into it. The top 0.5 cm^2 of the Ni foam was masked with Teflon, resulting in an effective geometric area of 1 cm^2 for the working electrode. The autoclave was placed in a hot air oven for 2 h at 120 °C. The $Ni(OH)_2$ coated Ni foam was then collected and washed thoroughly with water. The as prepared electrode was then directly used to study the urea electrooxidation activity.

2.3.3.5. Synthesis of $Ni(OH)_2$ by electrodeposition

The electrodeposition of $Ni(OH)_2$ was performed by a previously reported method[15]. Herein, the electrodeposition is carried out by the electrochemical reduction of aqueous $Ni(NO_3)_2.6H_2O$ solution. 50 mL of 0.1 M $Ni(NO_3)_2.6H_2O$ was taken in an electrochemical cell as the electrolyte. Ni foam of dimension 1 cm^2 area was used as the working electrode. Graphite rod and saturated calomel electrode (SCE) were used as the counter and reference electrode respectively. For the electrodeposition, the working electrode was subjected to a chronopotentiometry at 20 mA cm^{-2} for 10 mins to ensure the wetting of the electrode with the electrolyte. This is followed by the chronopotentiometry at a current density of 20 mA cm^{-2} for 10 mins. The electrodeposition was performed without stirring. The as prepared $Ni(OH)_2$ coated Ni foam was then thoroughly washed with water and dried.

2.3.3.6. Synthesis of Ni_3N by Nitridation

The $Ni(OH)_2$ coated Ni foam prepared by electrodeposition was placed in a quartz boat in a tube furnace[13,16]. The temperature was raised to 350 ^{o}C from the room temperature at a ramp rate of 5 $^{o}C/min$. It was then annealed at 350 ^{o}C for 2 h in an NH_3 atmosphere. NH_3 flow was maintained at 80 mL/min flow rate. Ni_3N coated Ni foam was collected obtained and washed thoroughly with water and used for further studies.

2.3.3.7. Activation of Ni_3N-coated Ni foam

For the activation, the as prepared Ni_3N coated Ni foam was used as the working electrode. Pt coil and Hg/HgO were used as the counter and reference electrode, respectively. 1 M KOH was used as the electrolyte. The working electrode was subjected to a chronopotentiometry at a current density of 100 mA cm^{-2} for 1 h. The as prepared A-Ni_3N was then washed with water and used for further studies.

2.3.3.8. Urea electrooxidation studies

The electrochemical reactions were carried out in a three-electrode configuration in a single cell as shown in *Figure 2.3.1*. As prepared, A-Ni_3N was used as the working electrode. Hg/HgO and Pt coil were used as the reference and counter electrodes, respectively. 0.33 M urea dissolved in 80 mL, 1M KOH was used as the electrolyte. The reference electrodes were calibrated before the experiment. The obtained potential (vs. Hg/HgO) was converted into a reversible hydrogen electrode (RHE) scale using the Nernst equation:

$$\mathbf{E_{RHE} = E_{Hg/HgO} + 0.059\ pH + E^{o}_{Hg/HgO}}$$

Here $E_{Hg/HgO}$ is the potential measured vs Hg/HgO in volts. The pH of the solution is ~14, and $E^{o}_{Hg/HgO}$ is the standard potential for Hg/HgO electrode in 1M NaOH.

The overpotential was calculated by the following equation:

$$\boldsymbol{\eta} \mathbf{= E_{RHE} - 0.37V}$$

Linear sweep voltammetry (LSV), cyclic voltammetry (CV), chronoamperometry (CA), and potentiostatic electrochemical impedance spectroscopy (PEIS) were the electrochemical techniques used to study the urea electrooxidation activity. Linear sweep voltammetry (LSV) was performed in the potential range of 0.2 V (vs. Hg/HgO) to 0.6 V (vs. Hg/HgO) with a scan rate of 5 mV s^{-1} with 85% iR compensation. The electrochemical impedance spectroscopy was conducted potentiostatically in the frequency range from 10^6 Hz to 0.1 Hz at different potentials. Chronoamperometric i-t measurement was performed with 85% iR compensation. Chronoamperometry at 1.45 V for a current density of 100 mA cm^{-2} was performed without iR compensation. The electrolyte used consisted of 1M KOH and 0.5 M urea. It was refreshed at different time intervals after a decay in the activity was observed, which was attributed to the decrease in the concentration of urea. The current density for LSV and CA was normalized with respect to the geometrical surface area of 1 cm^2.

To determine the electrochemically active surface area (ECSA), cyclic voltammetry was performed in the non-faradaic region at different scan rates to calculate the electrochemical double layer capacitance (EDLC). ECSA was calculated by the following formula:

$$\text{ECSA} = \frac{C_{dl}}{C_s}$$

Here, C_{dl} stands for double layer capacitance, and C_s stands for specific capacitance for a smooth surface (40 μF cm^{-2}). To compare the intrinsic activity, ECSA normalized polarization curves were plotted.

2.3.3.9. Operando Raman Spectroscopy

The operando Raman spectroscopy was performed in a custom made cell, as shown in *Figure 2.3.2*. The as prepared A-Ni_3N on Ni foam was used as the working electrode. Pt coil and Hg/HgO electrode were used as the counter and reference electrode, respectively. Raman spectra were recorded in 1M KOH in the presence and absence of urea (0.33 M). For the time dependent measurement, chronoamperometry was performed for 10 mins at 1.5 V vs RHE. The Raman spectra were recorded during chronoamperometry every 2 mins. A laser of wavelength 532 nm was used. The laser power was set at 50%, and exposure time to the laser was set at 10 sec. The obtained spectra were processed using the WiRE software.

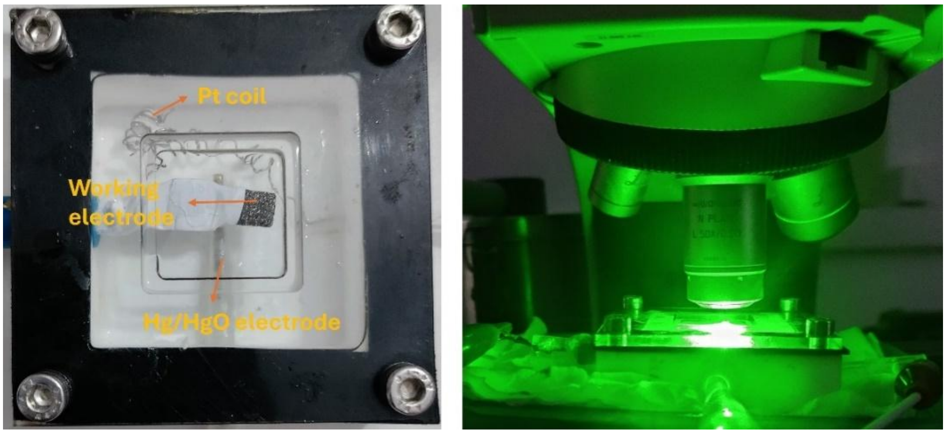

Figure 2.3.2 : (a) Custom made Raman Cell and **(b)** The working electrode irradiated with the laser during the reaction

2.3.4. Result and Discussion

A-Ni3N was synthesized by a three-step method. Herein, $Ni(OH)_2$ was electrodeposited over Ni foam by the electroreduction of nickel nitrate. The as prepared Ni foam was then annealed in NH_3 to form Ni_3N. The Ni_3N electrode was then subjected to chronopotentiometry at 100 mA cm^{-2} for 1h in 1M KOH to form A-Ni_3N. The PXRD of A-Ni_3N on Ni foam shows characteristic peaks of Ni_3N at 2θ 39.22°, 42.27°, 58.80°, 70.75°, 78.63°, 85.74° and 87.52° corresponding to (110), (002), (112), (103), (212), (302), (221), (311) and (222) planes. The peaks corresponding to metallic Ni were observed at 44.94°, 52.2°, 76.8°, 93.4°, and 98.7° for (111), (200), (220), (311), and (222) planes, respectively. No characteristic peaks for NiOOH were observed. The peaks were matched with the PDF cards in the XRD database: PDF card- 4320485 for Ni_3N, PDF card- 9009862 for metallic Ni and PDF card- 1011134 for $Ni(OH)_2$. The PXRD pattern for Ni_3N also showed peaks corresponding to Ni_3N and metallic Ni *(Figure 2.3.3)*. The PXRD pattern for $Ni(OH)_2$ showed peaks corresponding to metallic Ni and a broad hump at 60.5° corresponding to the (003) plane of $Ni(OH)_2$ *(Figure 2.3.3 (inset))*.

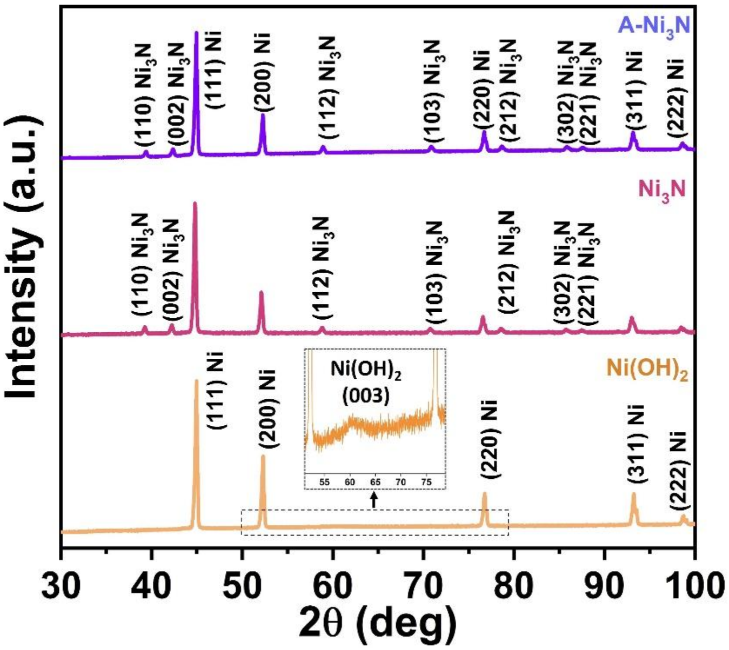

Figure 2.3.3: Powder X-ray diffraction pattern of A-Ni_3N, Ni_3N, and $Ni(OH)_2$ supported on Ni foam. (inset shows peak corresponding to $Ni(OH)_2$)

To determine the valence state of Ni in the catalyst, Ni 2p XPS spectra were collected before and after etching with Ar sputtering. Before etching, the Ni 2p XPS spectra for A-Ni_3N show a characteristic peak at 852.7 eV ($2p_{3/2}$) and at 870.8 eV ($2p_{1/2}$) for Ni-N[10,17–19]. The peaks at 855.5 eV ($2p_{3/2}$) and 873.1 eV ($2p_{1/2}$) correspond to Ni^{2+} *(Figure 2.3.4)*. It is observed that the intensity of the peak corresponding to Ni-N is significantly low in comparison to Ni^{2+}. Likewise, in Ni_3N, the Ni 2p XPS spectra showed a characteristic peak at 853.1 eV ($2p_{3/2}$) and at 870.3 eV ($2p_{1/2}$) for Ni-N. The peaks at 856.1 eV ($2p_{3/2}$) and 873.8 eV ($2p_{1/2}$) correspond to Ni^{2+}*(Figure 2.3.4)* arising because of the surface oxides. The Ni 2p XPS spectra for $Ni(OH)_2$ electrodeposited on Ni foam show characteristic peaks at 855.9 eV ($2p_{3/2}$) and 873.5 eV ($2p_{1/2}$) corresponding to Ni^{2+} while the peaks for Ni^0 appear at 852.4 eV ($2p_{3/2}$) and 867.2 eV ($2p_{1/2}$)[20]. It is observed that the intensity of the metallic Ni peak is significantly low *(Figure 2.3.4)*.

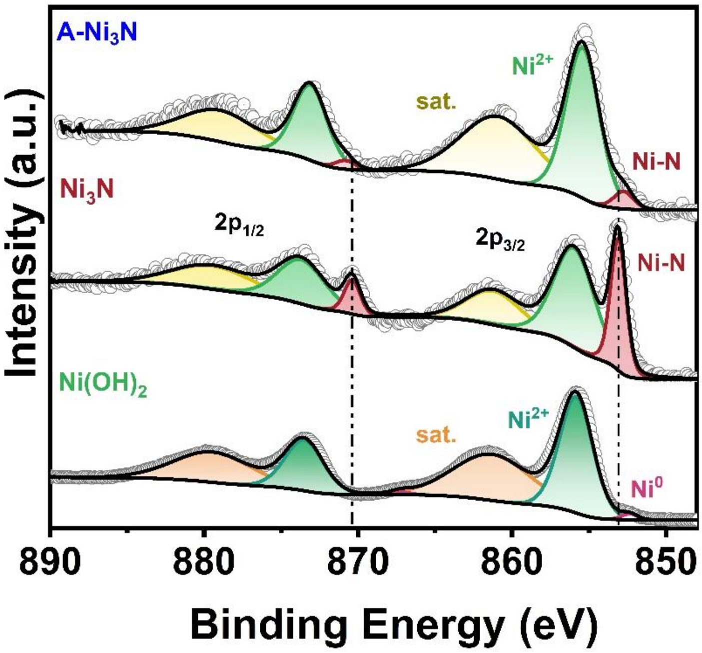

Figure 2.3.4: High resolution Ni 2p XPS spectra for $Ni(OH)_2$, Ni_3N and A-Ni_3N before etching

However, after etching the Ni 2p XPS spectra for A-Ni_3N shows an increase in the intensity of the peak corresponding to Ni-N at 852.3 eV ($2p_{3/2}$) and at 869.5 eV ($2p_{1/2}$) for Ni-N. The peaks at 855.0 eV ($2p_{3/2}$) and 872.8 eV ($2p_{1/2}$) correspond to Ni^{2+}. This could be attributed to the removal of the oxides upon etching *(Figure 2.3.5)*. In the case of Ni_3N, the removal of the surface oxide post-etching resulted in a significant decrease in the intensity of the Ni^{2+} peak at 854.8 eV ($2p_{3/2}$) and 873.1 eV ($2p_{1/2}$), while the intensity of the peak corresponding to Ni-N at 852.6 eV ($2p_{3/2}$) and 869.8 eV ($2p_{1/2}$) does not show any change in the intensity*(Figure 2.3.5)*. Likewise, the Ni 2p XPS spectra for $Ni(OH)_2$ after etching show characteristic peaks at 855.8 eV ($2p_{3/2}$) and 873.6 eV ($2p_{1/2}$) for Ni^{2+}, while the peaks corresponding to Ni^0 appear at 852.5 eV ($2p_{3/2}$) and 869.8 eV ($2p_{1/2}$). Upon comparison of the A-Ni_3N and Ni_3N, it can be observed that the intensity of the peak corresponding to Ni^{2+} increases upon activation. This could be attributed to the increased formation of NiOOH, which is converted to $Ni(OH)_2$ when exposed to the atmosphere.

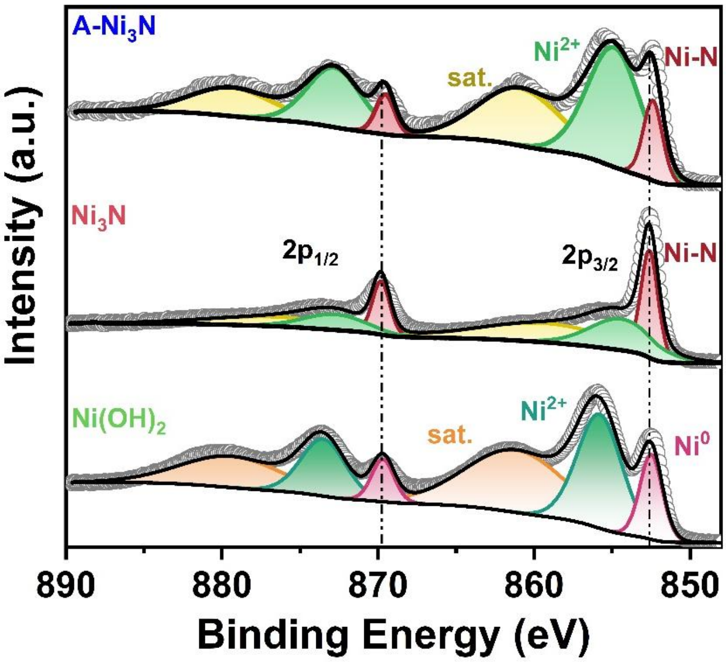

Figure 2.3.5: High resolution Ni 2p XPS spectra for $Ni(OH)_2$, Ni_3N and A-Ni_3N after etching with Ar sputtering for 30 sec

The N1s XPS spectra for A-Ni_3N and Ni_3N *(Figure 2.3.6)* show characteristic peaks for Ni-N bonds at 397.7 eV and 397.8 eV, respectively. The peak at 399.5 eV (A-Ni_3N) and 399.7 eV(Ni_3N) correspond to N-H moieties[17–19]. This further confirms that the as prepared electrode contains abundant Ni-N sites.

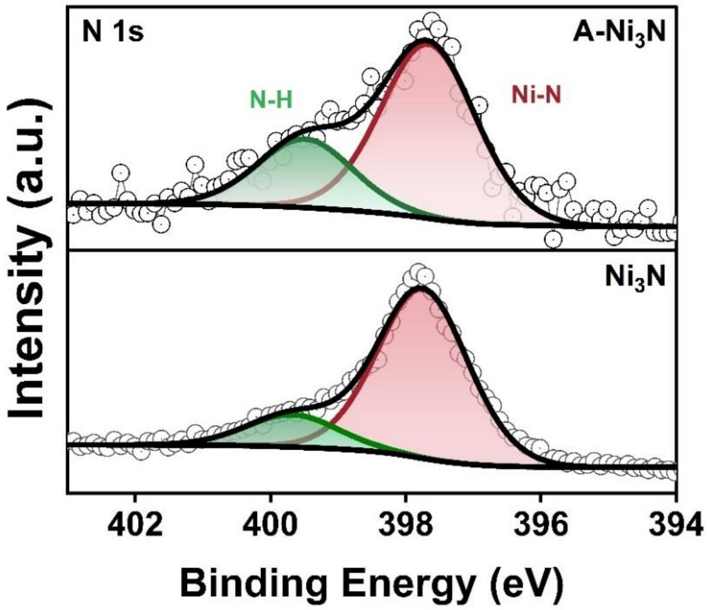

Figure 2.3.6: High resolution N 1s XPS spectra for $Ni(OH)_2$, Ni_3N and A-Ni_3N after etching with Ar sputtering for 30 sec

FESEM analysis was conducted to examine the morphological changes in the catalyst *(Figure 2.3.7)*. Electrodeposited $Ni(OH)_2$ exhibited sheet-like structures of thickness ~ 1 µm, with spongy structures on the surface *(Figure 2.3.7 b)*. After nitridation, the particle size became smaller *(Figure 2.3.7c)*. Subsequent activation through chronopotentiometry in 1M KOH results in the formation of NiOOH on the surface of Ni_3N, transforming the morphology into well-defined dodecahedral structures *(Figure 2.3.7 d)*. Further, the elemental mapping of A-Ni_3N shows uniform dispersion of N and O on the Ni foam *(Figure 2.3.8)*.

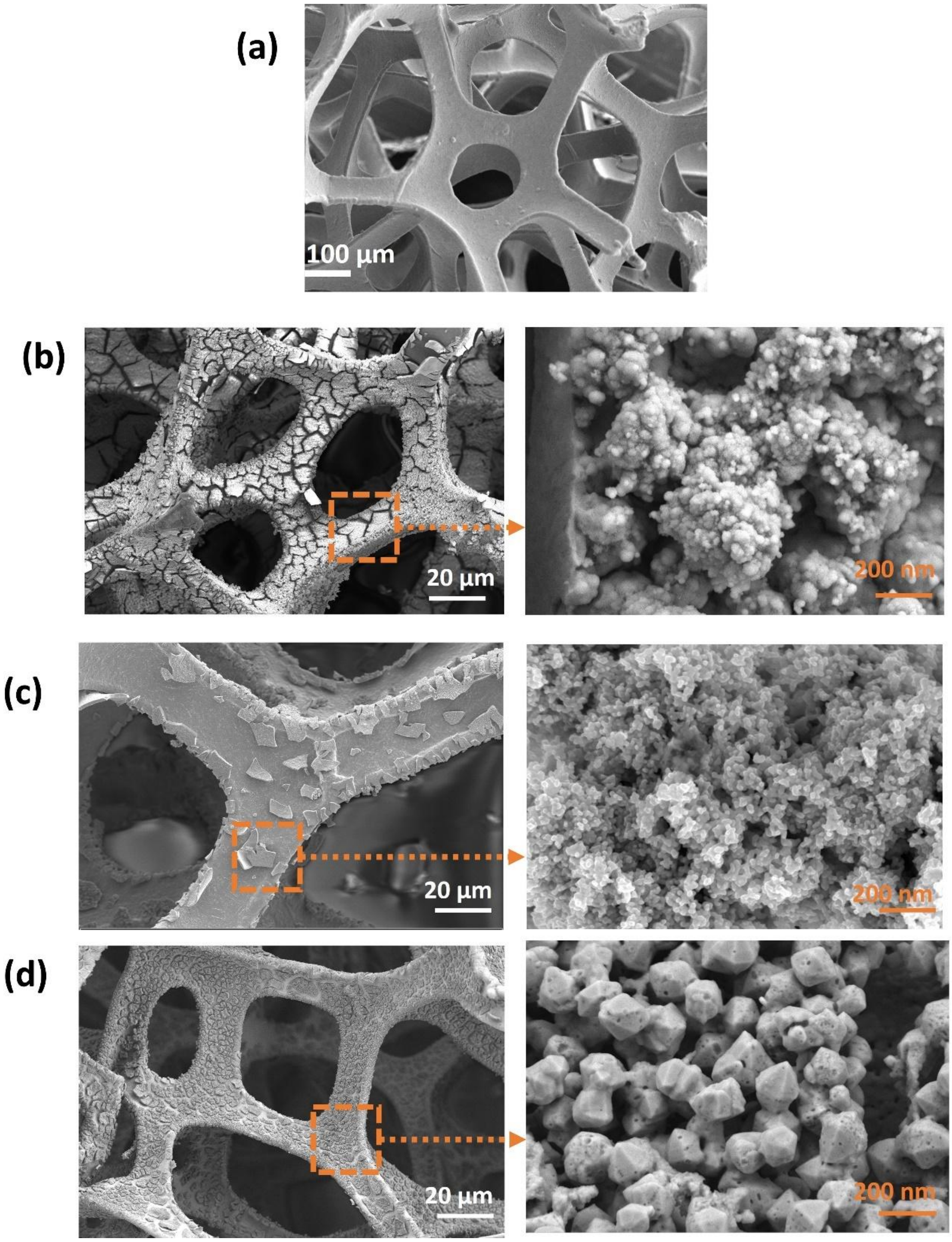

Figure 2.3.7: FESEM image of **(a)** Blank Ni foam, **(b)** Ni foam electrodeposited with $Ni(OH)_2$, **(c)** Ni_3N formed after nitridation, and **(d)** A-Ni_3N formed after activation

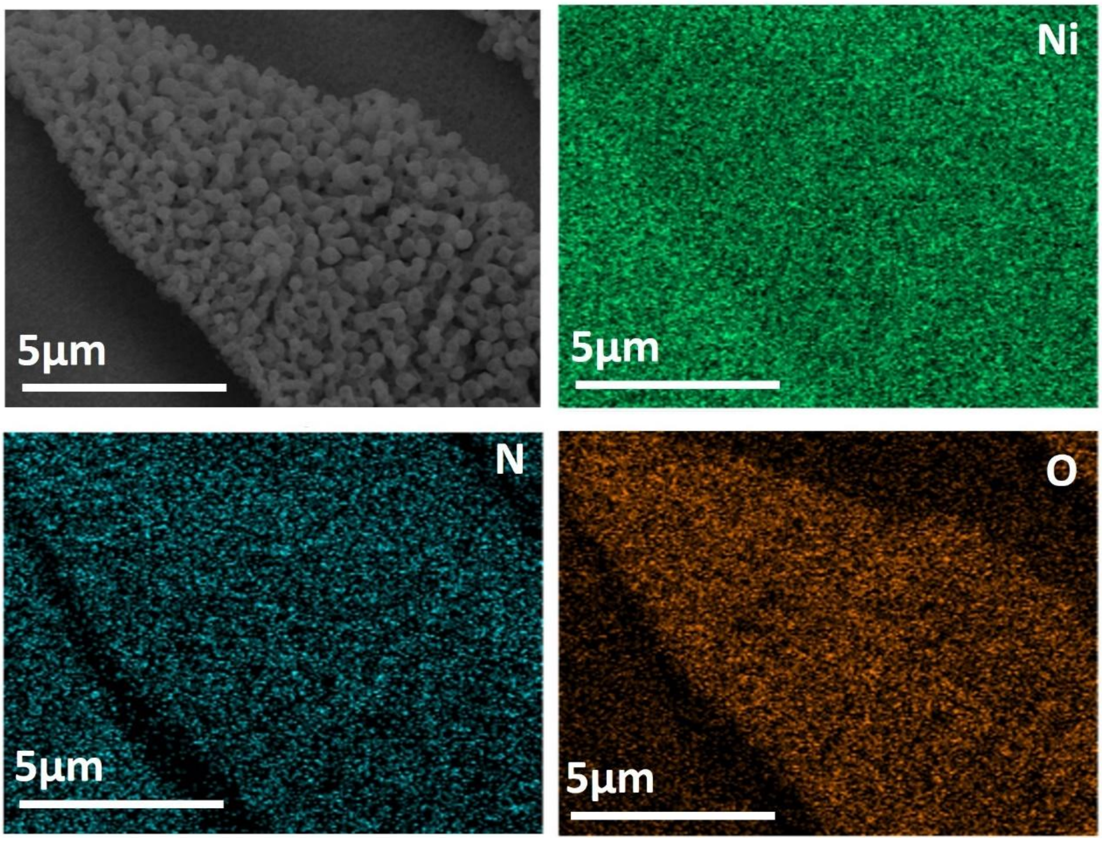

Figure 2.3.8: FESEM-Elemental mapping of A-Ni_3N before reaction

Evaluation of Electrochemical Urea Oxidation

The as prepared working electrode was used to study the urea electrooxidation reaction in the alkaline medium. Performance metrics used to evaluate the catalytic activity are overpotential, stability, Tafel slope, ECSA and charge transfer resistance. First, $Ni(OH)_2$ synthesized by different strategies was tested using linear sweep voltammetry. Herein, $Ni(OH)_2$ prepared by hydrothermal synthesis, $NaBH_4$ assisted synthesis, and electrodeposition were compared. From the linear sweep voltammetry curve, it was observed that electrodeposited $Ni(OH)_2$ outperformed in comparison to the $Ni(OH)_2$ prepared by hydrothermal and $NaBH_4$ assisted synthesis *(Figure 2.3.9)*. Electrodeposited $Ni(OH)_2$ exhibited a maximum current density of 800 mA cm^{-2} at 1.5 V_{RHE} in comparison to hydrothermally synthesized $Ni(OH)_2$, which showed negligible activity, while $Ni(OH)_2$ synthesized using $NaBH_4$ showed a maximum current density of 380 mA cm^{-2} at 1.5 V_{RHE}. Hence, electrodeposited $Ni(OH)_2$ on Ni foam was used for further studies and converted to Ni_3N.

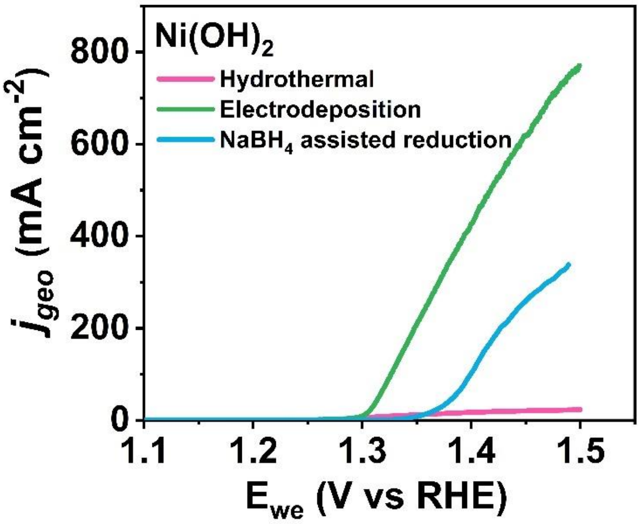

Figure 2.3.9: Linear sweep voltammetry for $Ni(OH)_2$ synthesised by different routes

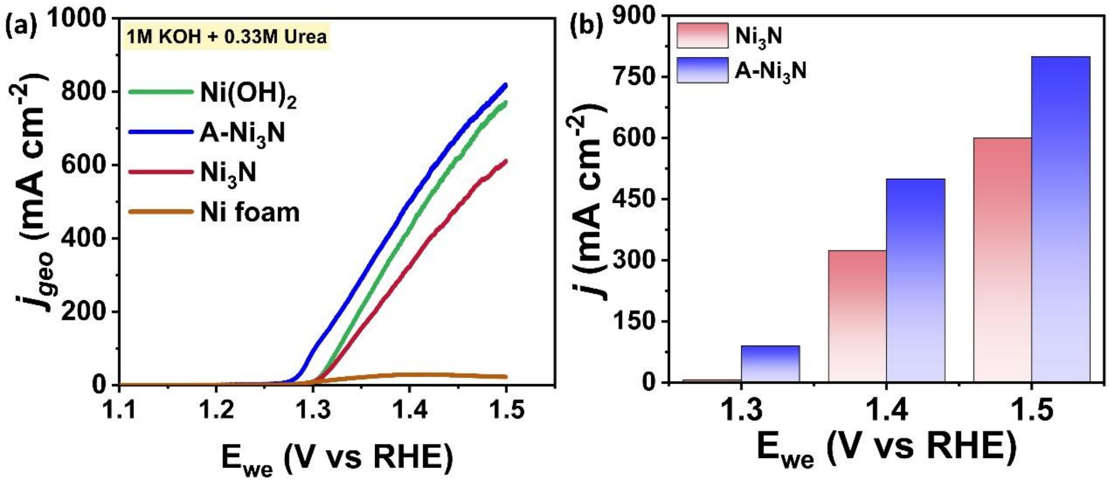

Figure 2.3.10 : (a) Linear sweep voltammogram for $Ni(OH)_2$, Ni_3N, and A-Ni_3N performed in 1 M KOH containing 0.33 M urea and **(b)** Comparison of current density obtained at different potentials for Ni_3N and A-Ni_3N

The polarization curve for $Ni(OH)_2$ exhibits a maximum current density of 780 mA cm^{-2}, while Ni_3N demonstrates a maximum current density of 600 mA cm^{-2} during urea electrooxidation. In comparison to $Ni(OH)_2$, Ni_3N requires a higher overpotential for the reaction. After activation, the overpotential significantly decreases, and the activated Ni_3N (A-Ni_3N) achieves a maximum current density of 800 mA cm^{-2} at 1.5 V_{RHE} *(Figure 2.3.10 a)*. A comparative analysis of current density at different potentials highlights the reduction in overpotential upon activation, underscoring the improved catalytic efficiency of A-Ni_3N *(Figure 2.3.10 b).*

Comparison of UOR activity of A-Ni_3N with OER shows a decrease in the overpotential by 280 mV for urea assisted water electrolysis, making the process energy efficient *(Figure 2.3.11a)*. Moreover, a broad peak is observed at 1.34 V_{RHE}. This peak arises from the oxidation of $Ni(OH)_2$ to NiOOH. However, the onset for urea electrooxidation is found to be at 1.29 V_{RHE}. This is attributed to the oxidation of urea on the pre-formed NiOOH active site upon activation of Ni_3N.

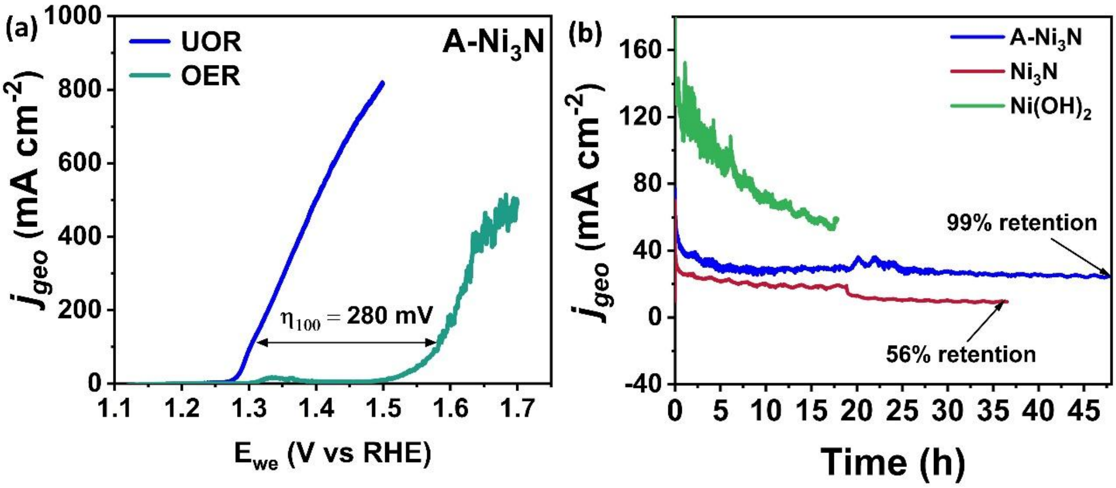

Figure 2.3.11 : (a) Comparison of OER and UOR activity performed in 1 M KOH in the presence and absence of urea, respectively, for A-Ni_3N **(b)** Chronoamperometry at 1.37 V comparing $Ni(OH)_2$, Ni_3N and A-Ni_3N performed in 1 M KOH containing 0.33 M urea

The stability of the catalysts was evaluated through chronoamperometric studies at 1.37 V *(Figure 2.3.11 b)*. The $Ni(OH)_2$ completely loses its performance within 15 h, while Ni_3N retains only 56% of its initial performance after 35 h. On the other hand, the activated Ni_3N (A-Ni_3N) retains 99% of its initial performance even at 48 h. Furthermore, the electrochemical performance of A-Ni_3N at 1.45 V could be repeated over several cycles *(Figure 2.3.12 a)*.

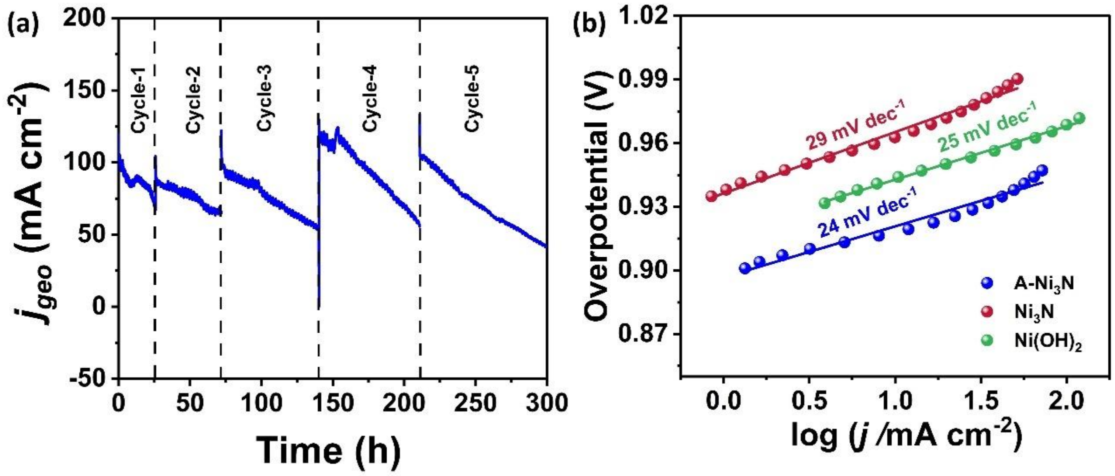

Figure 2.3.12: (a) Chronoamperometry at 1.45 V at 100 mA cm^{-2} current density for A-Ni_3N performed in 1 M KOH containing 0.5 M urea and **(b)** Tafel plots

Tafel slope is a measure of the kinetics of the electrooxidation process *(Figure 2.3.12 b)*. The faster kinetics result in a lower Tafel slope value. Tafel plot shows that upon activation, the value decreases to 24 mV dec^{-1} for A-Ni_3N in comparison to Ni_3N (25 mV dec^{-1}) and $Ni(OH)_2$ (29 mV dec^{-1}). This could be attributed to the faster oxidation of urea on the NiOOH site formed during activation.

To determine the electrochemically active surface area, electrochemical double layer capacitance measurement was performed *(Figure 2.3.13 a-c)*. The double layer capacitance value was determined to be 10.85 mF cm^{-2} for A-Ni_3N, 5.98 mF cm^{-2} for Ni_3N, and 1.54 mF cm^{-2} for $Ni(OH)_2$ *(Figure 2.3.13 d)*. Correspondingly, the ECSA determined were 271.25 cm^2, 149.5 cm^2 and 38.5 cm^2 for A-Ni_3N, Ni_3N and $Ni(OH)_2$ respectively *(Figure 2.3.14 a)*. This shows that nitridation followed by activation significantly increases the electrochemically active surface area. However, the ECSA normalized polarization curve shows that the overall current density decreases upon nitridation and activation *(Figure 2.3.14 b)*. Thus, it can be inferred that nitridation and activation do not improve the intrinsic activity of the catalyst; rather, it creates a greater number of NiOOH sites for the electrooxidation process.

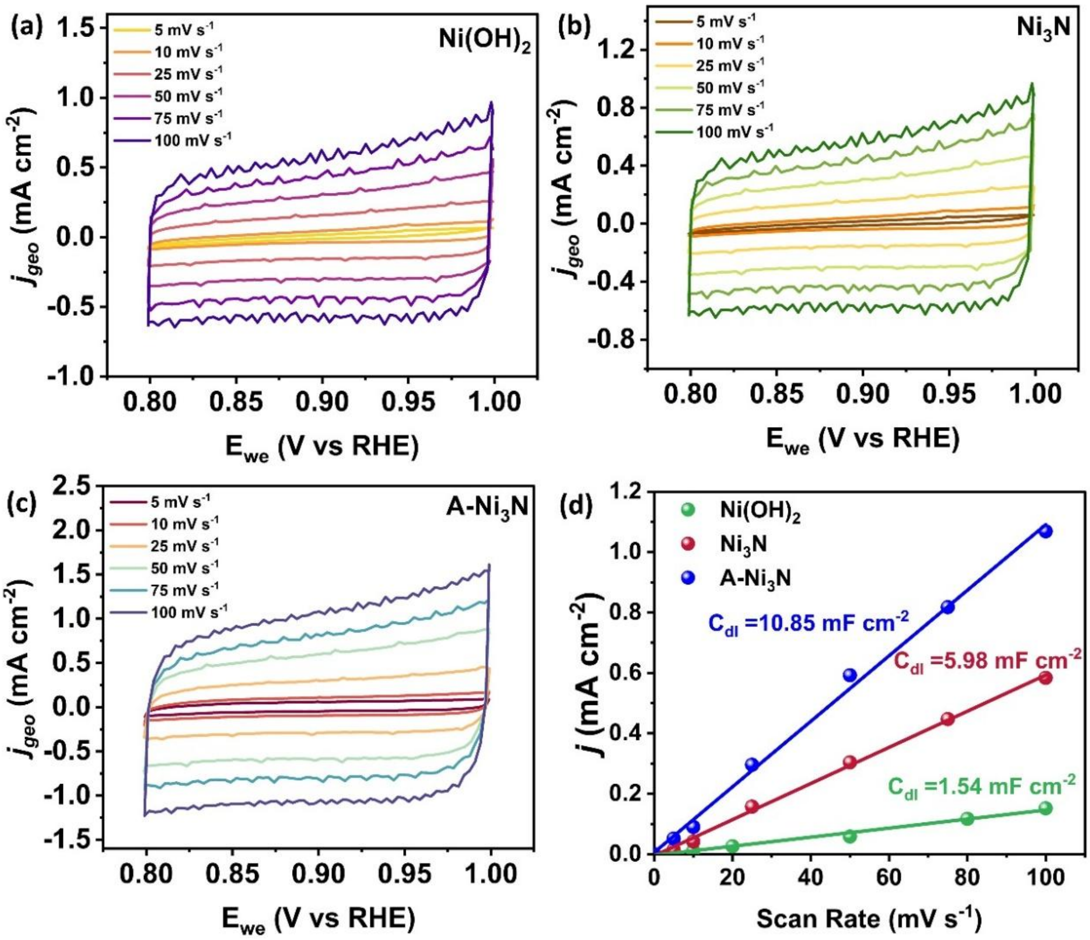

Figure 2.3.13: Cyclic voltammetry plot in the non-faradaic region for **(a)** Ni(OH)$_2$, **(b)** Ni$_3$N, and **(c)** A-Ni$_3$N and **(d)** plot of scan rate vs current density to determine the electrochemical double layer capacitance

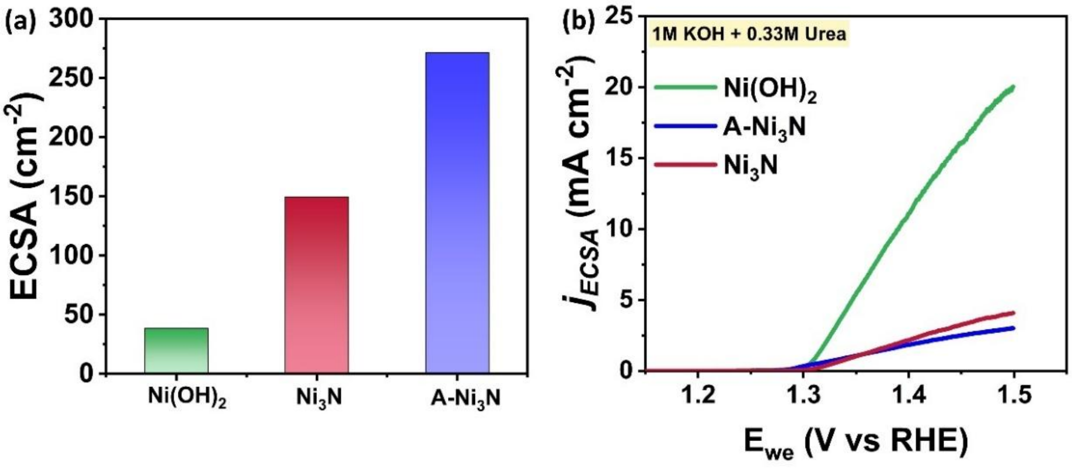

Figure 2.3.14 : (a) Comparison of the electrochemically active surface area obtained by dividing the C$_{dl}$ with a specific capacitance value of 40 µF cm^2 and **(b)** Linear sweep voltammetry showing ECSA normalised current density for Ni(OH)$_2$, Ni$_3$N and A-Ni$_3$N.

As discussed in chapter 2.1, potentiostatic impedance spectroscopy can be used to determine the electrooxidation pathway for urea electrooxidation. For $Ni(OH)_2$, the Bode plot shows one peak in the low frequency region attributed to the direct pathway and a broadening near the high frequency region attributed to the indirect pathway *(Figure 2.3.15 a)*. From this, it can be concluded that the catalyst exhibits a combination of direct and indirect pathways. Upon nitridation, Ni_3N shows only one peak in the low frequency and no peak/ broadening near the high frequency region, indicating that Ni_3N follows only a direct pathway for urea electrooxidation. Similarly, A-Ni_3N follows a direct pathway, as is evidenced by the single peak in the low frequency region of the Bode plot *(Figure 2.3.15 b)*.

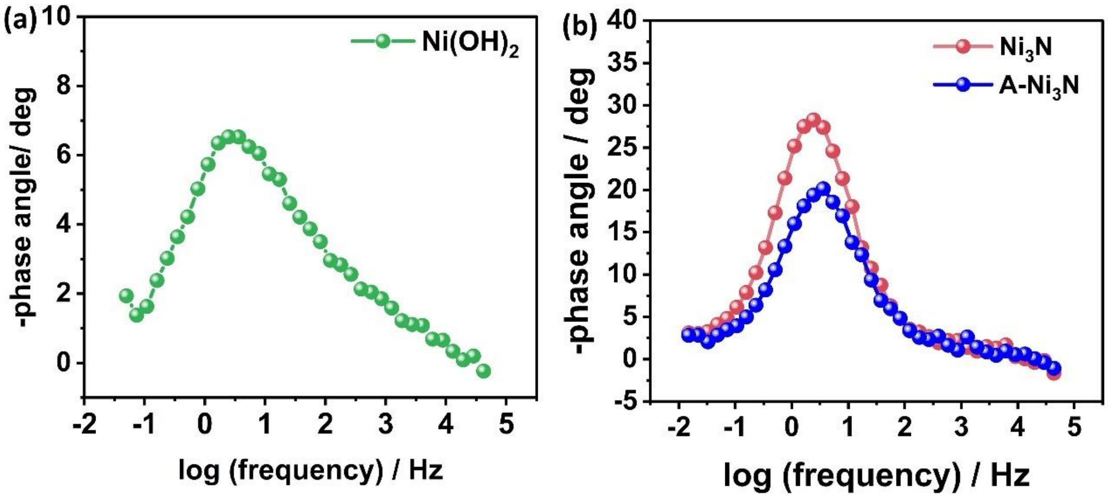

Figure 2.3.15: Bode plot obtained from potentiostatic impedance spectroscopy for **(a)** $Ni(OH)_2$ and **(b)** Ni_3N and A-Ni_3N

The Nyquist plot was used to determine the charge transfer resistance associated with the electrooxidation pathway *(Figure 2.3.16)*. It was observed that the charge transfer resistance associated with $Ni(OH)_2$ was significantly lower in comparison to that of Ni_3N and A-Ni_3N. This could be attributed to the increased number of accessible active sites consisting of NiOOH, resulting in a faster electrooxidation process. In comparison, Ni_3N and A-Ni_3N show an increase in the charge transfer resistance, which could be attributed to the slower electrooxidation process.

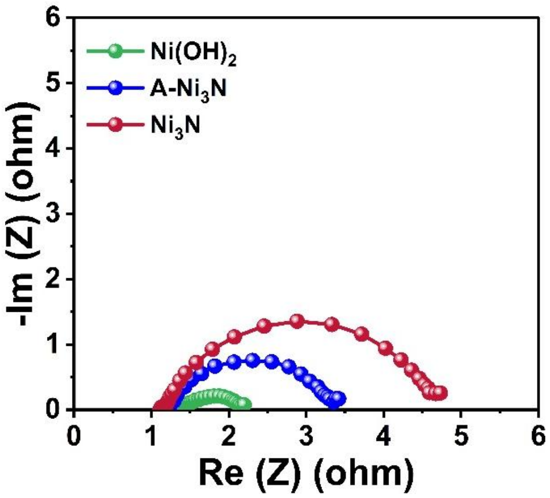

Figure 2.3.16: Comparison of Nyquist plot obtained from potentiostatic impedance spectroscopy for Ni(OH)$_2$, Ni$_3$N and A-Ni$_3$N

To determine the charge transfer resistance value, the Nyquist plots were fitted with the equivalent circuit. The Nyquist plot for Ni(OH)$_2$ was fitted with the equivalent circuit 1, shown in *Figure 2.3.17 (a)*. Here, Rs stands for the solution resistance, which is in series with the parallel components R1/Q1 and R2/Q2. R1 and Q1 represent the charge transfer resistance and constant phase element, respectively, associated with the direct pathway. R2 and Q2 represent the charge transfer resistance, and the double layer capacitance associated with the indirect pathway[21,22]. From the fitting, R1 and R2 values were estimated to be 0.52 Ω and 0.38 Ω (*Figure 2.3.17 c)*. The Nyquist plot for Ni$_3$N and A-Ni$_3$N were fitted with the equivalent circuit 2 shown in *Figure 2.3.17 b)*. Here, Rs stands for the solution resistance, which is in series with the parallel components R1/Q1. R1 and Q1 stand for the charge transfer resistance and double layer capacitance associated with the direct pathway, respectively[23]. The charge transfer resistance (R1) associated with Ni$_3$N and A-Ni$_3$N were estimated to be 3.6 Ω and 2.2 Ω, respectively, *(Figure 2.3.17 d, e)*. From these values, it can be concluded that activation results in the formation of an increased number of NiOOH sites, which leads to an enhancement in the kinetics of the reaction. This results in a decrease in the charge transfer resistance. A plot of comparison for the charge transfer resistance for the three catalysts is shown in *Figure 2.3.17 (f)*.

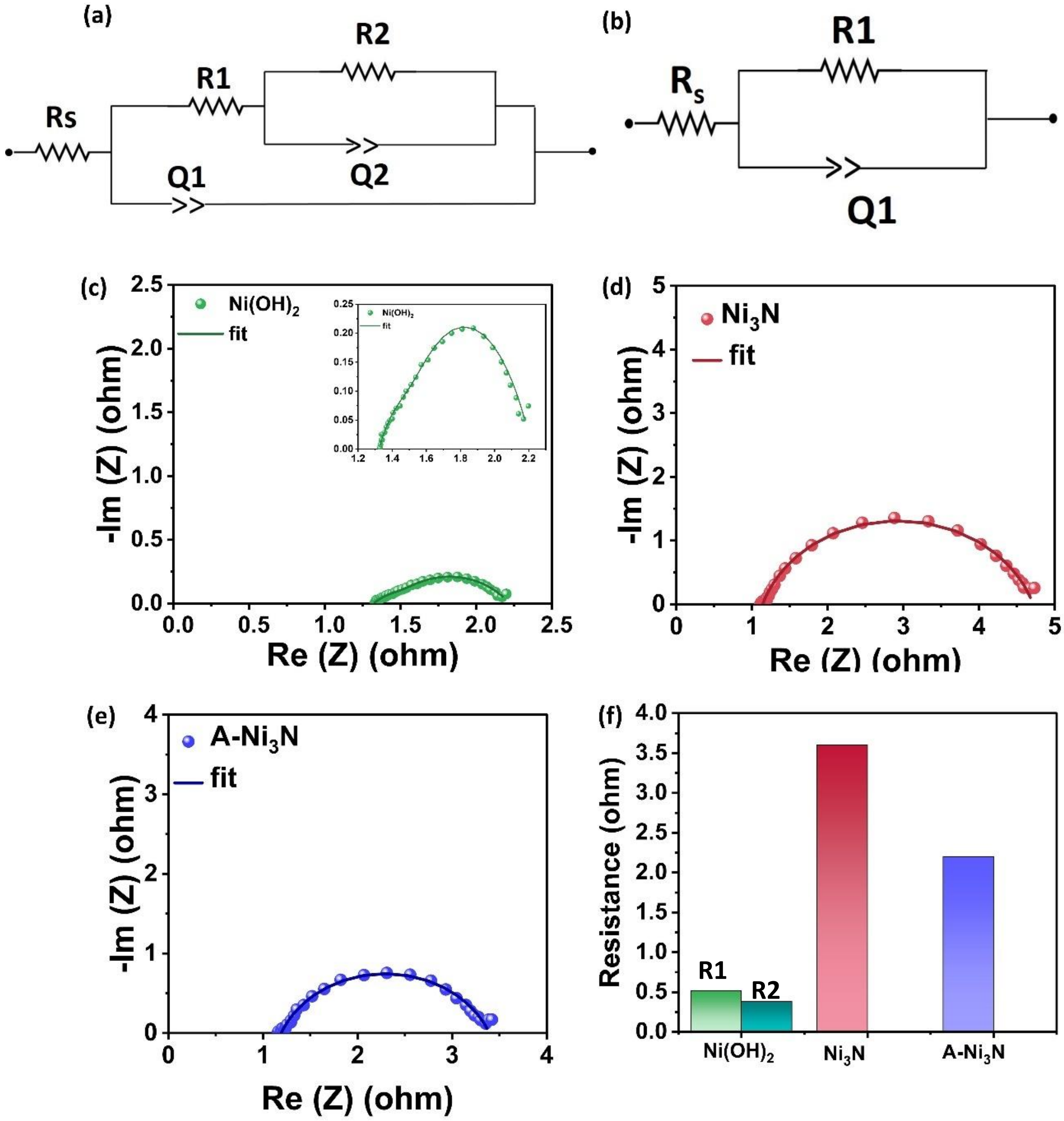

Figure 2.3.17: (a) Equivalent circuit 1 for a combination of indirect and direct pathway, **(b)** Equivalent circuit 2 for direct pathway, **(c)** Nyquist plot for $Ni(OH)_2$ fitted using equivalent circuit 1, **(d)** Nyquist plot for Ni_3N fitted using equivalent circuit 2, **(e)** Nyquist plot for A-Ni_3N fitted using equivalent circuit 2 and **(f)** Comparison of charge transfer resistance values obtained after fitting. The green bar denotes the charge transfer resistance associated with the direct (R1) and indirect pathway (R2) in $Ni(OH)_2$. The red and blue bars indicate the charge transfer resistance associated with the direct pathway (R1) for Ni_3N and A-Ni_3N.

In the case of the direct pathway, the urea electrooxidation takes place on the NiOOH site. Following the electrooxidation, NiOOH does not undergo reduction to $Ni(OH)_2$. The products formed get desorbed from the catalytic site, making it available for the oxidation of other urea molecules[23]. This mechanism was studied using the operando Raman spectroscopy *(Figure 2.3.18)*. Before the reaction, The Raman spectra did not show any characteristic peak for NiOOH. After activation of Ni_3N in 1 M KOH (A-Ni_3N), a peak corresponding to the Ni-O bond of NiOOH was observed at 468 cm^{-1} (Eg) and 554 cm^{-1} (A1g) along with a small peak at 996.6 cm^{-1} corresponding to C-N stretching of the urea molecule[24,25]. During the chronoamperometry at 1.5 V_{RHE}, the urea electrooxidation takes place on the NiOOH site. The intensity of the peak corresponding to the Ni-O bond does not show any change. However, after the reaction, the intensity of the Ni-O peak decreases and eventually disappears. This could be attributed to the fact that post-reaction, the indirect pathway takes over. As a result, the chemical oxidation of urea takes place, resulting in the simultaneous reduction of NiOOH to $Ni(OH)_2$.

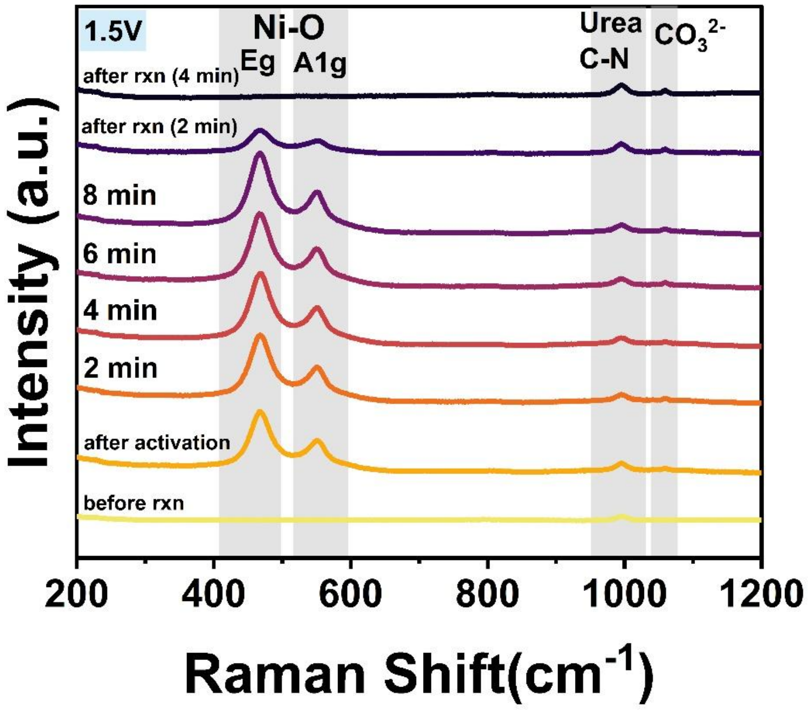

Figure 2.3.18: Operando Raman spectroscopy measurement performed in 1M KOH containing 0.33 M urea.

FESEM of the A-Ni_3N electrode after reaction for 300 h at 100 mA cm^{-2} shows a change in morphology. The dodecahedrons formed upon activation get converted to flake like structures, as shown in *Figure 2.3.19*. However, the elemental mapping shows the uniform distribution of N and O on the electrode *(Figure 2.3.20).*

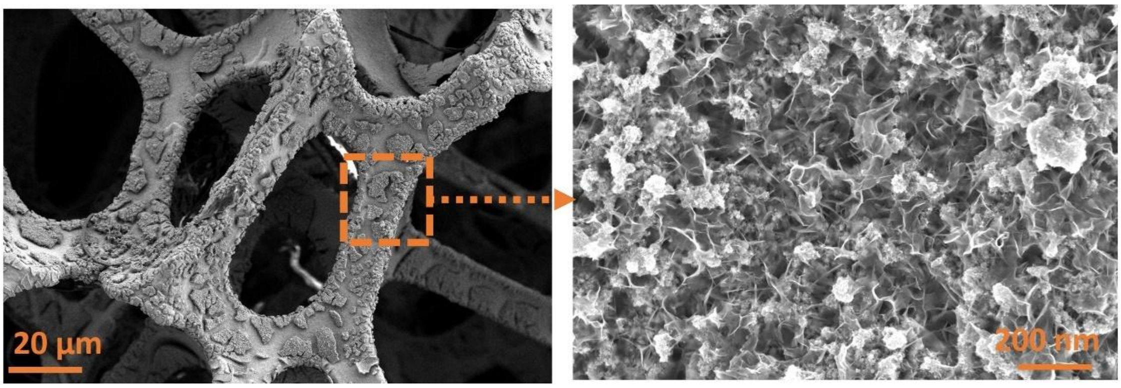

Figure 2.3.19: FESEM image of A-Ni_3N after chronoamperometry for 300 h at a current density of 100 mA cm^{-2}

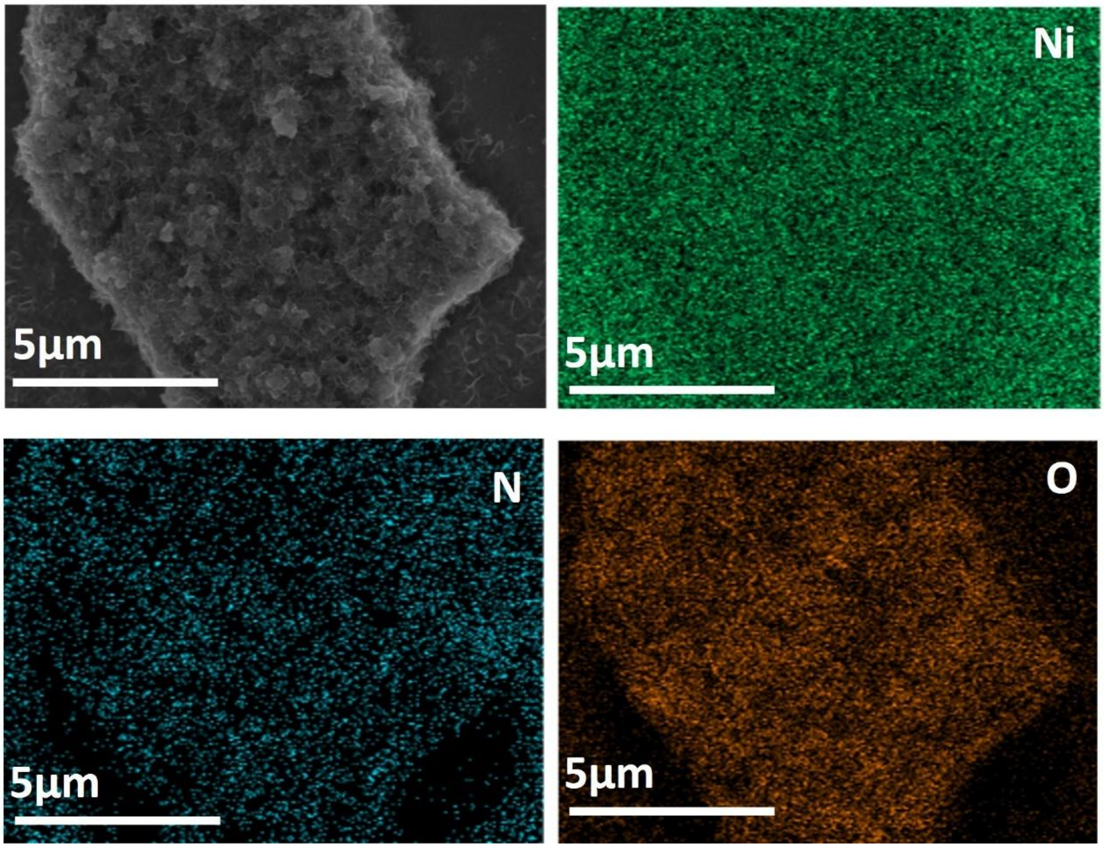

Figure 2.3.20: FESEM elemental mapping of A-Ni_3N after chronoamperometry for 300 h at a current density of 100 mA cm^{-2}

The Ni 2p XPS spectra were collected for A-Ni_3N post-reaction (*Figure 2.3.21*). Before etching, the peak corresponding to Ni^{2+} is observed at 855.4 eV ($2p_{3/2}$) and at 873.3 eV ($2p_{1/2}$). This peak is attributed to $Ni(OH)_2$, which is formed by the reduction of NiOOH. The peaks corresponding to Ni-N are not observed. However, upon removal of the surface oxides by Ar sputtering, the peak for Ni-N appears at 852.6 eV ($2p_{3/2}$) and 869.8 eV ($2p_{1/2}$), while the peaks for $Ni(OH)_2$ appear at 855.0 eV ($2p_{3/2}$) and at 872.9 eV ($2p_{1/2}$).

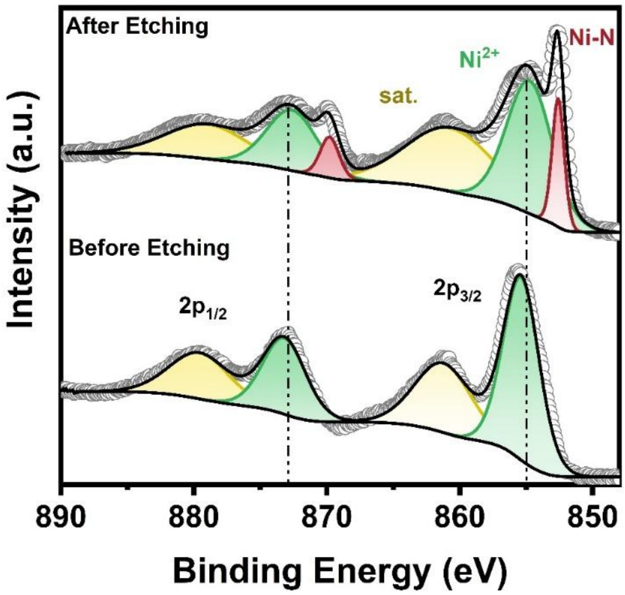

Figure 2.3.21: High resolution Ni 2p XPS spectra of A-Ni_3N post reaction obtained before and after etching with Ar sputtering

2.3.5. Conclusion

In this work, A-Ni_3N supported on Ni foam was synthesized by the chronopotentiometric activation of the Ni_3N. A-Ni_3N showed enhanced urea electrooxidation activity in comparison to Ni_3N and $Ni(OH)_2$. Stability in performance for UOR for 300 h at 100 mA cm^{-2} was achieved. Additionally, A-Ni_3N achieved a maximum current density of 800 mA cm^{-2} at 1.5 V_{RHE}. FESEM analysis revealed significant surface morphological changes upon activation, with the shapeless particles transforming into dodecahedral structures. Furthermore, PEIS analysis showed that A-Ni_3N and Ni_3N followed a direct pathway wherein the NiOOH sites are retained post urea electrooxidation. In comparison, $Ni(OH)_2$ follows a combination of direct and indirect pathways. Operando Raman spectroscopy was used to gain mechanistic insights. It was observed that during the reaction, NiOOH sites were retained. However, post-reaction, the indirect pathway takes over, and the NiOOH is gradually reduced to $Ni(OH)_2$ following the chemical oxidation of urea.

2.3.6. Reference

(1) Zhong, Y.; Xia, X.; Shi, F.; Zhan, J.; Tu, J.; Fan, H. J. Transition Metal Carbides and Nitrides in Energy Storage and Conversion. *Advanced Science* **2016**, *3* (5), 1500286. https://doi.org/10.1002/advs.201500286.

(2) Wang, H.; Li, J.; Li, K.; Lin, Y.; Chen, J.; Gao, L.; Nicolosi, V.; Xiao, X.; Lee, J.-M. Transition Metal Nitrides for Electrochemical Energy Applications. *Chem Soc Rev* **2021**, *50* (2), 1354–1390. https://doi.org/10.1039/D0CS00415D.

(3) Jamil, R.; Ali, R.; Loomba, S.; Xian, J.; Yousaf, M.; Khan, K.; Shabbir, B.; McConville, C. F.; Mahmood, A.; Mahmood, N. The Role of Nitrogen in Transition-Metal Nitrides in Electrochemical Water Splitting. *Chem Catalysis* **2021**, *1* (4), 802–854. https://doi.org/10.1016/j.checat.2021.06.014.

(4) Chen, J. G. Carbide and Nitride Overlayers on Early Transition Metal Surfaces: Preparation, Characterization, and Reactivities. *Chem Rev* **1996**, *96* (4), 1477–1498. https://doi.org/10.1021/cr950232u.

(5) Shalom, M.; Ressnig, D.; Yang, X.; Clavel, G.; Fellinger, T. P.; Antonietti, M. Nickel Nitride as an Efficient Electrocatalyst for Water Splitting. *J Mater Chem A Mater* **2015**, *3* (15), 8171–8177. https://doi.org/10.1039/C5TA00078E.

(6) Song, F.; Li, W.; Yang, J.; Han, G.; Liao, P.; Sun, Y. Interfacing Nickel Nitride and Nickel Boosts Both Electrocatalytic Hydrogen Evolution and Oxidation Reactions. *Nat Commun* **2018**, *9* (1), 4531. https://doi.org/10.1038/s41467-018-06728-7.

(7) Irfan, M.; Khan, I. U.; Wang, J.; Li, Y.; Liu, X. 3D Porous Nanostructured Ni3N–Co3N as a Robust Electrode Material for Glucose Fuel Cell. *RSC Adv* **2020**, *10* (11), 6444–6451. https://doi.org/10.1039/C9RA08812A.

(8) Lin, X.; Wen, H.; Zhang, D.-X.; Cao, G.-X.; Wang, P. Highly Dispersed Nickel Nitride Nanoparticles on Nickel Nanosheets as an Active Catalyst for Hydrazine Electrooxidation. *J Mater Chem A Mater* **2020**, *8* (2), 632–638. https://doi.org/10.1039/C9TA11023B.

(9) Tareen, A. K.; Priyanga, G. S.; Khan, K.; Pervaiz, E.; Thomas, T.; Yang, M. Nickel-Based Transition Metal Nitride Electrocatalysts for the Oxygen Evolution Reaction. *ChemSusChem* **2019**, *12* (17), 3941–3954. https://doi.org/10.1002/cssc.201900553.

(10) Wang, T.; Miao, L.; Zheng, S.; Qin, H.; Cao, X.; Yang, L.; Jiao, L. Interfacial Engineering of Ni3N/Mo2N Heterojunctions for Urea-Assisted Hydrogen Evolution Reaction. *ACS Catal* **2023**, *13* (7), 4091–4100. https://doi.org/10.1021/acscatal.3c00113.

(11) Li, R.-Q.; Liu, Q.; Zhou, Y.; Lu, M.; Hou, J.; Qu, K.; Zhu, Y.; Fontaine, O. 3D Self-Supported Porous Vanadium-Doped Nickel Nitride Nanosheet Arrays as

Efficient Bifunctional Electrocatalysts for Urea Electrolysis. *J Mater Chem A Mater* **2021**, *9* (7), 4159–4166. https://doi.org/10.1039/D0TA09473K.

(12) Li, M.; Wu, X.; Liu, K.; Zhang, Y.; Jiang, X.; Sun, D.; Tang, Y.; Huang, K.; Fu, G. Nitrogen Vacancies Enriched Ce-Doped Ni3N Hierarchical Nanosheets Triggering Highly-Efficient Urea Oxidation Reaction in Urea-Assisted Energy-Saving Electrolysis. *Journal of Energy Chemistry* **2022**, *69*, 506–515. https://doi.org/10.1016/j.jechem.2022.01.031.

(13) Zhao, Z.; Zhao, J.; Wang, H.; Li, X.; Yang, L.; Zhao, Z.; Liu, X.; Liu, Y.; Liu, P.; Cai, Z. Porous Flower-like Nickel Nitride as Highly Efficient Bifunctional Electrocatalysts for Less Energy-Intensive Hydrogen Evolution and Urea Oxidation. *Int J Hydrogen Energy* **2020**, *45* (28), 14199–14207. https://doi.org/10.1016/j.ijhydene.2019.11.007.

(14) Maity, S.; Harish, S.; Eswaramoorthy, M. Controlled Galvanic Replacement of Ni in Ni(OH)2 by Pd: A Method to Quantify Metallic Ni and to Synthesize Bimetallic Catalysts for Methanol Oxidation. *Mater Chem Phys* **2019**, *221*, 377–381. https://doi.org/10.1016/j.matchemphys.2018.09.071.

(15) Yan, Z.; Sun, H.; Chen, X.; Liu, H.; Zhao, Y.; Li, H.; Xie, W.; Cheng, F.; Chen, J. Anion Insertion Enhanced Electrodeposition of Robust Metal Hydroxide/Oxide Electrodes for Oxygen Evolution. *Nat Commun* **2018**, *9* (1), 2373. https://doi.org/10.1038/s41467-018-04788-3.

(16) Hu, S.; Wang, S.; Feng, C.; Wu, H.; Zhang, J.; Mei, H. Novel MOF-Derived Nickel Nitride as High-Performance Bifunctional Electrocatalysts for Hydrogen Evolution and Urea Oxidation. *ACS Sustain Chem Eng* **2020**, *8* (19), 7414–7422. https://doi.org/10.1021/acssuschemeng.0c01450.

(17) Zhang, B.; Wang, J.; Liu, J.; Zhang, L.; Wan, H.; Miao, L.; Jiang, J. Dual-Descriptor Tailoring: The Hydroxyl Adsorption Energy-Dependent Hydrogen Evolution Kinetics of High-Valance State Doped Ni3N in Alkaline Media. *ACS Catal* **2019**, *9* (10), 9332–9338. https://doi.org/10.1021/acscatal.9b01637.

(18) Gao, X.; Li, X.; Yu, Y.; Kou, Z.; Wang, P.; Liu, X.; Zhang, J.; He, J.; Mu, S.; Wang, J. Synergizing Aliovalent Doping and Interface in Heterostructured NiV Nitride@oxyhydroxide Core-Shell Nanosheet Arrays Enables Efficient Oxygen Evolution. *Nano Energy* **2021**, *85*, 105961. https://doi.org/10.1016/j.nanoen.2021.105961.

(19) Song, F.; Li, W.; Yang, J.; Han, G.; Liao, P.; Sun, Y. Interfacing Nickel Nitride and Nickel Boosts Both Electrocatalytic Hydrogen Evolution and Oxidation Reactions. *Nat Commun* **2018**, *9* (1), 4531. https://doi.org/10.1038/s41467-018-06728-7.

(20) Grosvenor, A. P.; Biesinger, M. C.; Smart, R. S. C.; McIntyre, N. S. New Interpretations of XPS Spectra of Nickel Metal and Oxides. *Surf Sci* **2006**, *600* (9), 1771–1779. https://doi.org/10.1016/j.susc.2006.01.041.

(21) Guo, F.; Ye, K.; Du, M.; Huang, X.; Cheng, K.; Wang, G.; Cao, D. Electrochemical Impedance Analysis of Urea Electro-Oxidation Mechanism on Nickel Catalyst in Alkaline Medium. *Electrochim Acta* **2016**, *210*, 474–482. https://doi.org/10.1016/j.electacta.2016.05.149.

(22) Guo, F.; Ye, K.; Du, M.; Huang, X.; Cheng, K.; Wang, G.; Cao, D. Electrochemical Impedance Analysis of Urea Electro-Oxidation Mechanism on Nickel Catalyst in Alkaline Medium. *Electrochim Acta* **2016**, *210*, 474–482. https://doi.org/10.1016/j.electacta.2016.05.149.

(23) Rao, N. N.; Alex, C.; Mukherjee, M.; Roy, S.; Tayal, A.; Datta, A.; John, N. S. Evidence for Exclusive Direct Mechanism of Urea Electro-Oxidation Driven by In Situ-Generated Resilient Active Species on a Rare-Earth Nickelate. *ACS Catal* **2024**, *14* (2), 981–993. https://doi.org/10.1021/acscatal.3c04967.

(24) Yang, X.; Zhang, H.; Yu, B.; Liu, Y.; Xu, W.; Wu, Z. An Unveiled Electrocatalysis Essence of NiCo Hydroxides through in Situ Raman Spectroscopy for Urea Oxidation. *Energy Technology* **2022**, *10* (5), 2101010. https://doi.org/10.1002/ente.202101010.

(25) Yang, X.; Zhang, H.; Xu, W.; Yu, B.; Liu, Y.; Wu, Z. A Doping Element Improving the Properties of Catalysis: In Situ Raman Spectroscopy Insights into Mn-Doped NiMn Layered Double Hydroxide for the Urea Oxidation Reaction. *Catal Sci Technol* **2022**, *12* (14), 4471–4485. https://doi.org/10.1039/d2cy00308b.

Conclusions and Future Outlook

The increasing demand for energy has resulted in excessive burning of fossil fuels leading to increased greenhouse gas emissions of which the major contributor is CO_2. Hence there is a need to develop technologies which can help in mitigating the emitted CO_2. To address this challenge, this work focusses on development of nanostructured materials for applications in CO_2 utilisation and urea electrooxidation. Nanostructured materials have garnered significant attention in catalysis for their high surface area, enhanced reactivity from unique nanoscale properties, and tunable sizes, shapes, and compositions. In bimetallic systems, nanostructuring promotes synergistic interactions between elements, further boosting catalytic efficiency.

Chapter 1.1 of this thesis emphasizes the importance of developing carbon utilisation technologies to mitigate the emitted CO_2. It explores thermocatalytic and electrocatalytic methods for CO_2 conversion discussing their mechanistic pathways, challenges and the various catalysts studied. Chapter 1.2 deals with the development of NiPd/C_3N_4 for the hydrogenation of CO_2 to formic acid. Herein various characterisation techniques and operando studies have been used to understand the nature of the active site and gain insights into the mechanistic pathway. The synergistic interaction between Ni, Pd, and C_3N_4 was found to enhance catalytic activity. However, catalyst exfoliation during the reaction led to a loss in catalytic performance over successive cycles. Anchoring NiPd/C_3N_4 on a suitable support while preserving its activity could help in addressing this issue. Furthermore, the catalyst can be made cost effective by developing noble-metal-free catalysts. Chapter 1.3. deals with investigation of trimetallic CuSnBi catalyst for electrochemical reduction of CO_2 to formate. Herein the improvement in the activity of the CuSn catalyst was attributed to the increased formation of the stable CuO_x-SnO_x interface by the incorporation of Bi_2O_3. CuSnBi showed higher selectivity for formate in comparison to CuSn and SnO_2 catalyst. Further studies using flow cells can be performed to evaluate its scalability for industrial applications.

Chapter 2.1 highlights the importance of H_2 economy as a cleaner and sustainable alternative to the conventional energy production. It explores electrochemical water splitting, highlighting its challenges followed by a discussion on urea assisted water electrolysis (UOR) as an energy efficient alternative. $Ni(OH)_2$ has been identified as the main catalyst for urea oxidation. However, sluggish kinetics associated with the 6 electron transfer process and active site poisoning presents itself as a major challenge for this reaction. In chapter 2.2, inspired by the CO binding ability of the noble metals, $Ni(OH)_2$ has been modified by the incorporation of Pd. This leads to an improvement in the intrinsic activity of the catalyst resulting in enhanced kinetics and stability. Chapter 2.3 deals with modified Ni_3N, as a potential catalyst for urea oxidation. The A-Ni_3N catalyst shows a significant enhancement in the electrochemical activity achieving a high current density of 800 mA cm^{-2}. Furthermore, operando Raman spectroscopy and PEIS were used to gain an in depth understanding of the urea electrooxidation pathway on the catalyst. While these catalysts exhibit exceptional activity for UOR, further development is needed to make them bifunctional. They can be tested in MEA electrolysers to evaluate their potential for H_2 production at a commercial scale. The urea electrooxidation can be combined with other reduction reactions such as CO_2 electroreduction or nitrate reduction to reduce the overpotential for the overall electrolysis process. Furthermore, designing a catalyst that is active for both ORR and UOR can be used for developing Zn-urea batteries.

List of Publications

List of Publications based on thesis

1. **Nijita Mathew**, Radha Rathod, Sougata Saha, Pralay K. Santra, Swapan K. Pati, M. Eswaramoorthy, Engineering $Ni(OH)_2$ with Pd for Efficient Electrochemical Urea Oxidation., *Chem. Asian J.*, 2025, 20, e202401188.
2. **Nijita Mathew**, Radha Rathod, Pralay K. Santra, M. Eswaramoorthy, Work in tandem- CO_2 hydrogenation over $NiPd/C_3N_4$ (manuscript under preparation)
3. **Nijita Mathew**, M. Eswaramoorthy Synergistic Effects of Bismuth on CO_2 electroreduction to formate in Cu-Sn catalyst. (manuscript under preparation)
4. **Nijita Mathew**, M. Eswaramoorthy Elucidating the urea electrooxidation pathway on Ni_3N (manuscript under preparation)

List of miscellaneous publications

1. Soumita Chakraborty, Daizy Kalita, Sakshi Agarwal, Surishi Vashishth, **Nijita Mathew**, Sisir Maity, Devender Goud, Ankit Rao, Sebastian C. Peter, Abhishek K. Singh, Muthusamy Eswaramoorthy, Tuning the electrocatalytic activity Pd nanocatalysts towards hydrogen evolution and carbondioxide reduction reaction by Nickel incorporation., *Chemistry of Materials***,** 2024, 36, 13, 6547–6557

2. Ashish Singh, Soumitra Barman, Faruk Ahamed Rahimi, Anupam Dey, Rohan Jena, Ravi Kumar, **Nijita Mathew**, Dibyendu Bhattacharyya and Tapas Kumar Maji, Atomically dispersed Co2+ in a redox-active COF for electrochemical CO2 reduction to ethanol: unravelling mechanistic insight through operando studies**.** *Energy & Environmental Science*, 2024, 17, 6, 2315–2325.

Response to Comments

Comment 1: In terms of turnover number, the NiPd/C_3N_4 catalyst had the highest of all tested catalysts. It was unclear how this related to overall conversion though, so there was some ambiguity in the meaning of this.

Response 1: The conversion cannot be calculated from the turnover number. However, the % conversion can be calculated from the solubility of CO_2 under the reaction conditions employed as well as the product formed as quantified by NMR.

The reaction conditions employed in this work: 30 mg catalyst, 348 K, 20 bar CO_2, 20 bar H_2, 10ml solution of 0.5 M Na_2CO_3

Under the above reaction conditions, the number of moles of formate formed = 0.00479 mols

From the literature, the molality of CO_2 dissolved in a solution of 0.43 moles of K_2CO_3 in 1 kg of water at 22 bar and 353 K = 0.647 mol kg^{-1}

(*Data obtained from reference: Kamps et al, Solubility of CO_2 in Aqueous Solutions of KCl and in Aqueous Solutions of K_2CO_3, J. Chem. Eng. Data, 2007, 52, 3, 817–832*)

Since the density of aqueous solution is 1 g/mL, the number of moles of dissolved CO_2 in 1000 mL of aqueous solution of K_2CO_3 = 0.647 mols

Hence, number of moles of CO_2 soluble in 10 mL of K_2CO_3 would be:

$$n_{CO2} = \frac{0.647}{1000} \times 10 = 0.00647 \text{ mols}$$

We know, $CO_2 + H_2 \rightarrow HCOOH$

Therefore, 1 mol of CO_2 produces 1 mol of HCOOH

Therefore, $$\% \text{ Conversion} = \frac{\text{Total moles of formate formed}}{\text{Total moles of soluble } CO_2} \times 100$$

Hence, $$\% \text{ Conversion} = \frac{0.00479}{0.00647} \times 100 = \mathbf{74.2\%}$$

Comment 2: I question much of the ATR work especially how they achieved surface sensitivity and how they saw multiple intermediates that are beyond the rate limiting step. One would expect very low surface coverages of these species. The student should clarify the results obtained via the ATR-FTIR

Response 2: In case of ATR-FTIR, the interaction of the incident IR beam with the ATR crystal results in total internal reflection. This results in generation of evanescent wave which interacts with the sample. To achieve high sensitivity, the interaction of the sample with evanescent wave is enhanced. This is achieved by multiple total internal reflection of the IR beam within the ATR crystal, generating more evanescent waves. This increases the overall path length of the IR beam through the sample, thereby enhancing the sensitivity.

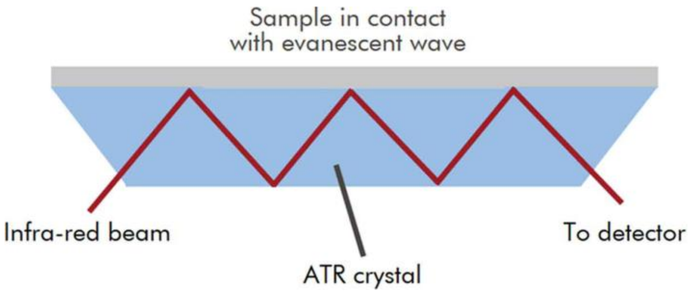

Figure R1: Reprinted with permission from reference: *Valand, R., et al, Food Additives & Contaminants: Part A, 37(1), 19–38.*

The sensitivity also depends on the sample preparation. To achieve the significant intensity of the intermediates formed during the reaction, the catalyst loading on the carbon paper substrate was increased. The catalyst coated carbon paper was placed very close to the Si window which ensured interaction of the evanescent wave with the catalyst surface.

A significant intensity of the peaks was observed at high potentials of -1.45 V where the current density was -70 mA cm^{-2}. We believe that the surface concentration of these intermediates was enhanced under this applied potential. The peaks were matched with the reported literature to further support the analysis.

Comment 3: I get the impression that the candidate seems to think that changing a half reaction of a given electrochemical reaction changes the energy efficiency of a reaction. It changes the potential, but it also changes the energy needed to drive the reaction as these two are coupled, and thus changing the half reaction has no effect on energy efficiency. I think it would be beneficial if the student could make corrections in re-analysing the energy efficiencies of the urea part of the thesis.

Response 3: We agree with reviewer, that the energy efficiency is dependent on both the thermodynamic and kinetic parameters. Here, we have calculated the energy efficiency for hydrogen production with urea oxidation and oxygen evolution reaction using $Pd/Ni(OH)_2$ catalyst as follows:

According to Faraday's law : $Q = nF$

HER: $2H^+ + 2e^- \rightarrow H_2$ $n = 2$

Therefore, to produce 1 mole of H_2, $Q = 2 \times 96485 = 192970$ C/mol

We Know, Energy = Power × time = $V \times I \times t = V \times Q$

Hence, the energy required to achieve a current density of 100 mA cm^{-2} is calculated as follows:

For urea assisted hydrogen evolution reaction, with UOR as the counter reaction, the voltage required is 1.35 V. Hence, the energy required to produce 1 mol of H_2 would be:

$$E = 1.35 \times 192970 = 260{,}509.5 \text{ J/ mol}$$

Since 1kWh = 3600000J

Therefore, $E = 260509.5/3600000 = 0.072$ kWh/mol

To produce 1kg of H_2, $E = (0.072 \times 1000)/2 =$ **36 kWh/kg$_{H2}$**

For the conventional hydrogen evolution reaction with OER as the counter reaction, the voltage required is 1.55 V. Hence, the energy required to produce 1 mol of H_2 would be:

$$E = 1.55 \times 192970 = 299{,}103.5 \text{ J/ mol}$$

Since 1kWh = 3600000J

Therefore, E = 299103.5/3600000 = 0.083 kWh/mol

To produce 1kg of H_2, E = (0.083 × 1000)/2 = **41.5 kWh/kg$_{H2}$**

Therefore, the UOR-HER system demonstrates a reduction in energy consumption than a conventional water electrolyzer to produce 1 kg of hydrogen.

Comment 4: I was not completely convinced that the candidate understood what causes the Tafel slope to have a given value. I think it would be beneficial if the student could make corrections in fundamental explanation of why Tafel slopes shift?

Response 4: The Tafel equation is derived from the Butler Volmer equation, and it connects the rate of the reaction with the overpotential.

$$\boldsymbol{\eta = \frac{2.303RT}{\alpha F}\, log\; i - \frac{2.303RT}{\alpha F}\, log\; i_o}$$

$$\boldsymbol{\eta = \beta\; log\; i + constant}$$

Here, $\boldsymbol{\beta = \frac{2.303RT}{\alpha F}}$ and is determined from the slope of the Tafel plot. η stands for overpotential, i stands for current density, i_o stands for exchange current density, α stands for transfer coefficient, , R stands for universal gas constant and T stands for temperature

The Tafel slope is used to determine the transfer coefficient (α). The transfer coefficient is a measure of the fraction of the applied energy that is required to drive the redox reaction. From, the above equation, the Tafel slope is inversely proportional to the value of the transfer coefficient. Hence, the lower the Tafel slope value, the higher the value of the transfer coefficient indicating faster reaction kinetics.

From, the intercept of the Tafel plot, the value of the exchange current density (i_o) can be determined. The exchange current density indicates the current flowing in both the anodic and cathodic directions at equilibrium. The higher the value of i_o the faster is the exchange of the ions and charge across the electrode/electrolyte interface.

Comment 5: The work on the CO_2 adsorption on Pd was unclear as CO_2 does not typically adsorb on metals. This did not influence the rest of the work, so I was just a bit confused of what was going on. the student should clarify the experiments done in regard to CO_2 adsorption on Pd.

Response 5: CO_2 adsorption has been studied on Pd and has been reported in the literature in the following references:

1. M.-P. Habas et al., Surface Science, 1999, 431, 208–219
2. Jose A. Hinojosa, Jr. et al, J. Phys. Chem. C 2012, 116, 4, 3007–3016
3. Renata Sechi et al, J. Phys. Chem. A 2023, 127, 21, 4596–4608
4. R. Pothu et al, Mat. Sci. for Energy Tech., 2023, 6, 484–492

During urea electrooxidation, CO_2 is generated as a byproduct. According to theoretical studies by Daramola et al. (*J Phys Chem A, **2010**, 114 (43), 11513–11521*), the desorption of CO_2 from the NiOOH site is the rate-determining step, which limits the overall catalytic activity.

In this study, CO_2-TPD and Linear Sweep Voltammetry (LSV) under CO_2 purging were employed to investigate CO_2 interactions with $Ni(OH)_2$ and $Pd/Ni(OH)_2$. The CO_2-TPD results revealed two prominent desorption peaks at 182.6 °C and 434.2 °C for $Ni(OH)_2$. CO_2 TPD for Pd also shows two prominent peaks at 125 °C and 383 °C. The peak at higher temperatures is about 50 °C lower in the case of Pd as compared to $Ni(OH)_2$. On the other hand, $Pd/Ni(OH)_2$ prepared by $NaBH_4$ reduction shows no peak at lower temperatures but a very strong peak at 412 °C, suggesting a strong binding affinity for CO_2 by Pd dispersed on $Ni(OH)_2$. The comparison of the high temperature desorption peaks indicate that the incorporation of Pd weakens the interaction of CO_2 to $Ni(OH)_2$.

LSV measurements following CO_2 purging further corroborated this. $Ni(OH)_2$ showed decrease in catalytic activity within 10 minutes of CO_2 exposure, whereas $Pd/Ni(OH)_2$ retained activity for up to 25 minutes. These experimental findings were supported by theoretical calculations, which showed a reduced CO_2 desorption energy upon Pd incorporation, as illustrated in the figure below. The theoretical findings have been published in *N. Mathew et al, Chem. Asian J. 2025, 20, e202401188.*

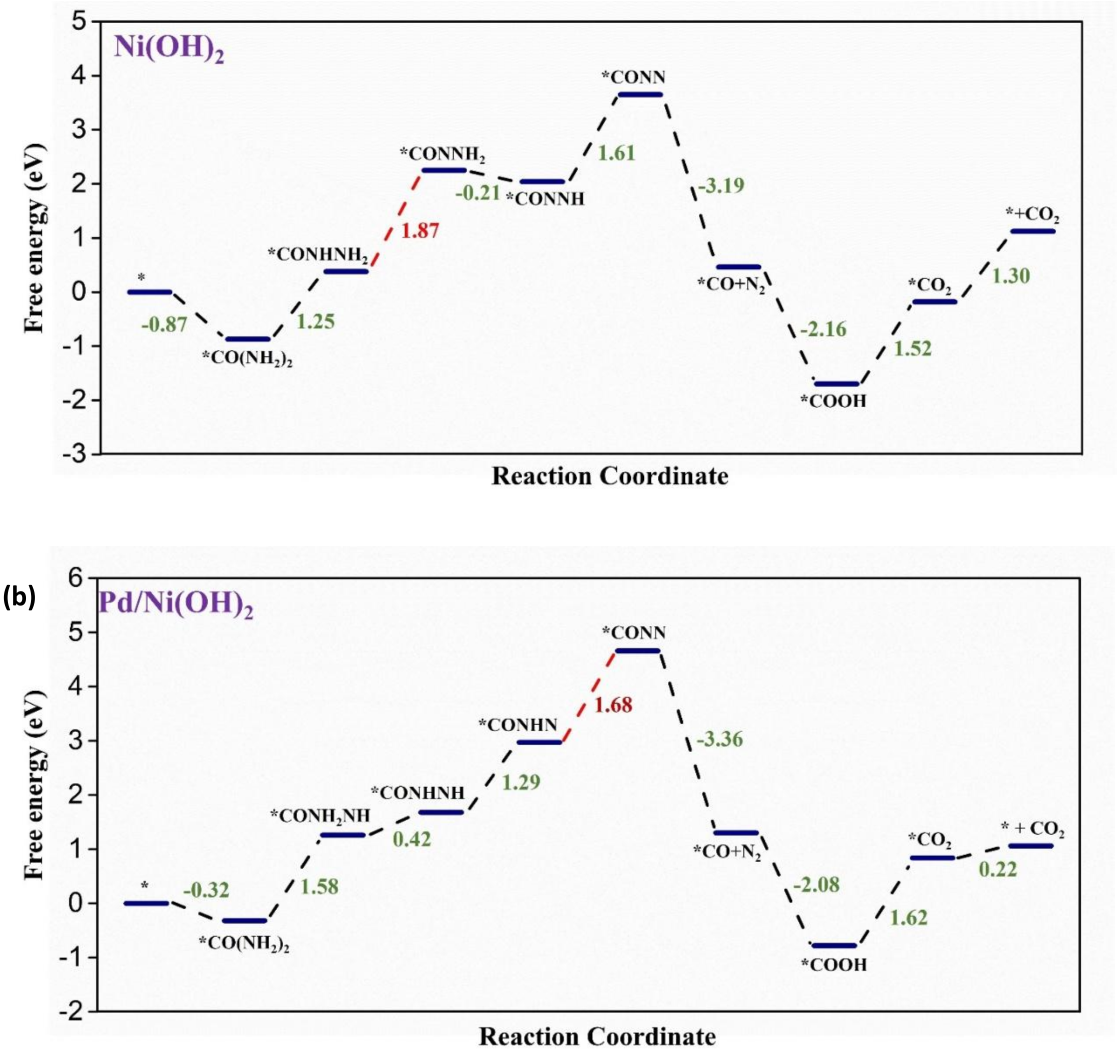

Figure R2: Energy profile diagram of the urea oxidation on **(a)** $Pd/Ni(OH)_2$ and **(b)** $Ni(OH)_2$ surface